ENHANCING THE PERFORMANCE OF PV SYSTEM IN DUSTY ENVIRONMENT

By

Adel Aldihani

Thesis Submitted in Partial Fulfilment of Requirements for the Degree of

Doctor of Philosophy

Department of Mechanical Engineering
School of Engineering
The University of Birmingham
Edgbaston, Birmingham, UK
May - 2017

ABSTRACT

Recently, Solar Photovoltaic has been reported to be one of the fastest growing renewable energy technologies for electricity generation due to its eco-friendly and flexible operation. Solar Concentrated Photovoltaic can enhance the performance of photovoltaic by increasing the received radiation, a technology that is developing and further investigation is needed to improve the overall performance. Kuwait is blessed with abundant solar energy reaching 2100 kW.hr/day/year but suffers from frequent dust storms and high ambient temperature particularly in the summer season which adversely affect the performance of photovoltaic. The aim of this research is to investigate the effect of dust on the performance of photovoltaic panels in Kuwait and develop a Concentrated PV system utilising three dimensional solar concentrators with water cooling to maintain low PV module temperature. A detailed investigation was carried out to develop a 3D concentrator for the Pseudo-Squared shaped PV cells (3D-PSCPV) including optical, electrical and thermal performance under the effect of dust where raw dust particles from Kuwait were deposited on the aperture of the concentrators and water cooling channels were attached underneath the cells.

The optical performance of clean and dusty 3D-PSCPV systems was investigated through advanced ray tracing techniques using OptisWorksTM software. The optical model was developed using the optical characteristics of the concentrator material and geometry, the optical properties of the concentrator cover and the measured optical properties of the Kuwaiti raw dust including size, reflectivity and transmissivity. Results showed that with the increase of the concentrator surface reflectivity, the optical efficiency and irradiance uniformity improved where the highest optical efficiency of 91.6% was achieved with reflectivity of 90%. The optimal concentrators' height for concentration ratio of 2X, 4X and 6X are 45, 145 and 250mm, respectively. While, the achieved optimal side angles of the concentrators are 56°, 60° and 70° for concentration ratios of 2X, 4X and 6X, respectively. Regarding the effect of dust on the system efficiency, results showed that the average irradiance received by the PV was reduced by up to 17%.

Using the predicted irradiance from the optical modelling due to the accumulated dust, an electrical model for the PV was developed with Engineering Equation Solver (EES) software to predict the electrical performance of the 3D-PSCPV in terms of short circuit current, open circuit voltage, maximum power and efficiency. Results revealed that the short-circuit current of non-concentrated PV module (1X) at 1000 W/m2 incoming irradiance dropped by 26.25% due to dust layer with thickness of 80 micrometre. While, the change were 12.65%, 14.65% and 14.71% for 3D-PSCPV with concentration ratios of 2X, 4X and 6X, respectively. COMSOL Multi-physics software was used to model the thermal performance of the 3D-PSCPV with water cooling channels attached underneath the PV cells for both dusty and clean conditions. Results, indicated that PV module temperature can be maintained at 25.5, 26.5, 28.6 and 29 °C for concentration ratios 1X, 2X, 4X and 6X, respectively with water inlet velocity of 0.037 m/s.

Indoor and outdoor experimental results showed that the optical, electrical and thermal performance of the water cooled 3D-PSCPV were in good agreement with the modelling results giving a deviation of 7%, 2% and 5% respectively. Experimental results showed that using cooling, the overall system efficiency has improved to reach 16% for the 2X dusty concentrators compared to 9% for dusty concentrator without cooling.

ACKNOWLEDGEMENTS

Praise be to Allah for his blessing, assistance and guidance to the achievement of this thesis. I express my sincere gratitude to Dr Raya Al-dadah my supervisor for her patience, guidance and support throughout my research study. Her supervision supported me throughout my study, research papers, and revising my work. Dr. Raya Al-dadah has supported me emotionally and academically throughout the difficult moments to complete this research. I am deeply thankful to Dr Saad Mahmoud for his support and valuable ideas, support and guidance during my research. I would like to thank Mr Simon Rowan for assisting me to assemble and build my experiment setups. My deepest sincere appreciation goes to my parents for their prayers, my Wife for her support and patience throughout my PhD study. I am greatly thankful to all my colleagues and best friends in Birmingham, Abdulmaged, Ali, Abdulrahman, Suliman, Ahmed and Bala.

Adel Aldihani

2017

CONTENTS

ABSTRACT I

ACKNOWLEDGEMENTS III

CONTENTS IV

LIST OF FIGURES X

LIST OF TABLES XVII

ABBREVIATIONS XVIII

NOMENCLATURE XIX

LIST OF PUBLICATIONS XXI

CHAPTER 1 1

1. INTRODUCTION 1

1.1 General background 1
1.2 Solar energy potential in Kuwait 2
1.3 Research aim and objectives: 4
1.4 Thesis Outlines 5

CHAPTER 2 7

2 LITERATURE REVIEW 7

2.1 Introduction 7
2.2 Photovoltaic technology 7
  2.2.1 Crystalline silicon (C-Si) PV Cells 8
  2.2.2 Thin film (TF) PV cells 9
  2.2.3 Multijunction (MJ) PV cells 9
  2.2.4 PV cell current and voltage characteristics (I/V curve) 10
  2.2.5 Photovoltaic cell circuit modelling 12
  2.2.6 Effect of irradiance variation on PV 14
  2.2.7 Effect of PV cell operating temperature 15
2.3 Dust effect on PV performance 16
  2.3.1 Experimental Studies of dust effect on PV 18
    2.3.1.1 The effect of Inclination Angle 19
    2.3.1.2 The attenuation of light by dust 20
    2.3.1.3 PV electrical performance under dust accumulation 23
  2.3.2 Theoretical studies of dust effect on PV 25
2.4 Solar concentrators 27
    2.4.1 Concentration ratio 28

2.4.2 Concentrator acceptance angle 28
2.4.3 Solar concentrated system types and categorises 29
2.5 Review on concentrated Photovoltaics (CPV) 31
2.5.1 Low concentration (CPV) 32
2.5.2 Medium concentration (CPV) 34
2.5.3 High concentration (CPV) 36
2.6 CPV cooling systems 38
2.6.1 CPV with active cooling systems 39
2.6.2 CPV with passive cooling systems 42
2.7 Review on CPV performance in dusty condition 45
2.8 Ray tracing modelling 48
2.9 Summary 49
CHAPTER 3 51
3 Outdoor Experiment in Kuwait 51
3.1 Introduction 51
3.2 Kuwait environment: 51
3.2.1 Weather data collection 51
3.2.2 Solar radiation availability 52
3.2.3 Ambient temperature 55
3.2.4 Atmospheric dust 56
3.2.5 Wind speed 57
3.3 Outdoor experimental setup and analysis procedure 58
3.3.1 Measurement setup and procedure 59
3.3.2 Visual Inspections of Dust Accumulation Uniformity 63
3.3.3 In plane measured solar radiation 64
3.3.4 Measured PV power output 66
3.3.5 Effect of ambient temperature on the PV 68
3.3.6 Influence of dust on PV modules efficiency 70
3.4 Physical and optical characteristics of dust 71
3.5 PV modules performance degradation 75
3.5.1 Long term dust accumulation effects 75
3.5.2 Influence of dust on short-circuit current 78
3.5.3 Influence of dust on open-circuit voltage 79
3.5.4 Current/voltage (I/V) and power/voltage (P/V) Characteristics of clean and dusty PV module 80

3.5.5 Dust accumulation ratio.......... 82
3.6 Summary 84
CHAPTER 4 85
4 Optical Simulation and Concentrator Development.......... 85
4.1 Introduction 85
4.2 3D Ray tracing model development.......... 85
4.2.1 3D-PSCPV concentrator geometry development.......... 88
4.2.2 3D Ray tracing modelling process (OptisWorks^{TM}) 90
4.3 3D-PSCPV optical simulation results 95
4.3.1 Effects of height on optical efficiency 96
4.3.2 Effect of surface reflectivity.......... 100
4.4 The dust effects on 3D-PSCPV optical performance.......... 109
4.4.1 Dust particles distribution 110
4.4.2 Dust particles optical boundary conditions 111
4.4.3 Dusty 3D-PSPCV simulation results.......... 114
4.5 3D-PSCPV development and assembly 123
4.5.1 3D-PSCPV entrance cover 124
4.5.2 Engineering graphics development of planes methods 125
4.5.3 3D-PSCPV reflector materials 128
4.6 Summary 130
CHAPTER 5 131
5 Electrical and Thermal Modelling.......... 131
5.1 Introduction 131
5.2 3D-PSCPV electrical modelling.......... 131
5.2.1 PV module electrical modelling results: 132
5.3 Thermal modelling 134
5.3.1 Cooling system geometry.......... 135
5.3.2 Thermal modelling governing equations.......... 136
5.3.3 Thermal model setup and assumption.......... 139
5.3.4 Meshing and solver 140
5.4 Thermal and electrical modelling results 142
5.4.1 Effect of cooling on PV module and outlet temperature.......... 145
5.4.2 Effect of cooling on the I_{sc} and V_{oc} 146
5.4.3 Effect of cooling on the maximum power.......... 148
5.4.4 Effect of cooling on the electrical efficiency 150

5.5 3D-PSCPV performance in Kuwait 151
    5.5.1 3D-PSCPV system optical performance 151
    5.5.2 PV module predicted temperature with different concentration ratios 152
    5.5.3 Predicted electrical power output at different concentration ratios.......... 154
    5.5.4 Predicated efficiency at different concentration ratio 154
5.6 Summary 156
CHAPTER 6 158
6 CPV Experimental Setup.. 158
6.1 Introduction 158
6.2 Solar simulator types 158
6.3 Continuous solar simulator (light source) 160
    6.3.1 Light spectral characteristic.. 161
    6.3.2 Temporal instability characteristic 162
    6.3.3 Irradiance non-uniformity 163
    6.3.4 Light rays collimation and integrated lens system 163
6.4 Solar simulator characterisation experimental setup 164
    6.4.1 Solar simulator characterisation results... 166
6.5 Indoor and outdoor experimental setups 170
    6.5.1 Dust distribution methods 174
    6.5.2 3D-PSPCV receiver (PV Module) 176
    6.5.3 Cooling channels of the 3D-PSCPV 178
6.6 Measuring devices 179
    6.6.1 I/V curve measurements.. 179
    6.6.2 Radiation flux sensor.. 182
    6.6.3 Surface and cooling water temperature measurements 183
    6.6.4 Flow meter.. 184
6.7 Calibration and uncertainty of the instruments 185
    6.7.1 Calibration of the flow meter 186
    6.7.2 Calibration of the surface thermocouples... 186
    6.7.3 Uncertainty in PV electrical output 188
6.8 Experimental procedure for various performance characterisation.............. 188
    6.8.1 Optical performance characterisation... 188
    6.8.2 Electrical performance characterisation 189
    6.8.3 Thermal performance characterisation.. 190
6.9 Summary 190

CHAPTER 7 192

7 Indoor and Outdoor Experimental Results and Validation of Simulation 192

7.1 Introduction 192

7.2 Optical results.. 192

7.2.1 Optical performance of the dusty glass cover 192

7.2.2 Indoor optical experimental results of 3D-PSCPV 195

7.2.3 Outdoor optical experimental results of 3D-PSCPV............................... 198

7.3 Thermal experimental results 201

7.3.1 Temperature distribution under concentration in indoor condition.......... 201

7.3.2 Variation of PV module Temperature with cooling water inlet velocity in indoor condition 202

7.3.3 Temperature distribution under concentration in outdoor condition........ 204

7.3.4 Variation of PV module Temperature with cooling water inlet velocity in outdoor condition 205

7.3.5 Variation of Thermal power with cooling water inlet velocity in outdoor condition.. 207

7.4 Electrical experimental results and validation.. 208

7.4.1 Indoor experimental results 209

7.4.1.1 Indoor I/V curves characteristics.. 209

7.4.1.2 Effect of dust accumulation on the power output at different concentration ratios 211

7.4.1.3 Effect of dust accumulation on the voltage and current characteristics at different concentration ratios.. 214

7.4.1.4 The Effect of dust accumulation on 3D-PSCPV system Efficiency .. 216

7.4.1.5 Variation of Fill Factor with concentration ratio and PV Temperature 218

7.4.1.6 Effects of water cooling on the electrical performance of the dusty 3D-PSCPV.. 220

7.4.2 Outdoor experimental results 223

7.4.2.1 Water cooling effect on the I/V curve characteristics for clean and dusty module 224

7.4.2.2 Cooling effect on the maximum power characteristics 226

7.4.2.3 Cooling effect on the 3D-PSCPV efficiencies 227

7.5 Summary 229

CHAPTER 8 232

CONCLUSIONS AND RECOMMENDATIONS 232

8.1 Introduction 232

8.2 Conclusions 233
8.2.1 Optical performance 233
8.2.2 Electrical performance 234
8.2.3 Thermal performance 236
8.3 Future work 236
REFERENCES **238**
Appendix A **248**
Appendix B **249**

LIST OF FIGURES

Figure 1.1 Image of dust storm crossing Kuwait captured by NASA Earth Observatory [6].....3
Figure 1.2 Solar resource, Global Horizontal Irradiance [GHI], in Kuwait annual [8]...............4
Figure 2.1 A schematic diagram of a basic PV [10] 8
Figure 2.2 Two silicon PV cell types: (a) Monocrystalline silicon (b) and Multi-crystalline silicon 9
Figure 2.3 Standard I-V curve characteristics for C-Si PV cell connected to load with variable resistive. 10
Figure 2.4 An electrical circuit diagram of an ideal PV cell [20]. 12
Figure 2.5 PV cell with single-diode R_{sh} and R_s [20]. 13
Figure 2.6 Impact of R_s on the I-V curve demonstrated with increased R_s [21]. 14
Figure 2.7 Impact of R_{sh} on the I-V curve demonstrated with decreased R_{sh} [21]. 14
Figure 2.8 The effect of different Irradiance on the PV cells, and primarily on the (I_{sc}). 15
Figure 2.9 The effect of different cell temperature on the PV cells, and primarily on the (V_{oc}). 15
Figure 2.10 Monthly average visibility and dust fallout in Kuwait year 2013 [25]. 16
Figure 2.11 Accumulated dust on inclined PV modules surface mounted in Kuwait Institute for Scientific Research (KISR). 17
Figure 2.12 Dust accumulation changing factors [28] 18
Figure 2.13 Light transmission losses for glass samples tilted at 0°, 45°, and 90°,(a) annual average transmission loss for daily cleaned samples, (b) annual average transmission loss for weekly cleaned samples, (c) transmission loss of never manually cleaned samples after 56 days, (d) transmission loss of never manually cleaned samples in after 182 days, [32]. 20
Figure 2.14 The change of reflectance as function of wave lengths for clean and uncleaned mirrors exposed in New Mexico. Dust accumulation density increases from (a) to (d) [35]. .21
Figure 2.15 Measured transmittance loss of glass at different dust density and wavelengths [25]. 22
Figure 2.16 Light spectral transmittance of glass sample as a function of dust depositions: (a) lower dust depositions and (b) higher dust depositions. 22
Figure 2.17 (a) Comparison of current and voltage characteristics for clean and unclean PV modules installed outdoor. (b) Change of current and voltage output at different dust concentrations [36] 24
Figure 2.18 Types of solar concentrator systems [58]. 29
Figure 2.19 Different designs of solar concentrators: (a) Parabolic concentrator (b) Fresnel lens (c) Central receiver system with reflectors. (d) Tubular receivers (e) Plane receiver (f) Asymmetric compound parabolic concentrator [58]. 30
Figure 2.20 (a) Geometrical design of a single and (b) Geometrical linear PV cell concentrator [70]. 31
Figure 2.21 Ray tracing illustration for PV/T systems with mirror reflectors [73]. 32
Figure 2.22 Low concentrating compound parabolic concentrator integrated photovoltaic/thermal systems [74]. 33
Figure 2.23 (a) Graphic illustration of the modelled photovoltaic concentrator (ACPPVC) [75], (b) asymmetric compound parabolic and non-concentrating photovoltaic concentrators under outdoor experimental characterisations [76]. 34
Figure 2.24 The (EUCLIDES) solar PV system [79]. 35

Figure 2.25 (a) parabolic trough photovoltaic/thermal concentrator (b) Cross-section view of a receiver [80]. 36
Figure 2.26 (a) Photograph of (AMONIX) 25 kW CPV system. (b) Representation of the system [83]. 37
Figure 2.27 Graphics illustration of active and passive cooling designs[86]. 38
Figure 2.28 Active cooling design with liquid for multijunction PV cell under 2000X [87]. ..39
Figure 2.29 PV heat tube cooling system [89]. 40
Figure 2.30 Assembly of liquid immersion concentrated PV receiver [91]. 41
Figure 2.31 Heat tube cooling system with aluminium fins and copper saddle [95]. 42
Figure 2.32 Photovoltaic/thermal CPC solar concentrator attached to fins[98]. 43
Figure 2.33 Diagram of heat tube based solar cooling system 44
Figure 2.34 The current and voltage output characteristics of concentrated PV module with different amount of dust deposition: (a) clean mirror surface; dust rate at values of 0.85, 1.85 and 5.4 g/cm^2 for (b), (c) and (d), respectively [106]. 46
Figure 3.1 Solar radiation coming from the sun to the earth surface which incident on a particular place at specific latitude relies on air mass condition [121]. 52
Figure 3.2 Monthly average solar radiation availability in Kuwait..53
Figure 3.3 The average daily sunlight hours in year 2013 [123]..54
Figure 3.4 Monthly average clearness index in Kuwait. 55
Figure 3.5 The average maximum and minimum ambient temperature in Kuwait year 2013 [125] 56
Figure 3.6 Recorded (KEPA) measurement of average daily accumulated dust weight and visibility rate for the year 2013 in Kuwait [67]. 57
Figure 3.7 The monthly average wind speed and the number of days of dust storm. 58
Figure 3.8 Procedure to evaluate the impact of accumulated dust on PV performance. 59
Figure 3.9 UP: Installed PV Modules covered by dust and daily cleaned in KISR. Down: (A) Modules support frame (B) module temperature sensor (C) Data logger (D) PC cabinet (E) IV tracer (F) In plane Pyranometer (G) Wind speed and ambient temperature sensors. 60
Figure 3.10 Experimental data acquisition system at KISR. 62
Figure 3.11 Photos of the measured PV modules at separate days of the year. 64
Figure 3.12 Average hourly in plane solar radiation measured in KISR site for year 2013 65
Figure 3.13 Average monthly in plane irradiance and power output of clean and dusty PV modules during 12 months. 66
Figure 3.14 Percentage losses of the measured power output of dusty PV modules with respect to the clean PV module. 68
Figure 3.15 Monthly average measured ambient and PV modules temperatures. 69
Figure 3.16 Monthly average PV module efficiency and ambient temperature........................70
Figure 3.17 Particles size distribution of the dust samples. 72
Figure 3.18 Image of dust sample collected from the dusty modules surface magnified 30. ...72
Figure 3.19 Procedures of dust optical properties measurements [134]. 73
Figure 3.20 left: The spectral transmittance and reflectance dust sample was determined utilising a spectrophotometer. Right: 0.19 (mm) clear tape sample coated by dust. 73
Figure 3.21 The reflectivity of different grain sizes of dust sample. 74
Figure 3.22 The transmissivity of different dust particles sizes. 75
Figure 3.23 Amount of solar radiation in Kuwait during the 30th of July 2013. 76
Figure 3.24 Variation of maximum power generated by clean and dusty PV modules. 77
Figure 3.25 Variation of PV temperature of clean and dusty modules 78

Figure 3.26 Variation of short-circuit current output generated by the clean and dusty PV modules. 79
Figure 3.27 Change of open-circuit voltage output generated by the clean and dusty PV modules. 80
Figure 3.28 The I/V and P/V curves characteristics of clean and dusty modules at solar irradiance 1000 w/m^2 at an average module temperature of 41°C. 81
Figure 3.29 Synchronised dust accumulation ratio for PV modules to illustrate the difference throughout the outdoor testing period along with measured environmental factors. 83
Figure 4.1 Schematic drawing of the reflection law. 86
Figure 4.2 Behaviour of light rays in a concentrator. 87
Figure 4.3 Receiver area of the3D-PSPCV design. 88
Figure 4.4 3D view of the 3D-PSCPV model developed in SolidWorks. 89
Figure 4.5 The variation of the concentration ratio with the concentrator entrance aperture area of the 3D-PSCPV. 90
Figure 4.6 Flow chart of the simulation procedure of 3D- PSCPV utilising ray-tracing method. 91
Figure 4.7 optical irradiance distributions on the entrance aperture of the 3D-PSCPV 93
Figure 4.8 The concentrated light-ray direction acquired from the 3-D PSCPV demonstrated in (OptisWorks^{TM}). 94
Figure 4.9 The 3D-PSCPV entrance and receiver apertures screened with 2D solar radiation detectors. 95
Figure 4.10 Difference of the concentrators' height as a function of the optical efficiency for the optimised 3D-PSCPV with 2X, 4X and 6X. 97
Figure 4.11 Comparative 2D illustration of the three optimised 3D-PSCPV. 98
Figure 4.12 Distribution of irradiance with surface reflectivity of 90% at the entrance aperture and receiver aperture with different concentration ratio 99
Figure 4.13 Distribution of the received irradiance for the 3D-PSCPV with different reflectivity values at (GCR=2): (a) 3D contour mapping, (b) 2D distribution on the horizontal line. 102
Figure 4.14 Distribution of the received irradiance for 3D-PSCPV with different reflectivity values at (GCR=4): (a) 3D contour mapping, (b) 2D distribution. 104
Figure 4.15 Distribution of the received irradiance for 3D-PSCPV with different reflectivity values at (GCR=6): (a) 3D contour mapping, (b) 2D distribution. 107
Figure 4.16 Average received irradiance of clean 3D-PSPCV at different surface reflectivity. 108
Figure 4.17 The concentrator uniformity factor of four surfaces reflectivity's 90%, 80%, 70% and 60% at different concentration ratios of 2, 4 and 6. 109
Figure 4.18 The refracted light-ray when it passes from the air medium to a dust grain medium. 112
Figure 4.19 The light-rays transmission across a modelled dust grains. Left: The grain consists of a core and coating. Right: A close pictorial on the modelled crossing point between the coating, core and the air surrounding dust grain 112
Figure 4.20 The modelling of dust grains on the 3D-PSCPV entrance aperture covers with ray-tracing method (Optiswork^{TM}). 113
Figure 4.21 The optical irradiance distributions on a dusty entrance aperture of the 3D-PSCPV,(A) irradiance horizontal distribution and (B) 2D irradiance distribution with a closer pictorial of the dust distribution. 114

Figure 4.22 Optical irradiance distribution of the dusty 3D-PSCPV with different reflectivity values at (GCR=2): (a) 3D contour mapping, (b) 2D distribution on the horizontal line. 116
Figure 4.23 Optical irradiance distribution of the dusty 3D-PSCPV with different reflectivity values at (GCR= 4): (a) 3D contour mapping, (b) 2D distribution on the horizontal line. 118
Figure 4.24 Optical irradiance distribution of the dusty 3D-PSCPV with different reflectivity values at (GCR= 6): (a) 3D contour mapping, (b) 2D distribution on the horizontal line 120
Figure 4.25 Optical efficiency of clean and dusty 3D-PSPCV conditions at different surface reflectivity 121
Figure 4.26 Average received irradiance of clean and dusty 3D-PSPCV at different surface reflectivity 121
Figure 4.27 Actual optical concentration ratio for different 3D-PSPCV at different surface reflectivity 122
Figure 4.28 The dust accumulation effects on 3D-PSCPV uniformity factor......123
Figure 4.29 3D-PSCPV system aperture cover dimensions......124
Figure 4.30 3D-PSPCV housing 125
Figure 4.31 EGDP processes of the 2X, 4X and 6X concentration ratio profiles......127
Figure 4.32 (a) EGDP methods employed to build the 3D-PSPCV frame and support (b) Experimental model of 3D-PSCPV built with mirrors; (c) PV module jointed with 3D-PSCPV receiver......128
Figure 4.33 Reflectivity measurements for the 3D-PSCPV side reflectors. 129
Figure 5.1 I/V curve of the clean and dusty PV modules at various irradiance and module temperature (non-concentrated condition) 133
Figure 5.2 Power characteristics of the clean and dusty non-concentrated PV modules at 1000, 800, 600, 400 irradiance and 25C module temperature 134
Figure 5.3 3D-CAD drawing of the 3D-PSCPV with cooling channels......135
Figure 5.4 3D-PSCPV Cooling channels geometry obtained from Solidworks^{TM}......136
Figure 5.5 PV module assembly placed at the cooling channels 136
Figure 5.6 COMSOL mesh applied for the thermal simulation of a 3D-PSCPV cooling system 141
Figure 5.7 Average PV module temperature with different mesh type of the dusty 3D-PSCPV at different concentration ratios (2X, 4X and 6 X)......141
Figure 5.8 Temperature profile on PV module surface obtained by COMSOL at different concentration ratios in dusty condition. 142
Figure 5.9 Water velocity profile of the cooling channels......143
Figure 5.10 3D models of the cooling channels showing heat transfer mechanisms from the inlet to the outlet......144
Figure 5.11 Temperature variation in the concentrated PV module with water cooling at velocity of 0.018m/s and concentration ratio of 6X......144
Figure 5.12 Variation of PV module assembly back surface temperatures with water velocity at different concentration ratios......146
Figure 5.13 Influence of water velocity on the outlet temperature of 3D-PSCPV at different concentration ratios 146
Figure 5.14 Variation of open-circuit voltage with water velocity at different concentration ratios......147
Figure 5.15 Variation of short-circuit current with water velocity at different concentration ratios......147
Figure 5.16 Variation of the maximum power output and PV module temperature with water velocity at different concentration ratios......149

Figure 5.17 Variation of the maximum power output gain with the inlet velocity 149
Figure 5.18 Electrical efficiency of the cooled and uncooled dusty 3D-PSCPV compared with clean 3D-PSCPV electrical efficiency at different concentration ratios 150
Figure 5.19 Predicted optical losses due to dust accumulation on 3D-PSCPV during July....152
Figure 5.20 Temperature contours of the PV module assembly with cooling channels at concentration ratio of 6X and water velocity pf 0.037m/s 153
Figure 5.21 Predicted PV module operating temperature of 3D-PSCPV with and without cooling in both conditions clean and dusty during July 153
Figure 5.22 Predicted cooling effect on 3D-PSCPV maximum power with different optical concentration ratio..154
Figure 5.23 Predicted electrical efficiency of the dusty 3D-PSPCV with cooling effect 155
Figure 5.24 Predicted maximum power output losses due to dust accumulation and gain with cooling for the 3D-PSCPV 156
Figure 6.1 The installed continuous solar simulator for the indoor experimental of the 3D-PSCPV [175]...160
Figure 6.2 Schematic drawing of the solar simulator setup and controls...............................161
Figure 6.3 The Spectral distributions for MSR HMI 2500 W/GS lamp operated in continuous solar simulator Compared to the sun Spectral distributions [177] 162
Figure 6.4 Solar simulator Photometric Beam range with MSR lamp[175] 163
Figure 6.5 Pyranometer used in mapping the testing area. 164
Figure 6.6 Photograph of the solar simulator characterisation test 165
Figure 6.7 Schematic drawing of the irradiance mapping system..166
Figure 6.8 Irradiance mapping measurement regions 167
Figure 6.9 Irradiance distributions within a region of 310 x 310 mm^2 167
Figure 6.10 Non-uniformity percentage of the used solar simulator compared to ASTM standard class C...168
Figure 6.11 Temporal instability percentage of the used solar simulator compared to the ASTM standard class C...169
Figure 6.12 (L) frame stainless steel employed to calculate the collimation angle of the continuous solar simulator 170
Figure 6.13 The light collimation angles of the continuous solar simulator at illumination area of 310X310 mm^2 170
Figure 6.14 Schematic diagram of the indoor test setup of 3D-PSPCV system 171
Figure 6.15 Photo of the indoor experimental setup of the 3D-PSCPV.................................172
Figure 6.16 Picture of the outdoor experimental set up (a) electrical and thermal test set up (b) optical test set up...173
Figure 6.17 Schematic of the outdoor experimental setup 173
Figure 6.18 dust sample sieving test setup...174
Figure 6.19 Total light transmission across 3M™ transparent film [185] 175
Figure 6.20 Schematic diagram of the measurements set up of dusty glass transmittance 176
Figure 6.21 Photo of the measurement set up of the dusty glass transmittance 176
Figure 6.22 The original PV silicon cell modified to a 130 mm PV module to operate with 3D-PSCPV receiver...177
Figure 6.23 PV module encapsulation layers and 3D-PSCPV receiver (PV module) dimensions (mm)...178
Figure 6.24 Photo of the Aluminium cooling channels..179
Figure 6.25 Electric circuit diagram for the I/V curve data acquisition system 181
Figure 6.26 Photo of the indoor IV curve and electrical parameters measurements..............181

Figure 6.27 Image of the radiant flux sensor utilised in the 3D-PSCPV receiver mapping....183
Figure 6.28 3D representation of the radiation mapping arrangement (nine sensors frame) ..183
Figure 6.29 Diagram showing the position of thermocouples at the rear of the 3D-PSCPV receiver (PV module) 184
Figure 6.30 Image of the flow meter used in the experimental work (indoor and outdoor) ...185
Figure 6.31 Calibration curve of the calculated flow rate and flow meter....186
Figure 6.32 Calibration procedure of the surface thermocouples 187
Figure 6.33 Calibration curve between surface thermocouple and RTD 187
Figure 6.34 Schematic diagram of the experimental optical test 189
Figure 7.1 Measurements of different irradiance level at different combination of layers.....193
Figure 7.2 Measurements of irradiance under dusty sample at different positions....194
Figure 7.3 Variation of dusty glass transmission for indoor and outdoor tests....194
Figure 7.4 Comparison between experimental and ray-tracing simulation results of the dusty samples light transmission at different irradiance input....195
Figure 7.5 Comparison between ray-tracing simulation and experimental optical efficiency results for concentration ratio of: a) 2X, b) 4X and c) 6X 196
Figure 7.6 Photograph of the concentrated irradiance distribution on the receiver of the 3D-PSCPV, (A) obtained experimentally, (B) obtained by ray-tracing (OptisWork^{TM}) simulation 197
Figure 7.7 Comparison of the ray-tracing simulation and experimental results of the dusty concentrator optical efficiency: (a) 2X, (b) 4X, (c) 6X....198
Figure 7.8 Variation of optical efficiency with the concentration ratio of the 3D-PSCPV in different conditions (uncovered, clean glass cover and dusty glass cover)....199
Figure 7.9 Comparison between experimental and simulation optical efficiency results of the 3D-PSCPV with different optical concentration ratios 200
Figure 7.10 Irradiance distribution at the central line (62.5mm-horzintal) of the 3D-PSCPV receiver for light incident angle of 0° with different concentration ratio: 2X, 4X and 6X......201
Figure 7.11 Measured temperatures for the 3D-PSCPV receiver at a constant incident radiation of 1000W/m^2 and 24°C room temperature....202
Figure 7.12 Comparison of the experiment PV module assembly back surface temperature with the predicted at different velocity and concentration ratios in dusty condition 203
Figure 7.13 Comparison of the experimental water outlet temperature with predicted at different concentration ratios 204
Figure 7.14 Temperature distribution at the horizontal line of the 3D-PSCPV receiver for light incident angle of 0° with different concentration ratio: (a) 2X, (b) 4X and (c) 6X....205
Figure 7.15 Change of the PV module average temperature with the inlet water velocity magnitudes at ambient temperature and wind speed of 26°C and 3 m/s, respectively....206
Figure 7.16 Comparison between experimental and simulation results....206
Figure 7.17 Thermal output power of 3D-PSCPV system at various water inlet velocity and concentration ratios 208
Figure 7.18 Indoor experiment of I/V characterisations of clean and dust 3D-PSCPV system at solar radiation intensity of 1000 W/m^2 and 24°C ambient room ambient temperature,(a)1X, (b)2X, (c) 4X and (d) 6X....210
Figure 7.19 Comparison of the experimental maximum power output with predicted at various concentration ratio in clean and dusty conditions 213
Figure 7.20 Variation of the average 3D-PSCPV receiver (PV module) temperature and maximum power with concentration ratio (in clean and dusty states) 213

Figure 7.21 Variation of the open-circuit voltage and average PV module temperature with change in concentration ratio under clean and dusty states....215
Figure 7.22 Variation of short-circuit current and average PV module temperature with change in concentration ratio under clean and dusty states....215
Figure 7.23 Variation of the short-circuit current and open-circuit voltage with change in concentration ratio under clean and dusty states....216
Figure 7.24 Variation of the electrical system conversion efficiency and maximum power out with concentration ratio under clean and dusty states....217
Figure 7.25 Difference of fill factor for 3D-PSCPV with and without dust at different concentration ratio....219
Figure 7.26 Comparison of PV module average temperatures between clean and dusty covers at different concentration ratio....219
Figure 7.27 Comparison of the experimental I/V curves with predicted at different concentration ratios....220
Figure 7.28 Comparison of the experimental P/V curves with predicted at different concentration ratios....221
Figure 7.29 Variation of the maximum power out of the dusty 3D-PSCPV at different inlet water velocity and concentration ratios. (Experimental and simulation)....222
Figure 7.30 Electrical efficiency of the cooled and uncooled dusty 3D-PSCPV compared with clean 3D-PSCPV electrical efficiency at different concentration ratios....223
Figure 7.31 Variation of the I/V curve characteristics with water cooling at ambient temperature and wind speed of 26°C and 3 m/s, respectively, in clean and dusty condition. (a) Non-concentrated, (b) 2X, (c) 4X, (d) 6X....225
Figure 7.32 Variation of the PV module maximum power with inlet water velocity magnitudes at ambient temperature and wind speed of 26°C and 3 m/s, respectively....226
Figure 7.33 System electrical efficiency of the CPV and non-concentrating systems with variation of concentration ratio and inlet velocity in clean and dusty conditions....228
Figure 7.34 3D-PSCPV total efficiency at clean and dusty condition....229

LIST OF TABLES

Table 2.1 Summaries of reported research on the effect of dust accumulation on PV 25
Table 2.2 Various CPV systems projects worldwide [71] 31
Table 2.3 comparison of CPV design using various Ray tracing software 49
Table 3.1 Types of data obtained from (KEPA) and (KISR) 51
Table 3.2 Recommended Average Day for Months and Values of n and δ [124]. 55
Table 3.3 Characteristics of PV Modules tested outdoor 60
Table 3.4 Accuracies related to the monitoring devices of the PV outdoor measurement........62
Table 3.5 The clean and dusty PV modules performance and parameters values at 1000 (W/m^2) and average module temperature of 41^{o}C 81
Table 4.1 Geometrical and optical characteristics of the 3D-PSCPV 97
Table 4.2 Dust grains physical properties. 111
Table 4.3 Glass performance data (Pilkington$^@$) [147] 124
Table 4.4 Characteristics of the 3D-PSCPV. 129
Table 5.1 the 3D-PSCPV receiver (PV module) data information 132
Table 5.2 Thermophysical properties of the PV module and cooling channels layers 140
Table 6.1 General specifications of Philips MSR HMI [176]. 161
Table 6.2 Temporal instability percentage allowance[179, 180]. 162
Table 6.3 Non-uniformity distribution allowance [179-181] 163
Table 6.4 The specifications of CMP11 pyranometer[182]. 164
Table 6.5 The optical and physical specifications of 3M™ clear adhesive film [185] 175
Table 6.6 Sensitivity of the radiant flux sensors [167]. 182
Table 6.7 Thermocouple specifications for surface temperatures 184
Table 6.8 Uncertainty results of PV module electrical parameters 188
Table 7.1 Comparison between simulation and indoor experimental of 3D-PSCPV electrical outputs at different concentration ratios and conditions (clean and dusty) 211
Table 7.2 PV temperature and output power at non-concentrated and concentrated system with cooling and without cooling at clean and dusty states 227

ABBREVIATIONS

2D	Two dimensional
3D	Three dimensional
3D-PSCPV	Three dimensional pseudo-square concentrator
ACPPVC	Asymmetric compound parabolic photovoltaic
ASTM	American Society for Testing and Materials
a-Si	Amorphous silicon
C-Si	Crystalline silicon
CdTe	Cadmium telluride
CIGS	Copper indium gallium (di) selenide
CPC	Solar collector
CPV	Concentrated photovoltaic
CUF	Concentrator uniformity factor
DNI	direct normal irradiance
EES	Engineering Equation Solver Software
EGDP	Engineering Graphics Development of Planes
EMPA	Swiss Federal Laboratories for Materials Science
GaAs	Gallium Arsenide
GaSb	Gallium antimonide
GHI	Global Horizontal Irradiance
GTA	Gas Tungsten Arc welder
HTSP	Silicone Heat Transfer Compound Plus
InP	Indium phosphide
KEPA	Kuwait Environment Public Authority
KISR	Kuwait institute for scientific research
ME	Ministry of Energy
Mono-Si	Monocrystalline
MJ	Multijunction
NREL	National Renewable Energy Laboratory
PCB	printed circuit board
PEG	Programmable Electric Guillotine
PV	Photovoltaics
PV/T	photovoltaic/ thermal system
STC	Standard test condition
TF	Thin film

NOMENCLATURE

Symbol	***Description***	***Unit***
A	total area of the PV module	(m^2)
AR_{Ext}	Exit aperture area	(m^2)
AR_{Ent}	Entrance aperture area	(m^2)
C_{FS}	Soiling capacity factor	(-)
C_{FS}	Ratio of actual annual energy of dusty PV	(W)
C_{FC}	Clean capacity	(W)
CR	Optical concentration ratio	(-)
CR_{solar}	Concentrated solar radiation on PV module	(W/m^2)
CR_{max}	Maximum concentration of concentrator	(-)
D	Diode	(-)
D_p	Particle diameter	(mm)
D_{eff}	Particles extinction efficiency	(%)
$Diff_d$	Mie's dust diffusing factor	(-)
D_h	hydraulic diameter	(mm)
E_{array}	Energy yield of PV array	(W)
E_{int}	total internal-energy	(W)
FF	Fill-factor	(-)
G_{sc}	Solar constant	(W/m^2)
G_m	Mass of Particles occupying the unit area	(mg)
G_{month}	Monthly average solar radiation	(W/m^2)
h	heat transfer coefficient by convection	($W/m^2.k$)
$\overline{H}$	Monthly average hemispherical radiation	(W/m^2)
$\overline{H_o}$	Monthly average extraterrestrial radiation	(W/m^2)
I_{sc}	Short-circuit current	(A)
I_m	Maximum current	(A)
I_0	Diode reverse bias saturation current	(I)
I_{rr}	Irradiance	(W/m^2)
$\overline{K}_T$	Clearness index	(-)
MPP	Maximum power point	(W)
N_p	Number of dust grains	(-)
Opticalη	Optical efficiency	(%)
P_{clean}	Power output of cleaned module	(W)
P_{dusty}	Power output of dusty module	(W)
P_{loss}	Power drop caused by dust accumulation	(W)
P_{month}	PV module maximum power	(W)
P_m	Maximum power	(W)
Q_{rad}	rate of heat transfer by radiation	(W)
$Q_{thermal}$	Thermal energy	(W)
Q_{cond}	Rate of heat transfer by conduction	(W)
Q_{conv}	Rate of heat transfer by convection in	(W)
R	Incoming radiation	(W/m^2)
R_{max}	maximum irradiance	(W/m^2)
R_{min}	minimum irradiance	(W/m^2)
Re	Reynolds number	(-)

Rsh	Shunt resistance	(Ω)
Rs	Series resistance	(Ω)
S	sensitivity of voltage output	(-)
ST_d	Spectral transmittance	(nm)
T	PV cell temperature	(°C)
Tinstability	Solar simulator Instability	(%)
T_{amb}	ambient temperature	(K)
T_{surf}	surface temperature	(K)
U_{water}	Inlet water velocity	(m/s)
U_{Sys}^2	Fixed errors	(-)
U_{random}^2	Random errors	(-)
V_{oc}	Open-circuit voltage	(V)
V_m	Maximum voltage	(V)
Vs	output voltage	(μV)

Greek	***symbol description***	***Unit***
α	Scattering of dust grains	(-)
δ	Solar declination	(°)
ΔT	temperature difference between the PV surface and fluid	(K)
Σu	convective stress-energy	(W)
ε	Surface emissivity	(-)
K	Boltzmann’s constant	(J/K)
λ	Wavelength of light	(nm)
n	Diode ideality factor	(-)
n	Refractive Index	(-)
n_1	Refractive index of air medium	(-)
n_2	Refractive index of dust grain medium	(-)
$\boldsymbol{\eta}_{electrical}$	PV module electrical efficiency	(%)
$\boldsymbol{\eta}_{Tref}$	PV module efficiency at reference conditions	(%)
θ_T	Incidence angle	(°)
θ_s	Acceptance angle	(°)
θ_1	Incidence angle of light-ray	(°)
θ_2	Refraction angle of light-ray	(°)
q	Electron charge	(C)
ρ	Density	(g/cm^3)
σ	Stefan–Boltzmann	(kg/ m^2.K^4)
σu	Convective stress-energy	(W)
Φ	Conversion from irradiance into power	(Watt)
ω_s	Sun hour angle	(°)

LIST OF PUBLICATIONS

1. A. Aldihani , S. Mahmoud, R.K. AL-Dadah, A. Al-Qattan 2017. Performance and Cost Assessment of Three Different Crystalline Silicon PV Modules in Kuwait Environments. International Journal of Renewable Energy Research (IJRER). 2017, 7(1).128-136

2. A. Aldihani, S. Mahmoud, R. K. AL-Dadah. 3D CPV investigation of Low Concentrator under dusty Environment. Applied Energy 2017 (Under preparation).

3. A. Aldihani, A. Aldossary, R. K. AL-Dadah, S. Mahmoud, A. Alqattan. Effect of Dusty Environment on the Electrical Performance of Different Photovoltaic Modules. The 14th International Conference on Sustainable Energy Technologies (SET2015), University of Nottingham, August 2015.

4. A. Aldossary, A. Algareu, A. Aldihani, R. K. AL-Dadah, S. Mahmoud. Improving illumination and temperature distribution uniformity in high concentrating solar cells. The 14th International Conference on Sustainable Energy Technologies (SET2015), University of Nottingham, August 2015.

5. A. Aldihani, A. Aldossary, S. Mahmoud, R. K. AL-Dadah. The effect of cooling on the performance of Photovoltaic cells under dusty environmental conditions. International Conference on Applied Energy (ICAE), Taiwan, June 2014.

6. A. Algareu, S. Mahmoud, R. Al-Dadah, B. Abdullahi, and A. Aldihani. The Effect of Geometry on the Optical Efficiency of Small Scale Solar Concentrators. International Conference on Applied Energy ICAE, Pretoria, South Africa 2013

7. A. Aldihani, A. Algareu, S. Mahmoud, and R. K. Al-Dadah. The Effect of Sand on the Efficiency of PV Concentrators in Kuwait Environment. International Conference on Applied Energy ICAE, Pretoria, South Africa 2013

8. A. Aldossary, A. Algareu, A. Aldihani, S. Mahmoud, R. K. AL-Dadah. Effect of Concentrator Geometry and sand on the Efficiency of Concentrated PV System, University of Birmingham 2nd Mechanical Engineering Symposium, May 2013.

CHAPTER 1

INTRODUCTION

1.1 General background

The world reliance on fossil fuel causes energy crisis and devastating destruction to the environment. The critical environmental problems (pollution and global warming), the increase in cost of energy and the expected shortage in fossil fuel are one of the main motivations to harvest energy from sustainable and clean sources. One of the promising renewable energy sources is Solar Energy. According to the National Renewable Energy Laboratory (NREL), the amount of solar radiation received by earth during one day is sufficient to sustain the yearly energy demands globally. During 2016 solar energy was the fastest growing energy industry with up to a 35% increase [1]. Sunlight is a plentiful and basically limitless source of energy; however it is not delivered equally on the surface of earth. The arid and semi-arid regions within the 'Sun Belt' zone receive the highest direct normal irradiance (DNI), which makes them great areas for solar energy installations. On average the extraterrestrial irradiance is 1367 W/m^2 but as a result of reflection and absorption by the earth's atmosphere, the direct overall solar radiation hitting the earth's surface is typically around 1050W/m^2 [2].

One of the solar energy eco-friendly technologies is photovoltaics (PV). PV technology converts the sunlight into electricity directly with no need of moving parts or circulating fluids. Thus PV technology is suitable to be utilised domestically in areas with arid climate such as Kuwait, where the daylight hours reach nearly 3600 hrs per year [3]. However, the cost of PV system is relatively high where the cost of PV cells represents about 60% of the overall cost. Thus, to reduce the total cost of electricity produced by a PV system, minimising the number of PV cells required for given power demand. significant advantages using solar concentration techniques [4] offer. Solar concentrators such as lenses, dishes and mirrors are designed to collect sun rays from a large area and concentrate it on a small area enclosed by PV cells. Employing solar concentrators increases the amount of power which the PV cells can yield, furthermore reduces the system overall area and cost through decreasing the number of PV cells operated. These types of solar optical device is categorised, based on the concentration ratio as low, medium and high concentration [4]. Hence, studies of concentrated PV systems can help improving the PV applications in arid area, specifically Kuwait, as one of the aims in this research.

1.2 Solar energy potential in Kuwait

State of Kuwait is located on the northwest of the Arabian Peninsula, bordered by Iraq, Saudi Arabia and the Arabian Gulf, the state goes through low rainfall and regular dust storms during the year as its terrain consists mostly of flat and sandy desert land. The average rainfall is about 107 mm per year, which occur mostly during winter season. In summer season, the ambient temperature is high exceeding 44˚C during the day at noon in June, July and August where in winter season the ambient temperature is approximately 20˚C [5]. Dust storms are frequent during the year, Figure **1.1** shows satellite image of dust storm crossing from Saudi Arabia to Iraq through Kuwait. According to Kuwait institute for scientific research (KISR) the average number of dusty days in Kuwait is 250 days per year, in addition the maximum settled areal dust is approximately 113.5 ton/km^2 per year in Kuwait city [5].

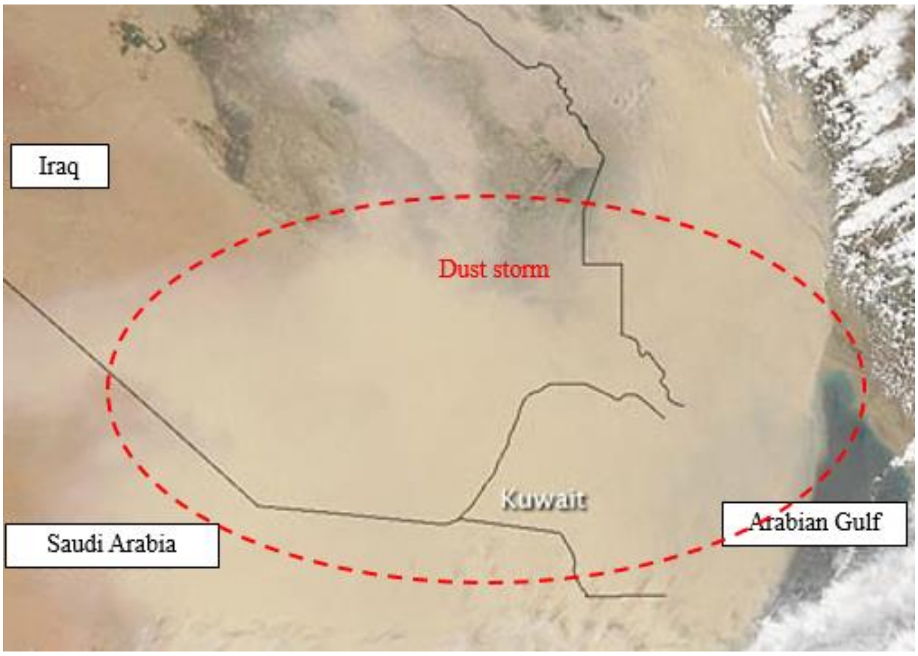

Figure 1.1 Image of dust storm crossing Kuwait captured by NASA Earth Observatory [6]

Kuwait relies entirely on fossil fuels for production of electrical power. Report by the Ministry of Energy (ME) stated that energy demand in Kuwait is increasing at up to 8% annual rate [3], and that pauses challenges to find different sources of electrical power. One of the leading energy research institutes in Kuwait, (KISR), has started exploring the potential of solar energy by carrying out research on PV technologies, also exploring the capability and challenges of operating solar energy technologies in Kuwait's harsh climate. Figure 1.2 shows the total amount of solar radiation received in Kuwait per year where the high amount of solar radiation makes Kuwait an attractive of solar concentrator PV application. KISR has built a 100 kWp parabolic CPV system with 20X concentration ratio that contains monocrystalline, thin-film PV technologies to evaluate their performance and feasibility. Also, KISR developed large-scale solar power plant with 70 MW, located north of Kuwait [7].

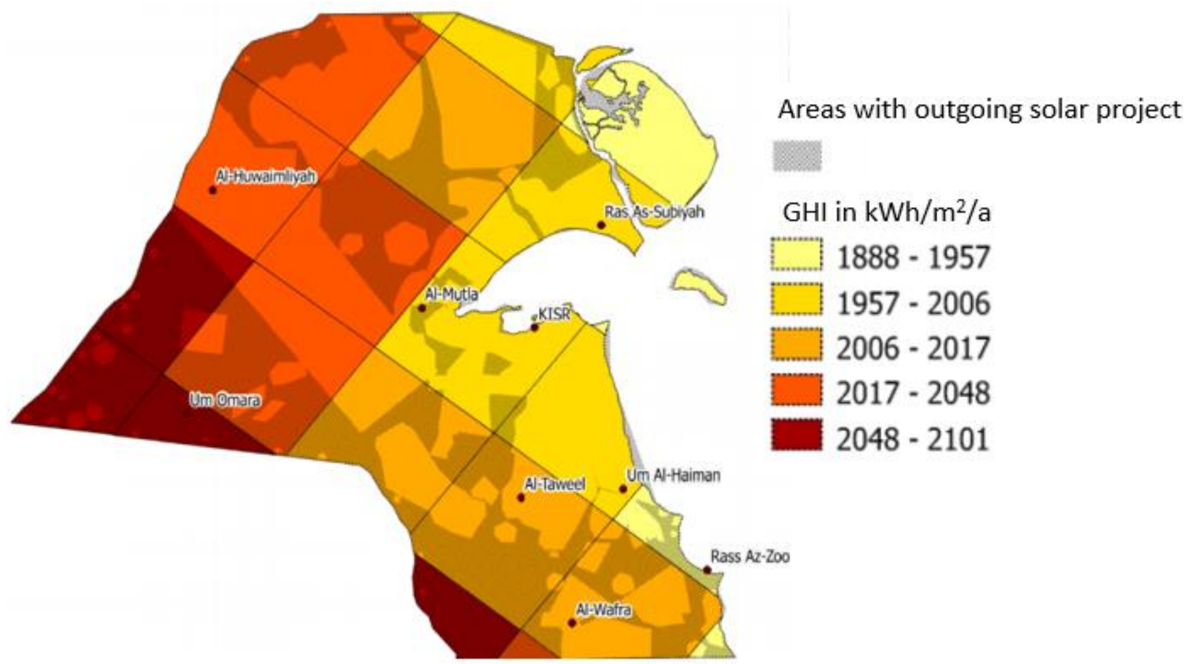

Figure 1.2 Solar resource, Global Horizontal Irradiance [GHI], in Kuwait annual [8]

Two major environmental issues that decrease the efficiency of PV systems in Kuwait, first is deterioration of irradiance, which is caused by natural obstructions such as dust accumulation on the solar system surface. Once small particles such as dust or sand fall on concentrated or flat PV system, they interrupt the incident sunlight by scattering and absorbing rays further varying the solar spectrum which impact on PV cells performance. Second issue is the high ambient temperature, which leads to increasing the PV operating temperature causing power reduction.

1.3 Research aim and objectives:

The solar concentrated PV system is a developing technology in Kuwait and there is a significant need to evaluate the overall system’s performance under the harsh environmental condition of Kuwait. This research aims to study the performance of concentrated Photovoltaic using three dimensional concentrator with Pseudo Square shaped entrance and receiver apertures having cooling system under harsh environment of Kuwait.

This can be accomplished with the following objectives:

- Detailed investigation of Kuwait environment including solar radiation availability, ambient temperature, wind speed, atmospheric dust accumulation and dust optical characteristics.
- Detailed experimental analysis of the impact of settled dust on different non-concentrated PV modules technologies.
- Developing a new small-scale solar concentrator with low concentration ratios (2,4 and 6) using three dimensional ray-tracing simulation analysis.
- Detailed characterisation of the developed solar concentrator optical performance at various input radiation and dust thickness.
- Conduct outdoor and indoor experiments to validate the optical, thermal and electrical simulations and investigate the performance of the developed solar concentrated PV at clean and dusty conditions and with cooling system.
- Predict the performance of solar concentrated PV with active cooling system at Kuwait environment condition and determine the optimum system performance.

1.4 Thesis Outlines

Eight chapters are provided in this thesis. Chapter one offers an introduction of the research and thesis main objectives. Chapter two contains detailed literature review on the solar concentrated PV technology including the cells types, performance enhancement and cooling techniques, in addition to experimental and simulation studies of dust accumulation effects on concentrated and non-concentrated PV characteristics. Chapter three introduces a detailed experimental study of non-concentrated PV carried out in

Kuwait to establish a baseline for the dust effects in Kuwait. Chapter four describes the methodology used for the development of the solar concentrator based on 3D advanced ray-tracing modelling taking into account dust accumulation. Chapter Five presents the electrical and thermal modelling using single-diode circuit model and COMSOL Multiphysics modelling software, respectively. The electrical and thermal models were developed to generate an I/V, P/V curves and operating temperature for the concentrated PV module in order to predict the electrical performance under different concentration ratios and water velocity. Chapter Six provides detailed description of the indoor and outdoor experimental setup developed for measuring the optical, electrical and thermal performances of solar concentrated PV with and without cooling system under different conditions (clean and dusty), including calibration of the instruments used. Chapter Seven presents the indoor and outdoor experimental results of the 3D-PSCPV system under the effects of dust accumulation including the optical, electrical and thermal performances. Chapter eight summaries the main conclusion and future work of this research.

CHAPTER 2

LITERATURE REVIEW

2.1 Introduction

A detailed literature review of research studies concerning solar energy technology and dust effect on photovoltaic is described in this chapter. It starts with background review of the fundamental principles of photovoltaic and dust effect on photovoltaic. It also includes reviews on various types of Photovoltaic (PV) technology and experimental studies on the concentrated photovoltaic system (CPV) with different cooling techniques in solar systems.

2.2 Photovoltaic technology

A PV cell transforms the energy of sun light to electricity via the effect of photovoltaic which includes the formation of free electron and hole sets as they are isolated through the electric field on the depletion region of a semiconductor diode, leading to a current passing throughout its terminals [9]. As electrical component or load connected to the PV cell, the circuit is closed as illustrated in Figure **2.1**

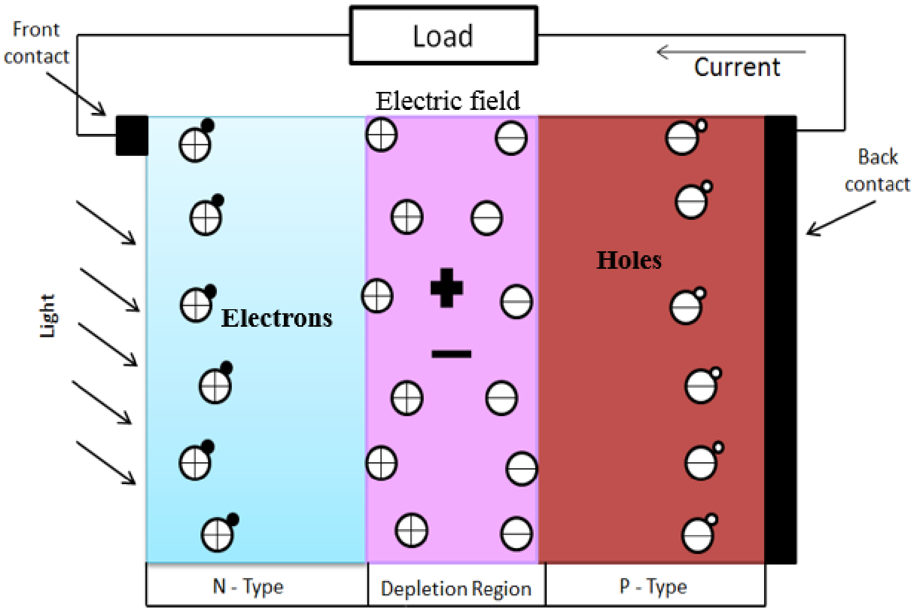

Figure 2.1 A schematic diagram of a basic PV [10]

Various PV cell types are obtainable in the market with numerous manufacturing process and substances are used to formulate PV cells. Following a description of the various of PV technologies is given.

2.2.1 Crystalline silicon (C-Si) PV Cells

There are different types of crystalline silicon PV cells based on assembling procedure, the size of the crystal material and the form of the silicon wafers namely such as; monocrystalline (Mono-Si) and multi-crystalline silicon cells. The highest efficiency of the Mono-Si PV cell achieved recently is 25.6% [11]. The Mono-Si PV cells are recognised in their unvarying black colour, and the cell edges are typically sliced due to the manufacturing process as can be seen in Figure **2.2** (a) [12]. Multi-crystalline PV cells are inexpensive to manufacture compared to Mono-Si cells. As a result of the minority carrier recombination (due to intragain imperfection precipitates and impurities) the multi-crystalline PV cell efficiency is limited. The multi-crystalline PV cell can be recognised through its dissimilarity of colours, as can be seen in Figure **2.2**(b) [12]

Figure 2.2 Two silicon PV cell types: (a) Monocrystalline silicon (b) and Multi-crystalline silicon

2.2.2 Thin film (TF) PV cells

Thin-film PV cells are second generation of PV cell technology where enhanced doping substance utilisation can be achieved as the PV cell film thickness decreased to a few microns. Some of the main thin-film PV cells are Cadmium telluride (CdTe), Copper indium gallium selenide (CIGS) and amorphous silicon (a-Si). CIGS and CdTe thin-film PV cells have received extensive research with today developed commercial production worldwide extending to a few GW annually. Of these, CIGS thin-film PV cells have highest efficiency with 23.3% reported by NREL, USA and 20.4% reported by EMPA, Switzerland [13], while CdTe PV cells have accomplished module efficiency of 22.1% as reported by First Solar [14]. The thin-film PV technology has an advantage include less substance or material, a range of low cost manufacturing techniques and lighter panels. With thickness around 2-4.2 micrometres of PV cell layer is sufficient for absorption of light wave, while for (C-Si) to absorb light wave efficiently requires a 180-300 micrometres thickness.

2.2.3 Multijunction (MJ) PV cells

The light wave absorption can be improved significantly through employing multi layers of several materials with various band-gaps aimed at improved utilisation of the sun light spectrum. The (MJ) are known as third generation PV cell. Substances like gallium antimonide (GaSb), Gallium Arsenide (GaAs) and indium phosphide (InP) are found to have superb optoelectronic characteristics to produce PV cell with high electrical efficiency[15, 16] . The Fraunhofer Society and their manufacturing partner Soitec have reached electrical efficiency of 46% for multi-junction PV cell [17, 18].

2.2.4 PV cell current and voltage characteristics (I/V curve)

The current and voltage curvature characterizing a conventional PV cell has the form shown in Figure **2.3** (solid curve with red colour). A number of parameters characterising the PV cell can be defined from this (I/V) curve, including open-circuit voltage (V_{oc}), short-circuit current (I_{sc}), maximum current (I_m), maximum voltage (V_m), fill-factor (FF) and maximum power (P_m).

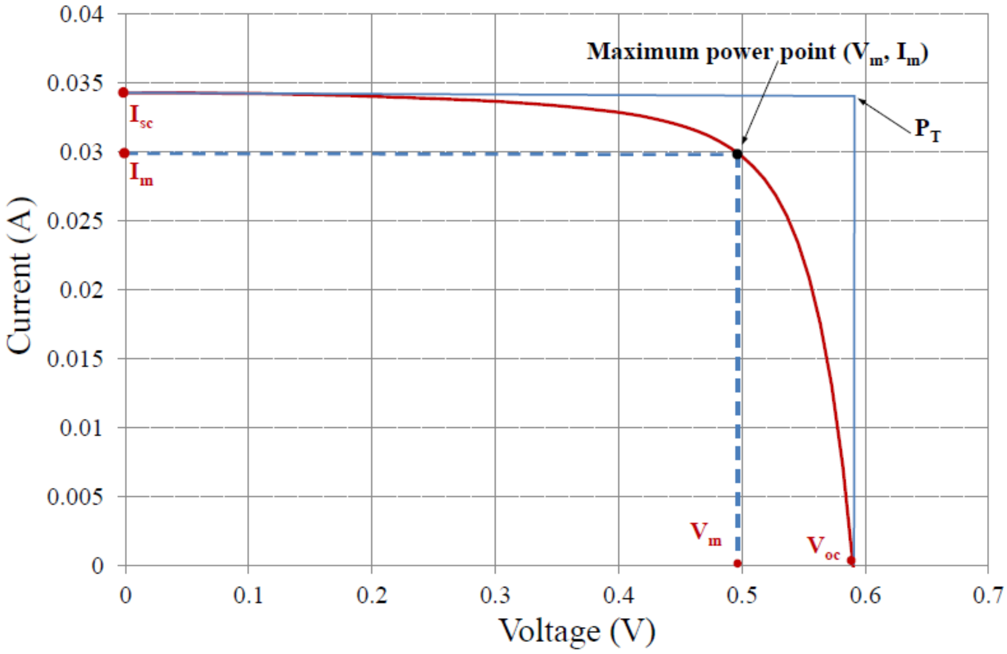

Figure 2.3 Standard I-V curve characteristics for C-Si PV cell connected to load with variable resistive.

The short-circuit current (I_{sc}) refers to the short circuit state when the electrical impedance is low and is measured when the voltage across the PV cell is equal to zero (I at V=0). The open-circuit voltage (V_{oc}) known as the highest voltage produced in PV module or cell under light radiation without resistive load connected (V at I=0) = V_{oc}. The maximum output power (P_{max}) corresponds to the maximum electrical power generated through the PV cell in wattage. It can be computed using equation 2.1:

$$P_{max} = I_{max} \times V_{max} \tag{2.1}$$

The PV module or cell needs to function at their maximum output power to reach the highest electrical efficiency of system. Nevertheless, the (Pmax) is directly affected by the combination of temperature and illumination of the PV cell effecting the current and voltage. Therefore, the dynamic control of (P_{max}) is important for the PV system output optimisation [16].

The fill factor is the ratio of the (P_{max}) maximum power output with the (P_T) theoretical ideal maximum output power which presented in Figure **2.3** and obtained by the product of the (I_{sc}) and (V_{oc}).

$$P_T = V_{oc} \times I_{sc} \tag{2.2}$$

The fill factor (FF) can be expressed as equation 2.3.

$$FF = \frac{P_{max}}{P_T} = \frac{V_{max} \times I_{max}}{V_{OC} \times I_{sc}} \tag{2.3}$$

Standard PV modules have a fill-factor exceeding 0.74.

The PV cell electrical efficiency is the ratio of the PV maximum power output to the incident light (G) determined in (W/m^2) multiplied by the area of the PV cell surface (A) in (m^2) (equation 2.4). It is generally determined at nominal operating conditions which are irradiance of 1000 W/m^2, module temperature of 25^{o}C and Air Mass of 1.5.

$$\eta = \left(\frac{V_{OC}\ I_{SC}\ \ FF}{G\,A}\right) \times 100\% \tag{2.4}$$

The performance of PV cell or module is determined through the amount of energy it delivers throughout a period of time (Y_{TOT}) estimated in kilowatt-hour (kWh). Also the energy yield of an array (E_{array}) [19], defined as the energy produced over a period of time divided by the maximum PV power at peak (W_p). This is signified as (kWh/kW_p) and given by equation 2.5.

$$E_{array} = \frac{Y_{ToT}}{W_p} \tag{2.5}$$

2.2.5 Photovoltaic cell circuit modelling

Figure **2.4** shows the ideal PV circuit model consisting of a photo-generated current source (I_{ph}) connected in parallel with a single-diode (D) (diode presents the PN junction in the PV cell with current (I_D)) [20].

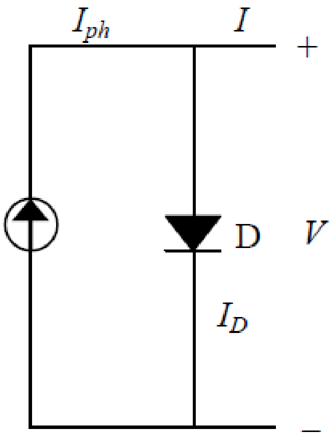

Figure 2.4 An electrical circuit diagram of an ideal PV cell [20].

The output current (I) can be expressed with following equation [20]:

$$I = I_{ph} - I_D \tag{2.6}$$

Where I_D is given as,

$$I_D = I_{ph} + I_o \left[e^{\frac{q \times V}{n \times K \times T}} \right] + 1 \tag{2.7}$$

Where I_0 is the diode reverse bias saturation current, n is the diode ideality factor, K is the Boltzmann’s constant (1.381×10^{-23} J/K), T is the PV cell temperature in Kelvin, q is the electron charge with (1.602×10^{-19} C) and V is the voltage across the PV cell.

The single-diode model considers the resistivity of the material (R_s), the ohmic resistance losses attributable to internal contacts and the effects of the shunt resistance (R_{sh}) in the PV cell/system, as shown in Figure **2.5**.

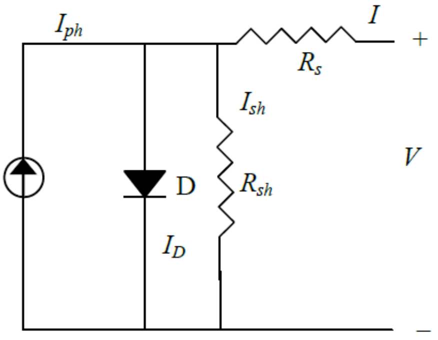

Figure 2.5 PV cell with single-diode R_{sh} and R_s [20].

The current output in the single-diode circuit model with Rsh and Rs is given with following equation [20]:

$$I = I_{ph} - I_D - I_{sh} \tag{2.8}$$

The current through the shunt resistance is given as

$$I_{sh} = \frac{V + I \times R_s}{R_{sh}} \tag{2.9}$$

Substituting equations 2.7 and 2.9 into equation 2.8 the output current can be expressed as:

$$I = \left[I_{ph} - I_o e^{\frac{q \times V}{n \times K \times T}} - 1\right] - \frac{V + I \times R_s}{R_{sh}} \tag{2.10}$$

All real photovoltaic systems are not ideal and involve shunt (R_{sh}) and series (R_s) resistances. The series resistance (R_s) within a PV cell includes the resistance in the top contacts, the emitter, rear contact, contact between ribbons with silicon and the input and output terminal of the PV cell. This resistance affects the PV cell (FF) and the (IV) characteristic curve as the (V_{oc}) will shift further from the origin as R_S increases. Figure **2.6** shows the impact of increasing (R_s) on the PV module (IV) curve. The shunt resistance (R_{sh}) occurs between the terminals of the PV cell junction and accounts for the current not passing through the junction plus the PV cell manufacturing defects. Once the current is infused less voltage will be produced throughout the PV cell terminal causing a decrease in the PV cell (FF) and therefore output power as shown in Figure **2.7**.

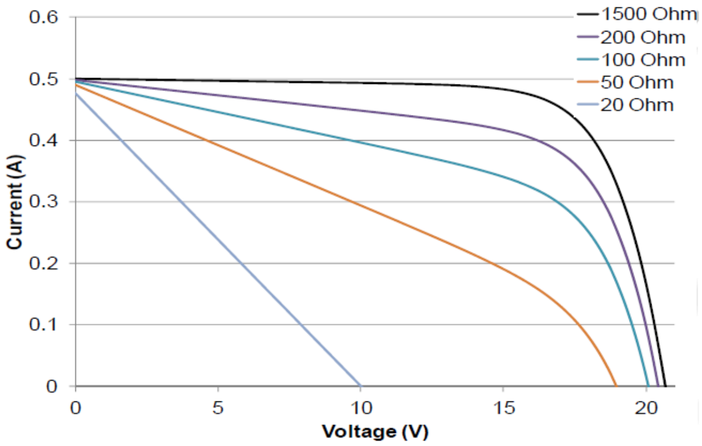

Figure 2.6 Impact of R_s on the I-V curve demonstrated with increased R_s [21].

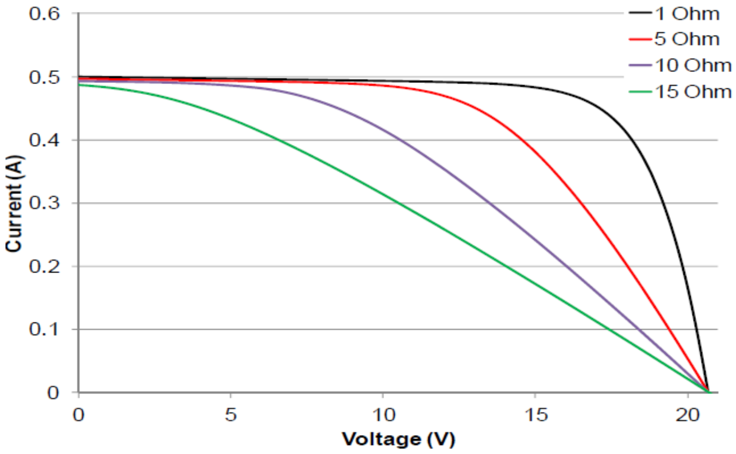

Figure 2.7 Impact of R_{sh} on the I-V curve demonstrated with decreased R_{sh} [21].

2.2.6 Effect of irradiance variation on PV

The generation of the PV cell photo-current increases with light intensity, hence the PV cell photo-current can be presumed to change linearly with the light intensity as presented in Figure **2.8**.

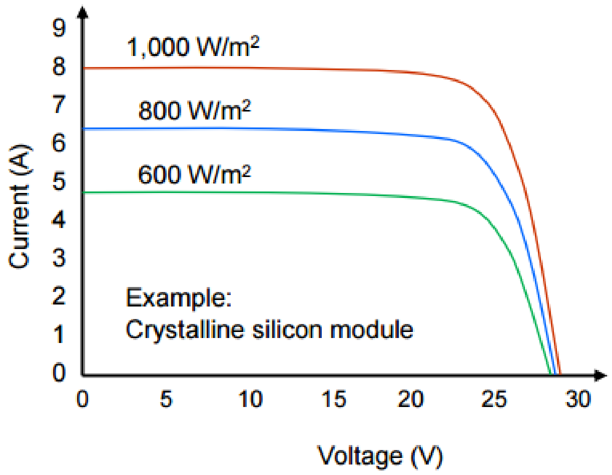

Figure 2.8 The effect of different Irradiance on the PV cells, and primarily on the (I_{sc}).

2.2.7 Effect of PV cell operating temperature

The PV cells are sensitive to temperature. As the cell temperature increases, the dark saturation current increases and band gap decreases due to less bond energy being required to develop electron-hole sets and thereby (V_{oc}) is decreased [22]. This implies that with increased cell temperature, the PV cell (V_{oc}) decreases as the (I_{sc}) is insignificantly increased, as presented in Figure **2.9**. Applying equation 2.10 to solve for (V_{oc}), the linear relation between temperature and (V_{oc}) is given in the following equation [23].

$$V_{oc} = \frac{n \times K \times T}{q} \text{In} \frac{I_{ph}}{I_o} \tag{2.11}$$

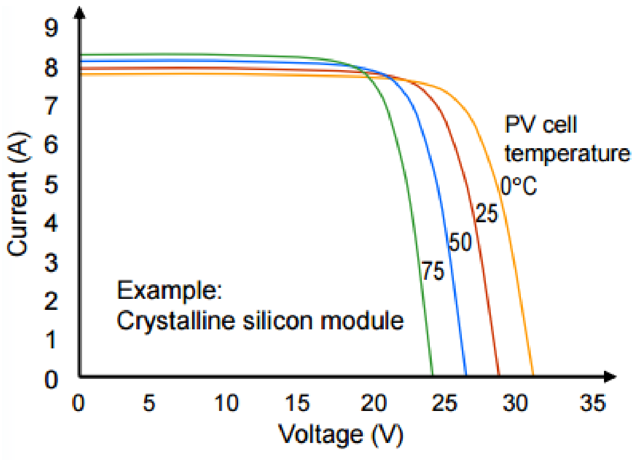

Figure 2.9 The effect of different cell temperature on the PV cells, and primarily on the (V_{oc}).

2.3 Dust effect on PV performance

Sand dust is a disadvantageous agent in arid areas around the globe; at least as far as PV applications are concerned. Once particles are accumulated on PV module surface, they obstruct illumination of the PV by scattering, reflecting and absorbing incident sunlight. The extent to which the dust particles interfere depends on their size, type, density and time period of settlement [24]. Particles fall on a surface caused by gravity force, electrostatic force or mechanical forces (rain drops or airstream). After accumulation, they are captured through the variation of electrical field potential around the surface, interface energy effects along with forces of electrostatic and gravity. Ariel dust is present nearly in all environments, but the particle composition and size depend on the region. In various regions, dusty climate turn to be harsher than in other regions. In Kuwait from May to August dust present 27% of the daytime and causes drop in visibility as shown in Figure **2.10** [25].

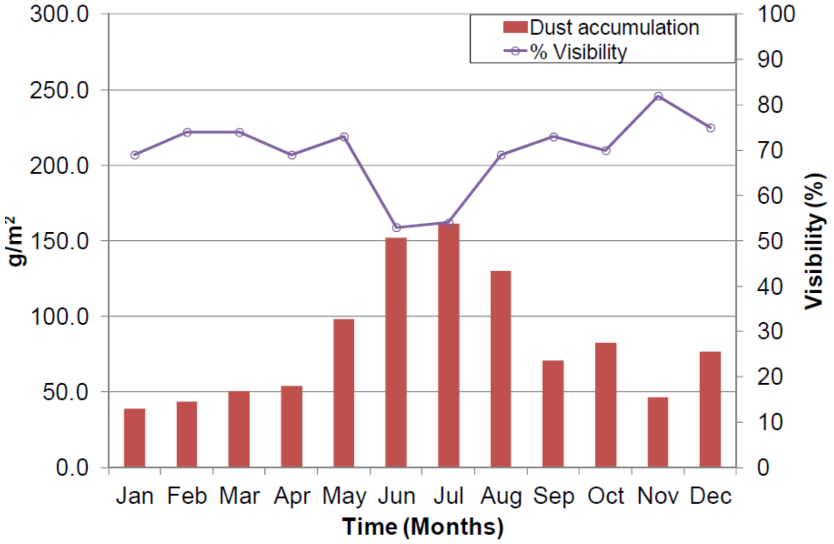

Figure 2.10 Monthly average visibility and dust fallout in Kuwait year 2013 [25].

Various parameters are stated to impact dust deposition for instance wind speed, electrostatic charges, gravitational forces and the moistness of the surface [26], [27]. The non-uniform deposition of dust on the PV cell/module glass cover surface can generate layers with different concentrations of dust, as presented in Figure **2.11**. These layers alter in dust thickness and location which can cause varied transmittance of illumination into the PV cell or module.

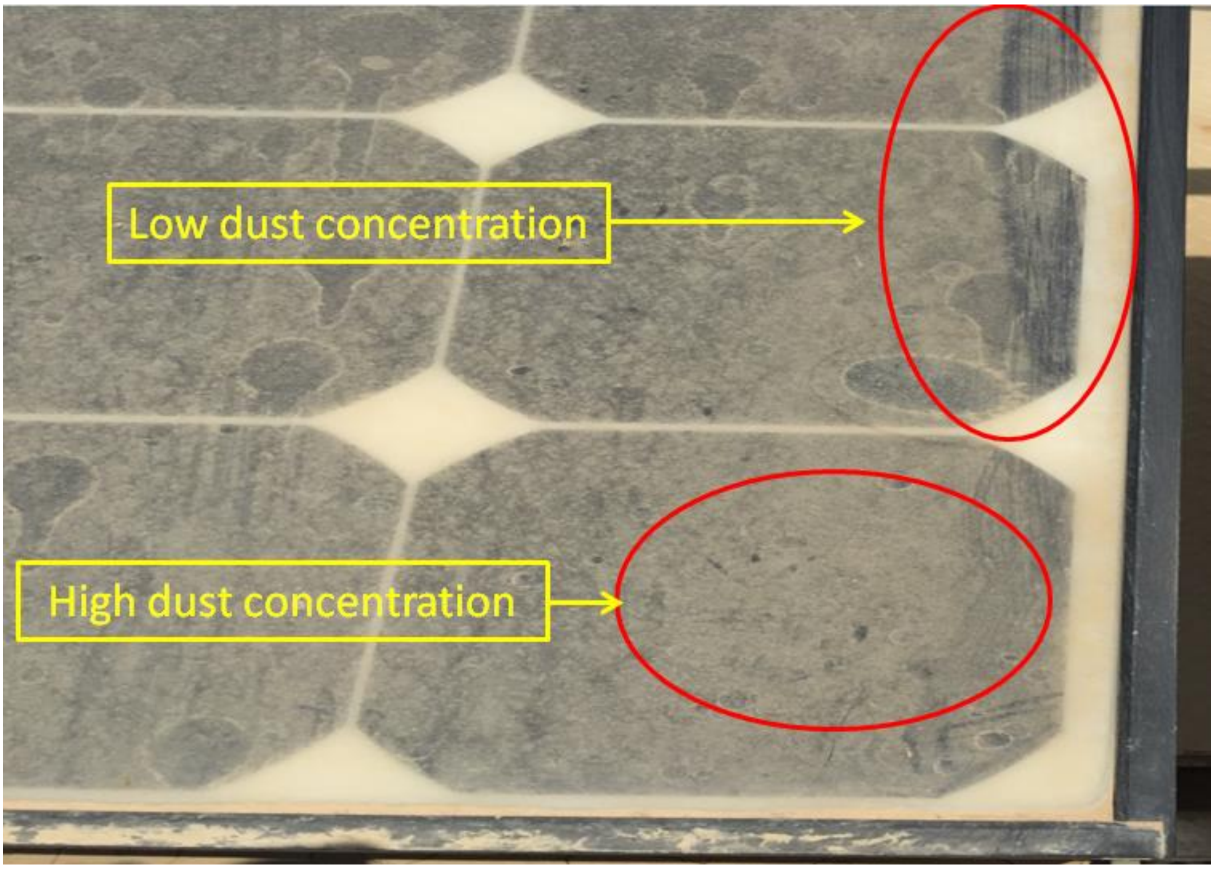

Figure 2.11 Accumulated dust on inclined PV modules surface mounted in Kuwait Institute for Scientific Research (KISR).

The characteristics of dust deposition on PV installed systems are determined through two main factors that affect one another, specifically, the type of dust and the local environment:

- The type of dust includes weight, shape, size, chemical and electrostatic property.
- The site-specific local environment aspects include climate conditions, human activities and the characteristics of the built environment.

Figure **2.12** shown different factors that affect the assimilation and falling of dust [28]. It is clear that the development of dust accumulation is complicated to practically control / understand given all the factors which impact on dust accumulation.

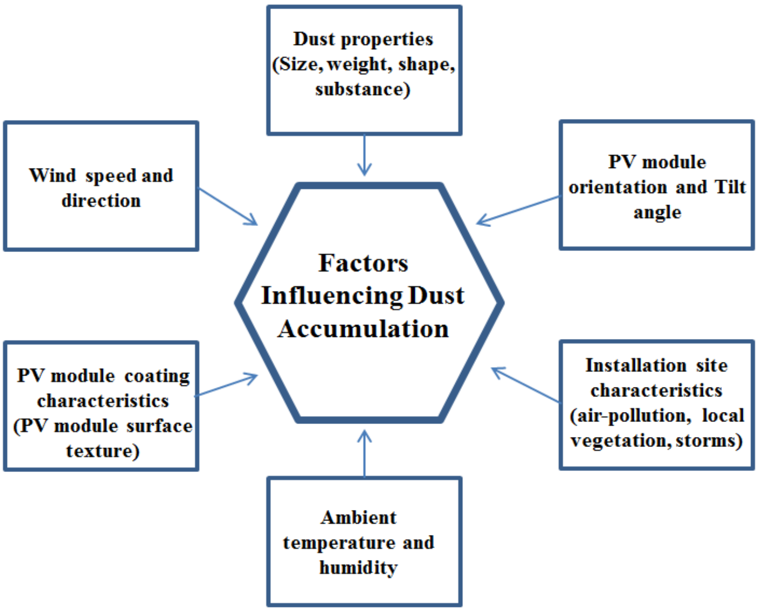

Figure 2.12 Dust accumulation changing factors [28]

2.3.1 Experimental Studies of dust effect on PV

Salim et al. [29] investigated the effect of long term accumlated dust on power output from an array of fixed circular silicon PV cells in northern Saudi Arabia over 8 months period and observed 32% decrease in the monthly power output due to sand accumulation with 2.78% drop in PV modules output current per day. This was in comparison with same PV module array that was washed regularly. On similar lines, a study implemented by Wakim [30] measured a 17% drop in PV monocrystalline modules power output after one week period due to dust accumulation caused by the severe sand storm in Kuwait city. Moreover, the research also pointed out that the impact of dust on PV module performance was more in mid-year seasons (in 6 months up to 20%) than other seasons.

2.3.1.1 The effect of Inclination Angle

Tilt angle of the PV modules has a great impact on dust accumulation., Sayigh et al. [31] investigated the impact of airborne settled dust on sloped glass plates of 4-mm thickness in Kuwait and observed a decline in glass transmissivity of 17 to 64% for slope directions varying from 0° to 60° correspondingly, over exposure period of 38 days. In each glass pairs, one was wiped clean frequently while one was kept exposed to dust accumulation. The measured solar radiation on the exposed glass plate was recorded and compared to that of the cleaned glass plate. During the experiment time period a dust collection of 2.5 $g/m^2/day$ was measured. Additionally, a 30% decrease in useful energy was reported in the horizontal collector following 3 days of dust deposition.

The transmittance of solar light through dust layer accumulated on surface of glass samples unprotected from the open-air environment in India, for 18 months was investigated by Nahar and Gupta [32]. Figure **2.13** present the accumulated dust layer data for various cleaning up periods. Maximum decrease in light transmission was measured in the early stage of the experiment, after the region experienced several sand storms, of around 4% , 3%, and 1% for inclined angle of 0°, 45° and 90° respectively, for the regularly cleaned glass samples. For the glass samples cleaned on weekly bases, the maximum decrease in light transmission was noted after 56 days period of around 15%, 10% and 5% for 0° 45° and 90° tilted angles, respectively. The glass samples light transmission suffered considerably higher losses after 60 days than the ones after 180 days even though the exposure period was shorter due to the frequent rain occurrences during the 180 days period that improved the light transmittance whereas the region suffered infrequency of rainfall in the 60 days period.

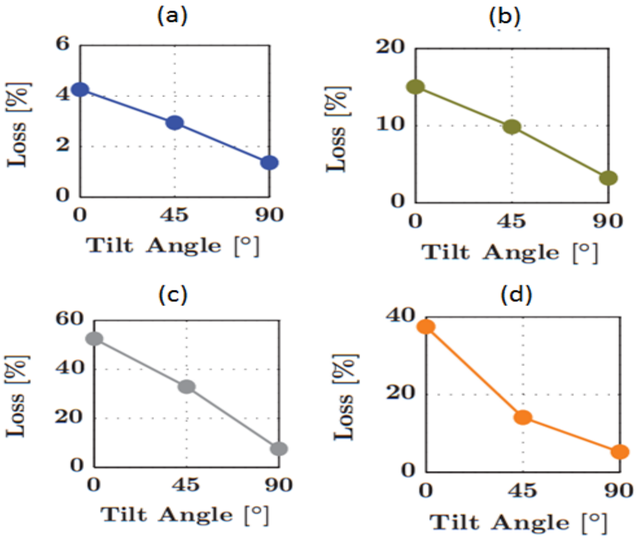

Figure 2.13 Light transmission losses for glass samples tilted at 0°, 45°, and 90°,(a) annual average transmission loss for daily cleaned samples, (b) annual average transmission loss for weekly cleaned samples, (c) transmission loss of never manually cleaned samples after 56 days, (d) transmission loss of never manually cleaned samples in after 182 days, [32].

In addition to the inclination angle of the surface plane, the influence of azimuth position was also studied by Elminir et al [33]. Glass specimens were fixed on stands at various inclined angles and azimuth in the open-air condition in Egypt with latitude of 28.23°N. The highest reduction in sunlight transmission was observed to be 27.26% for the glass specimens on horizontal position, while the lowest transmittance optical loss of glass specimen was 4.94% at tilt angle of 90° and plane positioned at southeast. Hasan et al. [34] measured the rate of dust accumulation in Kuwait between April and June is around 2.5 g/m²/day, it was found that after 1, 13, 30 days, the drop in power output of 2%, 14% and 30%, respectively.

2.3.1.2 The attenuation of light by dust

The dust deposition layer scatters and reduces the transmitted light-rays on glass or cover of PV modules. Pettit et al. [35] preformed an investigation in which silver coated glass mirrors were mounted for 2 months at the outdoor conditions of a 5 MW solar collector plant sited in

New Mexico, USA. They measured reflectance of light at various wave length and dust accumulation density. Figure **2.14** presents the reflectance as function of wavelength for clean and dusty mirror samples. The percentage reduction in reflectance of the dusty mirrors (a, b, c and d) were 6%, 10% 17% and 25%, respectively, compared to the clean mirror at wavelength of 500 nm. In addition, the reflectance loss decreased at large wavelengths, where the reflectance loss values ranged from 3.8% -14% at wavelength of 900 nm.

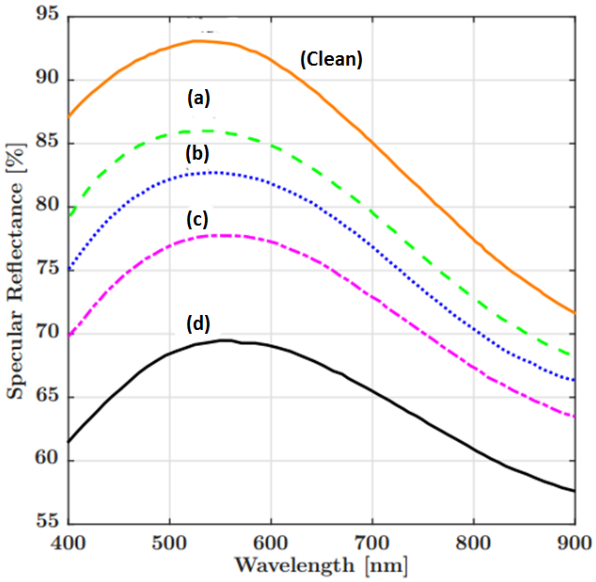

Figure 2.14 The change of reflectance as function of wave lengths for clean and uncleaned mirrors exposed in New Mexico. Dust accumulation density increases from (a) to (d) [35].

Qasem et al. [25] examined the impact of dust after one month on different photovoltaic modules to correlate light spectrum transmittance with dust deposition rate using glass samples covered with dust from Kuwait. Their results indicated that for dust deposition rate of 8.5 mg/cm^2, a spectral photocurrent reduction of 28.5%, 28.6% and 33% were measured for crystalline silicon (monocrystalline and polycrystalline), copper and indium gallium diselenide (CIGS) and amorphous silicon PV modules respectively. Figure **2.15** presents the measured reduction in the glass transmittance at different dust density and wave length range. The light transmission optical losses are higher at shorter wavelengths between 350–500 nm compared to the other wavelengths. Moreover, the wavelength transmission loss significantly decreased when dust density reaches 20 g/cm^2 or higher.

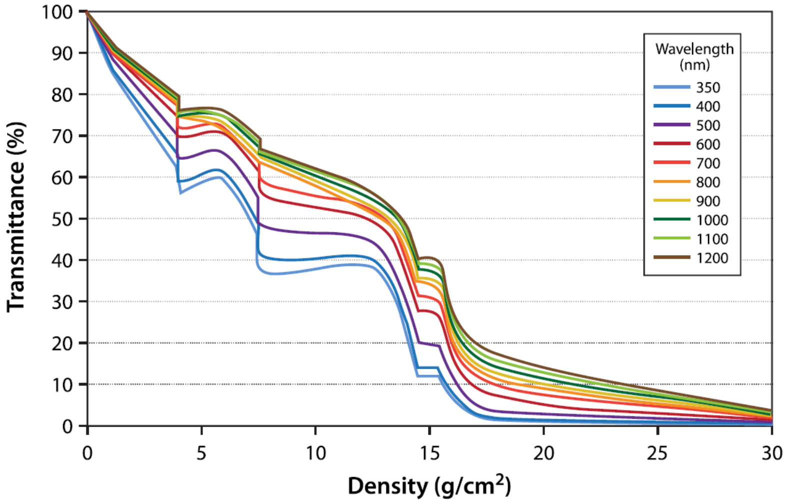

Figure 2.15 Measured transmittance loss of glass at different dust density and wavelengths [25].

Al-Hasan and Ghoneim [24] investigated experimentally the effects of sand accumulation on the reflectance and transmittance of glass to light with wavelengths varying from 180 to 900 nm using spectrophotometer. The average size of sand dust particles used was 60.4 microns. Figure **2.16** shows the measured transmittance where clear reduction is observed as the dust total mass weight increases.

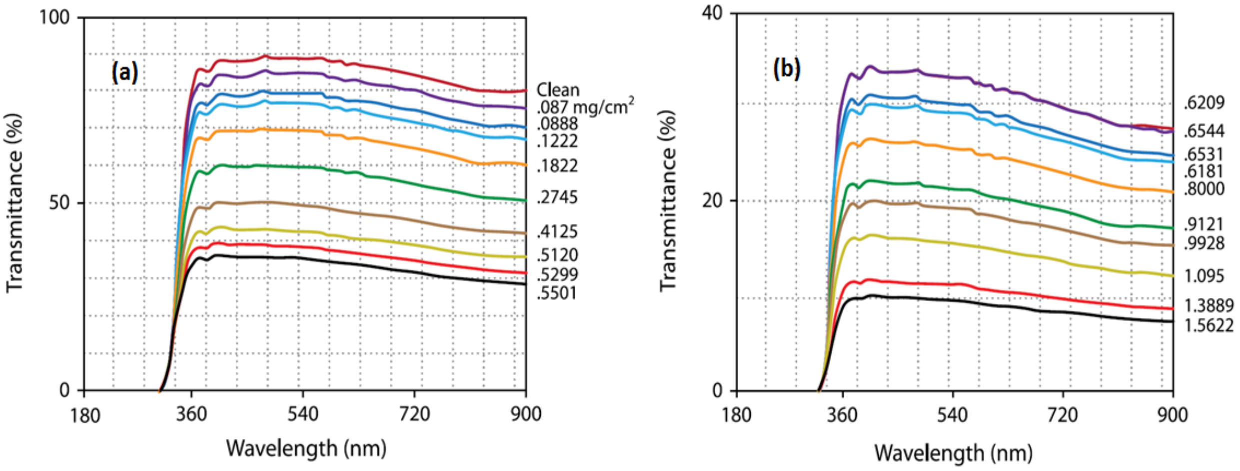

Figure 2.16 Light spectral transmittance of glass sample as a function of dust depositions: (a) lower dust depositions and (b) higher dust depositions.

2.3.1.3 PV electrical performance under dust accumulation

Al-Hasan and Ghoneim [36] carried out an outdoor study in Kuwait to evaluate the degradation of PV modules performance due to dust accumulation on their surface. They mounted two Multi-crystalline PV modules at inclined angle of 30° in the Institution of Technological Energy Studies building, Kuwait. One of the modules was wiped clean frequently, while the other one was kept exposed to outdoor locations. Figure 2.17 (a) shows the current and voltage characteristics for both clean and dusty modules installed outdoor. It has been observed that with 1.5 g/m^2 dust concentration on the module glass cover, the short-circuit current and maximum output power was reduced by 40 and 34%, respectively. Moreover, the clean PV module was then made dusty in indoor laboratory using dust particles collected from the nearby desert. Dust particles were sprayed using a fan blowing air onto the target PV module so as to apply a nearly uniform dust layer on the glass cover. Figure 2.27(b) shows the measured IV curves at three different dust concertation densities showing clearly that the short-circuit current decreased with the increase in the rate of dust accumulation while the open circuit voltage was not affected.

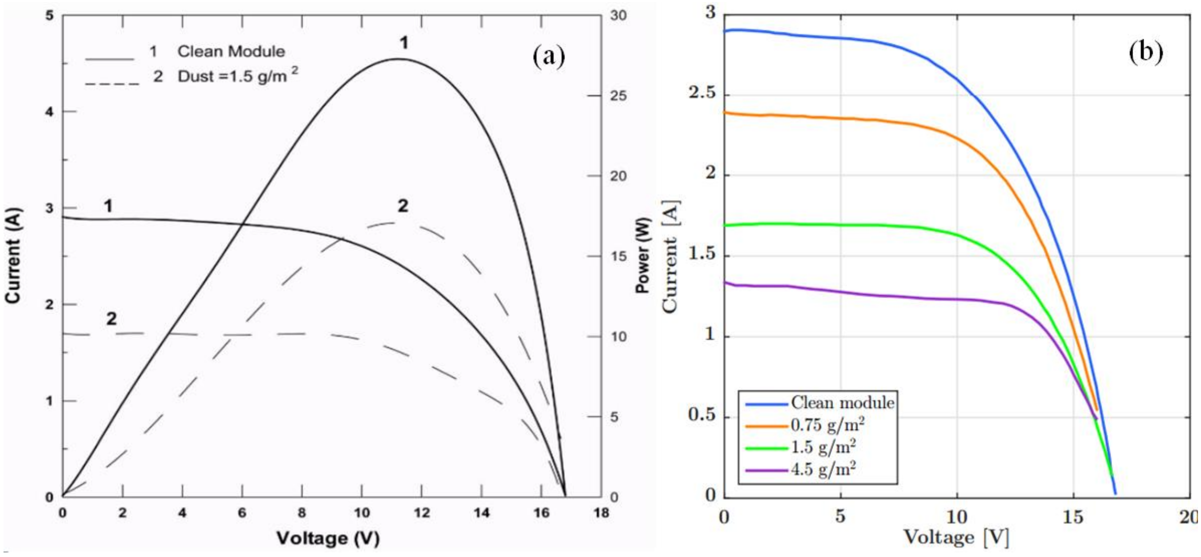

Figure 2.17 (a) Comparison of current and voltage characteristics for clean and unclean PV modules installed outdoor. (b) Change of current and voltage output at different dust concentrations [36]

The influence of dust deposition on the PV cell performance was considered by El-Shobokshy and Hussein [37]. In their investigations, different sizes of dust particles with average diameters of 80, 60, 50, 10 and 5µm were studied. The particles were accumulated on a PV cell cover in a regulated surface mass density and the PV module output power was calculated. The findings indicated that smaller size particles have a greater light deteriorating impact on PV cell performance than larger size particles on similar surface accumulation density of 25.5 g/m^2. The findings also indicate that output power in the case of 10 and 5µm diameter particles declined by around 20% and 40%, respectively. Table **2.1** presents a list of reported dust accumulation effect on PV. It can be concluded form the table that the dust effects of dust accumulation on PV performance varies based on the the installation site and PV cell type.

Table 2.1 Summaries of reported research on the effect of dust accumulation on PV

Reference	Type of PV technology	Period of exposure	Location	Type of environment	Outcome results
Adinoyi et al. [38]	Monocrystalline	6 months	Saudi Arabia	residential, arid	50% decrease in power
Salim et al. [29]	circular silicon PV cells	8 months	northern Saudi Arabia	arid	32% decrease in power
Nimmo and Saed [39]	silicon PV	6 months	Saudi Arabia	residential, arid	40% decrease in the efficiency
, El-Shobokshy and Hussein [40]	Polycrystalline	Indoor experiment	Saudi Arabia	Indoor	35% decrease in power
Touti et al. [41]	Monocrystalline	3 months	Qatar	residential, semi-arid	10% reduction in efficiency
Alnaser et al. [42]	polycrystalline and monocrystalline	7 months	Bahrain	residential, semi-arid	60% decrease in power
Al Hanai et al. [43]	amorphous silicon and thin-film	1 month	UAE	Industrial, arid	5.7% decrease in efficiency
brahim et al. [44]	Thin Film	6 months	Egypt	Industrial, semi-arid	25% decrease in power
Hassan et al. [45]	Polycrystalline	6 months	Egypt	Industrial, semi-arid	65.8% decrease in power
Al-Alawy [46]	PV glass	9 years	Iraq	Urban, semi-arid	50% decrease daily solar radiation

2.3.2 Theoretical studies of dust effect on PV

Limited theoretical studies of the effect of dust were found in the literature. In Greece, Kaldellis and Capsali [47] modelled the effect of dust on the PV performance based on experimental measurements. The model depends on particles composition type and sizes as the aspects causing the PV output power reduction. Different particles samples were simulated with size of 10 µm, 60 µm and 150 µm and the types are limestone and red soil, respectively. Kaldellis and Capsali [47] developed an expression for the soiling capacity factor (C_{FS}) defined as the ratio of actual annual energy generated by dusty PV compared to that produced by clean PV, as a function of clean capacity factor (C_{FC}), coefficient (A_T, where $_T$ signifies the particles type), and the amount of dust accumulation (ΔM),as [47] :

$$C_{FS} = C_{FC} e^{-A_T \Delta M} \tag{2.12}$$

Sanusi [48] investigated amorphous thin film PV at harsh climate conditions in Nigeria during the Harmattan period (dusty seasons) showing that after two months exposure without cleaning there was decrease of 20% in solar absorption, the PV modules were in horizontal angle. Sanusi used solar radiation diffusing models due to aerosols or aerial dust reported by Iqbal [49]. The models were Mie's model at any particle size and Rayleigh's model for spherical shape particles with diameters smaller than the wavelength of light (λ) expressed as [48]:

Case A: where diffusing is directed via Rayleigh's model

$$\frac{\pi D}{\lambda} < \frac{0.6}{n}$$

Case B: where diffusing is a reflection.

$$\frac{\pi D}{\lambda} < 0.6$$

Case C: where diffusing is directed through Mie's model

$$\frac{0.6}{n} < \frac{\pi D}{\lambda} < 0.6$$

Where D is particle diameter and n is index of refraction.

The Mie's dust diffusing factor ($Diff_d$) is:

$$\mathrm{Diff_d} = 0.08128\lambda^{-0.75} \tag{2.13}$$

This is applicable for a varied range of particles diameter (m_a), starting from 1 up to 800 micrometre. Hence the spectral transmittance (ST_d) can be written as [48]:

$$\mathrm{ST_d} = \exp\left[-\mathrm{Diff_d}\left(\frac{\mathrm{D}}{800}\right)\mathrm{m_a}\right] \tag{2.14}$$

Martin and Ruiz [50] suggested a theoretical model to define the incidence angle losses as a function of the dust deposition density. The theoretical model involves a phrase for the angular loss factor of the incident light component, $\mathrm{FT_b}(\theta_T)$ represented as the division of the light transmittance on a specific incidence angle,(θ_T), and the light transmittance on normal incidence expressed as [50]:

$$\mathrm{FT_b}(\theta_T) = 1 - \frac{\exp\left(-\frac{\cos\theta_T}{D_F}\right) - \exp\left(-\frac{1}{D_F}\right)}{1 - \exp\left(-\frac{1}{D_F}\right)} \tag{2.15}$$

D_F is a modifiable function of dust deposition at a plane, where the volume of dust at the plane can be separated through the division of the normal incidence light transmittance at a dusty plane on the normal incidence light transmittance at a clear plane.

2.4 Solar concentrators

Integrating concentrators with PV cells or modules can enhance the power output and reduce the cost of PV systems. Various solar concentrator designs were utilised in the past years for various PV systems to obtain high optical efficiency [51]. Taking into consideration the optics of the refractor and reflector the solar concentrators (refractor or reflector) classified with two types namely nonimaging and imaging [52, 53]. As the name describes solar concentrator with imaging develop an optical image of the sun on the target area such as linear lenses and solar tower. While solar concentrators with nonimaging optics simply concentrate the sunlight on target (a receiver area) but do not develop somewhat appearance of the sun such as compound parabolic [51].

2.4.1 Concentration ratio

The concentration ratio has different representations , namely geometric concertation ratio and optical concertation ratio [2] where the geometric concentration ratio is the most commonly used name for concentration ratio, defined as the ratio between the entrance ($\mathrm{A_{Ent}}$) and exit ($\mathrm{A_{Ext}}$) areas of the concentrator [54]:

$$\mathrm{C_{GC}} = \frac{\mathrm{A_{Ext}}}{\mathrm{A_{Ent}}} \tag{2.16}$$

The second description of the concentration ratio is named as 'optical concentration ratio' (CR) and that take into consideration the ratio of averaged energy flux over the exit area ($\mathrm{AR_{Ext}}$) to the average energy flux over the entrance area ($\mathrm{AR_{Ent}}$) of the concentrator [55]. The optical concentration ratio is given as (suns) i.e., assuming the flux at the exit aperture is 3 times higher than the flux on entrance aperture, the term 3X or 3 suns referred to the concentration ratio [53].

$$\mathrm{C_{opt}} = \frac{\mathrm{AR_{Ext}}}{\mathrm{AR_{Ent}}} \tag{2.17}$$

2.4.2 Concentrator acceptance angle

The acceptance angle (θ_s) described where the incidence angle with respect to 90% of the maximum optical efficiency at normal incidence [22]. The maximum concentration of concentrator ($\mathrm{CR_{max}}$) is a function of acceptance angle (θ_s) and the enclosed dielectric material (*n*) refractive index and described as follow [2] :

$$\mathrm{CR_{max}} = \frac{\mathrm{n^2}}{\mathrm{sin^2\theta_s}} \text{, for 3D concentrators} \tag{2.18}$$

$$\mathrm{CR_{max}} = \frac{\mathrm{n}}{\mathrm{sin\theta_s}}\text{, for 2D concentrators} \tag{2.19}$$

Mostly, 3D concentrator are used in obtaining high concentration by decreasing the acceptance angle, but complicated equipment such as sun tracking are required in order to keep the concentrator directed at the sun [56],[57]. Furthermore, small acceptance angle may cause optical losses to the system from misalignment causing degradation of the CPV system overall performance.[58]

2.4.3 Solar concentrated system types and categorises

Solar concentrators are utilised in many solar power systems including thermal, PV and hybrid systems as photovoltaic/thermal (PV/T) [51, 53, 59-61], as presented in Figure **2.18**.

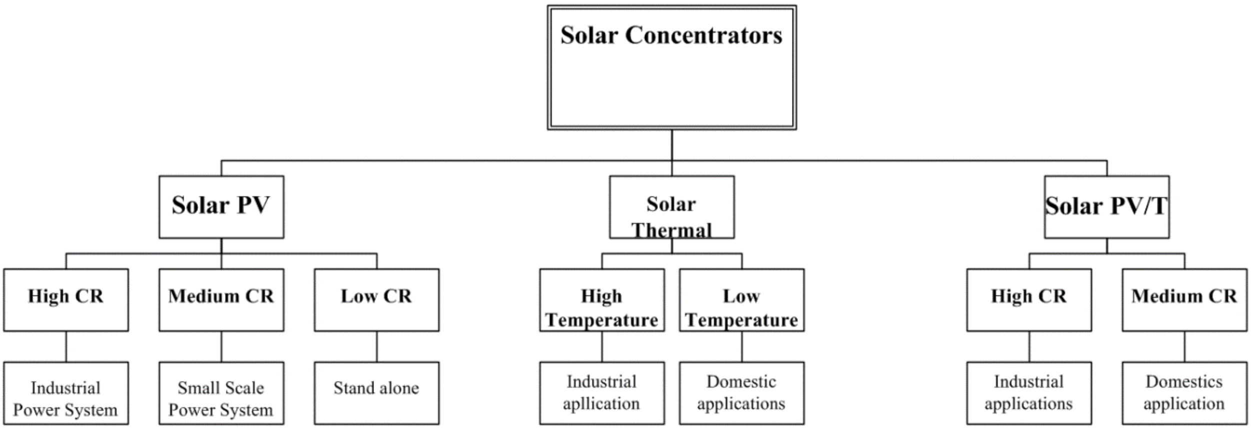

Figure 2.18 Types of solar concentrator systems [58].

The concentrating systems of solar power can be arranged in three classes based on the optical concentration ratio [62-69]:

- High solar concentrating system with (100X and higher) concentration ratio.
- Medium solar concentrating system with (10X – 100X) concentration ratio.
- Low solar concentrating system with (1X-10X) concentration ratio.

Figure **2.19** presents a number of concentrator designs with different receiver configurations. The concentrator designs presented in Figure **2.19** (a-c) presents designs operated for high and medium solar concentrating system that involve solar tracking, while Figure **2.19** (d-f) are for solar concentrator system with low concentration ratio.

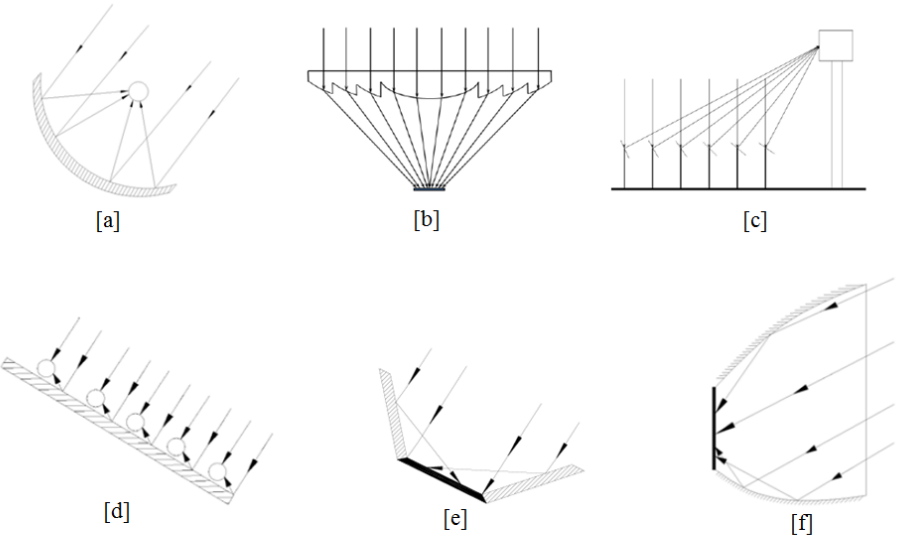

Figure 2.19 Different designs of solar concentrators: (a) Parabolic concentrator (b) Fresnel lens (c) Central receiver system with reflectors. (d) Tubular receivers (e) Plane receiver (f) Asymmetric compound parabolic concentrator [58].

A detailed categorisation of PV concentrator systems presented by Royne et al. [70] in regard to the geometries of PV cells layout. The categorisations are single PV cell and array of PV cells geometries. First category, single PV cell geometrical design involves a single spot concentration which focuses the received irradiance on single PV cell, as presented in Figure **2.20** (a). In this geometrical design if the concentration is 200X, the surface of PV cell should ideally receive 200 times the falling irradiance on the entrance of the concentrator. Second category, linear array PV cell geometrical design involves a concentrator which focuses the received irradiance on a strip of PV cells positioned in single line. Figure **2.20** (b) is a graphic diagram of the linear array concentrator. Typically, linear Fresnel lens or asymmetric compound parabolic concentrators are employed in this type of geometry. The PV cells are assembled next to each other on the irradiated linear area. This type of arrangement involves complicated cooling design.

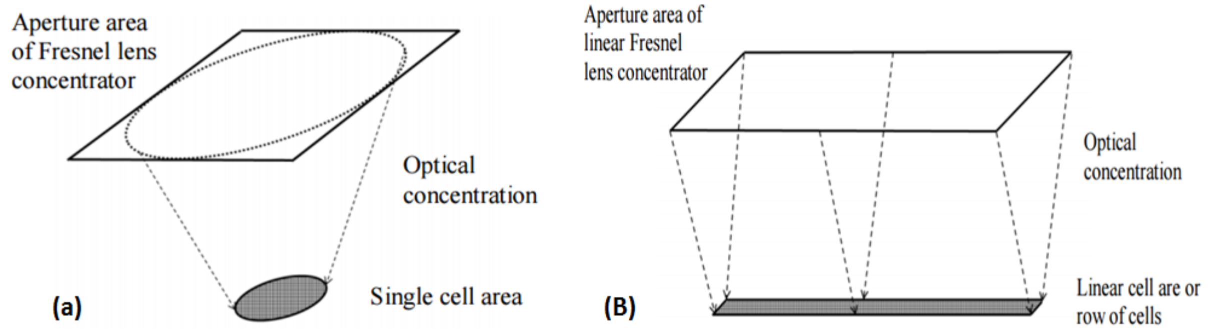

Figure 2.20 (a) Geometrical design of a single and (b) Geometrical linear PV cell concentrator [70].

2.5 Review on concentrated Photovoltaics (CPV)

Various types of CPV systems were investigated from 1970 to 1995 that enhanced the research in this area [55]. The performance of various CPV systems based on the concentration ratio, power production and design are presented in Table **2.2**.

Table 2.2 Various CPV systems projects worldwide [71]

Company	**Concentrator Geometry**	**Concentration Ratio**	**Production capacity in (MWp)**	**Site**
Soitec	Lens, pedestal	500	79	France
Arzona Solar	Lens, pedestal	≥1000	12.3	USA
Abengoa Solar	Lens, pedestal	≥1000	0.2	Spain
RedSolar	Lens	≥1000	0.2	China
Silex	solar tower	500-1000	4.3	Australia
Magpower	Lens, pedestal	≥1000	4.2	Portugal
Arima	Lens, pedestal	476	2.1	Taiwan
Sahaj Solar	Lens, pedestal	500	-	India
Saturno	Refractive type	700	-	Italy
Mega Watt Solar	Reflective linear, Pedestal	20	-	USA
Skyline	Reflective linear, floating	14	-	USA
EUCLIDES	Reflective linear	40	-	Spain
Whitfield Solar	Fresnel lens	40	0.1	Sweden
SunPower	Linear reflective trough	7	8	USA
Absolicon Solar	Reflective mirror	10	0.1	
LCOC	Reflective linear	7	-	USA
JXC	Reflective linear mirror	3	-	USA

2.5.1 Low concentration (CPV)

The simplest low concertation system is the V-trough concentrator which can produce up to 3X concertation ratio. Shaltout et al [72] used V-trough concentrator with PV cells. They used tracking system to maintain uniform concentrated light on the PV and used ambient air circulation (passive method) for cooling the PV cells to maintain low operating temperature. Results showed that a concentration ratio of 2.6X enhanced the power output by 40%. Tripanagnostopoulos et al. [73] studied the hybrid of a photovoltaic/thermal system with diffuse booster mirror reflectors. The mirror reflectors were positioned between the parallel PV cells lines. Figure **2.21** shows the ray tracing of the concentrated photovoltaic/thermal system. Their results showed an average concentration ratio of 1.35X, and the electrical efficiency of a photovoltaic/thermal system was increased up to 16% after utilising diffuse booster reflectors, in comparison with non-concentrating system.

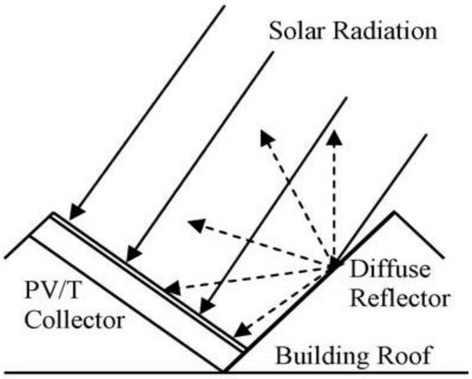

Figure 2.21 Ray tracing illustration for PV/T systems with mirror reflectors [73].

Brogren et al. [74] investigated experimentally and theoretically the optical performance of a photovoltaic water thermal system integrated with a compound parabolic concentrator in Sweden. The combined PV and thermal system is shown in Figure **2.22**. The optical concentration was 4X for the truncated symmetric compound parabolic concentrator and the PV module area was 1.5 m^2. The measured optical efficiency was in good agreement with the numerical calculation, at nearly 70%. The results showed that this solar system can provide 800kWh of low temperature heat and 270kWh electricity per m^2 module area annually.

Figure 2.22 Low concentrating compound parabolic concentrator integrated photovoltaic/thermal systems [74].

Mallick et al. [75] applied ray tracing method to study the optical characteristic of asymmetric compound parabolic photovoltaic concentrators (ACPPVC) in UK. The air sealed ACPPVC had an optical concentration ratio of 2X with half acceptance angles of 0° and 50° as illustrated in Figure **2.23** (a). An optical efficiency of 91% was predicted theoretically for a varied range of sunlight incidence angles. Mallick et al. [76] constructed the 2X optical concentrations (ACPPVC) system and integrated it with BP Saturn PV cells connected in series and parallel. The solar system was fixed at title angle of 18° as presented in Figure **2.23**(b). The highest system efficiency of 8% was achieved under a solar irradiance of 700W/m^2, and 26W was the maximum power produced. The maximum output power reached was 1.63 times higher than flat PV (nonconcentrating) similar system. The optical efficiency loss of the (ACPPVC) system was approximately 15%, as a result of the transmittance and reflection losses. A 4% power loss occurred, as a result of the increased PV cells temperature to 72°C.

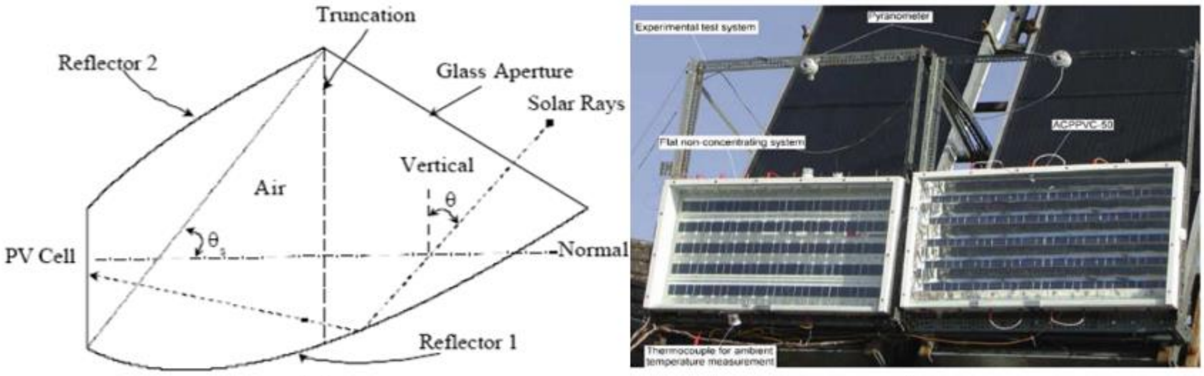

(a) (b)

Figure 2.23 (a) Graphic illustration of the modelled photovoltaic concentrator (ACPPVC) [75], (b) asymmetric compound parabolic and non-concentrating photovoltaic concentrators under outdoor experimental characterisations [76].

Sangani and Solanki [68] experimentally investigated a (V) Trough solar concentrator for standard PV module with concentration of 2X. The solar concentrator PV system output power was improved by about 44% in comparison with non-concentrator PV system. The rate per unit watt of power produced is increased by around 24% for the concentrated PV system in comparison with the identical non-concentrator PV system.

2.5.2 Medium concentration (CPV)

Medium concentration concentrators can commonly be classified into two types: Fresnel lenses and parabolic troughs. Nakata et al. [77] studied a 300W single axis tracking concentrator. The system consists of 36 Fresnel lenses (40 cm × 40 cm) which was constructed to achieve a uniform direct irradiance distribution over n on p type silicon cell with low resistivity. Results showed that the lenses optical efficiency is 83% and the output power was increased by 50%. The output power from a concentrated PV cell was 9W at 38^{o}C cell temperature under 47X with 12% cell efficiency. The output power from a set of five concentrator modules was 253.7W with total cell efficiency of 10.2%.

In 1983, Entech company, O’Neill [78] investigated linear Fresnel lenses to build a CPV system with polysilicon PV cells. The optical concentration was 23X with 15% system efficiency at standard tests conditions. The system has been patented due to its unique design. Sala et al. [79] studied the (EUCLIDES) concentrated PV system with concentration ratio of 20X-40X. The (EUCLIDES) CPV system consists of parabolic trough with mirror reflectors, receiver of PV cells encapsulated with heatsink and single axis tracking system shown in Figure **2.24**. The mirror reflectors are coated with 3M polymers silvered sheet. The system optical efficiency is found to be up to 95%.

Figure 2.24 The (EUCLIDES) solar PV system [79].

Coventry [80] investigated the performance of parabolic trough photovoltaic/thermal concentrator performance with 37X geometrical concentration ratio. The system efficiency was 69% at test conditions of 1000W/m^2 solar radiation and 25°C ambient temperature. The PV silicon cells were constructed to have low inner series resistance. The PV cells efficiency decreased with rising temperature was of the scale of 4% per 10°C. Figure **2.25** (a) shows the photovoltaic/thermal concentrator, while Figure **2.25** (b) shows the design of the receiver.

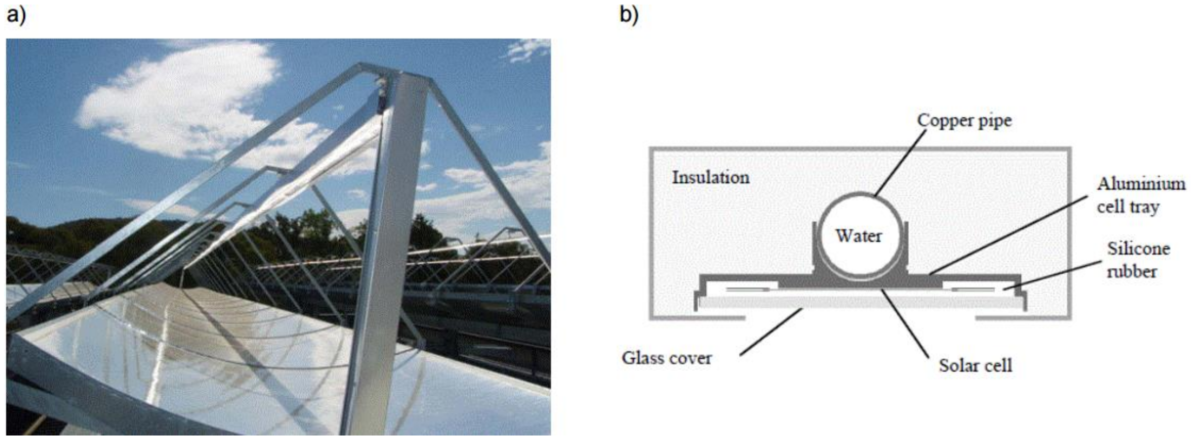

Figure 2.25 (a) parabolic trough photovoltaic/thermal concentrator (b) Cross-section view of a receiver [80].

Bhatnagar and Joshi [81] conducted a 3 year outdoor experiment to test the performance of concentrated silicon PV modules at 40X. The concentrated radiation was formed via point focus technique using Fresnel lens, and the PV cells were attached to aluminium strips. The recorded PV module output power, direct radiation and surface temperature measurements revealed that such concentrating system is inefficient for the Indian outdoor environment. The PV modules suffered from degradation of 3% at the normal efficiency of 7.5% mostly due to increase in series resistance and decrease in light-generation current.

2.5.3 High concentration (CPV)

High concentration systems are dominantly based on Fresnel lenses and involve dual axis sun tracking with high accuracy (tolerances under 0.25). Yamaguchi et al [82] described their experimental investigation on multijunction PV cells and determined high optical efficiency of 400X and 550X units on dual axis sun trackers applying open loop control methods. The 400X units has power rating of 150W while the 550X units has 200W power rating. The large area (7000 m^2) Fresnel lenses concentrator enhanced the PV modules efficiency by approximately 27%. The system efficiency increased due to the combination of high efficiency multijunction PV cells and high optical efficiency of the lenses.

Similar to the above study, Stone et al. [83] studied and analysed the (AMINOX) high concentrating system. The system optical concentration ratio was 250X and 1000X with dual axis sun tracking. It is a large scale solar concentrating system consisting of multijunction PV modules with Fresnel lenses on each PV cells. The Fresnel lenses are constructed using 4 mm polymers with antireflective layer and aperture area of 182m^2. The (AMONIX) solar system rated power output is 25 kW under direct beam of 850 W/m^2 at 25°C cell temperature. Figure **2.26** a & b shows the optical principle and picture of the (AMONIX).

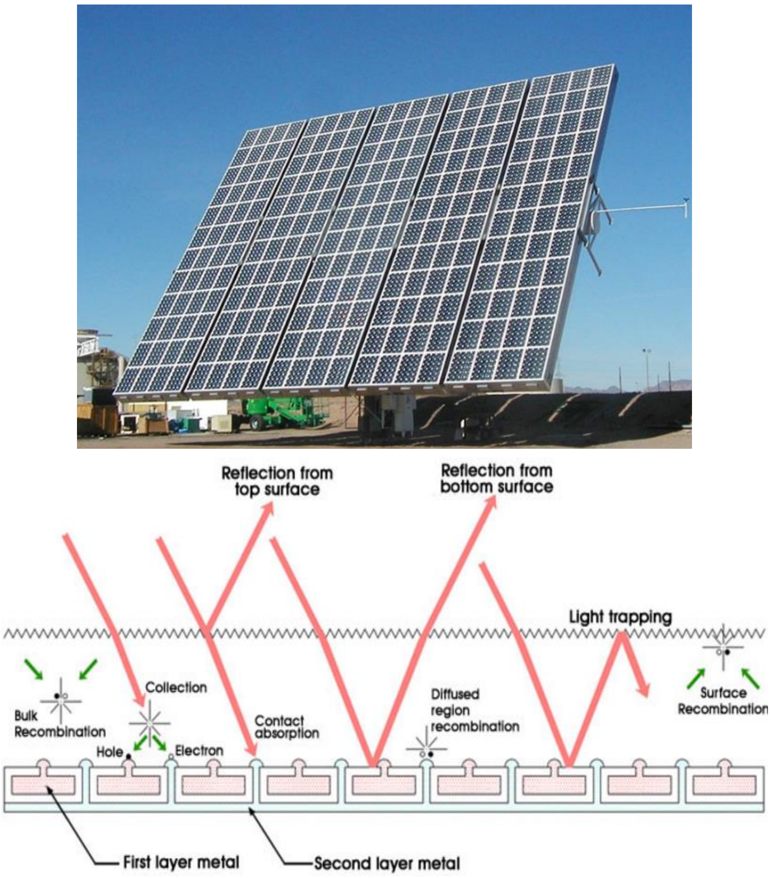

Figure 2.26 (a) Photograph of (AMONIX) 25 kW CPV system. (b) Representation of the system [83].

Hein et al. [84] described a solar concentrator system up to 300X using a parabolic trough mirror concentrating solar light into second stages of 3D concentrator of compound parabolic with one axis sun tracking. The efficiency of the multijunction PV cell used as receiver in the system was approximately 26%. Hence, the system losses were around 75%, and that includes high temperature and optical losses. The optical efficiency loss of 20% of the parabolic trough was evaluated in outdoor setup, where the optical efficiency losses of the compound parabolic 3D concentrator should be nearly 25%.

2.6 CPV cooling systems

In concentrated PV, as a result of the high irradiance on the PV cells, they will reach high cell temperatures. Increases in PV cell temperature will affect the band-gap causing a drop in the cell output voltage and efficiency and the cell may get damaged [85]. Therefore, the PV cell should be sustained at low operating temperatures, i.e. the generated heat need to be extracted from the PV cell [85]. Concentrated PV cooling systems are classified into active and passive as presented in Figure **2.27**. In active cooling, a fluid is utilised to absorb the heat generated in the PV cells. Normally, liquid is utilised as the cooling fluid with cooling capability to maintain operating temperature below 100°C. Regarding passive cooling, heatsinks with high thermal conductivity are integrated into the system. The passive cooling selection is mostly adopted for low and medium optical concentrations, while active cooling is used with high optical concentration systems.

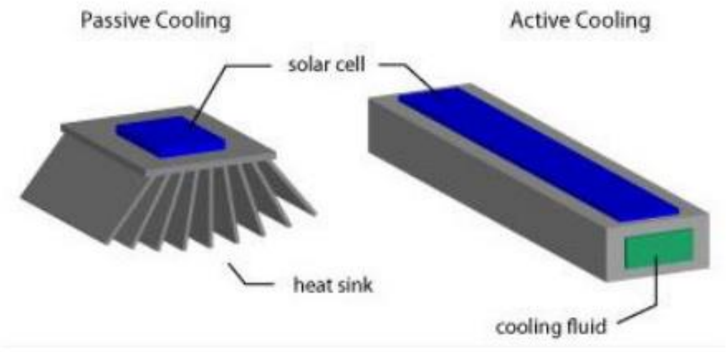

Figure 2.27 Graphics illustration of active and passive cooling designs[86].

2.6.1 CPV with active cooling systems

Kessel et al. [87] reported a Fresnel lens integrated with a multijunction (CDO-100-C3MJ) PV cell manufactured by SPECTROLAB. Figure **2.28** shows the developed water cooling system with Fresnel and PV cell. The PV cell had an efficiency of 35% with a maximum operating temperature of 180°C. The cooling design included an active water cooling technique and a high performance metal (copper channels) for extracting the concentrated solar heat. Their study indicated that at 2000X, the temperature of PV cell was sustained below 85°C on 35°C ambient temperature condition.

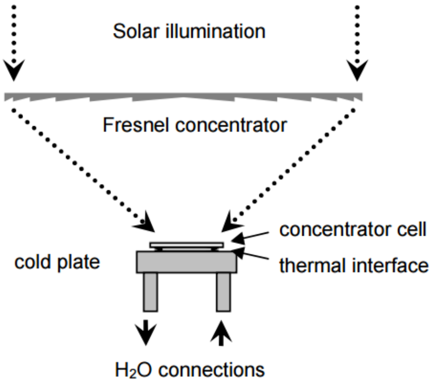

Figure 2.28 Active cooling design with liquid for multijunction PV cell under 2000X [87].

Florschuetz et al. [88] studied two types of active cooling systems applying forced water and air. A single duct for forced water and multiple ducts for forced air were utilised for cooling PV cells strip under solar concentration of 10X. They stated that with forced air cooling there was a high cell temperature increase compared to water cooling. The air specific heat capacity and low thermal conductivity are the causes of the elevated PV temperature compared with water active cooling. On other hand, Water cooling allows operation at high solar concentration. Russell [89] patented and constructed a heat tube cooling system to operate with Fresnel lens. A string of PV cells was attached on a cylindrical heat tube as presented in Figure **2.29**. The heat tube had an internal wick structure for transporting the liquid up to the heated side. The absorbed heat was removed from the tube through connection of an inner coolant system. In order to provide a uniform surface temperature in the tube, the coolant inlet and coolant outlet were lined-up at the same position. Figure **2.29** illustrates the fitted heat tubes which are1.52 m long and 7.62 cm in diameter. No specific details of the design performance, such as PV cell temperature and solar concentration level, were stated.

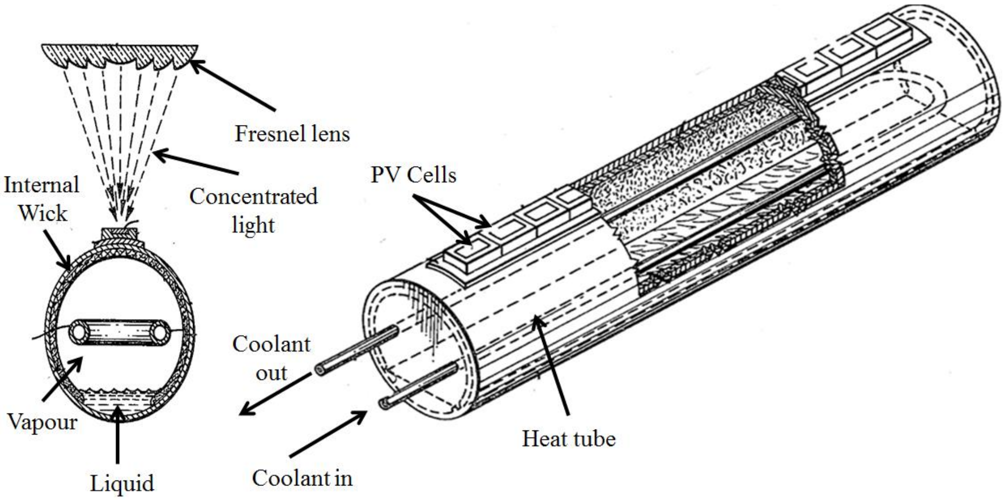

Figure 2.29 PV heat tube cooling system [89].

Conventry [90] presented a hybrid PV and thermal system (CHAPS) at the Australian National University in Canberra, Australia. It consists of a parabolic solar system with narrow and long cells of single crystal silicon PV cooled via water flow throughout a finned aluminium tube. The solar concentrator was experimented with optical concentration of 37X and the results indicated that the water temperature of 65°C was sustained at 25°C ambient temperature. The electrical and thermal efficiencies obtained were 11% and 57%, respectively. The PV cells were made at the Australian National University with low internal series resistance. Zhu et al. [91] introduced a cooling system of dielectric liquid immersion for a high concentrated PV cells row fitted on a solar concentrator dish. Figure **2.30** shows the concentrated PV cell immersed in dielectric liquid at testing conditions of 30°C, 940W/m^2 direct normal irradiance and ambient temperature of 17°C. Their measurements revealed that at maximum solar concentration of 250X, the PV cell temperatures was 49°C and the distribution of temperature is relatively uniform. However, the output power of the system dropped after an extended time of de-ionized liquid immersion.

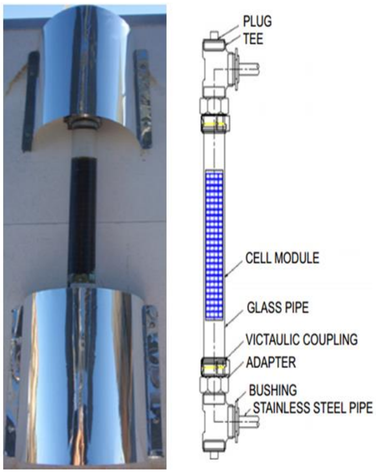

Figure 2.30 Assembly of liquid immersion concentrated PV receiver [91].

A setup of linear Fresnel lenses with cooled PV module through water circulation in a galvanised metal duct were studied by Chenlo and Cid [92]. The solar concentrator system has an optical concentration ratio of 24X. The PV cells are soft soldered to (copper/aluminium/copper) sheet, which is also soft soldered to the rectangular water circulation duct. This mounting provides an acceptable PV cell to metal duct thermal resistance of 8×10^{-5} Km^2/W. The thermal resistance of the coolant duct is 8.7×10^{-4} K m^2 /W at Reynolds number of 5000.

Verlinden et al. [93] reported a parabolic dish PV design utilising an active water cooling structure for a concentrated PV under solar optical concentration of 340X. The size and type of PV cells employed in the investigation were 575 cm^2 and (HEDA312) silicon PV cell, respectively. The electrical pumping power was 86W resulting in average PV cell temperature of 38.5°C. The obtained PV cell efficiency was 24% and with above 70% system efficiency if the excess temperature was reutilised through cooling as beneficial thermal energy. Lasich [94] patented an active liquid cooling circulation constructed of miniature water channels for cooling a row of PV cells in solar system with high concentration. The cooling channels on which the concentrated PV cells were attached to cooling channels which also provide mechanical reinforce for the receiver of the solar system. The designed solar system with cooling was capable of sustaining the PV cells temperature within 40ºC at 500X solar concentration. The reported water inlet and outlet temperature are 30°C and 40°C, respectively.

2.6.2 CPV with passive cooling systems

A study of passive heat tube cooling system for a concentrated PV system was conducted by Anderson et al. [95]. Their cooling system utilises aluminium fins soldered with a copper water heat tube to extract the waste heat through natural convection as shown in Figure **2.31**. A 40°C increase in cell temperature was noticed at solar concentration of 400X. The heat tube has the capability of transferring a great amount of heat from the evaporator into the condenser which considers an effective cooling process for solar system with high concentration. Yet, the dry out possibility of the tube evaporator part can reduce its heat transfer ability at high solar concentrations condition and break the PV cell.

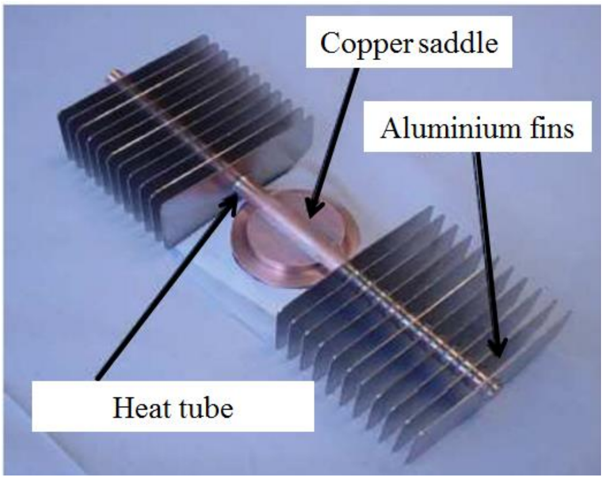

Figure 2.31 Heat tube cooling system with aluminium fins and copper saddle [95].

Araki et al. [96] performed a similar investigational study that showed the effectiveness of passive cooling of solar concentrated PV cells mounted on aluminium sheet as heatsink with fins. To reduce the thermal contact resistance within the heat sink and PV cells, thin layer of thermal adhesive were applied for bonding the surfaces. The system performance revealed that the difference between ambient temperature and PV cells temperature was 18°C under a solar concentration of nearly 500X. The drawback of this solar cooling system is the necessity of larger plane area for greater CPV system as restrains the system potentiality.

Chen et al. [97] performed an experimental study on a Fresnel lens passively cooled with concentrated PV cells employing a heat spreader made of aluminium sheet. The experimental outdoor measurements revealed that the PV cell temperature was less than 75.7°C with solar concentration around 20X. A prototype designed and fabricated by Othman et al. [98] a compound parabolic concentrator of double pass photovoltaic thermal collector with finned heatsink, The hybrid solar system includes an array of PV cells and fins affixed to the rear surface of the receiver plate to improve heat transfer to the streaming air. Figure **2.32** shows the design sketch, the performance of the solar system was studied at different operating conditions and observed that the heat sink improved the PV cells performance and power production. The temperature increase was related to the irradiance amount and the thermal efficiency increased from 40% to 80% as the air stream flow rate increased starting at 0.015 up to 0.069 kg/s under irradiance of 600 W/m^2. The achieved electrical conversion efficiency of the system was around 3%.

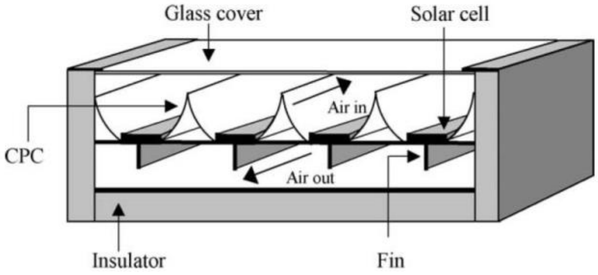

Figure 2.32 Photovoltaic/thermal CPC solar concentrator attached to fins[98]**.**

Sala et al. [99] carried out an experimental investigation of a trough solar concentrator (EUCLIDES) utilising aluminium finned heatsink for passively cooling PV cells array. The investigational outcomes of the optimised and enhanced fin dimensions indicate that the concentrated PV cell temperature was sustained nearly 58°C at a solar concentration of 30X. The drawback of this cooling system is the fins enhanced and optimised dimensions of 10mm fin space, 140mm and 1mm fin thickness made the manufacture process complicated and expensive

Feldsman et al. [100] investigated the performance of Edenburn's CPV/T design utilising the thermosyphon heat tube. The cooling system was assembled employing extruded aluminium tube and the operational liquid was Benzol. The highest recorded evaporator tube external temperature was around 140°C at approximately 24X solar concentration. They explained that the heat tube cooling system performance was greatly reliant on the condenser tube external part and the ambient conditions including ambient temperature, wind speed and inclination angle of the PV cell. Wadowski and Akbarzadeh [101] designed and constructed a solar linear trough concentrator system with passive cooling method using a heat tube as illustrated in Figure **2.33**. The heat tubes were built utilising compressed copper tube and fins. The PV cells were attached on the heat tube evaporator part and that was vertically placed. The outcomes specified that the PV cell temperature under 20X solar concentration did not exceed 46°C. They additionally stated that the PV cell temperature can go up to 84°C in similar ambient conditions but under no cooling system.

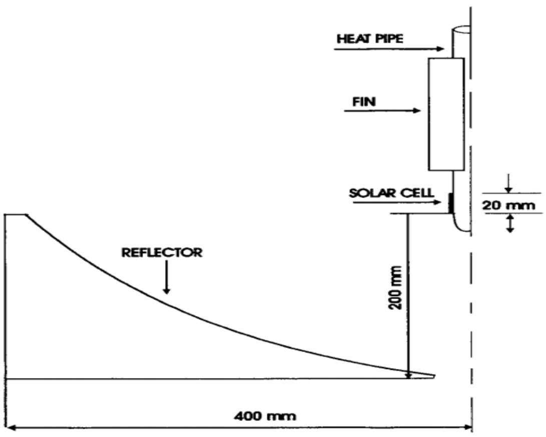

Figure 2.33 Diagram of heat tube based solar cooling system

2.7 Review on CPV performance in dusty condition

A limited number of studies have been conducted with the aim of measuring the loss in photovoltaic concentrator systems due to dust accumulation. Since the solar concentrators system can only utilise the direct solar radiation part of sunlight, a considerable amount of the sunlight is scattered and wasted once the concentrator cover surface are dusty and the optical system cannot concentrate the scattered sunlight on the PV cells [102].

In 1942, the first study on the phenomena of dust deposition on PV/thermal concentrators by Hottel and Woertz [103], when the research group presented various investigations of solar concentrator positioned at 30° angle. These modules exposed for three months uncleaned in a manufacturing district concluding that a drop in the output power of 5% was achieved due to dust. In 1986, Deffenbaugh et al. [104] considered the effect of dust on parabolic trough solar concentrator. The study evaluated the outdoor performance of three solar concentrators placed in there different locations in USA with arid weather conditions. Maximum average degradations on output power were 0.7%, 1.3% and 1.3% per day for the three different locations. Moreover, the solar concentrator placed in arid environments had higher possibility of degradation as a result of the low raining seasons and high rate of atmospheric dust. It was concluded that to maintain an output power of 95%, the solar concentrator should be cleaned on daily basis.

There are limited reports on the impact of natural dust on CPV systems, Gombert et al. [105] reported regarding Concentrix, solar system with multijunction PV cells receiver, a linear Fresnel lens set with 12.7 square centimetres single lens, and a cover container made out of glass. The Concentrix solar concentration system has an optical concentration of 500X. The performance of solar system installed in semi-arid climates conditions were investigated with direct normal irradiance of 600 W/m² in Oman. Gombert et. al. developed a method for the determination of daily dust accumulation rates at Oman. The system output power was 15.5%

at dusty condition then increased up to 20.6% after cleaning the surface of the solar concentrators. The achieved system efficiency was 25% at ambient temperature of around 43°C.

The impact of dust on the performance of concentrated PV was studied by El-Shobokshy et al. [106]. The dust concentration in the atmosphere was measured throughout the experimental period, along with the amount of dust particles accumulating on the mirror reflectors surfaces. To allow comparison, a similar regularly cleaned concentrator was analysed together with the dusty concentrator mirror reflectors. The variation in the light reflectivity of the mirror reflectors was measured together; with the variation in the electrical output of the PV module was employed as the determining factor. The variation of current and voltage output characteristics due to dust deposition was related to the dust deposited per unit area of the mirror reflectors surface. It was demonstrated that for output of short-circuit current, considerable reductions occur as the dust accumulate on the mirror reflectors surface; however the amount of reduction is slower for dust accumulations beyond dust value of 2 g/cm^2. These current and voltage output characteristics are shown in Figure **2.34**.

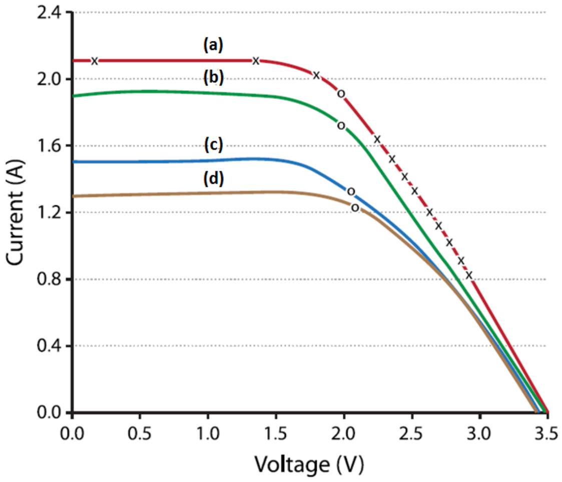

Figure 2.34 The current and voltage output characteristics of concentrated PV module with different amount of dust deposition: (a) clean mirror surface; dust rate at values of 0.85, 1.85 and 5.4 g/cm^2 for (b), (c) and (d), respectively [106].

Stone et al. [107] studied the Amonix solar system at soiled conditions. This is a solar concentration system which uses Fresnel lenses to reach an optical concentration of 300X. The system testing facility is located in Tempe, Arizona. Results of dust particles deposition on this system showed that after 30 days without cleaning, where pressured water spray of the solar contractors, the system array output current increased by approximately 15%. They attributed the degradation in the CPV performance to be due to the dust particles deposition and the conditions of the topography including pollution, grass and sand.

Vivar et al. [108] carried out outdoor simple experiment situated in Spain, consisting of five different solar concentrating technologies namely: high concentrator CPV (300X) and two medium concentrators CPV (20X and 40X) and two low concentrators CPV (2X and 10X). The different solar concentrating technologies used are described as follow:

- 2X: V trough mirrors and passive cooling with fins.
- 10X: cylindrical parabolic mirrors and passive cooling with fins
- 20X and 40X: cylindrical parabolic mirrors with single axis tracking system, the systems included a passive cooling with thin fins.
- 300X: Fresnel lenses point focus type dual axis tracking system, the systems included forced water convective cooling.

Over 4 months, all systems short-circuit current have been recorded for both unclean and clean, showing different reductions in short-circuit current. For low concentration system the short-circuit reduction is about 8% and 16.5% for 2X and 10X, respectively. For the medium concentration system, measurements showed a decrease in short-circuit current of around 23.2% and 26% for 20X and 40X, respectively, where the high concentration systems of 300X decreased by approximately 12.3%. No detailed information regarding the PV cell types have been reported in this study. Algora and Stolle [21] noted on their standards of CPV technology that dust cause 2% losses on system efficiency depending on the configuration utilised.

2.8 Ray tracing modelling

Initially, ray tracing technique was applied using logarithmic trigonometry charts. However, recently advanced ray tracing simulation software became available commercially and has been employed in designing optical components for instance reflectors and lenses [109]. In recent work, Marquez et al. [110] generated a numerical model applying ray-tracing method with the aim of simulating the direct ray reflection within a CPC. The investigation results showed that the amount of the energy distribution on the receiver relies on the surface properties. In addition, the energy distribution uniformity increases when the surface reflectivity of the solar concentrator increases. The generated mathematical model used 2D-CPC concentrator model, but in real application the sunlight rays change in three dimension concentrators throughout the daytime. A ray-tracing study carried out by Spongale and Gorulx [111] was performed on two-phase solar concentrator built with double parabolic glass mirrors. The MATLAB programing code was used to simulate the ray-tracing procedure. The impacts of the width of the concentrator unit, the focal length of the secondary mirror and the space between the target area and the secondary mirror, as well as the impacts of the misplacement of the concentrator unit under the sunlight were all considered. The ray-tracing model suits more 2D solar concentrator. Yet, it is unsuitable for 3D reflective solar concentrators fabricated from dielectric substance, as the executed equations are diverse; and the magnitude of the concentrated light rays and the substance properties have to be considered. The (LightTools) optical software was utilised in the ray-tracing work of Pei et al. [112] to examine truncated dielectric 2D-CPC. The study illustrated that in the 2D-CPC half acceptance angle, a portion of the entering rays do not go through a full interior reflection. Although the 2D-CPC optical and geometric performance is outstanding; the ray-tracing method was merely capable of identifying the losses due to the refraction in the dielectric 2D-CPC. The authors showed the advantage of using a mirror coating placed at the border of a truncated dielectric 2D-CPC causing an increase of up to 13.5% in the optical concentration performance. Different ray tracing models are compared using various softwares and presented in Table **2.3**

Table 2.3 comparison of CPV design using various Ray tracing software

Software	**Type of concentrator**	**Type of application**	**Dev with Exp.**
[113] Matlab	Mirror symmetrical dielectric	Photovoltaic	9%
[114] Zemax	Fresnel lens	Thermal-Photovoltaic	16%
[115] OptisWork	V-through	Photovoltaic	2 %
[116] OptiCAD	Parabolic Dish	Thermal	10%
[117] Trace Pro	Compound Parabolic	Photovoltaic	6.5%
[118] SolTrace	V-trough	Photovoltaic	10%
[119] MINSUN	Compound Parabolic	Thermal-Photovoltaic	13%

2.9 Summary

The following conclusions are set forth from the literature review:

- The CPV system performance is affected via different factors and that can be; availability of solar radiation, concentrator design and PV cell technology. Therefore, it is advantageous to consider the impacts of dust accumulation on these factors on a CPV with 2X – 6X for understanding and potential optimisation.
- Despite there are several studies reported on the effect of dust accumulation on CPV reported however they are limited either to specific CPV class or particular CPV aspects as electrical output measurement and cover coating. Numerous studies reporting the dust accumulation effect on non-concentrating (flat) PV but few on CPVs system which could be used to validate the impact of dust accumulation and the

basic dust related factors that impact CPV performance. Further quantitative and comprehensive information is essential.

- Passive cooling techniques have a major issue related to insufficient cooling performance as the heat-dissipation amount is depending on the atmospheric surroundings. Hence passive cooling is not commonly suggested for CPV applications in high ambient temperatures climate as Kuwait.
- Most studies are aimed at a specific region and environment, with regard to supply their energy demands. Thus, it is beneficial to conduct work to focusing on dust accumulation problems in hot arid climate countries (as Kuwait) where major PV system degradation can occur.

An experimental study of how dust affects non-concentrated PV system performance in Kuwait is presented in next chapter to establish the baseline which is used to correlate CPV with dust accumulation effect in the thesis later chapters.

CHAPTER 3

Outdoor Experiment in Kuwait

3.1 Introduction

This chapter describes outdoor testing of unconcentrated two types of PV modules in Kuwait. First, a detailed description of Kuwait environment including solar availability, ambient temperature, wind speed, atmospheric dust accumulation and dust optical characteristics is included. Then a detailed description of the testing setup including measuring devices, two type of PV technologies and dust accumulation throughout the outdoor exposure period. Finally, the chapter includes description of the results obtained regarding the effect of dust on the electrical performance of the two PV technologies.

3.2 Kuwait environment:

3.2.1 Weather data collection

Weather data are collected and analysed by The Kuwait Environment Public Authority (KEPA) and Kuwait Institute for Scientific Research (KISR). Table **3.1** shows the data collected at those two institutions, to obtain the required solar data for this work.

Table 3.1 Types of data obtained from (KEPA) and (KISR)

Data Type	**KEPA**	**KISR**
Solar irradiance (Diffused)	X	✓
Solar irradiance (Direct beam)	X	✓
Solar irradiance (global horizontal)	✓	✓
Dust concentration	✓	X
Ambient temperature	✓	✓
Aerial dust (Visibility)	✓	X
Wind Speed	✓	X

KEPA and KISR record the data using high resolution monitoring of 5 minute per interval for a 12 months, at several weather stations set at various areas in Kuwait. Hence to minimise the variation of recorded data from different locations, weather stations near to each other were chosen.

3.2.2 Solar radiation availability

The solar radiation level that strikes various areas on the surface of earth changes due to the seasonal shift and latitude. These changes involve daylight hours, atmospheric attenuation and sun light incidence angle. The decrease in solar radiation when it travel across the atmosphere is caused by absorption and scattering in earth's atmosphere agents such as carbon dioxide, water vapour and methane [120]. In addition, further decrease in solar radiation level in a specific area is due to the regional climate condition of the air such as pollution, cloud and airborne dust (Figure **3.1**). The solar radiation that strikes the surface of earth after scattering in the atmosphere is termed diffuse radiation whereas direct (DNI) is the radiation obtained without scattering. The total of these two elements is commonly characterised as normal global radiation (GHI).

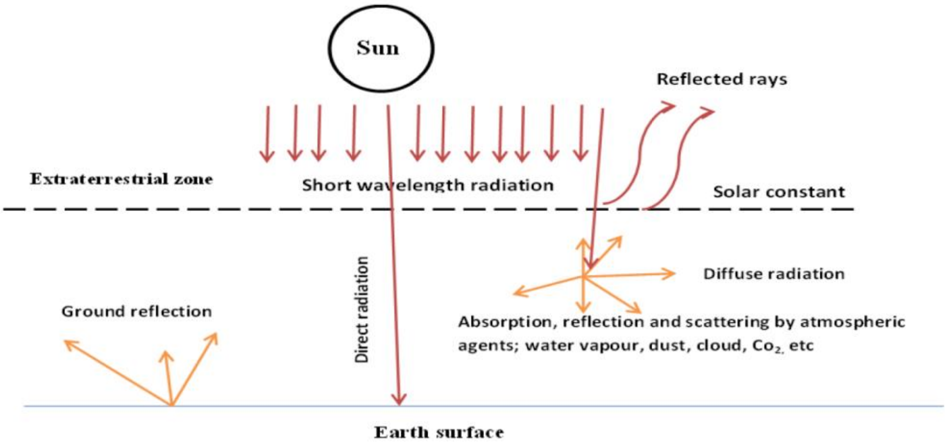

Figure 3.1 Solar radiation coming from the sun to the earth surface which incident on a particular place at specific latitude relies on air mass condition [121].

Kuwait situated in the Middle East with latitude at 29.32° north and longitude at 48.003° east. Figure **3.2** shows the monthly average solar radiation set of global horizontal, diffuse radiation and normal irradiance for the year 2013 [8, 122].

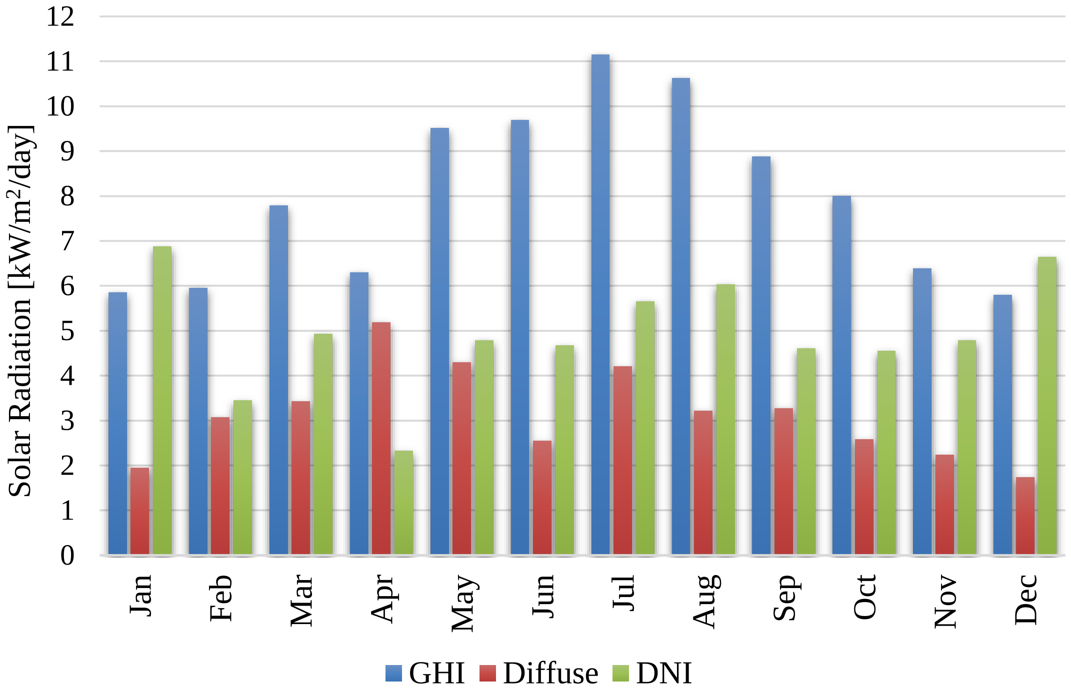

Figure 3.2 Monthly average solar radiation availability in Kuwait.

The above figure shows that, the highest amount of global horizontal solar radiation of 11.2 kW/m^2 per day occurs in July, whereas April has the maximum diffuse amount per day of 5 kWh/m^2 and January has 6.8 kWh/m^2 per day in DNI. The measurement of DNI and diffuse radiation provides indications of suspended dust impact throughout the specific month, For example the amount of DNI radiation is lower than the diffuse during the month of April. In spite of the low rate of DNI radiation could be related to various environmental factors like greenhouse gasses and clouds, the major factor which causes low DNI radiation in Kuwait is the suspended dust. Figure **3.3** shows the average daily hours of sunlight in Kuwait recorded by KEPA [123]. The month of July has highest sunlight hours, while the month of December has the shortest time of sunlight hours.

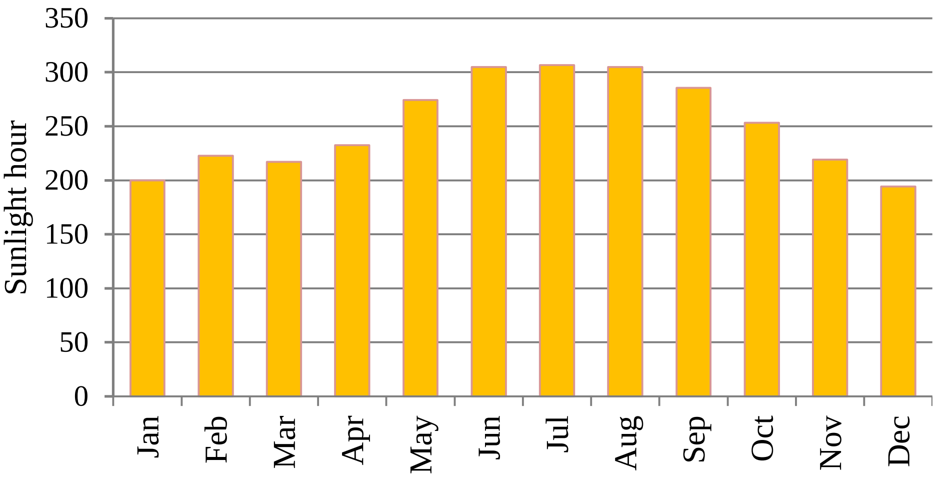

Figure 3.3 The average daily sunlight hours in year 2013 [123].

The monthly clearness index of Kuwait can be calculated as [124]:

$$\overline{K}_T = \overline{H} \big/ \overline{H}_o \tag{3.1}$$

Where $\overline{H}$ is the monthly average hemispherical radiation and $\overline{H}_o$ is the monthly average extraterrestrial radiation on a horizontal plane (see equation 3.2) in the nth day of the year as specified in Table **3.2** [124]:

$$\overline{H}_o = \frac{24 \times 3600 G_{sc}}{\pi}\left(1 + 0.033\cos\frac{360n}{365}\right) \times \left(\cos\phi\cos\delta\sin\omega_s + \frac{\pi\omega_s}{180}\sin\phi\sin\delta\right) \tag{3.2}$$

Where G_{sc} is the solar constant taken as 1367 W/m^2 and δ is the solar declination given as:

$$\delta = \left(23.45^o\right)\sin\left[360^o\left(284 + n\right)/365\right] \tag{3.3}$$

The solar declination depends on the day of the year, n, (with n = 1 for 1st January,)

The sun hour angle ω_s is given by [124]:

$$\omega_s = \cos^{-1}\left[-\tan\phi\tan\delta\right] \tag{3.4}$$

Table **3.2** shows the mean day of each month, n and corresponding solar declination δ. Figure **3.4** shows the monthly average clearance index of Kuwait as calculated by equations

3.1-3.4, where high clearness index ($\overline{K}_T$ > 0.5) relates to sunny atmosphere, as most of the solar radiation will be (DNI). On the other hand a low clearness index ($\overline{K}_T$ < 0.5) shows unclear atmosphere with diffuse solar radiation. The month of June has the highest clearness index value of 0.66, while the lowest clearness index is the month of March with around 40%.

Table 3.2 Recommended Average Day for Months and Values of n and δ [124].

Month	***n* for *i*th Day of Month**	**Date**	**n, Day of year**	**δ , Declination (°)**
January	*I*	17	17	-20.9
February	31 + *i*	16	47	-13.0
March	59 + *i*	16	75	-2.4
April	90 + *i*	15	105	9.4
May	120 + *i*	15	135	18.8
June	151 + *i*	11	162	23.1
July	181 + *i*	17	198	21.2
August	212 + *i*	16	228	13.5
September	243 + *i*	15	258	2.2
October	273 + *i*	15	288	-9.6
November	304 + *i*	14	318	-18.9
December	334 + *i*	10	344	-23.0

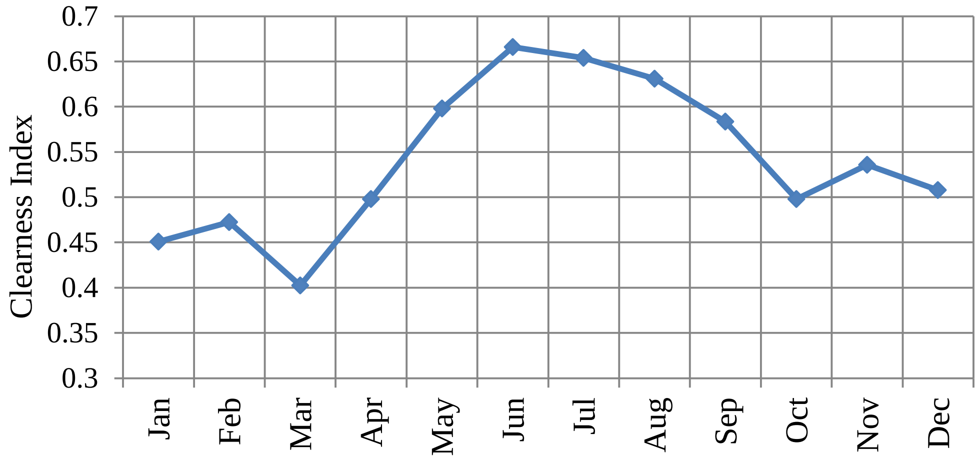

Figure 3.4 Monthly average clearness index in Kuwait.

3.2.3 Ambient temperature

Figure **3.5** illustrates the average maximum and minimum ambient temperature in Kuwait for year 2013. During July and August, the average daily maximum temperature is 48 °C while the maximum temperature reported in Kuwait was 53.9 °C at the desert area in July 2013 which is considered as the highest reported temperatures in Middle East and the third highest one worldwide [125]. The lowest minimum average ambient temperatures were found during December and January.

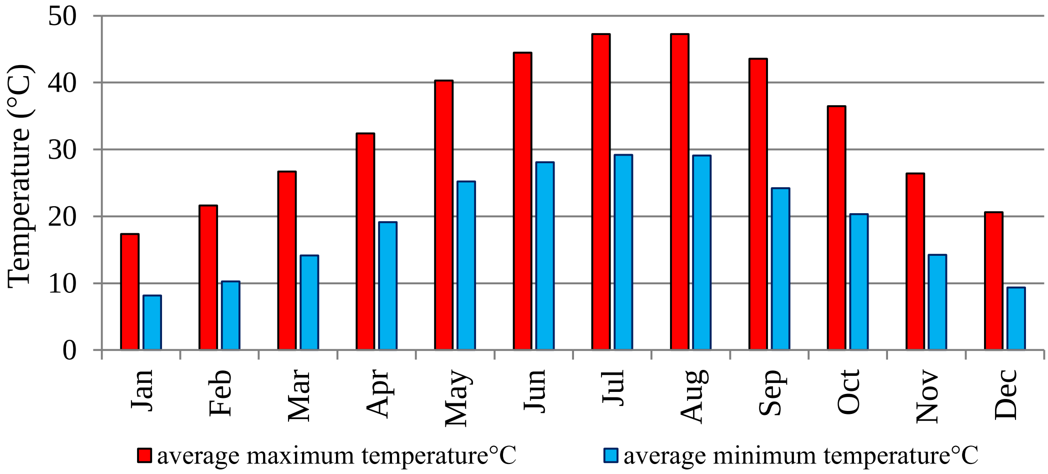

Figure 3.5 The average maximum and minimum ambient temperature in Kuwait year 2013 [125]

3.2.4 Atmospheric dust

Due to its low topographic position and little vegetation, Kuwait is vulnerable to dust storms. The storms crossing Kuwait carries substances of sediment containing 85% dust and the rest is silt [126]. The accumulated dust measurement was carried out at (KEPA) using a custom-built vessel placed horizontally outdoors to collect dust for the entire day. After dust is collected the vessel mass difference (initial mass when immaculate and final once dust accumulated) is calculated and recorded, the same technique was used daily for the entire year 2013 [127]. Figure **3.6** shows the results of average daily accumulated dust weight. The highest dust accumulation during the year occurs in April till July where regular dust storms are occurring. Al-Dousari [128] defined a dust storm in Kuwait as when the visibility is less than 1000 meter, where dust movement is low throughout winter, rises in April, and reaches its maximum in June as shown in Figure **3.6**.

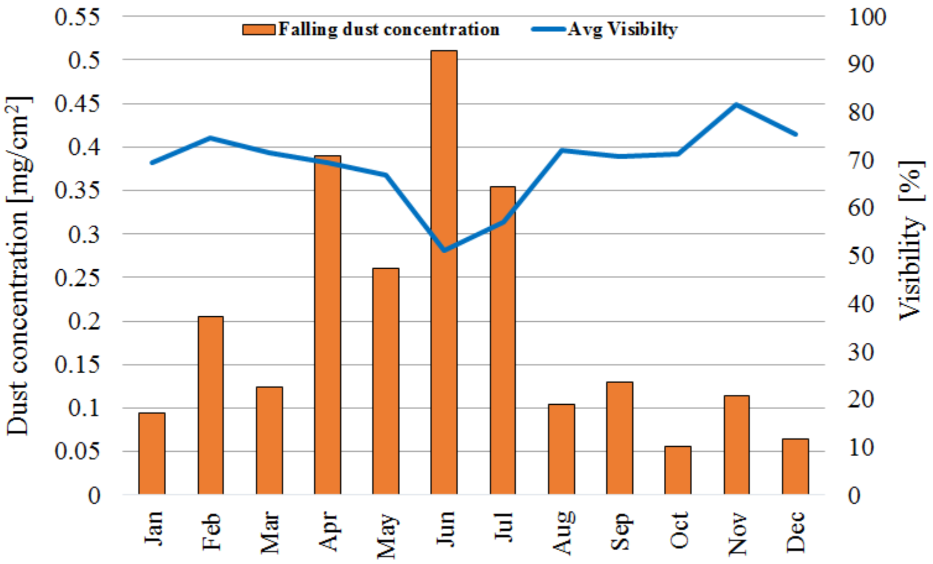

Figure 3.6 Recorded (KEPA) measurement of average daily accumulated dust weight and visibility rate for the year 2013 in Kuwait [67].

Figure **3.6** clearly illustrate that dust is (dust storm or suspended and aerial dust) capable of reducing visibility significantly. The month with the highest visibility was November, with a visibility percentage of 80%, where as the month of June had the lowest visibility percentage of 51%. Therefore, typical dusty months includes limited days of dust storms and suspended dust is in the range of 0.25 mg/cm^2 or more and whatever less than that is specified as a typical month.

3.2.5 Wind speed

It was observed from literature that as wind velocity increases, dust storm occurrence increases [129]. An increase in wind speed can lead to the increase of the accumulated dust layers on a PV surface [130]. An increase in wind speed leads to a low visibility due to suspended dust accumulation as shown in Figure **3.7**.

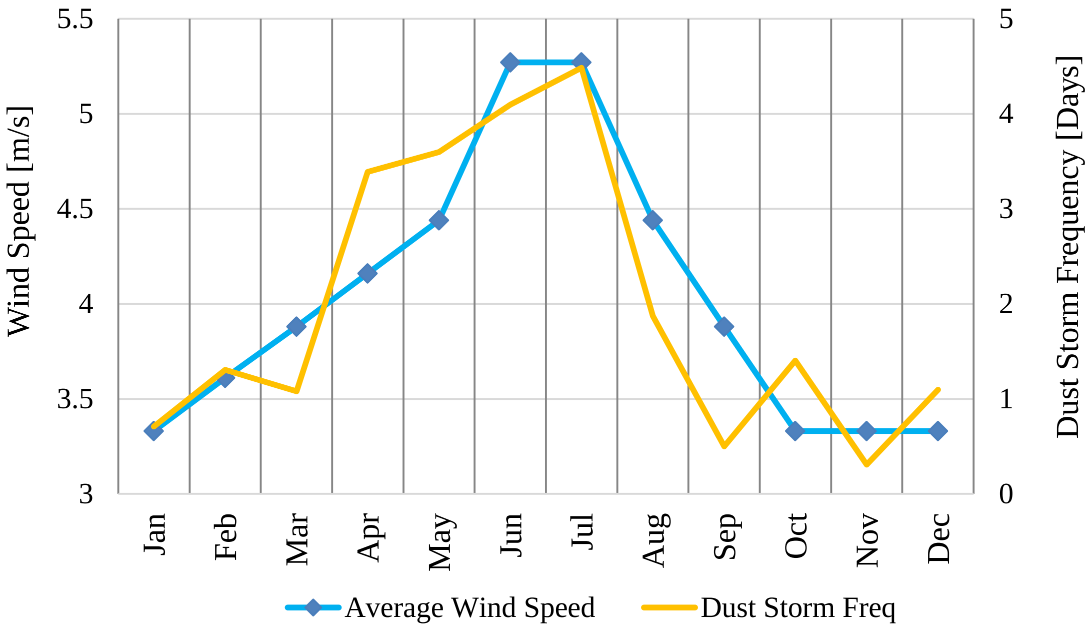

Figure 3.7 The monthly average wind speed and the number of days of dust storm.

Dust accumulation around 5 m/s wind speed starts to descend. Also the month of December is the calmest month at average wind speed of 3.33 m/s, where June is windiest month at an average wind speed of 5.27 m/s.

3.3 Outdoor experimental setup and analysis procedure

In this section a detailed description of the modules and the measuring facility developed for investigating the impact of dust accumulation on PV modules performance, in term of electrical parameter like; V_{max}, I_{max}, V_{oc}, I_{sc}, I/V and P/V curves and thermal parameter like temperature of modules along with weather data representing the ambient temperature, wind speed and in-plane solar irradiance. There are certain approaches to investigate the PV modules performance degradation [27, 37, 131], including measurements of I/V and P/V characteristics, visual examination and investigative estimates of degradation rates. In this study, the analysis of one year outdoor exposure was carried out using the methodology shown in Figure **3.8**.

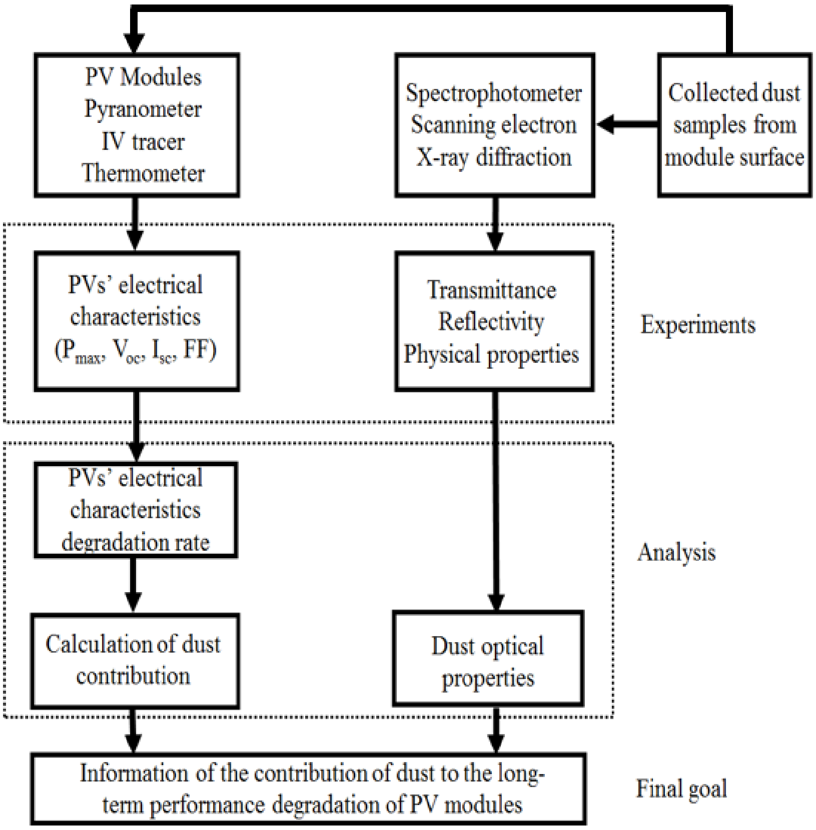

Figure 3.8 Procedure to evaluate the impact of accumulated dust on PV performance.

3.3.1 Measurement setup and procedure

The outdoor measurements for the PV modules were performed in KISR at the renewable energy department car park. As shown in Figure 3.9 the system consists of two pairs (clean and dusty) PV modules made from two different cell technologies. Table **3.3** presents the performance of the two PV modules under (STC) of solar irradiance 1000 W/m^2, air mass (AM) of 1.5 and cell temperature of 25 °C. They are installed facing south and tilted at 30° which corresponds to the latitude of Kuwait. The measurement arrangement includes uninterrupted readings of I_{sc}, V_{oc} and module temperature in addition to in plane module solar radiation. All the PV electrical outputs were determined by (IV) curves measurements of the fitted panels.

Table 3.3 Characteristics of PV Modules tested outdoor

Specification	**Monocrystalline (SP)**	**Polycrystalline (Poly)**
Technology	Monocrystalline back contact	Polycrystalline
Area (m^2)	1.24	1.66
No. of cells	72 in series	60 in series
Maximum power	225W	240W
Maximum voltage	41.0 V	29.4 V
Maximum current	5.49 A	8.17 A
Open circuit voltage	5.87 A	37 V
Short circuit current	48.5 V	8.61 A
Short circuit temp coefficient	3.5 (mA /°C)	0.06 (mA /°C)
Open circuit voltage temp coefficient	-0.132 (V /° C)	-0.32% (V /° C)
Maximum power Temperature Coefficient	-0.38% (W /° C)	-0.37% (W /° C)
Module efficiency	18%	15%

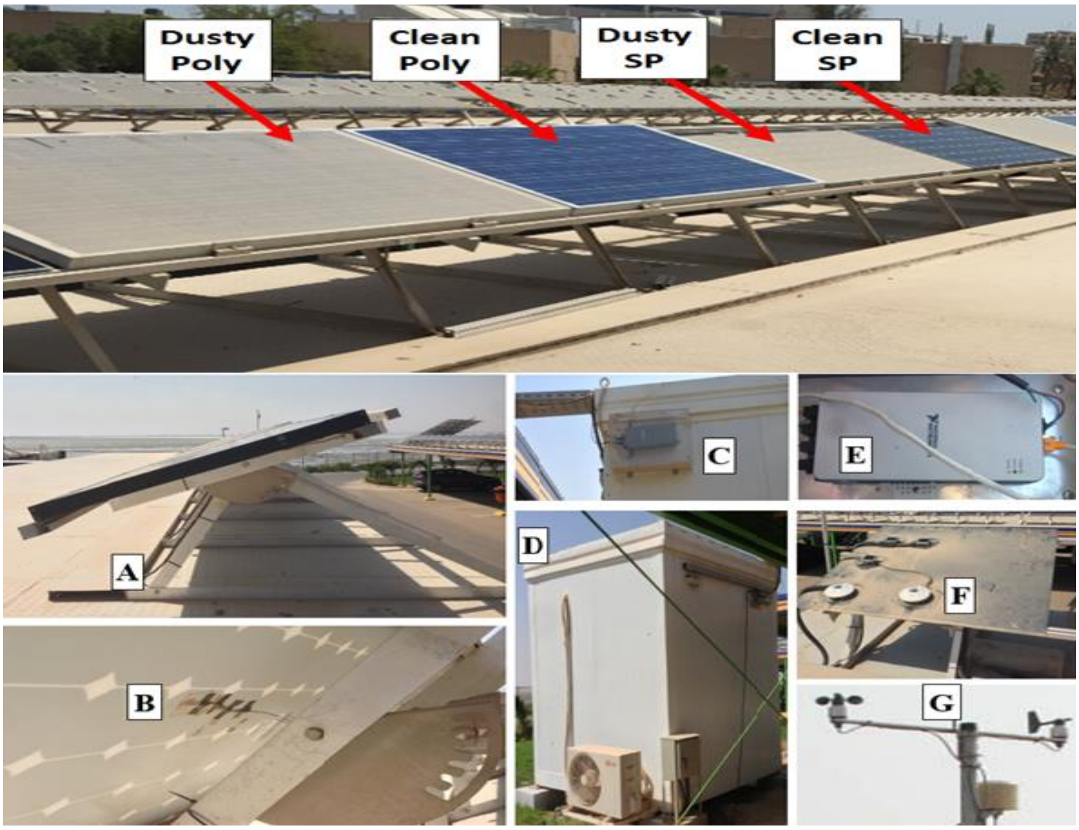

Figure 3.9 UP: Installed PV Modules covered by dust and daily cleaned in KISR. Down: (A) Modules support frame (B) module temperature sensor (C) Data logger (D) PC cabinet (E) IV tracer (F) In plane Pyranometer (G) Wind speed and ambient temperature sensors.

The experimental setup was equipped with a range of instrumentations including a Kipp & Zonen pyranometer with voltage sensitivity of 7 to 14 µV/W/m^2, operational temperature range of -40^{o}C to +80^{o}C and +/-10W/m^2 error in measuring the solar radiation on the module plane. The pyranometer was mounted on the inclined plane of the PV modules (30^o) and cleaned on daily basis. Moreover, the temperature of each module was measured with PT100 temperature sensor with temperature range of -50/+300°C and +/- 0.6°C accuracy attached on the back sheet of the PV modules investigated. The temperature sensor is thermally attached by a thermal conducting adhesive and insulated from the ambient temperature effect. Temperature sensors from each PV modules are coupled to IV tracer/maximum power tracker unit custom made for this project built by ONSET, which sweep 200-point IV data every minute, along with maximum power output. The IV tracer maximum voltage and current readings are 250V and 10A with sweep speed of < 5 seconds per channel at 50 steps. The PV modules are coupled by 4-wire 3mm^2 flexible cords connected to the IV tracer and data logger. The monitoring equipment preforms real time measurement of PV modules IV characteristics repeatedly. Readings from each single (I/V) curve tracer and maximum power point tracker (MPPT) are recorded to a file per day. The IV tracer device is connected to a Data Acquisition system (Texas Instruments) and to PC. The measurement instruments are scheduled and arranged by data recorder software which is integrated with the PC timer. The measurement of volts, ampere, power output and module temperature was carried out during 12 months periods. A planned data backup collection was taken every 1 month in addition to the regular data recording to indicate any non-uniformity of the modules outputs. The data acquisition system process is shown in Figure **3.10**.

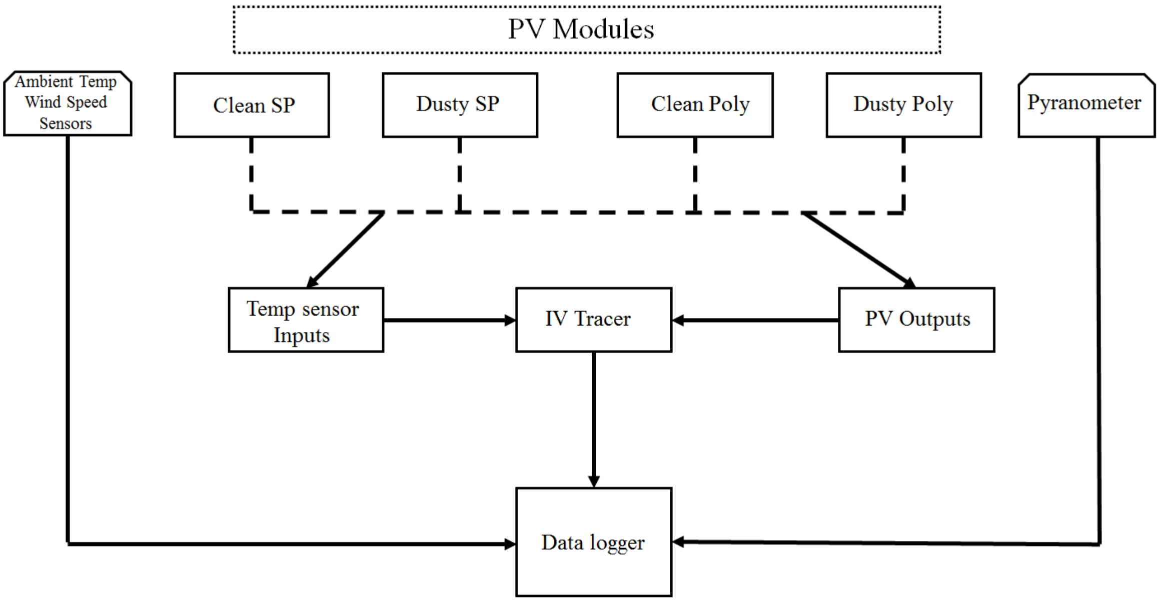

Figure 3.10 Experimental data acquisition system at KISR.

The ambient temperature sensor is a resistive type with solar shield measuring range of -50 to +50 ^{o}C, while the wind speed was measured by anemometer sensor with measuring range of 0-60 m/s which was fitted close to the PV module experimental setup. The wind speed and ambient temperature sensors are connected to a data recorder (Texas Instruments) which is connected to the PC by USB cord and data is recorded every 5 minutes. Finally, the measured module output data and meteorological data were transferred to a data acquisition system held at KISR renewable energy department. Table **3.4** shows the accuracy of the measuring devices used in the experimental work as obtained from their manufacturer data sheet.

Table 3.4 Accuracies related to the monitoring devices of the PV outdoor measurement

Data type	**Values**
PV parameters	
I/V tracer device	0.4%
MPPT computation	0.4-1%
Module temperature sensor	±0.3 (^{o}C)
Short circuit-current	0.28%
Open circuit voltage	0.32%
Maximum power	0.19%
Weather parameters	
Wind speed	±1.5% (±0.5m/s)
Ambient temperature	±0.1 (^{o}C)
Pyranometer	±3% (±1.1 W/m^{2})

3.3.2 Visual Inspections of Dust Accumulation Uniformity

The visual inspections began at 2 separate periods; the PV modules were mounted on 11/01/2013. The reference module (clean module) was cleaned on daily basis with low pressure water, to avoid any glazing substances from cloth or brush. Figure **3.11** illustrates the difference in modules condition at one and eight months after installation. To the end of the monitoring periods of the PV modules, the visual inspection did not indicate any visible defect or discoloration of the clean modules, while a clear sequence of dust deposition appeared on the uncleaned modules. During the outdoor exposure period, few high concentration dust spots appeared on the uncleaned PV modules surface, mostly caused by the insignificant impact of removal elements as humidity, rain drops and wind. Despite, the few concentrated dust spots, the dusty modules surface shows a uniformly accumulated dust layer. Furthermore, due to the incapability of the rainfall to remove all dust, the dust particles managed to remain on the PV modules glass. The module frame allowed more dust accumulation on the inner edges of the dusty modules perimeters but not on the active area of modules i.e. the PV cells. The accumulated dust can cause early malfunction as a result of hot spots, however no modules failure were detected during the measuring period.

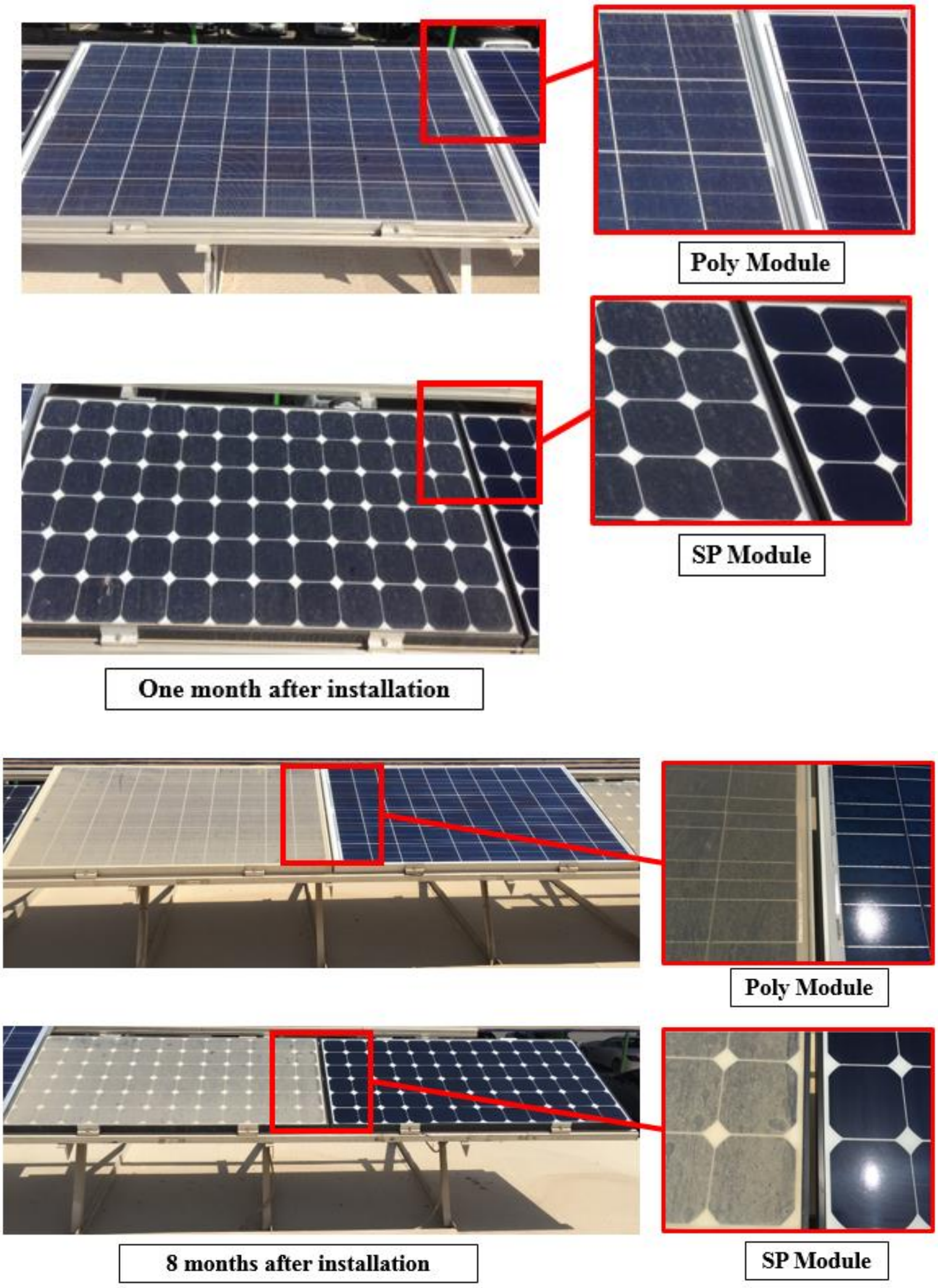

Figure 3.11 Photos of the measured PV modules at separate days of the year.

3.3.3 In plane measured solar radiation

Kuwait atmosphere is sunny and cloudless most of the year specifically during summer period in months of June, July and August, and that increases the amount of solar radiation delivered to PV modules. While, the winter period recorded less amount of solar radiation due to lower clearness index, specifically in months of January and December. Figure **3.12** shows the average hourly measured in plane solar radiation of every month for the year 2013. The months of June, July and August have the maximum with about 1000 W/m^2 at midday period whereas December and January have the minimal solar radiation with around 600 W/m^2 during midday period likewise. As a result of dust storms occurrences, the solar radiation slightly dropped before midday period during July. The amount of solar radiation in April and October are almost similar. It is obvious that the highest obtainable solar energy level is through the midsummer period and oppositely through the winter.

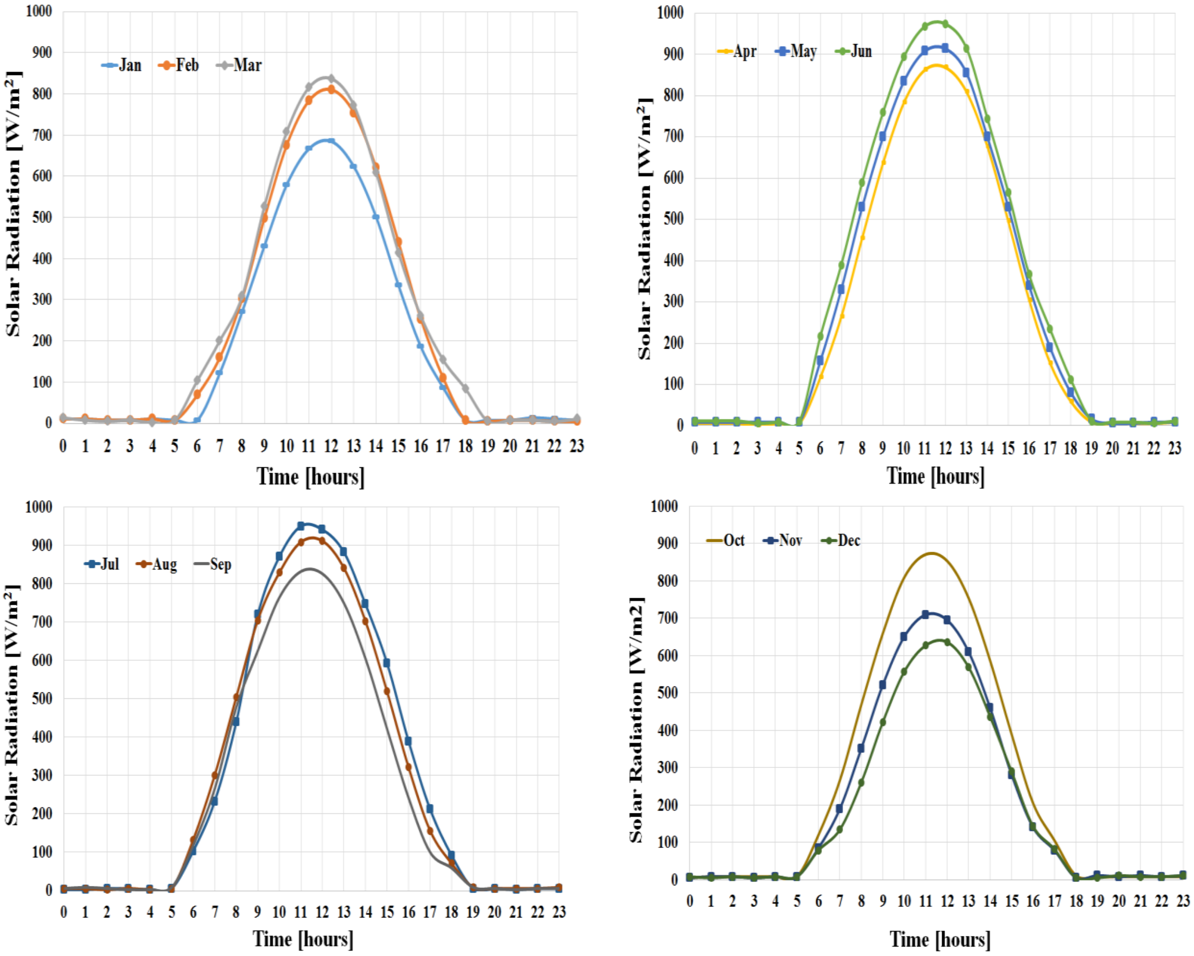

Figure 3.12 Average hourly in plane solar radiation measured in KISR site for year 2013

3.3.4 Measured PV power output

Figure **3.13** shows the measured data of PV average monthly output power throughout the year for clean and dusty PV modules, as the dust was evidently visible and a layer of dust built-up on PV module surface. It is clear that PV output power starts to increase considerably in the summer for clean and dusty PV modules as the average in plane solar radiation increases, and decreases in winter gradually. PV output power drop was unsteady in all modules condition, where highest power achieved for clean PV modules were 180W and 178 for Poly and SP, respectively. On the other hand, the lowest power output of the daily cleaned PV modules was in December for Poly with power output of 118W and 120W in January for SP.

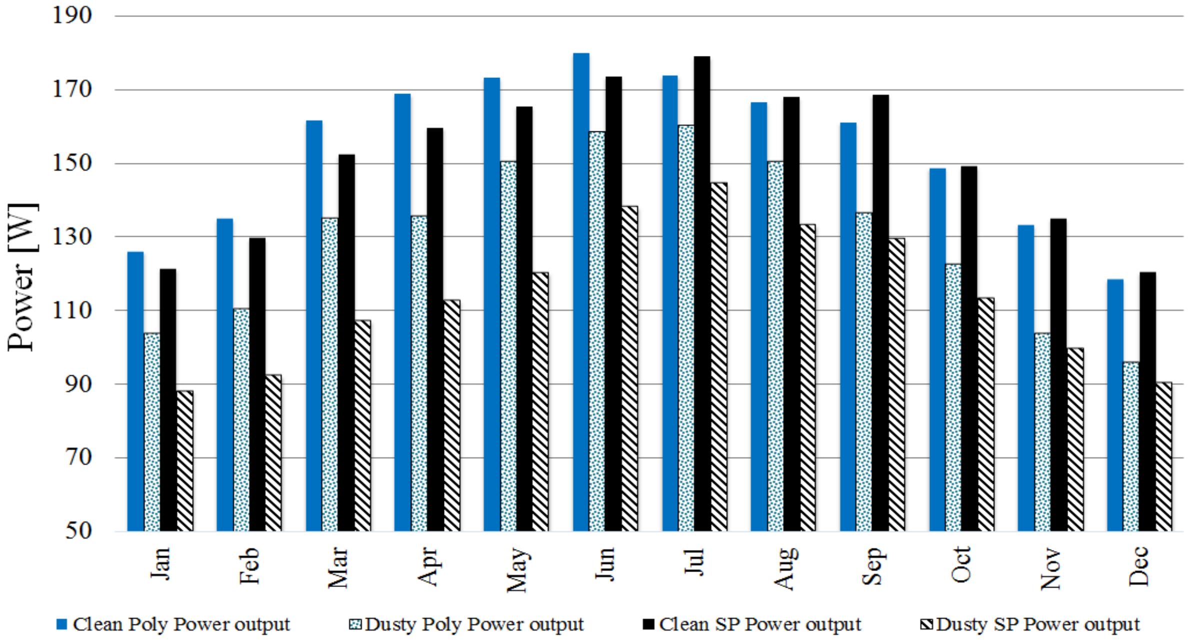

Figure 3.13 Average monthly in plane irradiance and power output of clean and dusty PV modules during 12 months.

Regarding the dust effect, the decrease in PV output power is significant, and the results are high in months with low radiation level. Actually, the PV module power output falls in winter as a result of a combination of dust and low clearness index (such as cloud), where this affects the solar radiation falling on the PV cells. The maximum PV output power was achieved by dusty module are 160W and 144W for Poly and SP, respectively, all in the month of July. While the minimum PV output power was received by dusty module are 95W and 88W for Poly and SP, respectively. It is evident that dusty poly power reduction was high in comparison with results using a daily cleaned Poly module, however the dusty SP power reduction was higher during the whole year with respect to the clean surface. The PV modules measured data was utilised to determine the losses of PV average output power. The percentage difference between the Poly and SP dusty modules with reference to its daily cleaned identical was determined through using equation 3.6 and illustrated in Figure **3.14**.

$$P_{\mathrm{Loss}}(\%) = \left[\frac{P_{\mathrm{clean}} - P_{\mathrm{dusty}}}{P_{\mathrm{clean}}}\right] \tag{3.5}$$

Where P_{clean} is the average power output of cleaned module, P_{dusty} is the average power output of dusty module, and P_{loss} is the percentage drop caused by dust accumulation. Comparing Poly and SP dusty modules to the clean ones, the months of January and November indicated the highest losses of 35% and 47% for Poly and SP modules, respectively. This can be attributed to reduction of the solar radiation level received by the module through the dust layer. The dusty Poly module showed lower power loss percentage of 11% in July compared to that of the dusty SP module of 27%. The dusty SP module had the highest average losses of 38% for the entire year compared to that of the dusty Poly module with 23%.

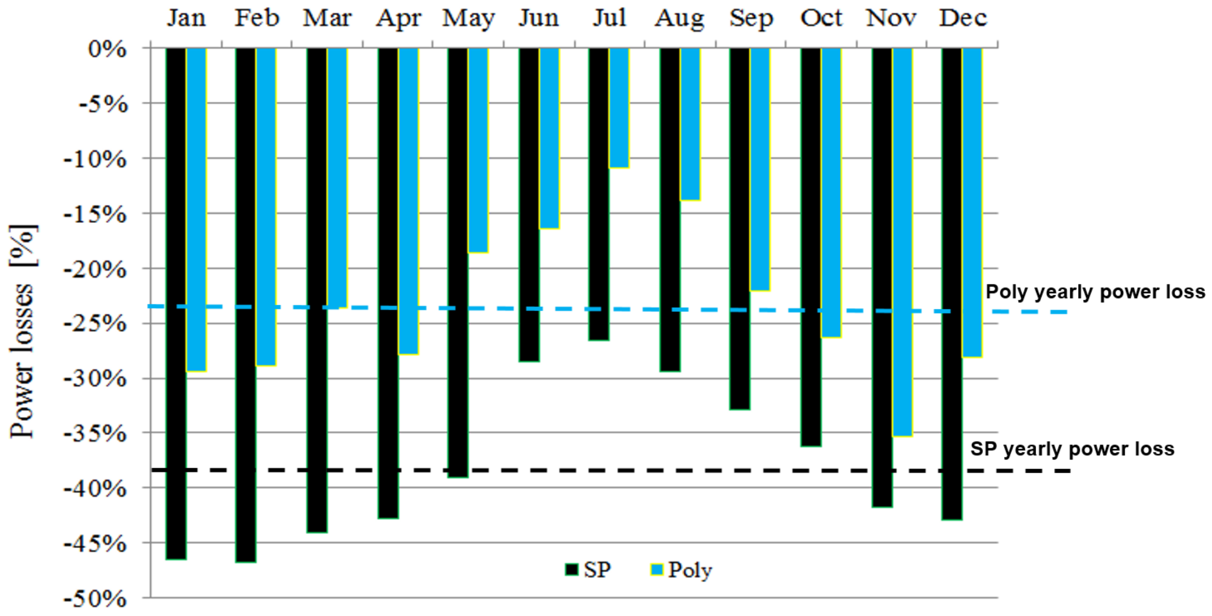

Figure 3.14 Percentage losses of the measured power output of dusty PV modules with respect to the clean PV module.

It can be concluded that the dust accumulation impact is more significant for PV modules with monocrystalline cells technology than modules with polycrystalline cells technology specifically in Kuwait.

3.3.5 Effect of ambient temperature on the PV

One of the factors affecting the PV module other than dust accumulation is ambient temperature. Figure **3.15** shows the monthly average measured temperature of the clean and dusty PV modules at various ambient temperatures during the year. It can be seen that as the ambient temperature increases, the PV modules temperature increases at all conditions dusty and clean. Also the clean and dusty modules temperature is highest in months with high amounts of solar radiation. In both type of PV modules, the clean modules temperatures are mostly higher than dusty module temperature during high ambient temperature. It implies that the module temperature slightly dropped due to the impact of dust particles absorbing and reflecting some of the solar rays falling on the dusty modules surface [132]. However, this drop is not large at several months, and that makes the impact of dust insignificant on the module temperature. The highest percentage values of module temperature difference as a result of dust accumulation are 4.8% and 8.8% for SP and Poly, respectively, in July.

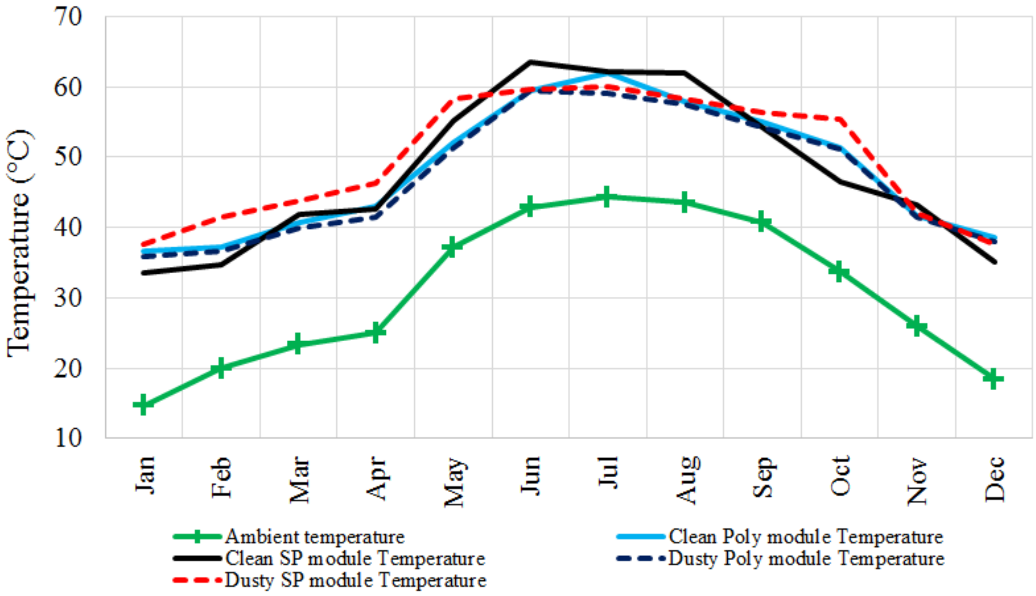

Figure 3.15 Monthly average measured ambient and PV modules temperatures.

From Figure **3.15**, it is shown that the ambient temperature reaches a top value of 44°C in July, while the lowest ambient temperature value is 14°C in January. The lowest mean monthly temperature of clean Poly module is 33 °C where the dusty Ploy module is 32.3 °C all in January. As for the SP modules, the lowest mean monthly temperatures of clean modules is 37 °C where that of the dusty is 35.8 °C also in January. The highest monthly module temperatures is 63°C and 60°C in June for the dusty and clean Poly modules, respectively. The SP highest monthly temperatures reach a mean of 62°C and 59°C in July for the dusty and clean, respectively. The annual mean module temperature is around 48 °C for all PV modules.

3.3.6 Influence of dust on PV modules efficiency

The modules monthly efficiencies were determined to study the dust effects on the modules performance as expressed by equation 3.6:

$$\eta = \frac{P_{month}}{G_{month} A} \tag{3.6}$$

Where P_{month} is monthly average of the PV module maximum power output (W), A is the total area of the PV module (m^2) and G_{month} is monthly average of the in plane solar radiation (W/m^2). The monthly average efficiencies of clean and dusty PV modules are illustrated in Figure **3.16** along with ambient temperature. This figure reveals that the efficiency of the dusty modules is lower than clean modules during the whole measurement period. However, the clean PV efficiency is also affected by the high ambient temperatures where lower values are observed in the summer months compared to the winter months, for both poly and SP PV modules. The photons within the PV cell increases and impede charge carrier interchange and that reduces efficiency [19].

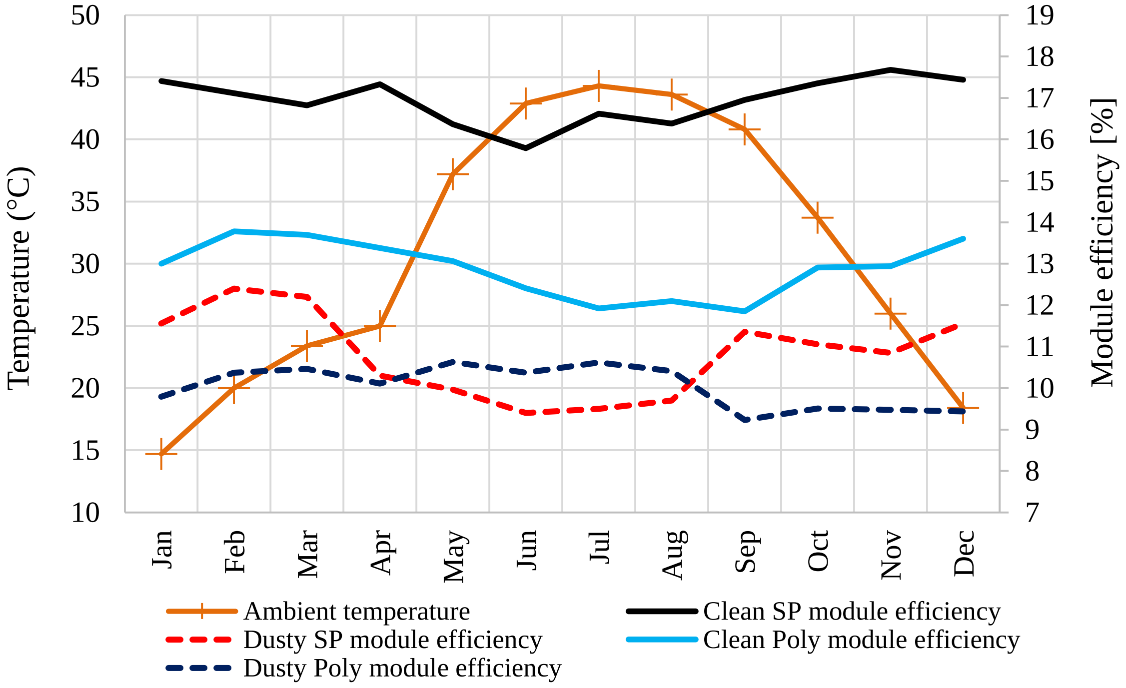

Figure 3.16 Monthly average PV module efficiency and ambient temperature.

The yearly average Poly modules efficiency of 13.11% and 10% were calculated for clean and dusty conditions, respectively, while the clean and dusty SP yearly average efficiency are concluded to be 17% and 10.8%, respectively. The topmost efficiency reduction was noticed on an ambient temperature of 44°C in July for dusty SP module of 42% drop and in November for dusty Poly of 30% drop at ambient temperature of 18°C with respect to the clean modules. The maximum efficiency reached for Poly module in clean and dusty conditions was around 13% and 10%, respectively. As for the SP module, the maximum efficiency reached was about 17% and 12% for clean and dusty conditions, respectively.

3.4 Physical and optical characteristics of dust

For investigating physical and optical properties of dust, samples were collected from the test site itself and tested, at KISR energy department laboratory. The collected layer of dust was removed using a small brush with small re-sealable plastic bag from the surface of the dusty module glass cover with area of 12.5cm x 12.5cm. The weight of the sample was 2500 mg as measured using Ohaus Advneturer digital weight scale with sensitivity of 0.001 mg. The spectral reflectance of the sample was measured using a Cary 100 spectrophotometer and the transmittance of the sample was measured utilising a digital Hazemeter. The Malvern Mastersizer 2000 laser diffraction particle size analyser was used to identify the dust particles size from the dust samples as shown in Figure **3.17**. It shows the dust particles in terms of cumulative distribution where the maximum size is 90 micrometres. The dust particles of the sample can be described as very fine dust as categorised by Al-Dousari and Al-Awadhi size [126].

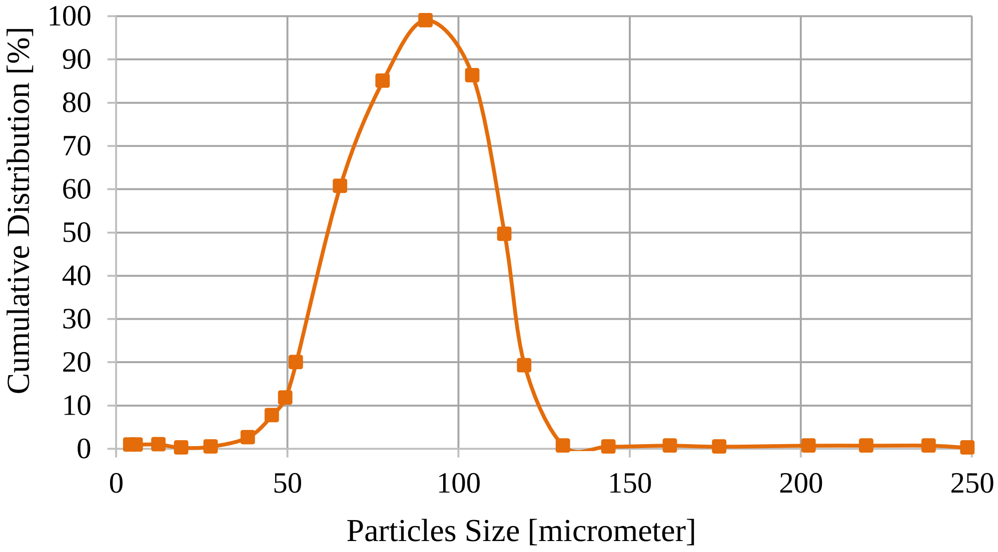

Figure 3.17 Particles size distribution of the dust samples.

To determine the dimension of dust particles, Alecona electron microscope was used with 30 magnifications as shown in Figure **3.18**. It can be observed that the dust particles have different shapes, but the main shape is spherical. Said et al. [133] determined that large dust particles have greater bond force than small particles. The larger are the particles, the larger is the area covered by the single particle over the surface of PV modules.

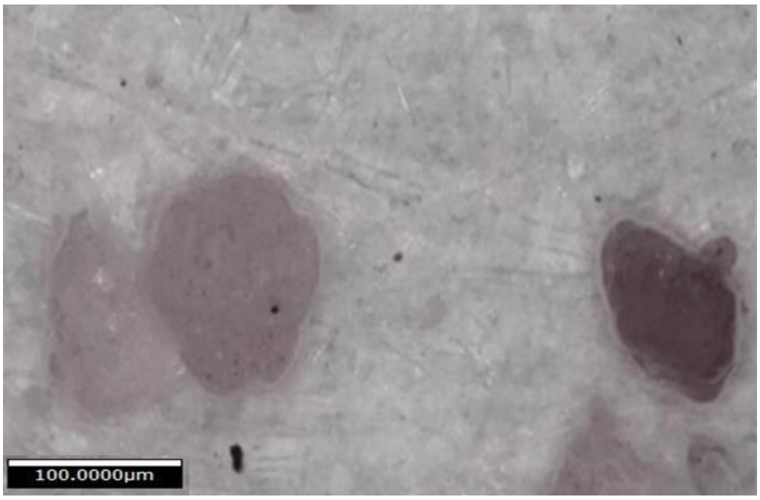

Figure 3.18 Image of dust sample collected from the dusty modules surface magnified 30.

The reflectivity measurements were carried out using the Cary 100 spectrophotometer fitted with extended life LED light source. Figure **3.19** and Figure **3.20** illustrate the reflectance and transmittance measurement process using the spherical light trapping technique. In this technique, the light source beam pass through spherical light trap into the sample container, then reflected to the detector which is the last element in the spectrophotometer. The silicon photodiode are typical detector used in spectrophotometer for the ultraviolet, visible and near-infrared regions.

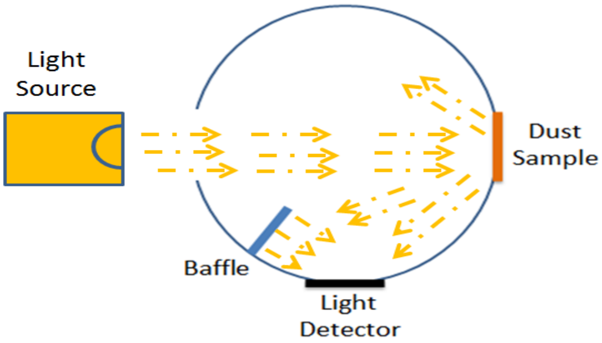

Figure 3.19 Procedures of dust optical properties measurements [134].

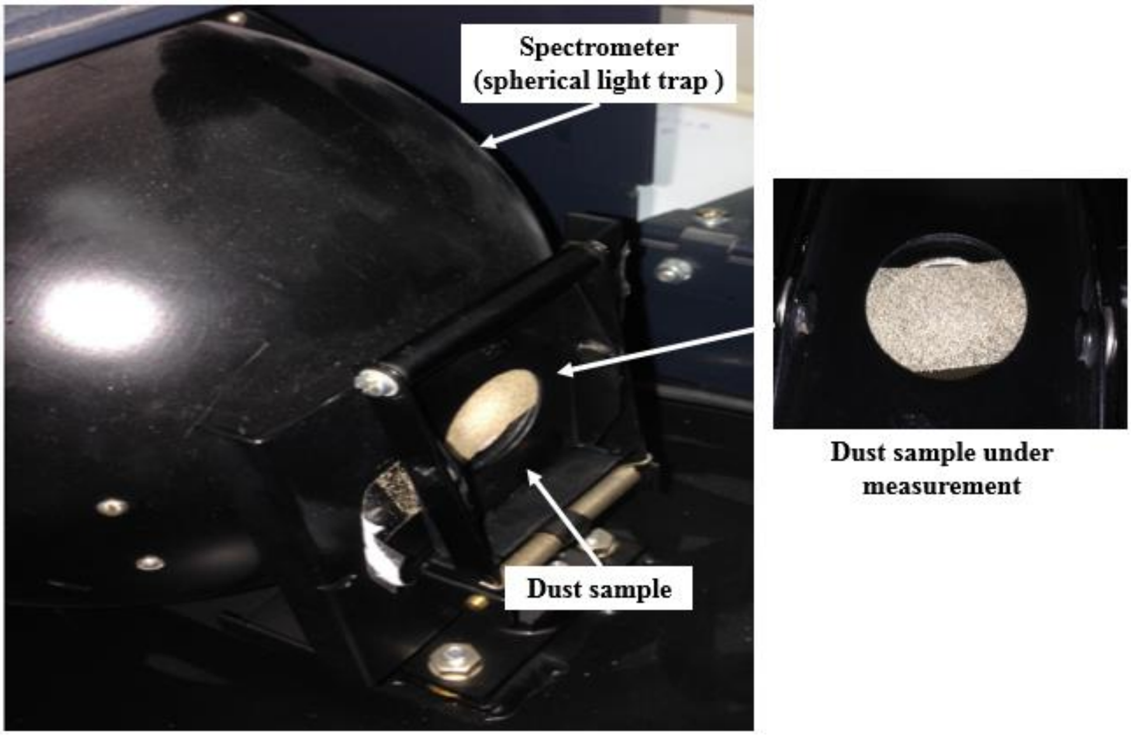

Figure 3.20 left: The spectral transmittance and reflectance dust sample was determined utilising a spectrophotometer. Right: 0.19 (mm) clear tape sample coated by dust.

Figure **3.21** shows the reflectivity measurement for the dust samples of three sizes namely 60, 80 and 100 microns over wavelength range of 300nm -1200nm. It is clear that the reflectivity increases, as the particle size increases. As for the effect of wavelength, the reflectivity increases with the increase in the wavelength reaching a maximum value at wavelength 800-900nm and then remains relatively constant. It can also be seen that as the particle size increases, the rate of increase in the reflectivity with the wavelength increases.

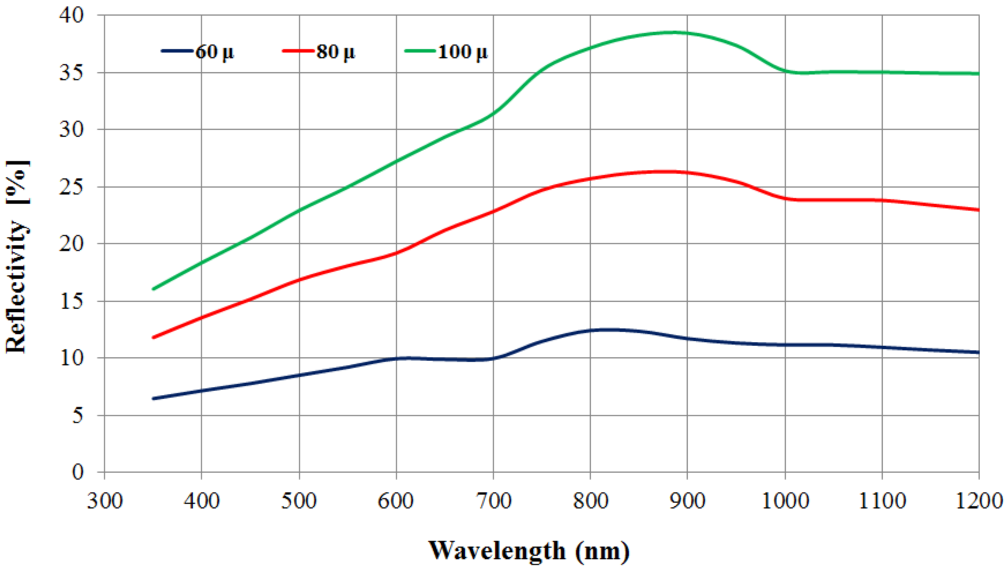

Figure 3.21 The reflectivity of different grain sizes of dust sample.

The transmittance measurement was carried out using spherical hazemeter (model EEL 057) with LED lamp as light source having 0 degree illumination. Equation (3.7) was used to calculate the samples Transmittance:

$$\%\text{Transmittance} = \frac{\text{Tdiffuse light}}{\text{Ttotal light}} \times 100 \qquad (3.7)$$

Figure **3.22** shows the transmissivity of different grain sizes of dust sample, compared to the transmissivity of the sample container given as 93%, where the particles with 60 microns diameter has slightly (around 5%) higher transmissivity than the other particles diameters. From Figure **3.22**, it can be concluded that the transmittance increases with the decrease in the dust particles size. For example 60 microns dust has transmittance of 71% while 100 microns dust has transmittance of 60%.

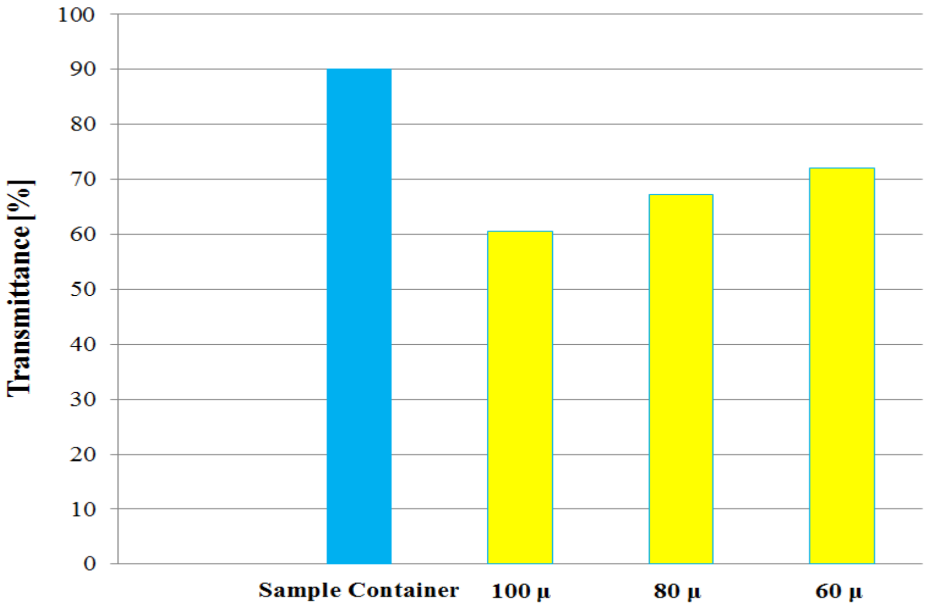

Figure 3.22 The transmissivity of different dust particles sizes.

3.5 PV modules performance degradation

3.5.1 Long term dust accumulation effects

In this section the evaluation of PV module performance based on one day measurement of electrical parameters after 7 months of outdoor exposure, to investigate the losses caused by dust. The solar radiation is the most important factor that affects directly the power and current output of PV module since the electrical output is proportional to the received solar radiation. Figure **3.23** shows the measured in plane solar radiation received on the 30th July 2013.

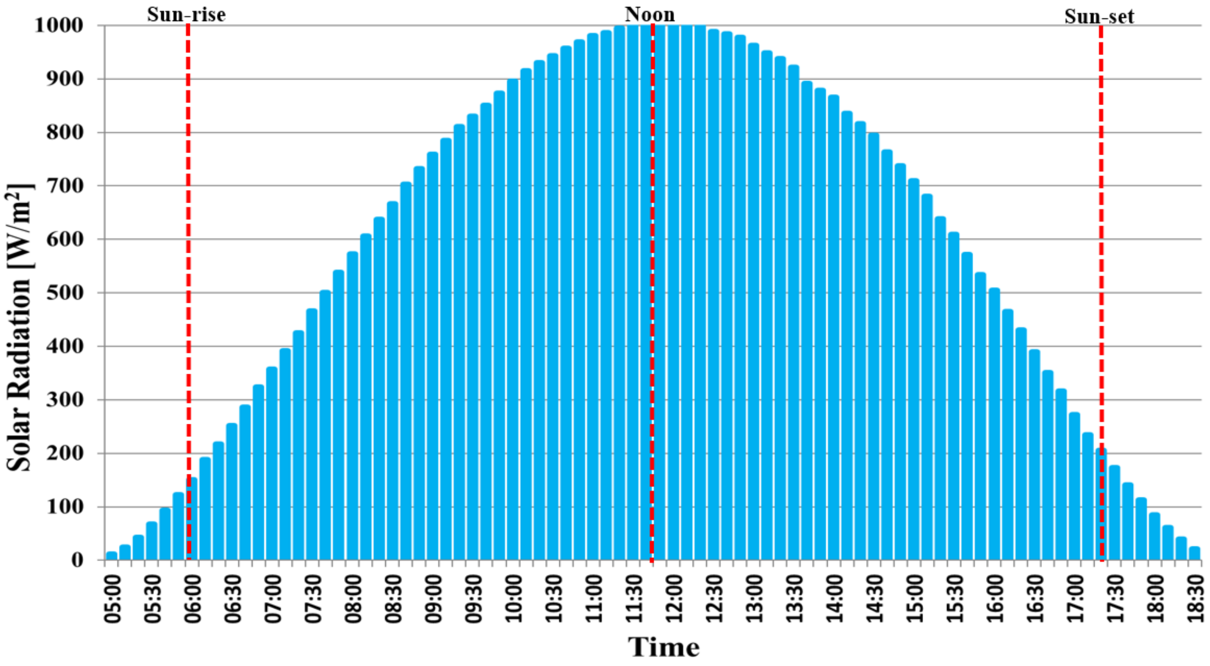

Figure 3.23 Amount of solar radiation in Kuwait during the 30th of July 2013.

Figure **3.24** shows the variation of the power generated by the clean and dusty PV modules during the 30th of July 2013. The maximum power output point measurement was taken when the solar radiation was between 100 and 1000 W/m², to minimise the effect of large AM during the morning and the evening. The power measured by each module was normalised to take into account the difference in the module surface area and represents the power out from a module with 1.24m^2. It is clear from Figure **3.24** that the clean SP module has the highest maximum power output of 183W at noon while the clean Poly module has the lowest maximum power output of 142W.

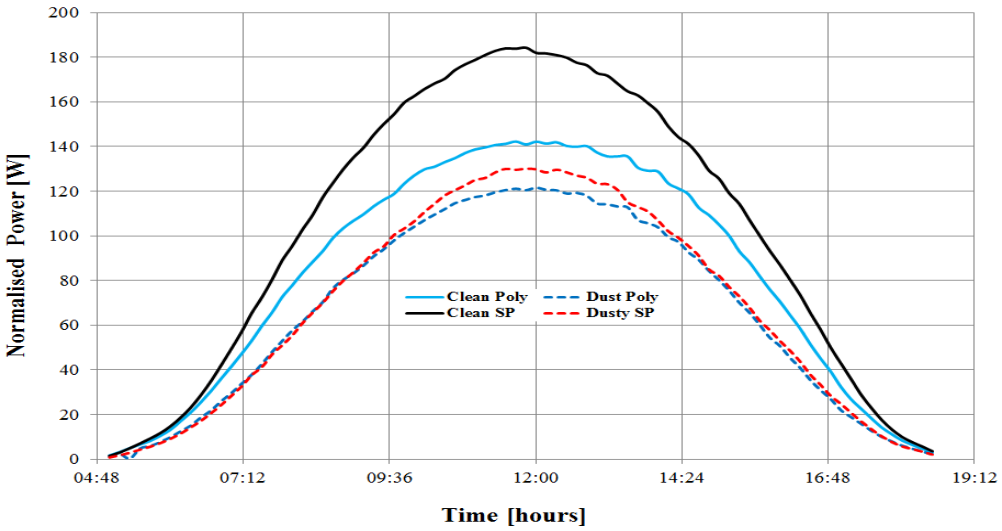

Figure 3.24 Variation of maximum power generated by clean and dusty PV modules.

Figure **3.24** shows that the power output of the clean PV modules are lower than those given in Table **3.3** at the standard testing conditions. This can be attributed to the higher module temperatures as shown in Figure **3.25** reaching 65^{o}C at noon. The power reduction due to the high ambient temperature is 42W (225W-183W), and 53W (195W-142W) for the clean SP and Poly respectively. It is clear from these measurements that the Poly module was affected most by the high ambient temperature compared to the SP module.

Also, Figure **3.24** shows that the power obtained from the modules under the dusty conditions with dust accumulated over a period of 7 months and the module temperature shown in Figure **3.25**. It can be seen that the power has decreased compared to the results obtained when the PV modules were clean where the maximum power of the dusty SP and Poly modules are 130W and 121W respectively. It is clear from this that the SP module is the most affected module by the dust with a drop of 53W while the Poly is the least affected by the dust with a drop of 21W. The Poly PV has shown the highest performance of power output in Kuwaiti harsh environment. Regarding the temperature of the PV panels, it is notable that the dusty PVs have relatively lower temperatures than the clean ones as shown Figure **3.25** which counteract the effect of dust.

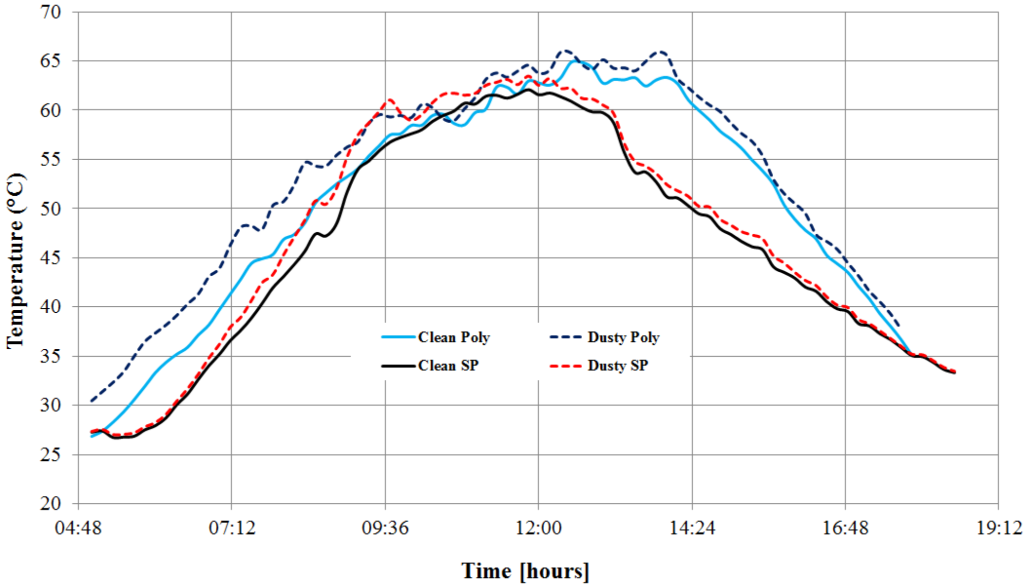

Figure 3.25 Variation of PV temperature of clean and dusty modules

3.5.2 Influence of dust on short-circuit current

Figure **3.26** shows the variation of short circuit-current between the dusty and clean modules for the 30th of July 2013. The (I_{sc}) output of the dusty and clean modules increased with an increase in the in plane solar radiation as can be shown in Figure **3.26**. The (I_{sc}) output of the clean and dusty PV modules varies between 15% and 30%, respectively. This can be due to the optical properties of the dust (as explained in section 3.5.1 and shown in Figure **3.21**) where the reflectivity of dusty surface is lower than that of clean surface.

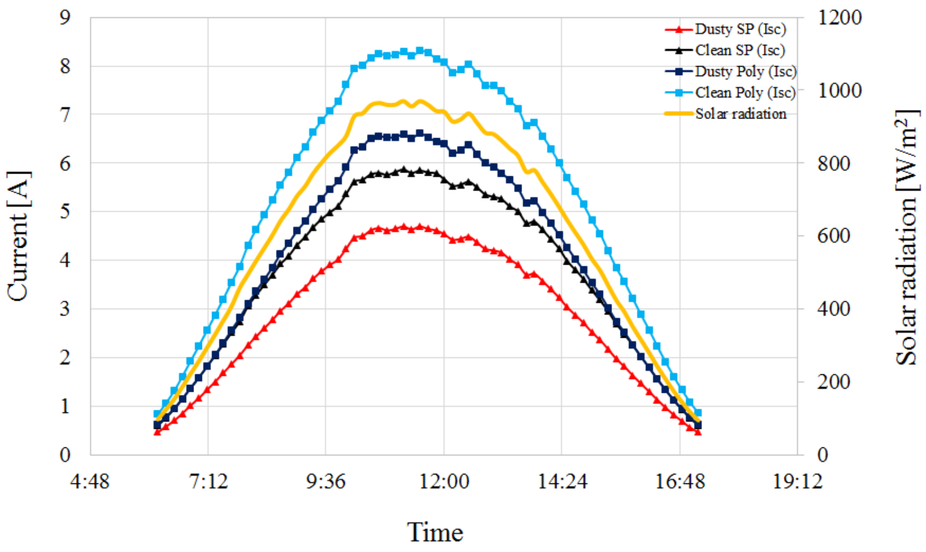

Figure 3.26 Variation of short-circuit current output generated by the clean and dusty PV modules.

3.5.3 Influence of dust on open-circuit voltage

Figure **3.27** shows the open-circuit voltage of clean and dusty modules during 30th of July 2013 with a clear day and stable solar radiation. In general, it was noticed that the open-circuit voltage rises marginally at low solar radiation level and stays mostly constant at high solar radiation level (midday). The average V_{oc} of SP and Ploy PV modules of 44V and 34V, respectively, were obtained. The dusty Poly and SP modules open-circuit voltages are slightly higher than the clean ones, due to the lower dusty modules temperature compared to the clean modules as shown in Figure **3.25**.

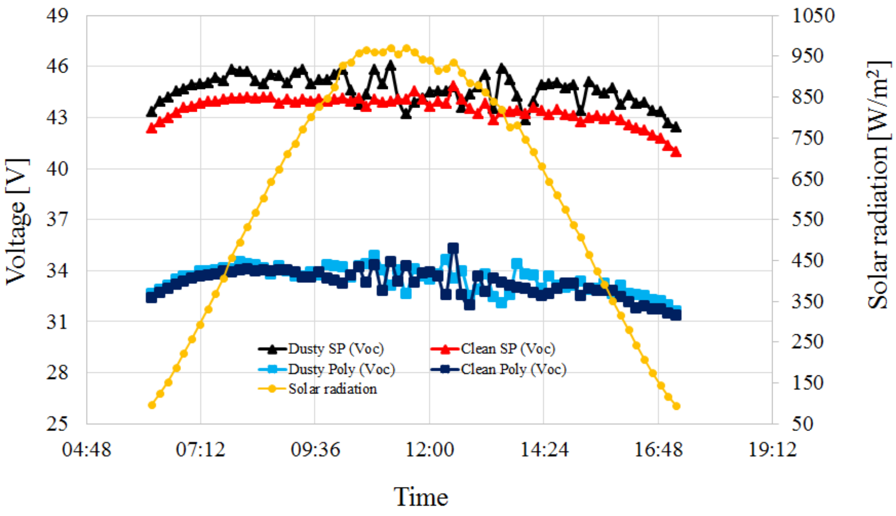

Figure 3.27 Change of open-circuit voltage output generated by the clean and dusty PV modules.

3.5.4 Current/voltage (I/V) and power/voltage (P/V) Characteristics of clean and dusty PV module

With the aim of investigating the degradation of PV modules in more details the measured I/V and P/V characteristics of the clean and dusty PV modules were investigated, after an extended period of outdoor exposure under Kuwait climate. The dusty PV modules I/V and P/V curves for the 30th of July 2013 are compared to the I/V and P/V of clean modules as shown in Figure **3.28**. The performance parameters for instance; maximum power output (P_{max}), short-circuit current (I_{sc}), open circuit voltage (V_{oc}), fill factor (FF), maximum output current (I_{max}), maximum output voltage (V_{max}) and module efficiency of the dusty modules have been degraded. The I/V and P/V curves produced by the PV modules at radiation intensity of 1000 W/m^2 at an average module temperature of 41°C have been presented in Figure **3.28**.

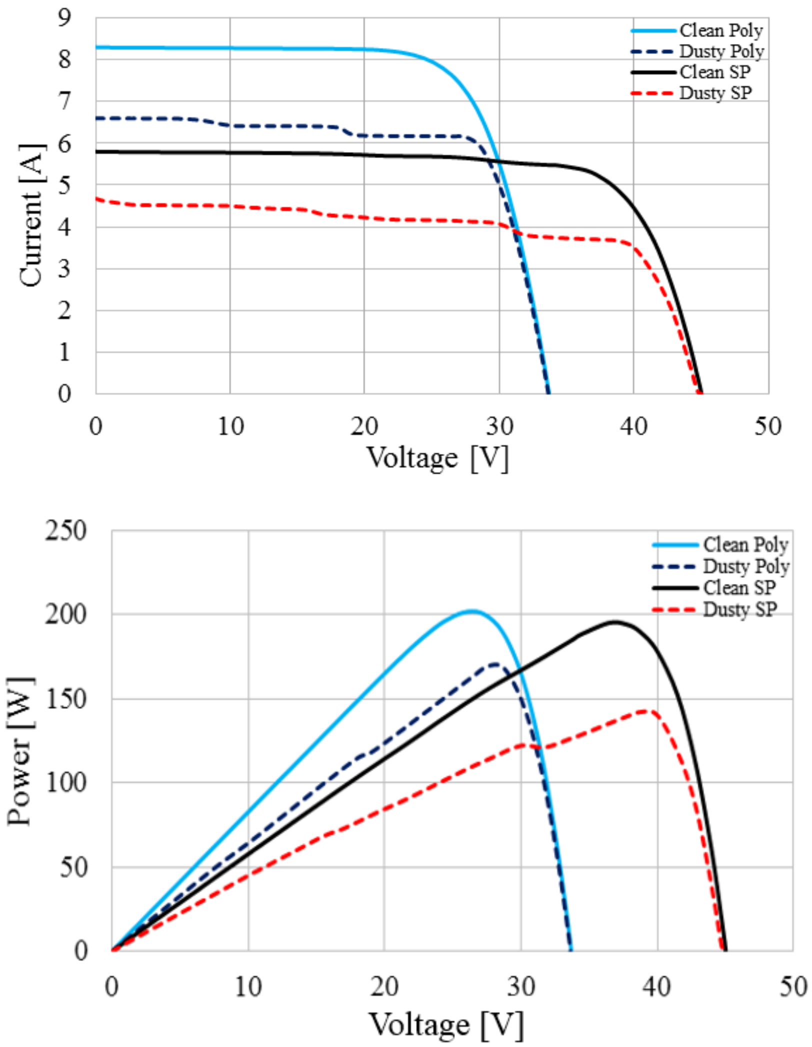

Figure 3.28 The I/V and P/V curves characteristics of clean and dusty modules at solar irradiance 1000 w/m^2 at an average module temperature of 41^{o}C.

Table 3.5 The clean and dusty PV modules performance and parameters values at 1000 (W/m^2) and average module temperature of 41^{o}C

PV module	**Paramaters**	**Clean**	**Dusty**	**Relative diffrerence (%)** $\frac{\text{Clean} - \text{dusty}}{\text{Clean}}$
Poly	P_{max} (W)	201.37	169.87	15.64
	I_{sc} (A)	8.31	6.61	20.45
	V_{oc} (V)	34.3	32.67	1.13
	FF (%)	74	70	5.4
	Eff%	12.3	10.23	16.8
SP	P_{max} (W)	197.28	140.71	28.67
	I_{sc} (A)	5.87	4.7	19.93
	V_{oc} (V)	46.09	43.95	4.64
	FF (%)	80	70	12.5
	Eff%	15.9	11.3	28.93

The irregular patterns of I/V and P/V curves produced by the dusty modules shown in Figure **3.28** were due to the dust particles reflecting and transmitting some of light rays [26, 40]. Mostly, the I/V and P/V curves show lower performance for all PV modules in dusty conditions compared to clean conditions. The difference among these curves is assumed to increase through the increase of dust accumulation period [33, 45]. The gap in the upper curves part of the I/V between the dusty and clean modules (I_{sc} region) shows degradation due to dust accumulation on modules plane which obstructs radiation passing through to the PV cells. Table **3.5** lists the values of reduction for each electrical performance parameter of the daily cleaned and dusty modules. Table **3.5** illustrates that (P_{max}) and (I_{sc}) decreased considerably as a result of the dust accumulation. In contrary, the (V_{oc}) and (FF) are less sensitive and decreased by around 4% in comparison to values measured of clean modules.

The results in Table **3.5** showed that the short-circuit current output of the dusty modules are greatly affected by dust accumulation with reducing by approximately 20% for both PV modules. Nevertheless, the PV module maximum power decreased greatly by the occurrence of dust, the Poly and SP maximum power dropped by around 29.5% and 37.7%, respectively. On the other hand, the insignificant decrease in (V_{oc}) of approximately 1.13% and 4.6 % of clean and dusty modules (V_{oc}) ,respectively, are clear due to the open circuit voltage being more related to junction temperature rather than the intensity of solar radiation. The result in Table **3.5** implies that Poly PV technology performs better in dusty condition on low and high solar radiation intensifies compared to SP.

3.5.5 Dust accumulation ratio

The dust accumulation ratios of the PV modules were determined using the short-circuit currents ratio of the dusty and clean modules, at solar radiation of (1000 W/m^2 ±3%) to minimise the impact of spectral sensitives variation. Figure **3.29** shows the dust ratio (I_{sc} ratio) for ploy and SP PV modules throughout 2013, also shown in Figure **3.29** the ambient temperature and wind speed. Figure **3.29** illustrates visibly that the SP module is affected more during the measurement period than Poly module. The dust accumulation ratios are only illustrated for the measurement period omitting several raining days. Figure **3.29** revealed direct relation of dust accumulation ratio with wind speed, where the dust accumulation ratio increases as the wind speed increases during the exposure time. On the other hand, the ambient temperature stays similar during the measurements period.

A considerable decline in dust accumulation ratio around 0.75 and 0.72 for Ploy and SP modules, respectively, was directly noticed after two months from the measurement system installation and an increase in wind speed was approximately 2.5 m/s. Figure **3.29** shows that the lowest dust accumulation ratio for Poly and SP were 0.66 and 0.61, respectively, during the mid-year days. Where, the wind speed is increased up to 4 m/s average speed.

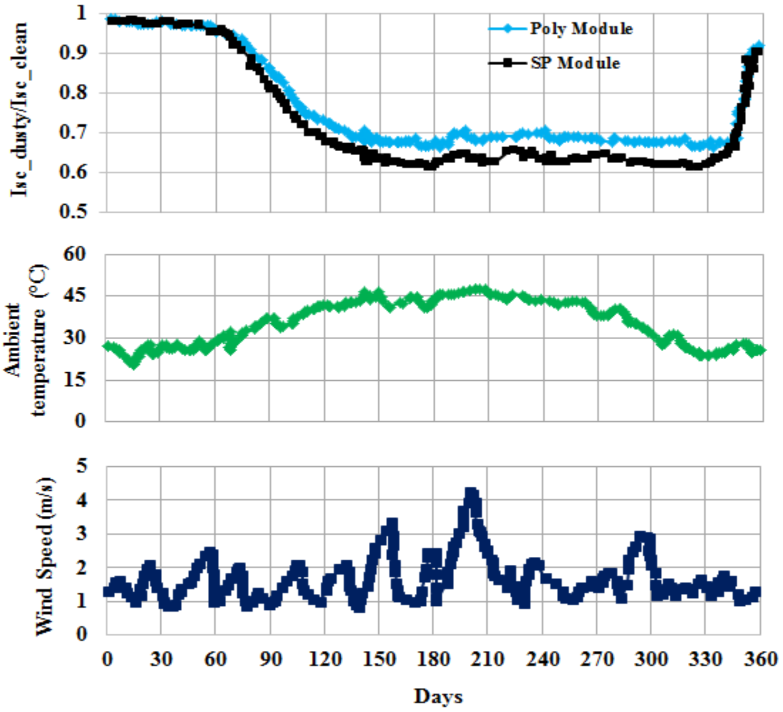

Figure 3.29 Synchronised dust accumulation ratio for PV modules to illustrate the difference throughout the outdoor testing period along with measured environmental factors.

3.6 Summary

In this chapter two experimental studies were described; one regarding the performance of two types of PV panels for a period of a year in Kuwait and the second regarding the optical and physical characteristics of dust in Kuwait. From these studies the following observations can be concluded:

- From the average hourly measured solar radiation, it is apparent that average in plane solar radiation is above 500 W/m^2 during the year 2013.
- The observations showed that open-circuit voltage of the clean modules is insignificantly lower than that of the dusty modules at all solar radiation levels. This relative difference was around 4% for all solar radiation levels.
- The dusty modules constantly generated a lower short-circuit current output than the clean modules. This variation in the short-circuit current outputs extended as the in plane solar radiation increased up to 1000 W/m^2.
- The dust optical properties show an average light reflectivity of 30%, while the measured light transmittance of the dust sample is 70%.
- The power losses related to dust accumulation is 25-45% of the highest possible power output with dusty modules.
- Dust accumulation has an effect on the module operational temperatures. The dusty modules were noticed to be working 2-4°C lower than the clean modules at different solar radiation amount and ambient temperature.
- As for the performance of the PV modules, measurements showed that the SP module efficiency is more affected by the dust with a drop of 29% while the Poly module is the less affected by the dust with a drop of 16.8%.

All of the concluded results will be used as baseline of the boundary conditions of the solar concentrator design and simulation in the later chapters.

CHAPTER 4

Optical Simulation and Concentrator Development

4.1 Introduction

In this chapter, a detailed study describing the development of three dimensional low concentration (2X, 4X and 6X), concentrator based on Pseudo-Square shape in term of their geometric and optical characteristics. Two separate tools were integrated and applied in the process of analysis and optimisation. A model was formed in Microsoft Excel to determine the concentrator's dimensions for various geometrical concentration ratios. Then, the ray-tracing method was employed to optically analyse and optimise the concentrator.

4.2 3D Ray tracing model development

The advanced ray-tracing software OptisWorks^{TM} was utilised to simulate the concentrator optical performance under clean and dusty conditions. A novel design of the concentrator based on Pseudo-Square cross section (PSCPV) is developed to suit the PV cell geometric shape is presented. The PSCPV concentrators are required to achieve the following functions:

- To generate the maximum electrical power output from the PV modules in cleaned and dusty environment.
- To obtain maximum optical efficiency with clean and with dust accumulation on concentrator surface.
- To maintain the structure of the commercial pseudo-square form of the PV cell.

Therefore there is a restraint on the size range of the concentrators and to be incorporated into the commercial size of the PV modules with minimum complication. To investigate the path of a light-ray once it is crossing through a solar concentrator, it is essential to apply the ray-tracing procedure to examine the solar concentrator performance. Once the light-ray reaches the concentrator plane, it will be either absorbed or reflected. According to Snell's law, the paths of the incident and reflected rays make a similar angle with respect to the normal surface as presented in Figure **4.1**. It is presumed that the interior wall reflectivity of the 3D-PSCPV is 90%; this indicates that the light ray of light will drop in the range of 10% of its magnitude with every reflection.

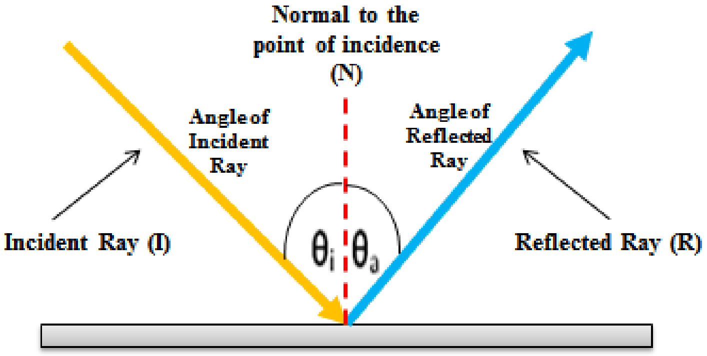

Figure 4.1 Schematic drawing of the reflection law.

To trace the rays for all reflections, the law of reflection can be expressed in a trajectory form as shown in equation (4.1) [135]:

$$R = \mathrm{I} - 2 \times N.I \times N \tag{4.1}$$

Where:

R is reflected ray, I is Incident ray and N is ray at normal incident point.

The concentrator entrance aperture is enclosed with optical glass; the light rays falling on the entrance aperture may be transmitted, emitted or absorbed by the glass causing a loss of energy. The transmitted rays' route is described according to the Snell–Descartes law. Some of the light rays transmitted through the entrance aperture cover are absorbed or reflected provoking more loss of energy determined by the reflectivity of the concentrator inside surfaces.

Figure **4.2** presents the behaviour of light rays crossing through the entrance aperture into a concentrator at various incident angles. Rays incident at the top region of concentrator are reflected toward the receiver area directly or once it going through a series of reflection. However, rays falling at the bottom region of the concentrator are reflected backward without striking the receiver area as wasted rays.

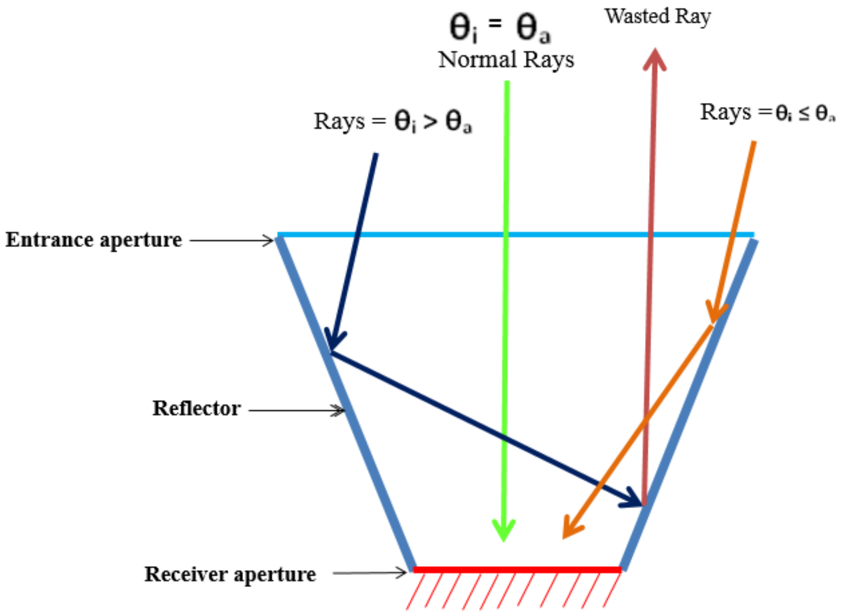

Figure 4.2 Behaviour of light rays in a concentrator.

In this work, OptisWorks^{TM} an advanced optical software commonly utilised in lighting and optical applications, was used to model the optical characteristics of the PSCPV. OptisWorks^{TM} takes into account various physical characteristics including the type of the light source and the optical properties of the surface substance. It is an adds-on module to the SolidWorks^{TM} software from Dassault Systèmes^{TM} providing a major advantage of 3D sketching in the same operated software. The optical software is capable of modelling the solar concentrator systems' performance using different irradiance, sun incident angle (or) sunlight hour, optical properties of material and concentrator geometries. The method is capable of demonstrating light intensity distributions on the concentrator entrance plane and on the receiver plane, to explain the hot spot produced by non-uniform irradiation [136].

4.2.1 3D-PSCPV concentrator geometry development

Figure **4.3** shows the PV cells with pseudo-square configuration which represents the receiver area of the concentrator. The pseudo-square cross section area was used through the concentrator while the height and side angle were varies to achieve concentration ratios of 2, 4 and 6. The designed 3D-PSCPV optical efficiency, and defined as the amount of the flux reaching the receiver, divided by the amount of the flux captured by the entrance aperture is computed through ray-tracing for the specific irradiance distribution defined based on the optical properties. The optimal 3D-PSCPV configuration is then determined numerically by increasing the concentrator height and reflectivity.

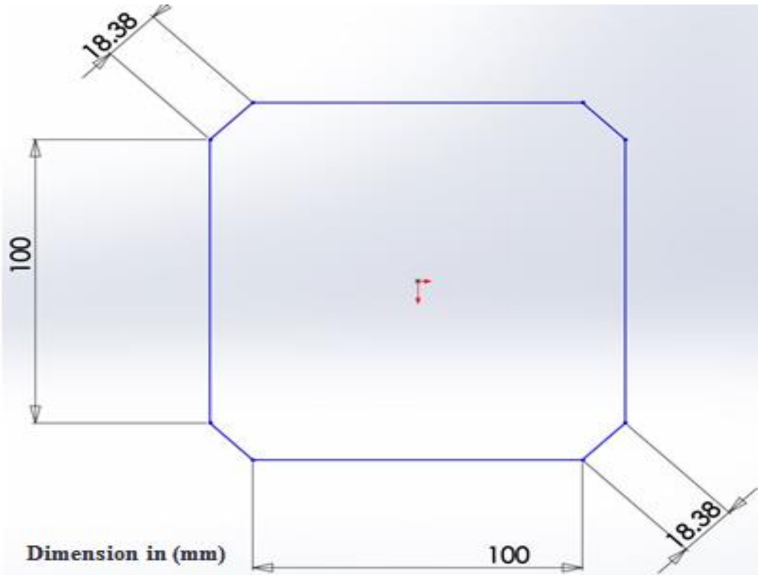

Figure 4.3 Receiver area of the3D-PSPCV design.

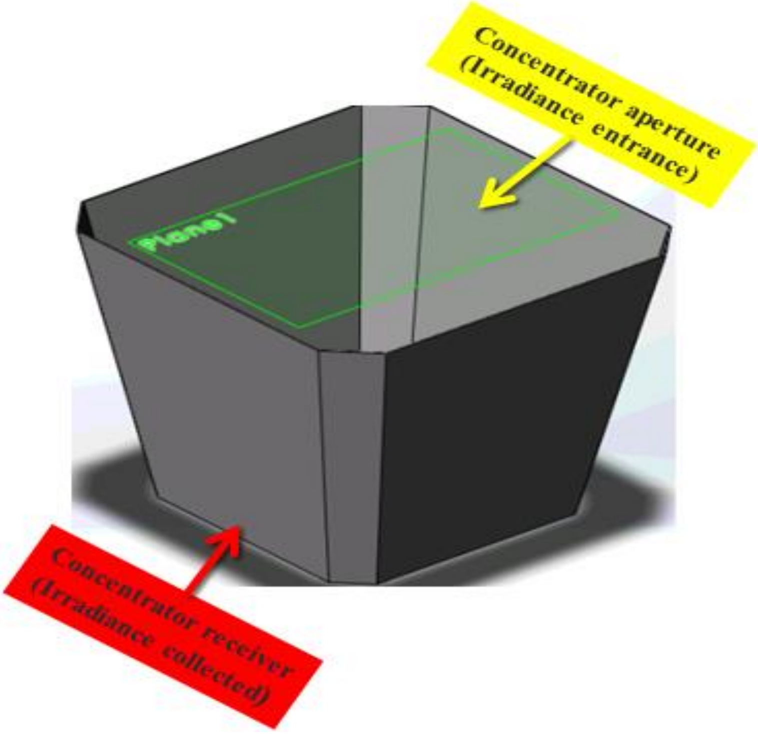

Figure 4.4 3D view of the 3D-PSCPV model developed in SolidWorks.

Figure **4.4** shows the 3D-PSCPV concentrator developed to fit the pseudo-square shape of the PV cell shown in Figure **4.3**. The 3D-PSCPV dimensions are determined for a fixed PV cell area of (0.015538 m^2) to produce geometric concentration ratios ranging from 2 to 6. The geometric concentration ratio, G_{CR}, is the ratio of the entrance aperture area (A_e) and receiver aperture area (A_r) calculated using equation 2.16. The geometric concentration ratio for 3D-PSCPV with different entrances aperture areas is presented in Figure **4.5**.

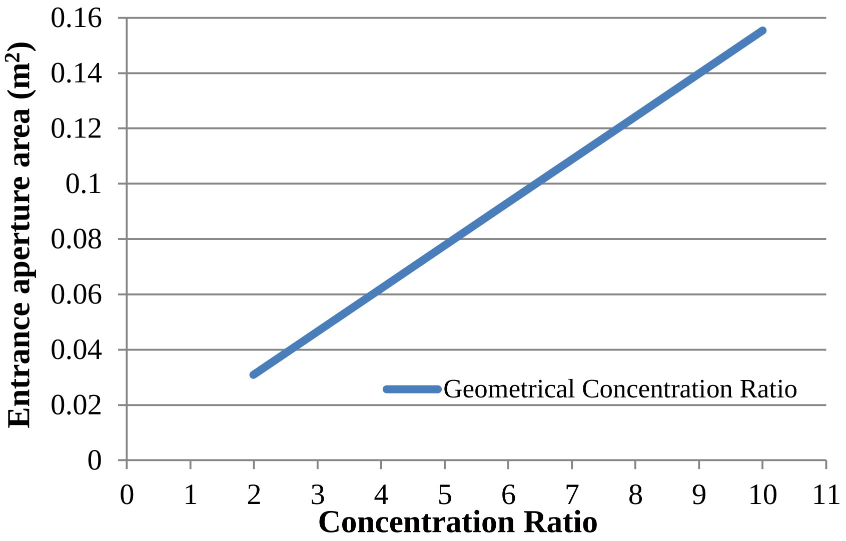

Figure 4.5 The variation of the concentration ratio with the concentrator entrance aperture area of the 3D-PSCPV.

Using ray tracing simulation at fixed geometric concentration ratio, the concentrator height and side angle were optimised to achieve the highest optical efficiency while maintaining the concentrator compact.

4.2.2 3D Ray tracing modelling process (OptisWorks^{TM})

The ray-tracing modelling of the 3D-PSCPV in (OptisWorks^{TM}) consist of six main steps (given in Figure 4.6) including constructing the PSCPV geometry, setup of the light source (sun radiation and spectrum), specifying concentrator material optical properties, specifying the entrance and receiver 2D radiation detectors, executing the pictorial ray-tracing and output analysis.

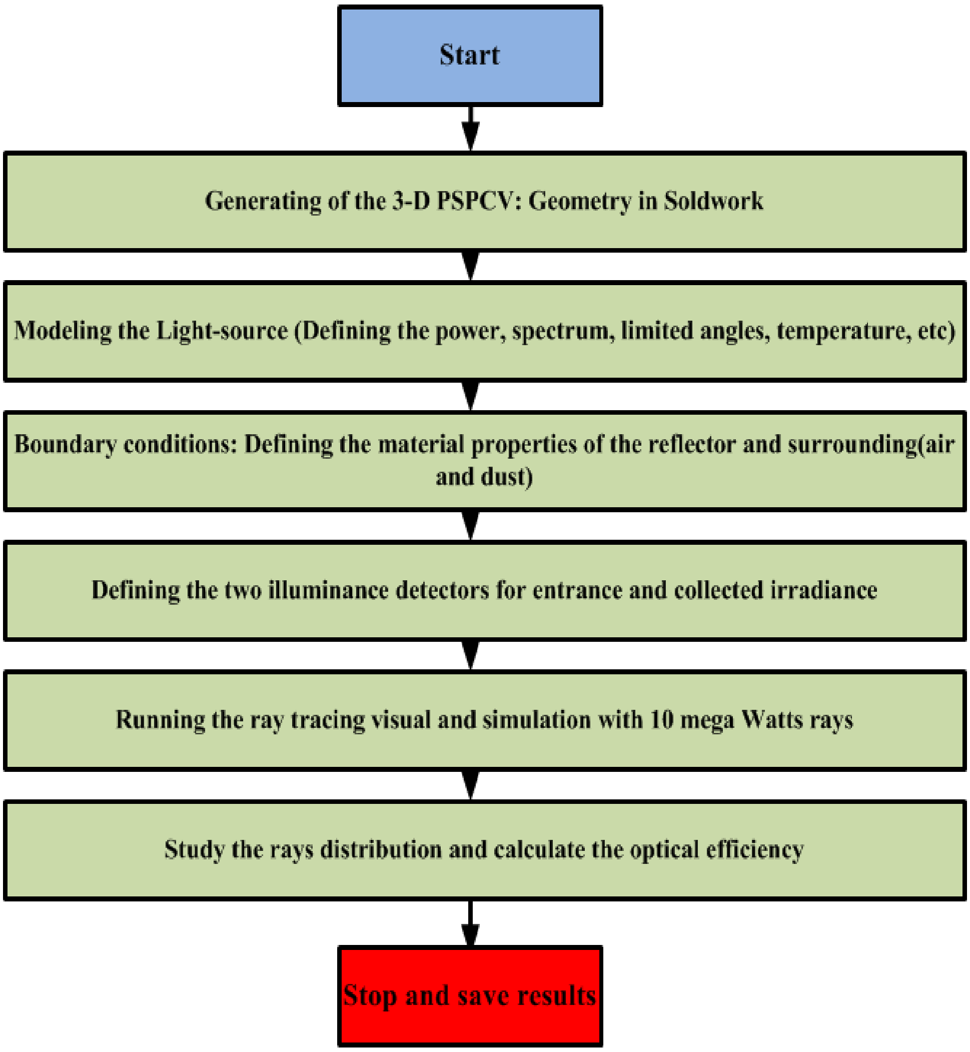

Figure 4.6 Flow chart of the simulation procedure of 3D- PSCPV utilising ray-tracing method.

The light source can be simulated to represent the sunlight or any other artificial light source. Its characterisation includes specifying the power magnitude (W), emittance form (uniform or irregular), intensity profile form (Gaussian or Lambertian), spectrum form (blackbody or Monochromatic), colour temperature, light ray (colour type) and the number of light source rays. The light source in this simulation was setup to produce light rays with 10 MW, the source form was represented as planar in addition to its dimensions were shaped bigger than the area of the 3D-PSCPV entrance aperture, to ensure the light-rays radiated cover the whole entrance aperture of the 3D-PSCPV. The intensity input form was set as “Lambertian” with 0^{o}

limited half angle was to producer rays normal to the concentrator aperture. The assumptions of a ray-tracing study summarised as follows [137]:

- The received solar radiation is in parallel rays having equivalent energy.
- The light rays form a specular reflection (i.e. the incidence angle is identical to the reflection angle).
- The Fermat law applied in all light rays denoting that rays travel from one location to another following the path of the least time and shortest distance.

The boundary conditions set contain the radiation of the light source, absorptivity, transmittance and reflectivity of the concentrator's parts. Consistent with the procedure described in Figure 4.6, a simulation based on the annual average radiation of the year (520 W/m^2, as measured in previous chapter) for Kuwait was implemented. Because (OptisWork$^{\text{TM}}$) simply takes Watt value as an input to simulate the irradiance from the sun, the following equation was used to convert irradiance (Watt/m^2) into power (Watt):

$$\Phi = \mathrm{A} \times \mathrm{I_{rr}} \tag{4.2}$$

Where Φ is the power, A is the area of the light source surface and I_{rr} is the irradiance. Figure **4.7** shows the irradiance distribution at the entrance aperture of 3D-PSCPV concentrator showing a uniform distribution with average flux of 520W/m^2.

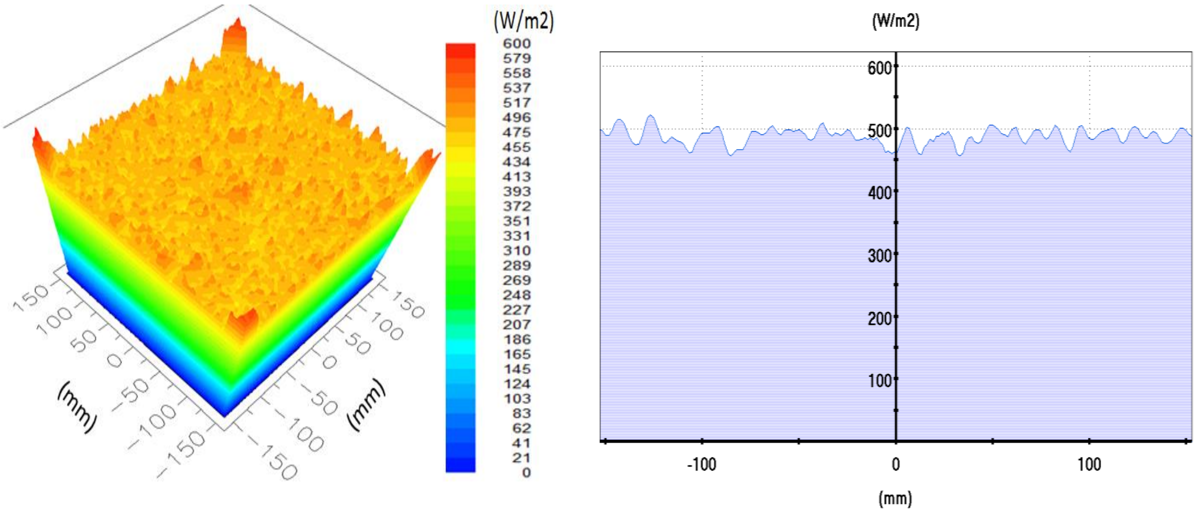

Figure 4.7 optical irradiance distributions on the entrance aperture of the 3D-PSCPV

In the OptisWorks^{TM} ray-tracing, simulation results can be assessed in two ways. The first is the "visual"; which allows a visual inspection of the directions of the light rays received or reflected out from the 3D-PSCPV. As the light-rays pass inside the 3D-PSCPV; they can encounter several conditions as demonstrated in Figure **4.8**:

- Light-rays refract once or several times within the 3D-PSCPV according to the total internal reflection law before crossing to the entrance aperture.
- Light-rays are lost from the walls of the 3D-PSCPV following once or several reflections.
- Light-rays reach the receiver aperture of the 3D-PSCPV either directly.

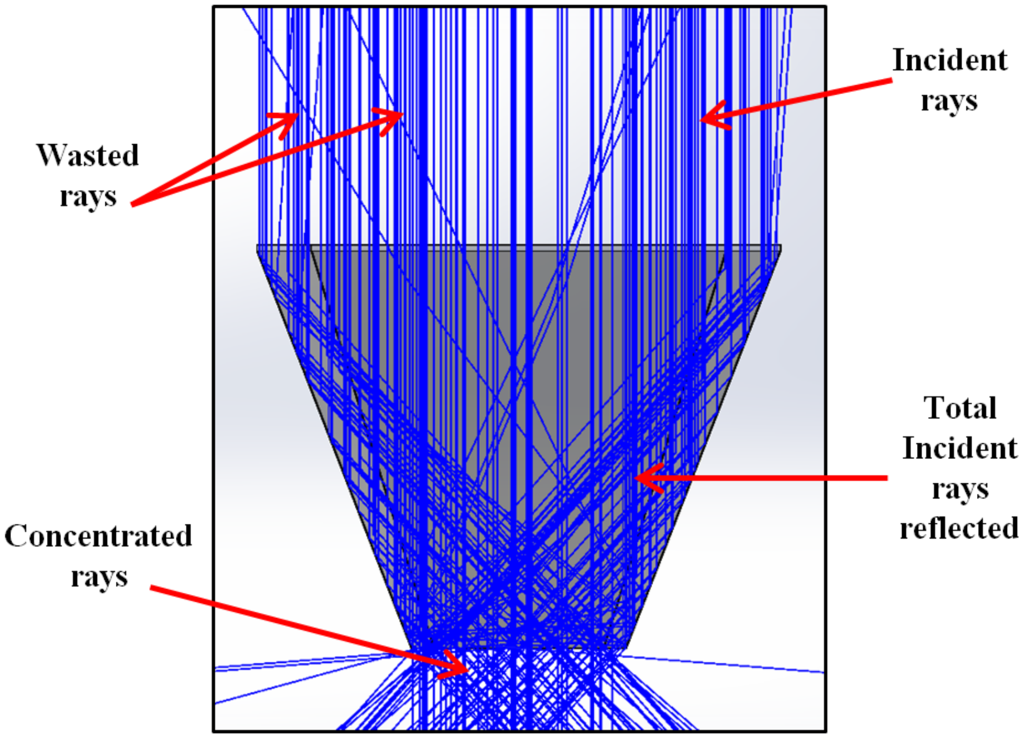

Figure 4.8 The concentrated light-ray direction acquired from the 3-D PSCPV demonstrated in (OptisWorks^{TM}).

The second results assessment method considers the entire optical characteristics of the 3D-PSCPV and the light source to acquire the total power and the irradiance distribution on the entrance and receiver planes of the 3D-PSCPV. In this second method a 2D solar radiation detector is positioned at the receiver plane of the 3D-PSCPV as presented in Figure **4.9**; this radiation detector computes the energy and irradiance of the received light at the receiver plane. An additional 2D detector is positioned on the entrance aperture of the 3D-PSCPV to compute the light-ray energy entering the aperture.

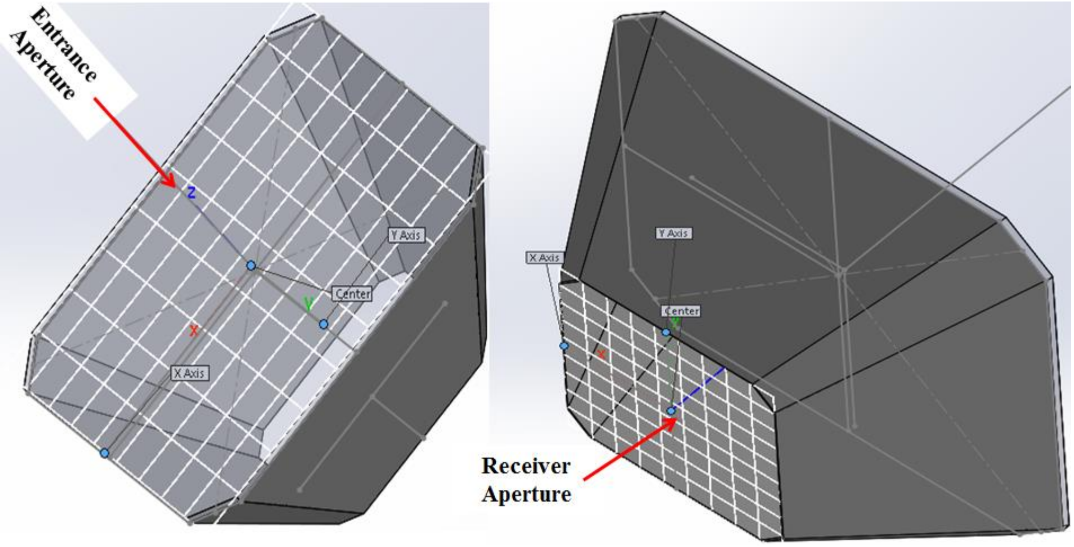

Figure 4.9 The 3D-PSCPV entrance and receiver apertures screened with 2D solar radiation detectors.

The 3D-PSCPV optical efficiency is determined using equation 2.17. The average power in W computed via the detectors on both the concentrator entrance and receiver plane apertures.

4.3 3D-PSCPV optical simulation results

The ray tracing simulation is used to study the impact of concentrator height and surface reflectivity on the 3D-PSCPV optical performance. The concentrator optical performances include the optical efficiency and the irradiance distribution on the receiver plane of the 3D-PSCPV, or the PV cell/module surface. The “optical irradiance distribution” terminology has been introduced with various terms in literature [52, 111, 138, 139] such as flux densities distribution, distribution, optical flux distribution and energy distribution”.

There are different approaches for computing the received irradiance uniformity, such as those which refer to the uniformity ratio (the maximum-to-minimum ratio) [140] or the standard deviation, which are recommended for 2D plane analysis for horizontal or vertical distribution. However, the irradiance uniformity estimation using these approaches depends on one line in the received plane leading to unsuccessful results. The first approach (the uniformity ratio) is inaccurate as there are various regions on the concentrator receivers' as their minimum received irradiance is very low compared to other ones and the second approach standard deviation is too complex. Ahmed et al. [141] used uniformity factor which was calculated using equation (4.3) to determine the solar concentrator concentrated light rays uniformity. Several other equations, which could be applied for estimating the uniformity, are found in [140, 142, 143]. Therefore, to study the uniformity of the 3D-PSCPV at different concentration ratios for various surface reflectivity values, the concentrator uniformity factor (CUF) can be expressed as follow in Equation (4.3) [141].

$$\mathrm{CUF} = \left[1 - \left(\frac{\text{Maximum received irradiance} - \text{Average received irradiance}}{\text{Maximum recived irradiance}}\right)\right] \times 100 \qquad (4.3)$$

In this study, the uniformity of the received irradiance on the receivers is computed by employing the concentrator uniformity factor as proposed by Ahmed et al [141]. The maximum and average irradiances were determined by taking the highest and average received irradiance values on the receiver surface.

4.3.1 Effects of height on optical efficiency

Figure **4.10** shows the variation of concentrator height with optical efficiency for geometric concentration ratios of 2X, 4X and 6X at concentrator surface reflectivity of 90%. Figure **4.10** shows that for concertation ratio 2X, the optical efficiency increases with increasing the height to reach maximum of 95% at height of 45mm and then decreases with further increase of the height. For the concertation ratio 4X and 6X, the optical efficiency increases with increasing the height to reach maximum of 88% and 67%, respectively, at height of 145mm and 250mm and then decreases with further increase of the height. The three optimised 3D-

PSPCPV with respect to height are presented in Figure **4.11** with the optical and geometrical characteristics given in Table **4.1**.

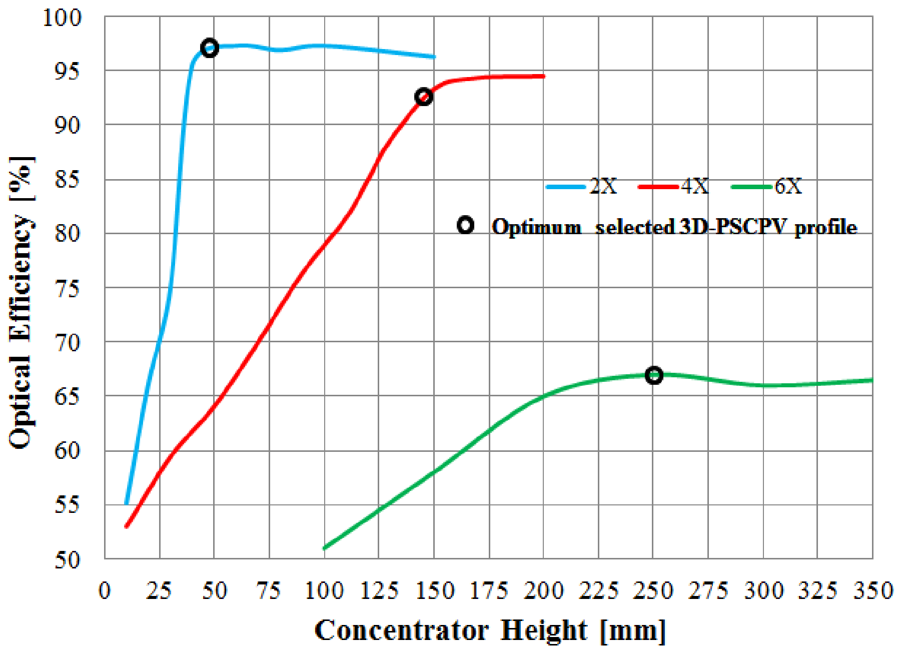

Figure 4.10 Difference of the concentrators' height as a function of the optical efficiency for the optimised 3D-PSCPV with 2X, 4X and 6X.

Table 4.1 Geometrical and optical characteristics of the 3D-PSCPV

Parameters	**2X**	**4X**	**6X**
H	45mm	145mm	250mm
Side angle	56.5°	60°	70°
R	125mm	125mm	125mm
Ent	180mm	250mm	307mm
G_{CR}	2	4	6
Optical$_{CR}$	1.9	3.48	3.96
Opticalη	95%	87%	66%
CUF	83%	75%	62%

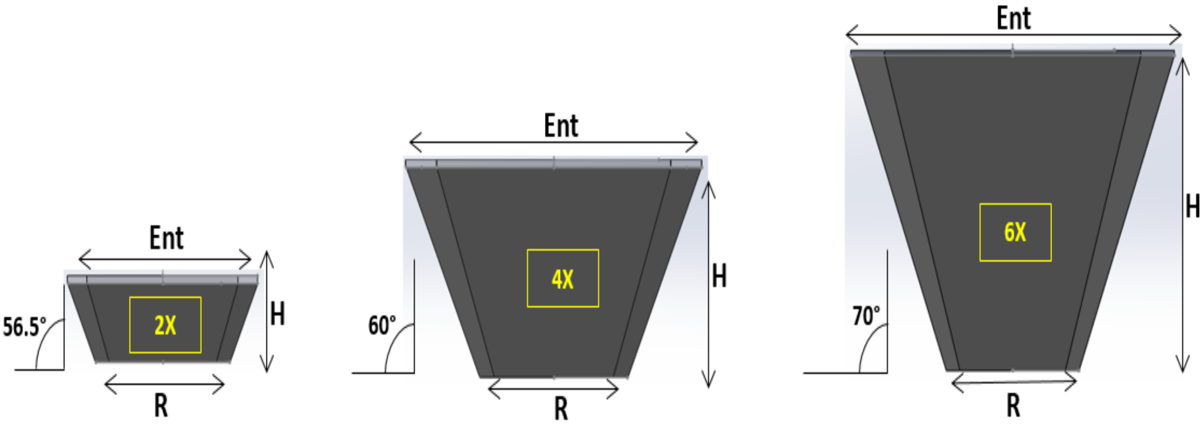

Figure 4.11 Comparative 2D illustration of the three optimised 3D-PSCPV.

Figure **4.12** presents the light rays emitted by the light source passing through the 3D-PSCPV concentrator, irradiance distribution on the entrance aperture and irradiance distribution on the receiver plane for the angles of 0^o and reflectivity of 90%. It is clear that the irradiance distributions on the entrance aperture of all concentrator are similar with an average value of 520 W/m^2. It indicates that as geometric the concentration ratio increases (i.e. 2X, 4X and 6X), the sum of rays inside the concentrator is increased due to the enlargement of entrance aperture area. The average flux received by 2X concentrator is 950 W/m^2 while that of 4X and 6X concentrators 1740 W/m^2 and 1980 W/m^2, respectively.

Light-Rays distributions at different Concentration ratio	Irradiance at Entrance Aperture [W/m^2]	Irradiance at Receive Aperture [W/m^2]
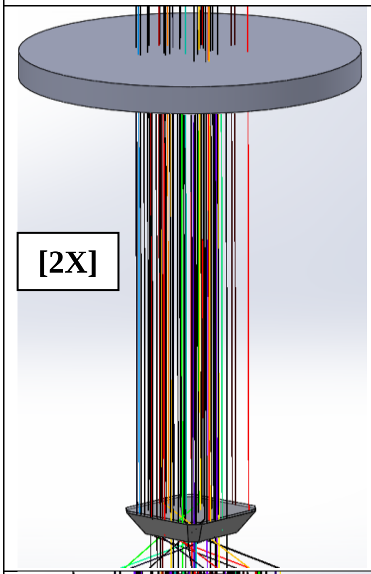	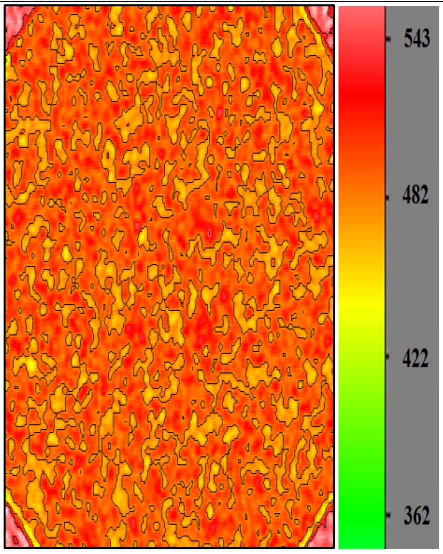	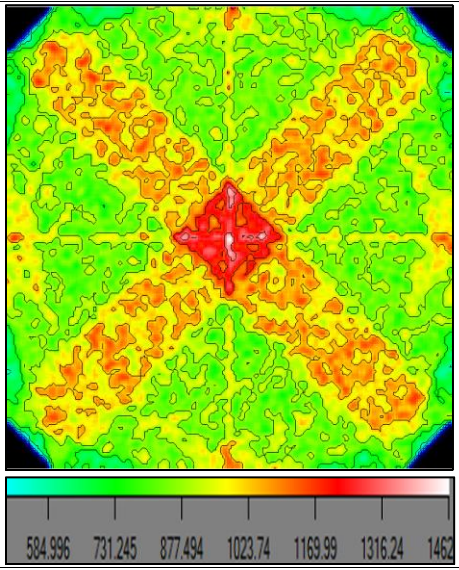
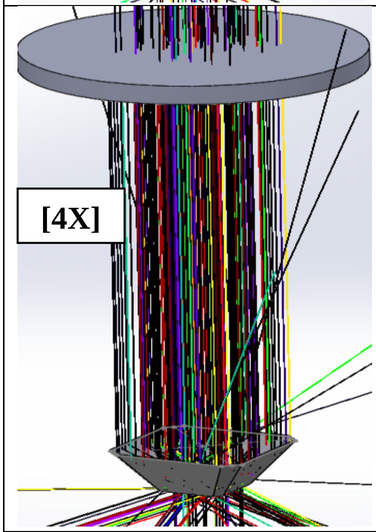	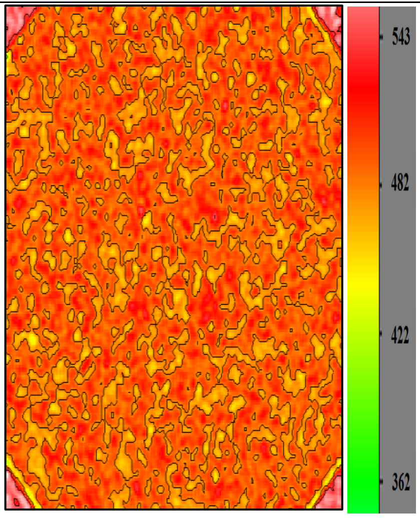	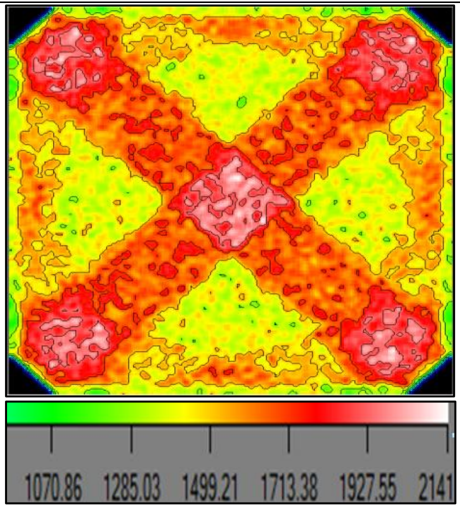
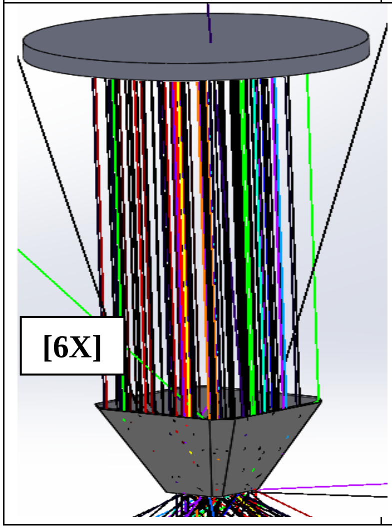	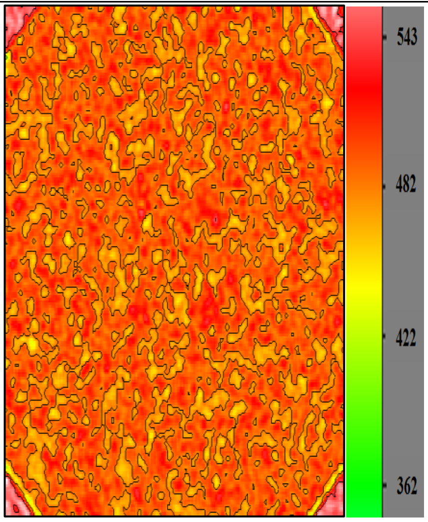	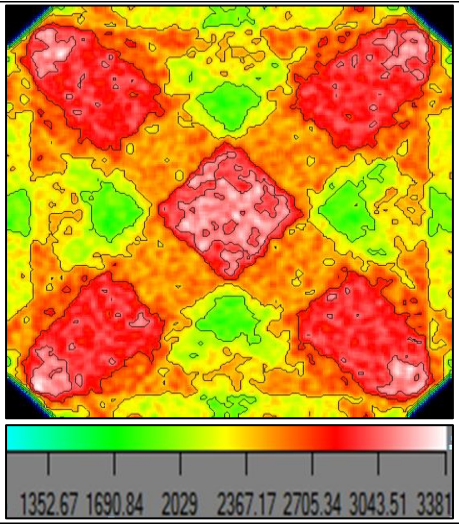

Figure 4.12 Distribution of irradiance with surface reflectivity of 90% at the entrance aperture and receiver aperture with different concentration ratio

4.3.2 Effect of surface reflectivity

Figures **Figure 4.13**,Figure **4.14** and **Figure 4.15** show the irradiance distribution at the receiver area of the 3D-PSCPV concentrator at various surface reflectivities of 60%, 70%, 80% and 90% for G_{CR} of 2X, 4X and 6X, respectively. Figure **4.13** illustrates that the optical irradiance distribution for the 3D-PSCPV with G_{CR}= 2 is nearly uniform (CUF=83%) on the receiver aperture getting a maximum of (1200-1460W/m^2) at the centre with average concertation ratio of 1.9X. This can be illustrated using Figure **4.13** (A) 3D contour mapping and Figure **4.13** (B) 2D distribution on a horizontal line at the centre of the receiver aperture where it can be seen that, a part from the centre region, the average of the received irradiance is 770, 890, 942 and 950W/m^2 for the reflectivity values of 60%, 70%, 80% and 90%, respectively.

Figure **4.14** illustrates that the distribution of the received irradiance for 3D-PSCPV with G_{CR}=4 is less uniformly distributed (CUF=75%) compared to the 3D-PSCPV with G_{CR}=2. For G_{CR}=2, the maximum irradiance (1580-2140 W/m^2) in hot points and regions at the receiver aperture area. Figure **4.14** (A) illustrates that the received irradiance is forming an (X) shape between the corners and the centre of the receiver aperture; Figure **4.14** (B) illustrates that the concentration is greater on the horizontal line in comparison with the concentration on the horizontal line in Figure **4.13** (B). The average received irradiance is 1130, 1360, 1530 and 1740W/m^2 for the reflectivity values of 60%, 70%, 80% and 90%, respectively.

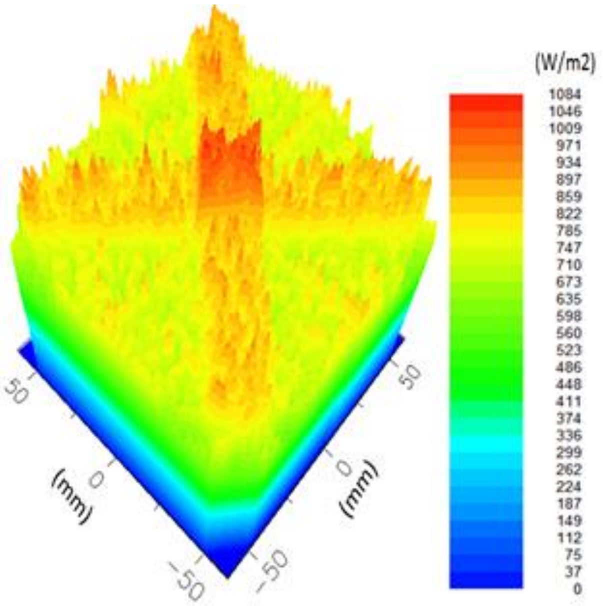

60% Reflectivity

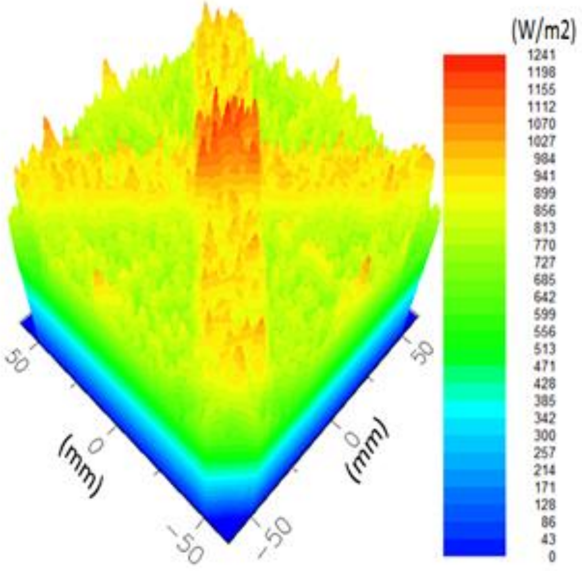

72% Reflectivity

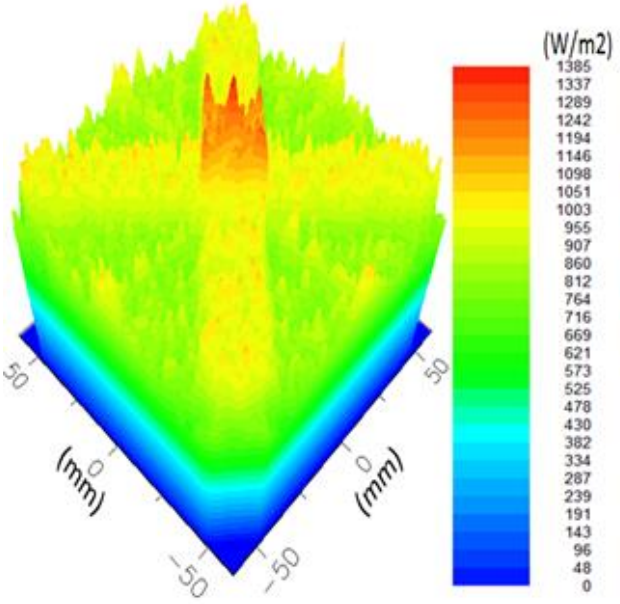

80% Reflectivity

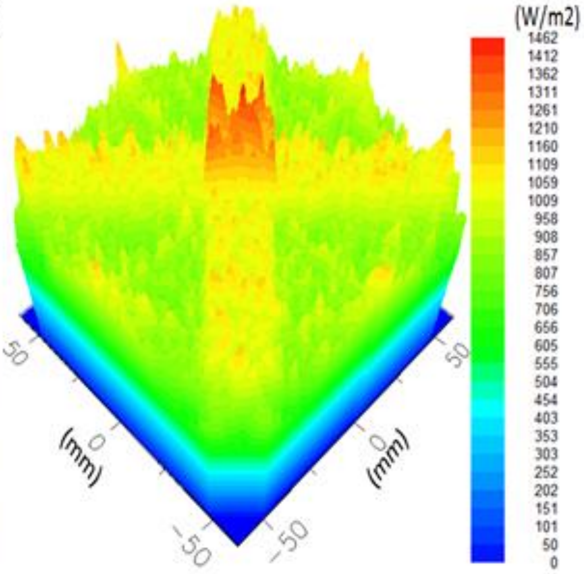

90% Reflectivity

[A]

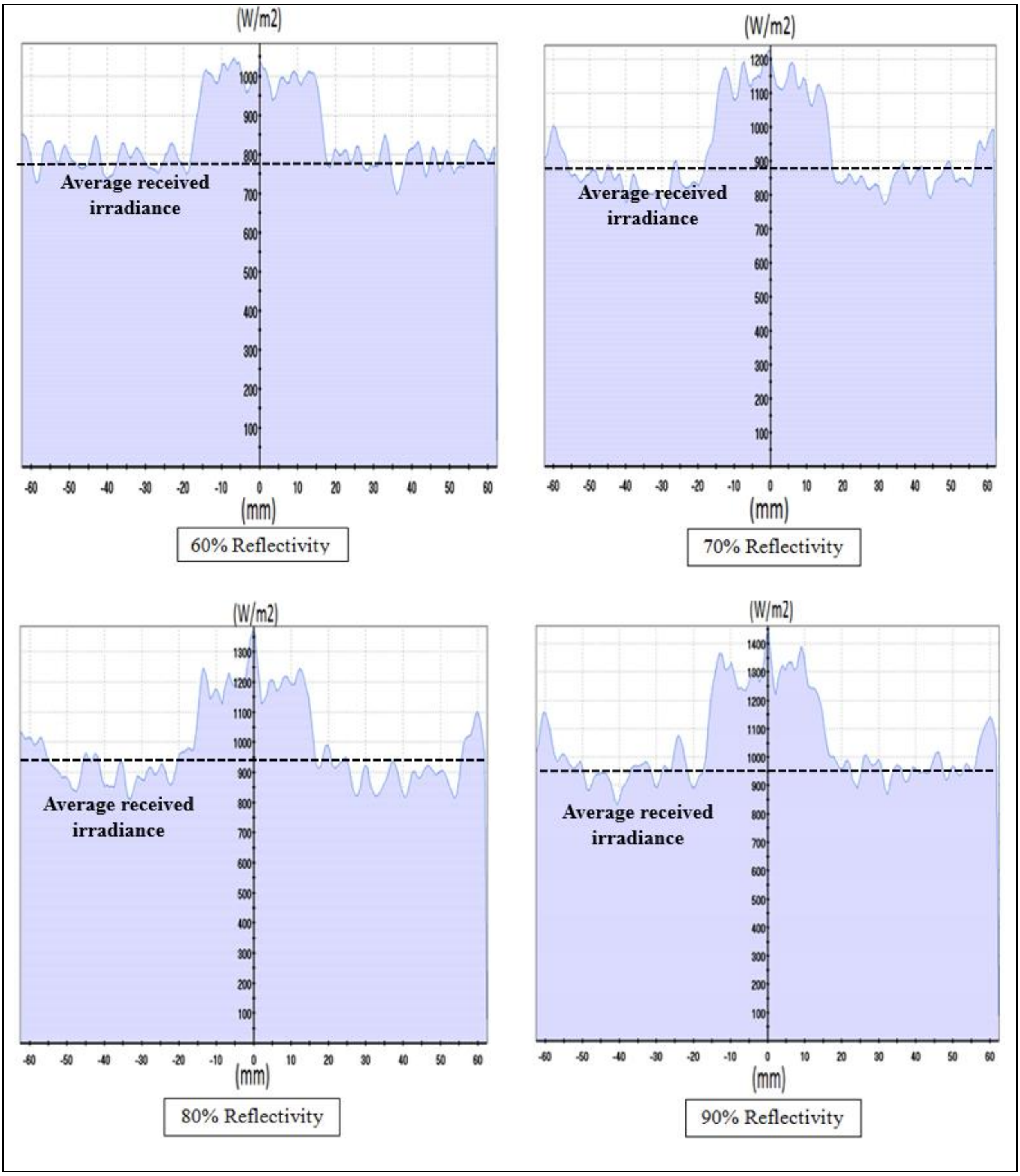

[B]

Figure 4.13 Distribution of the received irradiance for the 3D-PSCPV with different reflectivity values at (GCR=2): (a) 3D contour mapping, (b) 2D distribution on the horizontal line.

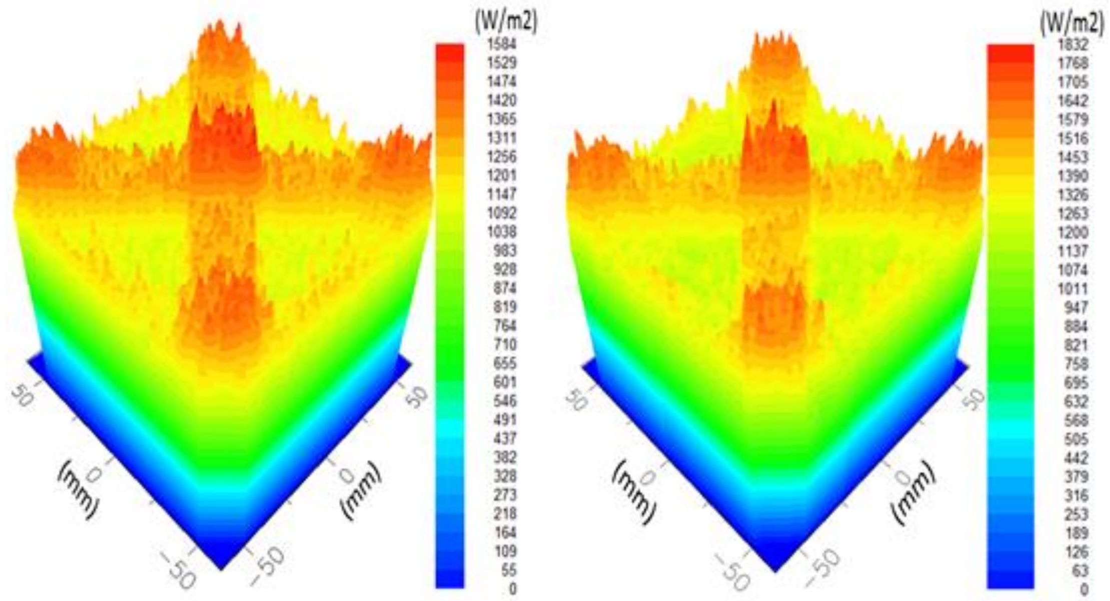

60% Reflectivity

72% Reflectivity

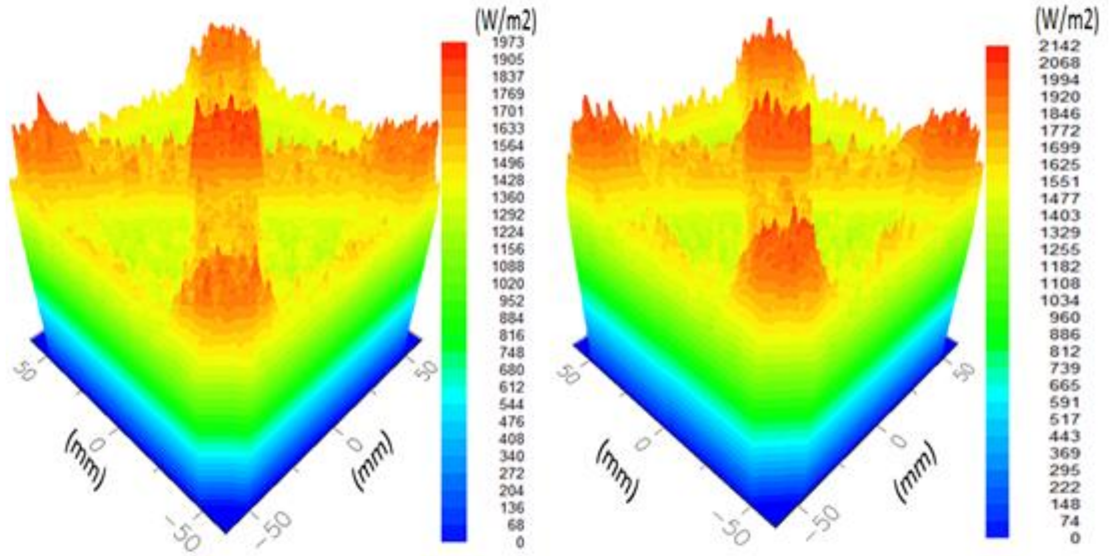

80% Reflectivity

90% Reflectivity

[A]

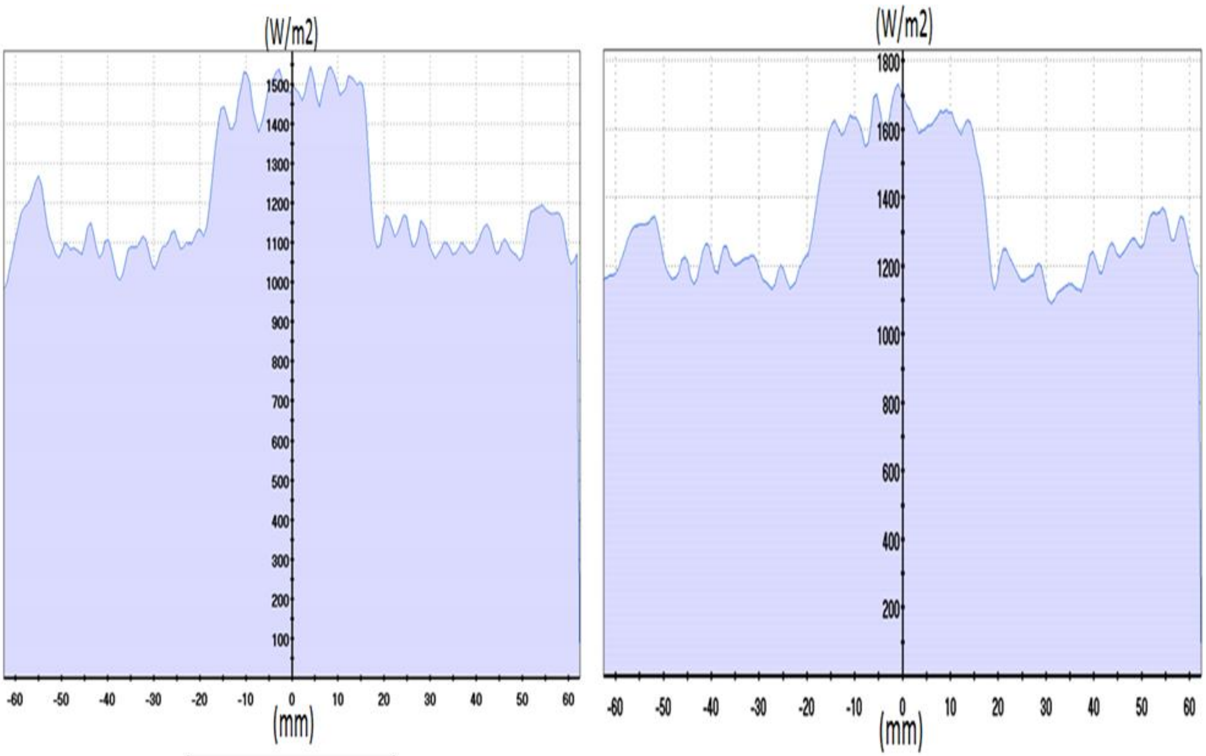

60% Reflectivity

70% Reflectivity

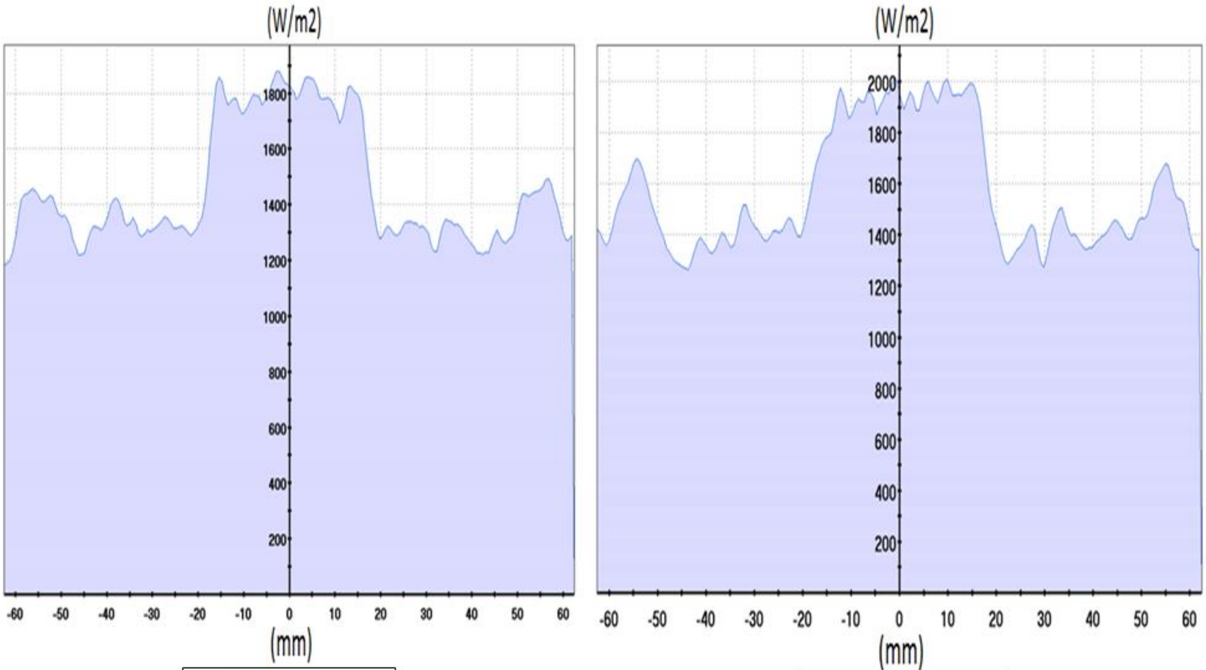

80% Reflectivity

90% Reflectivity

[B]

Figure 4.14 Distribution of the received irradiance for 3D-PSCPV with different reflectivity values at (GCR=4): (a) 3D contour mapping, (b) 2D distribution.

Figure **4.15** (A) illustrates that the distribution of the received irradiance is non-uniform (CUF=63%) for the 3D-PSCPV with G_{CR}=6 with several high irradiance regions. The irradiance is concentrated in the corners and central region of the receiver aperture with the value of (2360-3380 W/m^2) compared to the remaining regions of the receiver aperture for the 3D-PSCPV, as shown in Figure **4.15** (A). The average received irradiance is 1600, 1930, 1950 and 1980W/m^2 for the reflectivity values of 60%, 70%, 80% and 90%, respectively. Figure **4.15** (B) illustrates the concentration is greatly higher on the horizontal line in comparison with the concentration on the horizontal line in Figure **4.13** (B) and Figure **4.14** (B).

For the G_{CR}=6 concentrator the maximum irradiance concentrated in the corners and middle are different from other areas on the receiver with a concentration ratio value up to 6.76 at reflectivity value of 90%. Figure **4.16** shows average of the received irradiance with different surface reflectivity level and G_{cr} of the concentrators in clean conditions. Considering all the figures, it becomes clear that the high concentration ratio concentrators are creating an (X) shape: a light projection of the entrance of the 3D- PSCPV on receiver. The maximum irradiance concentrated in the centre of the receiver and the concentration ratio reaches a maximum of 2.92 and 4.28 at reflectivity value of 90%, for the geometrical concentration ratio of 4 and 6, respectively. While, the average irradiance concentrated in the centre of the receiver and the concentration ratio reaches an average of 1.9, 3.48 and 3.96 at reflectivity value of 90%, for the geometrical concentration ratio of 2 and 4, 6, respectively.

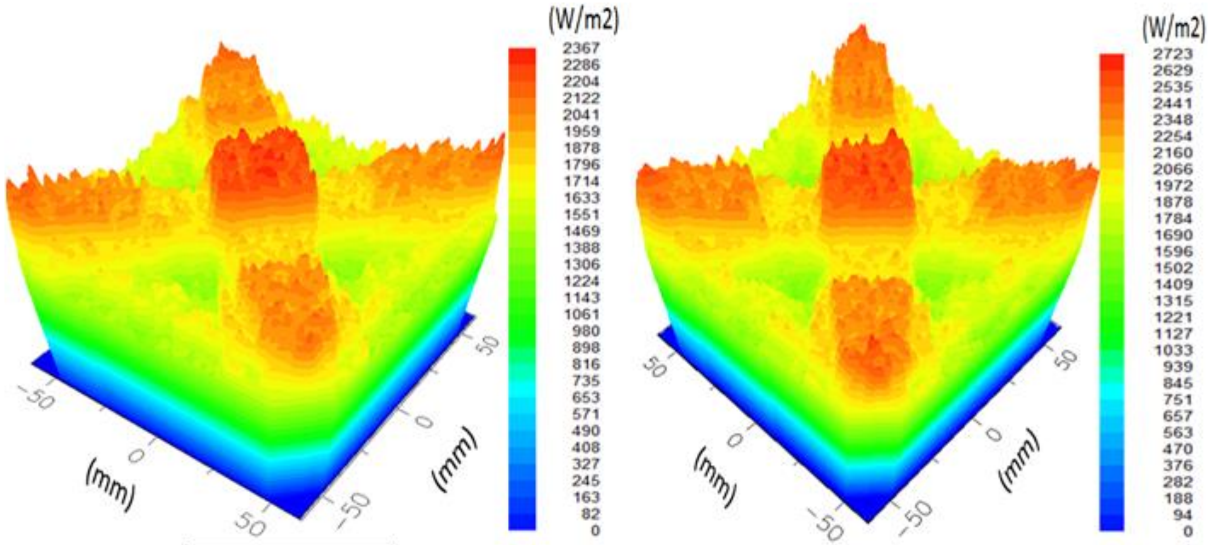

60% Reflectivity

72% Reflectivity

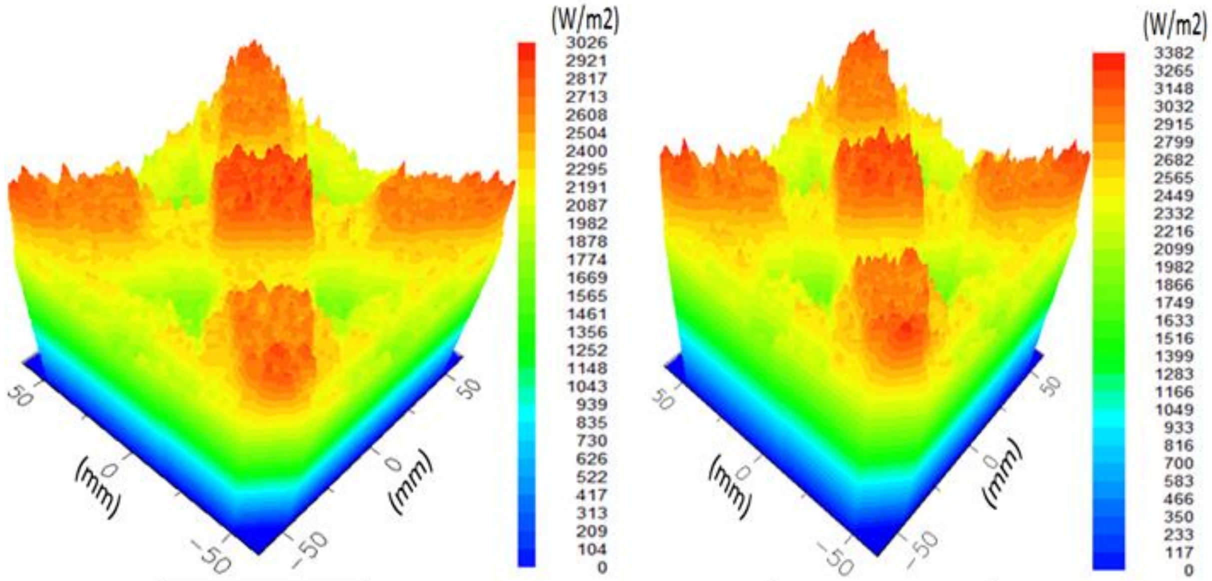

80% Reflectivity

90% Reflectivity

[A]

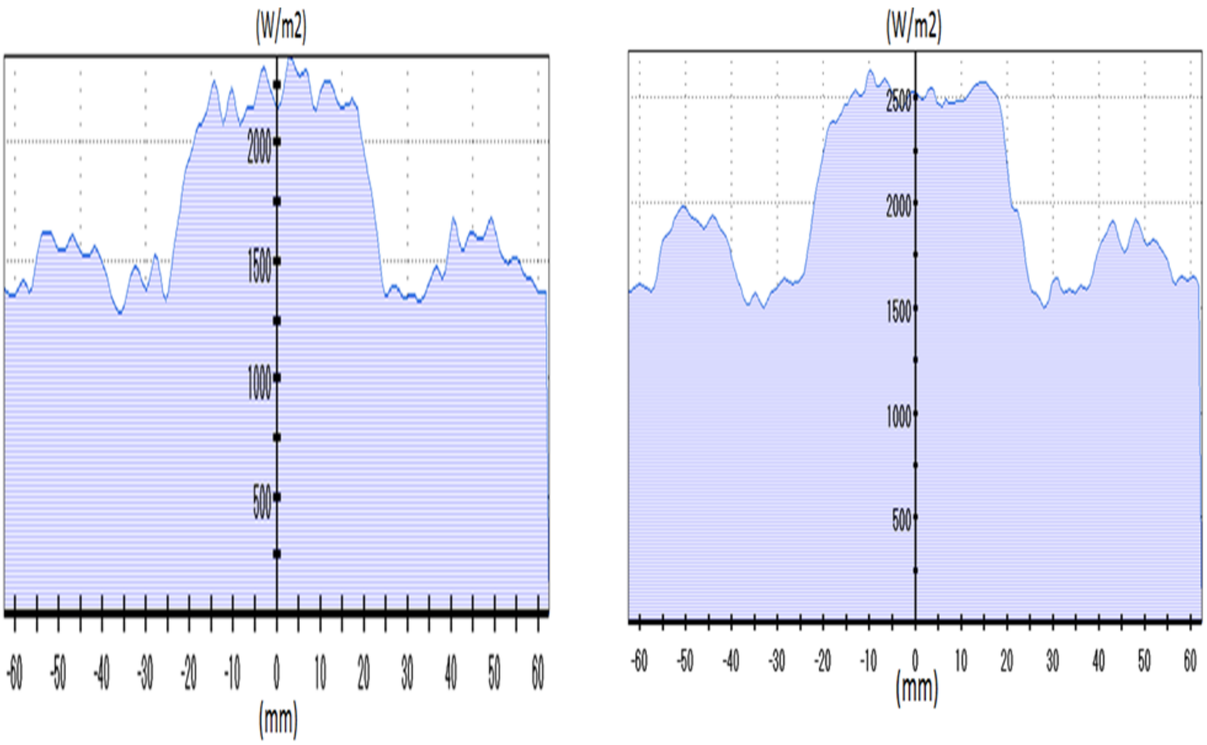

60% Reflectivity

70% Reflectivity

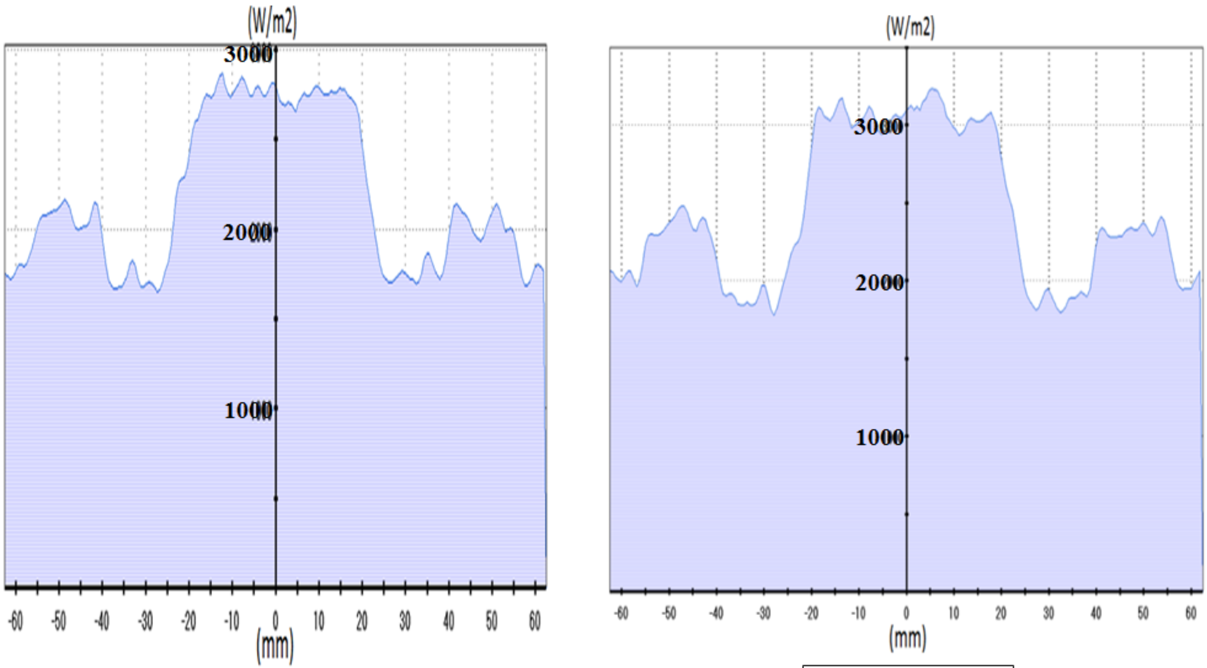

80% Reflectivity

90% Reflectivity

[B]

Figure 4.15 Distribution of the received irradiance for 3D-PSCPV with different reflectivity values at (GCR=6): (a) 3D contour mapping, (b) 2D distribution.

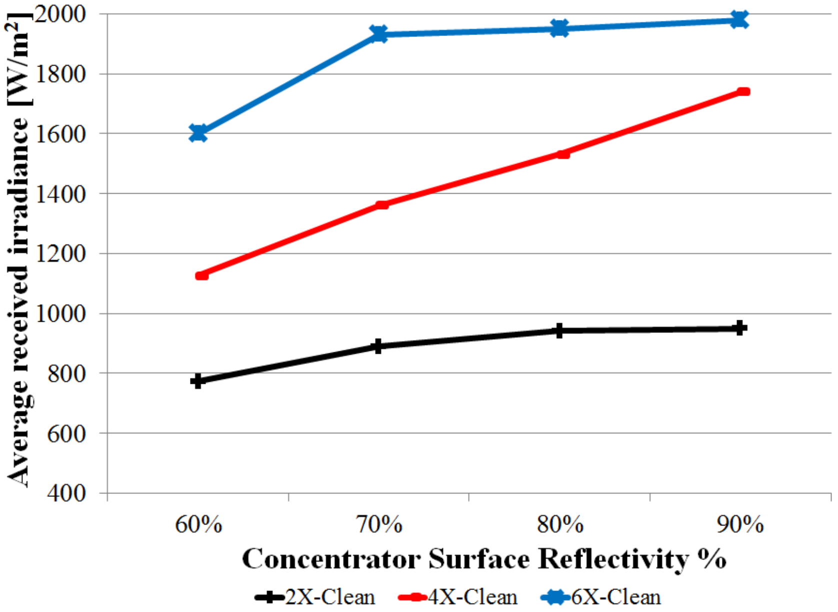

Figure 4.16 Average received irradiance of clean 3D-PSPCV at different surface reflectivity.

Figure **4.17** illustrates the irradiance uniformity factor of three different 3D-PSCPV concentration ratios of G_{CR}= 2,4 and 6 at four concentrator surface reflectivity values 60%, 70%, 80% and 90%. Overall the 2X concentrator showed the highest uniformity of received irradiance at all surface reflectivity values for example at reflectivity of 90% the uniformity of 2X is approximately 82% while the 4X and 6X concentrator produced uniformities of 74% and 63%, respectively. Furthermore, for all concentration ratios (2X, 4X and 6X), as the surface reflectivity increased up to 90%, the uniformity of all the received irradiance of all the concentration ratios increased; The rationale for that is when the surface reflectivity of the concentrator internal reflector is high; the amount of reflected light-rays inside the concentrator is higher; and that leads to a stronger chance of increasing the regions that are reached by the reflected light-rays.

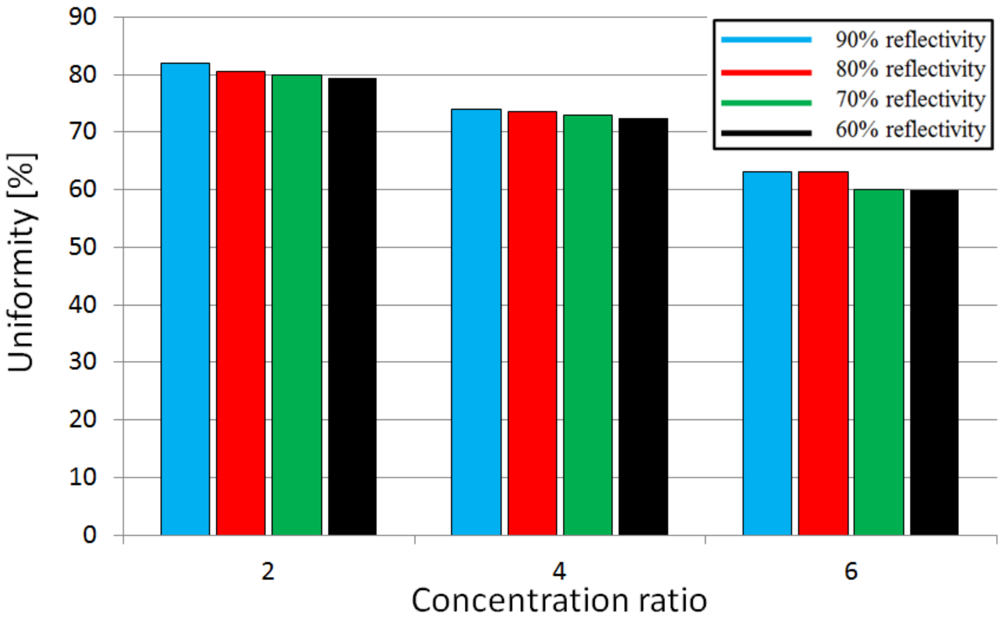

Figure 4.17 The concentrator uniformity factor of four surfaces reflectivity's 90%, 80%, 70% and 60% at different concentration ratios of 2, 4 and 6.

4.4 The dust effects on 3D-PSCPV optical performance

The accumulated dust particles will reflect or transmit some of the incident light-ray falling on the concentrator glass cover entrance, which will decrease the intensity of radiation [144, 145]. The scattering of dust grains (α) is determined based on the ratio of the dust particles size to the incoming radiation expressed as [36]:

$$\alpha = \frac{\pi D}{R} \tag{4.4}$$

Where, R is the incoming radiation and D is the grain diameter. The extinction of light-rays emitted by a grain is a function of the grain extinction efficiency, D_{eff} expressed as [36, 144, 145]:

$$D_{eff} = \frac{\text{Irradiance transmitted by a dust grain}}{\text{Irradiance on the dust grain}} \tag{4.5}$$

In order to assess the effect of dust grains on the optical performance of the 3D-PSCPV, the Monte Carlo ray-tracing procedure available in OptisWork^{TM} was used to evaluate the effect of the dust deposition on 3D-PSCPV irradiance distribution and optical efficiency. In the simulation model, the refractive index for dust grains and glass cover are set to 1.505 [146] and 1.53 [147], respectively. The transmittance of the 3D-PSCPV glass cover is about 94%. For the dust layer, the particle sizes and layer thickness are set as the average diameter of 80μm, and uniformly distributed on the 3D-PSCPV entrance aperture cover. The measured dust reflectance and transmittance of the dust sample (the experimental results in chapter 3) were inputted in the simulation model, as 30% and 70%, respectively.

4.4.1 Dust particles distribution

In this simulation model, for a certain number (N_p) of dust grains settled alongside each other on the glass cover surface of the 3D-PSCPV, they will overlay an area equivalent to ($N_p\pi r^2$). The grains will be presumed to be sphere-shaped with the average diameter D= 0.08 mm and density ρ= 2.4 g/cm^3. The number of grains (N_p) per unit area is determined using equation 4.6 [24, 36, 148]:

$$N_p = \frac{G_m}{(\frac{4}{3})\pi\rho(\frac{D}{2})^3} \tag{4.6}$$

where (G_m) is the mass of grains occupying the unit area. Therefore, these grains would cover part of the entrance aperture unit area which can be determined as [36]:

$$A_{\text{Entrance Aperture}} = \frac{1.5G_m}{\rho D} \tag{4.7}$$

Equation (4.7) describes the relation between the grain size and the covered area. This equation indicates the significant effect of the grain size on the total covered area ($N_p\pi r^2$) for a particular mass (G_m) and grains number of (N_p). The physical properties of the dust grains used in the modelling are presented in Table **4.2**.

Table 4.2 Dust grains physical properties.

Concentration ratio	Total mass of all particles (g/m^2)	Particles number ($million/m^2$)
1	2.5	3
2	6.86	9.7
4	8.83	12.43
6	13.32	18.72

The simulation model was built on the hypothesis of equally-sized, sphere-shaped and uniformly-scattered grains, as recommended by Al-Hasan [24]. All the estimated values in this simulation model for the mass or number of dust grains on 3D-PSCPV cover surface will be per unit area of the entrance aperture which is 0.0309, 0.0621 and $0.0923m^2$ for concentration ratio of 2, 4 and 6 respectively.

4.4.2 Dust particles optical boundary conditions

The simulation was carried out with ray-tracing of a 3D-PSCPV entrance covered with dust in order to characterise the 3D-PSCPV under the effect of dust. The light-rays scatter from one dust grain to another and transmitted into the concentrator's entrance aperture with an average value of transmittance and reflectivity, as measured in chapter 3. Figure **4.18** shows the optical behaviour of the dust grain. A light-ray is reaching the outer boundary of the dust grain domain; it is either refracted or reflected, with the probability of reflection presented by the law of reflection (explained in section 4.1). Once, the light-ray reaches the inner plane boundary of the dust grain, it is refracted through a probability specified by Snell's law of refraction [2]:

$$\frac{n_2}{n_1} = \frac{\sin\theta_1}{\sin\theta_2} \qquad (4.8)$$

Where,

n_1= Refractive index of air medium

n_2= Refractive index of dust grain medium

θ_1= Incidence angle of light-ray

θ_2= Refraction angle of light-ray

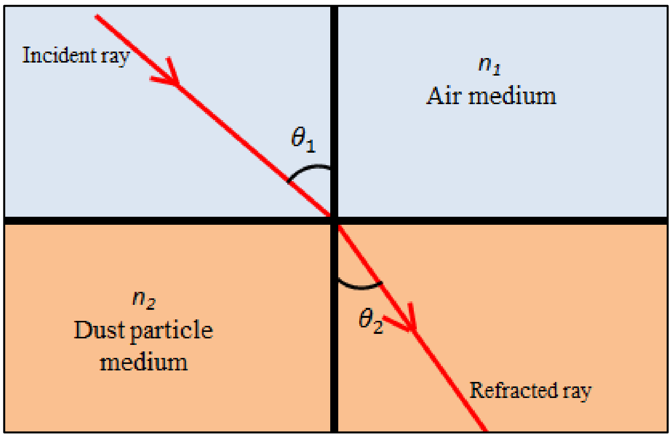

Figure 4.18 The refracted light-ray when it passes from the air medium to a dust grain medium.

If the light-ray is internally reflected, then it continues navigating the domain, or else, the light-ray leaves the domain and the reflected light-ray is absorbed or transmitted. The development of the light-ray transport model is illustrated in Figure **4.19**.

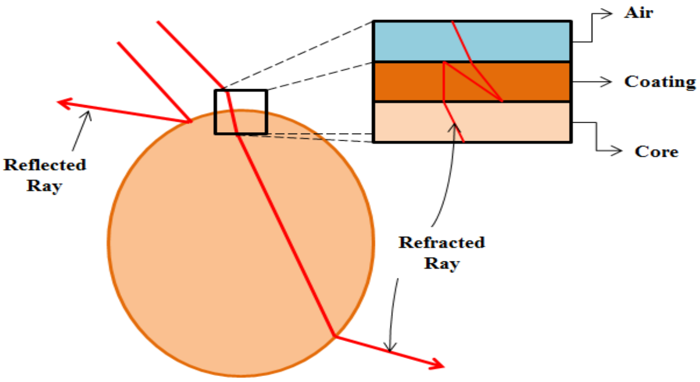

Figure 4.19 The light-rays transmission across a modelled dust grains. Left: The grain consists of a core and coating. Right: A close pictorial on the modelled crossing point between the coating, core and the air surrounding dust grain

The dust grains were simulated in (OpitsWork^{TM}) as semi-transparent to the light-rays. Some of the light-rays intercepting the grains will be reflected, where part of them will be absorbed and the other part will be transmitted.

Figure **4.20** illustrates the optical ray-tracing simulation model of the dust in (OptisWork^{TM}).

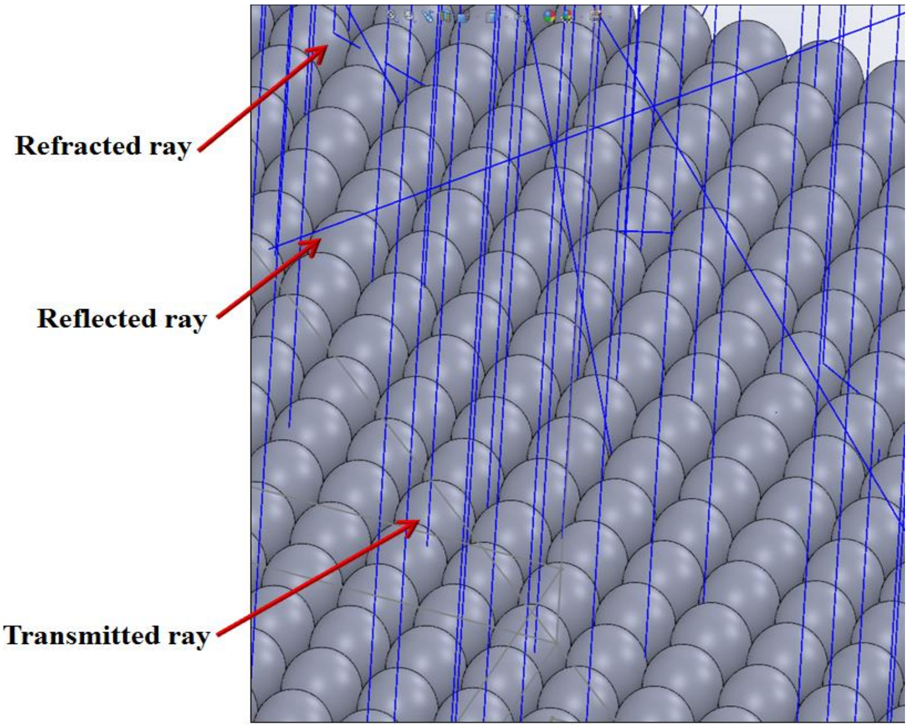

Figure 4.20 The modelling of dust grains on the 3D-PSCPV entrance aperture covers with ray-tracing method (Optiswork^{TM}).

The simulation results of the irradiance distribution on 3D-PSPCV glass cover after passing through the dust layer is illustrated in Figure **4.21**. It can be seen that the irradiance intensity decreased by approximately 34% due to dust accumulation from the input of 520 W/m^2 to an average of 350 W/m^2.

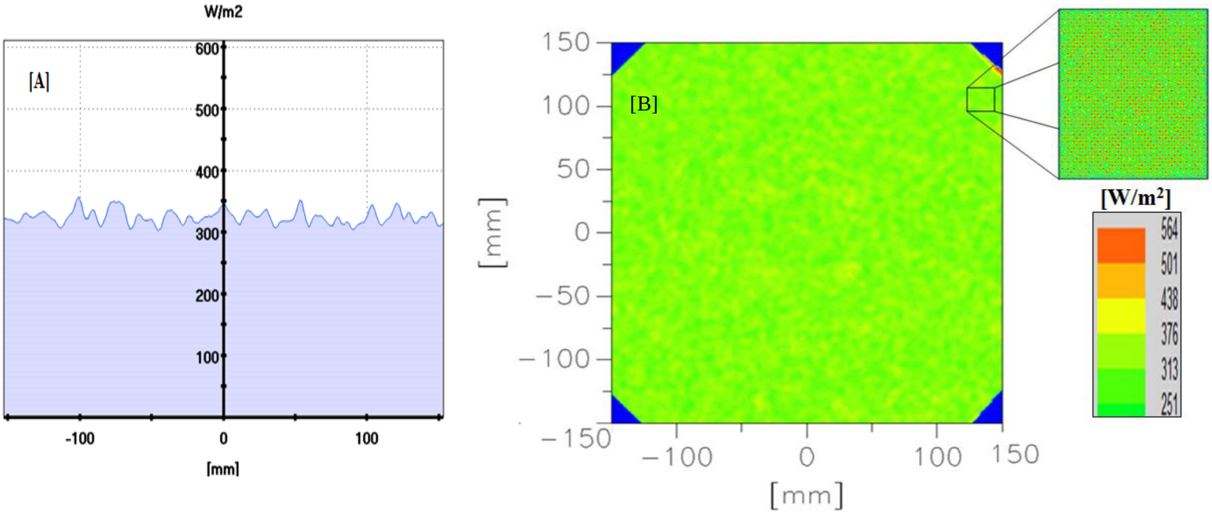

Figure 4.21 The optical irradiance distributions on a dusty entrance aperture of the 3D-PSCPV,(A) irradiance horizontal distribution and (B) 2D irradiance distribution with a closer pictorial of the dust distribution.

4.4.3 Dusty 3D-PSPCV simulation results

A simulation study using (OptisWork^{TM}) is carried out to investigate the effect of dust on the developed (3D-PSPCV) at input of 520 W/m^2. In this ray-tracing analysis, the irradiance distributions and the optical efficiency for three different G_{CR} (2X, 4X and 6X) with four different surface reflectivity values (60%, 70%, 80% and 90%) were investigated under the effect of dust accumlation on the 3D-PSPCV. From the ray-tracing simulation results shown in Figure **4.22** (a) and (b) to Figure **4.24** (a) and (b) the following can be observed concerning the effects of dust on 3D-PSPCV optical performance.

- Generally, there is a decrease in the received irradiance values compared to those received by the clean 3D-PSCPV for all values of G_{CR} (2X, 4X and 6X).
- Compared to other areas on the receiver, the centre area with high concentration on the clean 3D-PSPCV condition increased, due to the dust accumulation causing the uniformity to be decreased.

- There is a decrease in the dusty 3D-PSPCV optical efficiency as the G_{CR} increases, with the highest loss in G_{CR}=6X at 60% reflectivity. Hence G_{CR} =2X optical efficiency with a 90% reflectivity is the best among all other G_{CR} with different reflectivities.
- G_{CR} (2X and 4X) with the reflectivity of 90% tends to show better optical performance than the rest of the G_{CR} range and reflectivity values under the effect of dust.

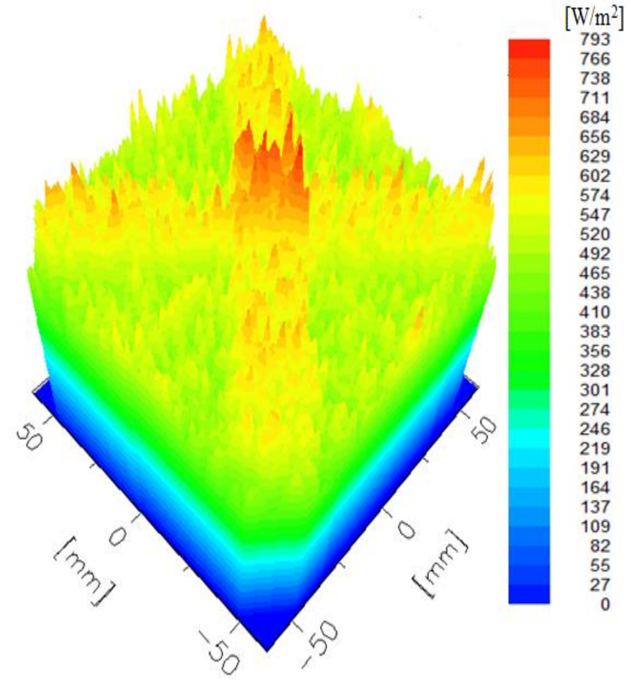

60% Reflectivity

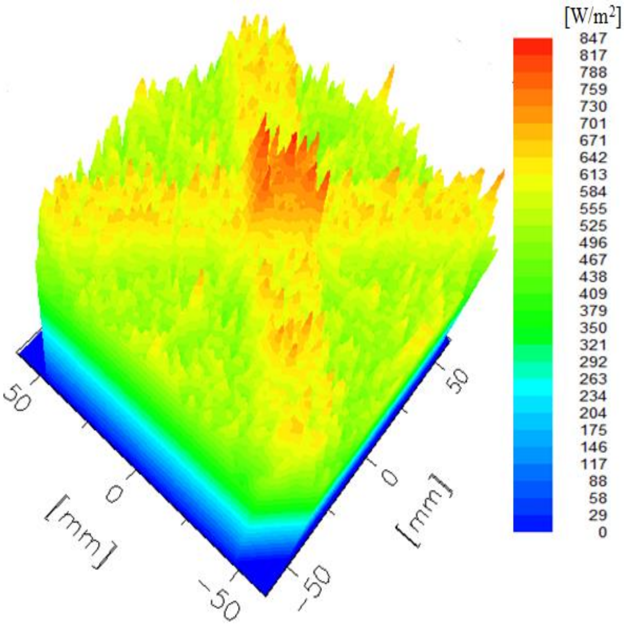

70% Reflectivity

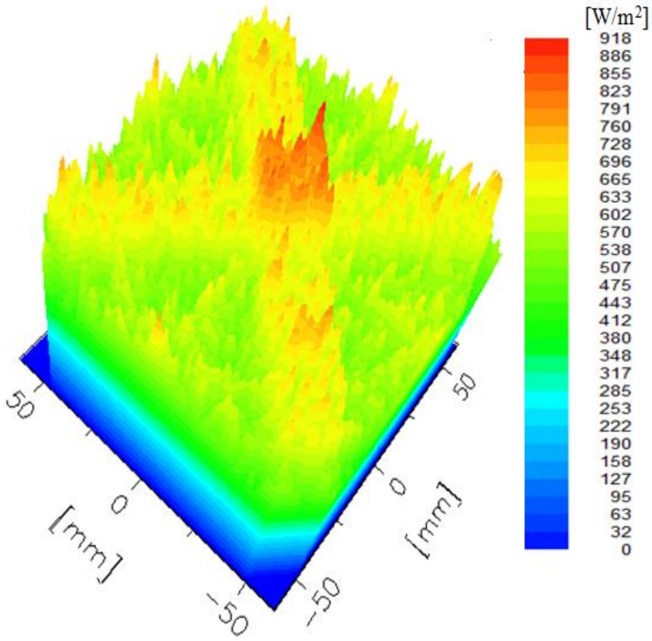

80% Reflectivity

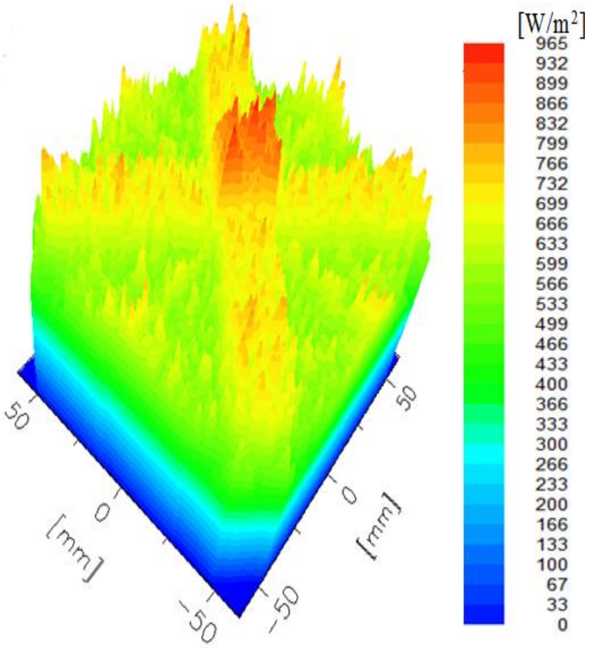

90 % Reflectivity

[A]

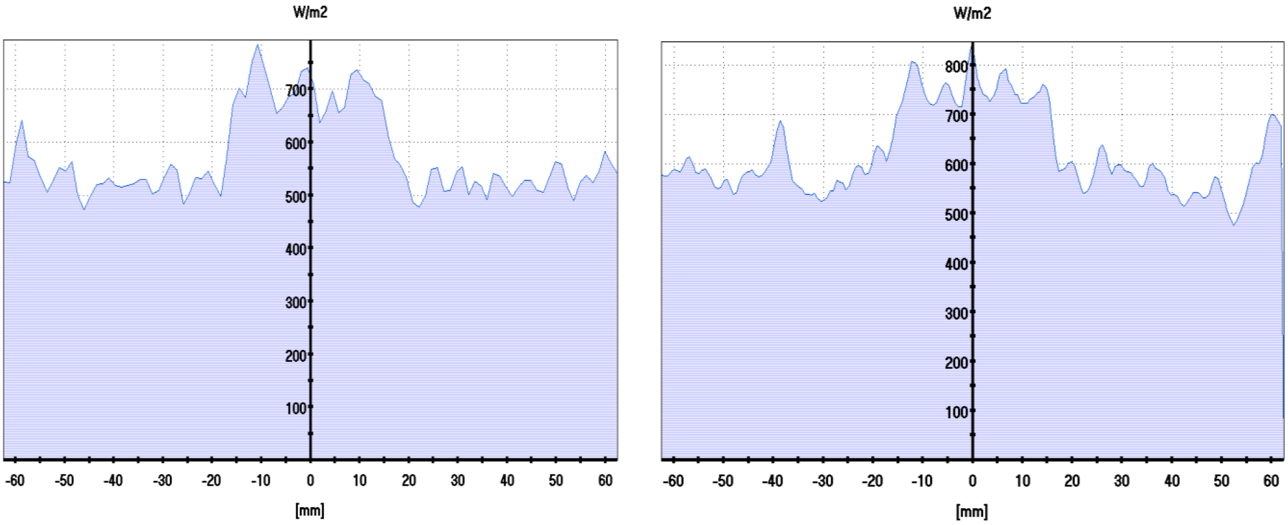

60% Reflectivity 70% Reflectivity

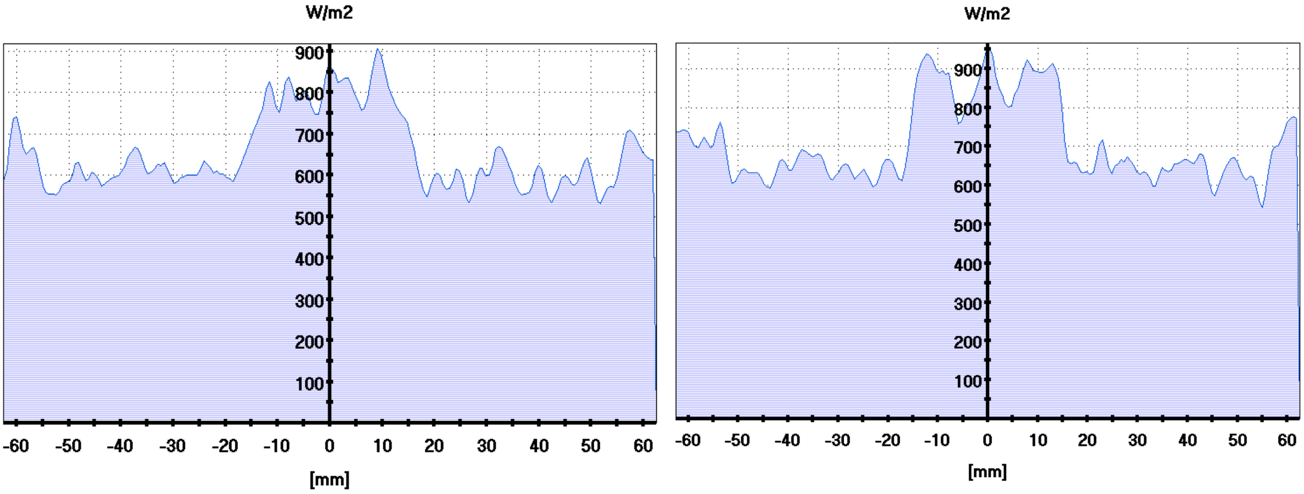

80% Reflectivity 90% Reflectivity

[B]

Figure 4.22 Optical irradiance distribution of the dusty 3D-PSCPV with different reflectivity values at (GCR=2): (a) 3D contour mapping, (b) 2D distribution on the horizontal line.

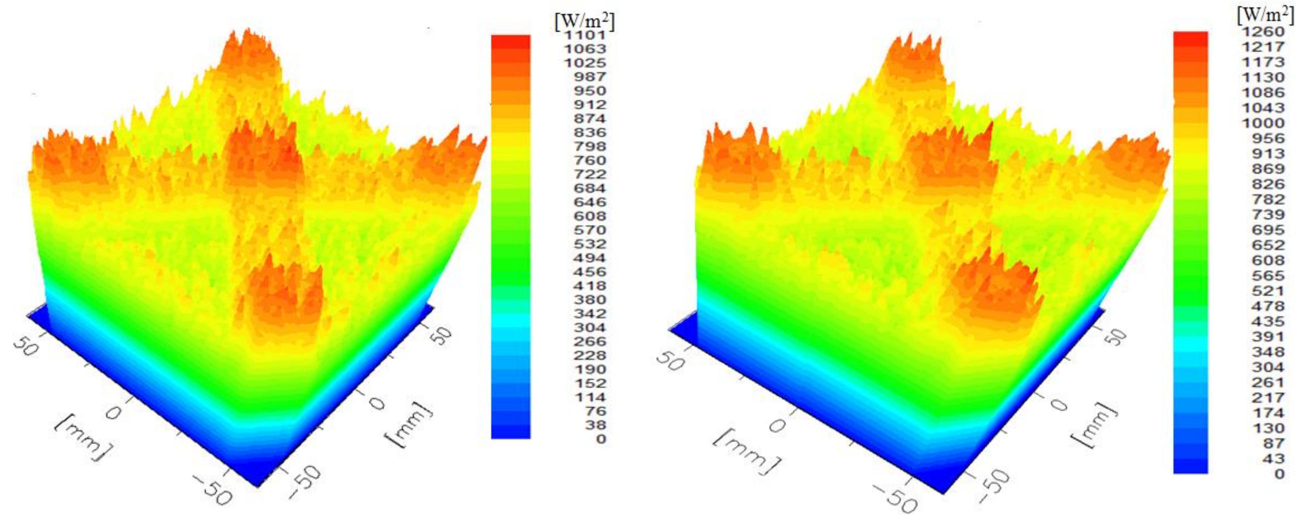

60% Reflectivity

70% Reflectivity

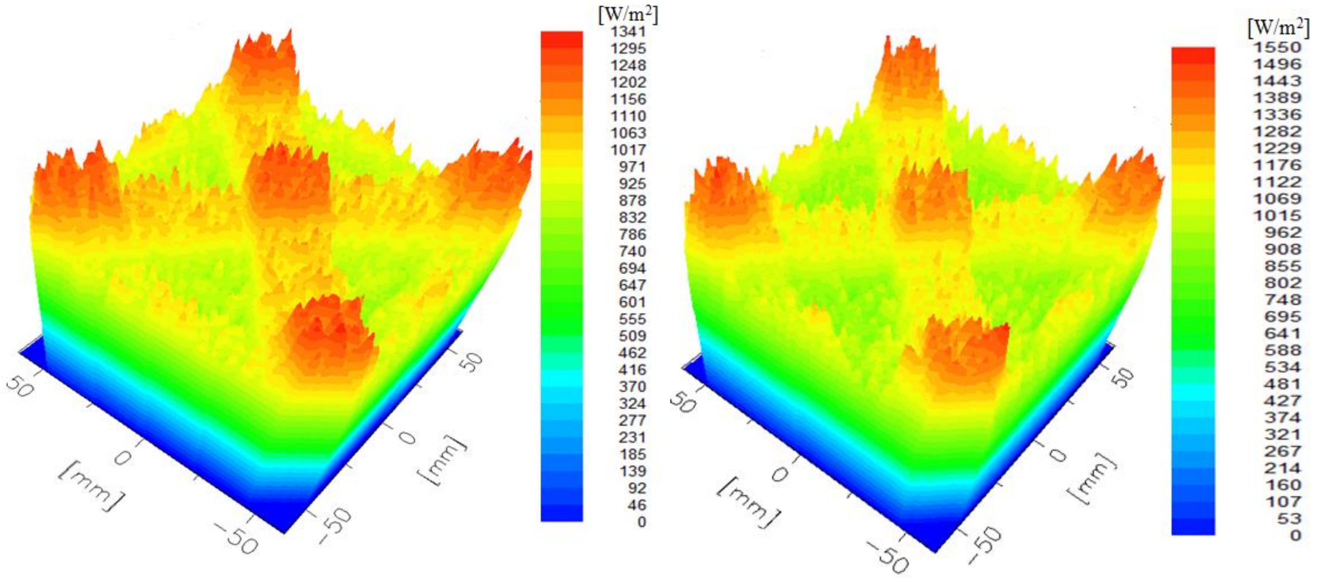

80% Reflectivity

90% Reflectivity

[A]

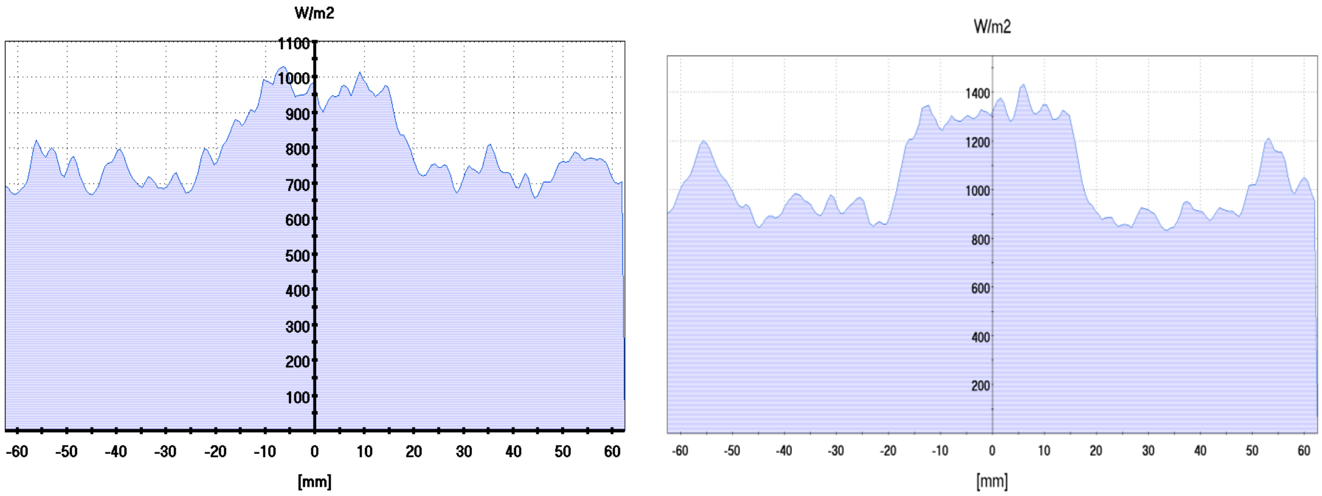

60% Reflectivity

70% Reflectivity

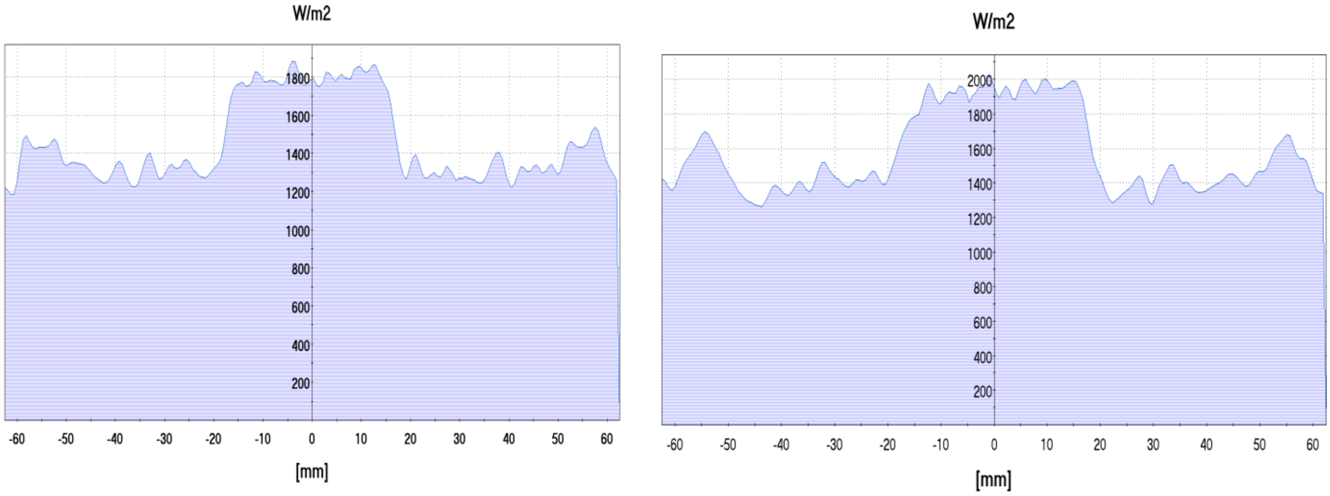

80% Reflectivity

90% Reflectivity

[B]

Figure 4.23 Optical irradiance distribution of the dusty 3D-PSCPV with different reflectivity values at (GCR= 4): (a) 3D contour mapping, (b) 2D distribution on the horizontal line.

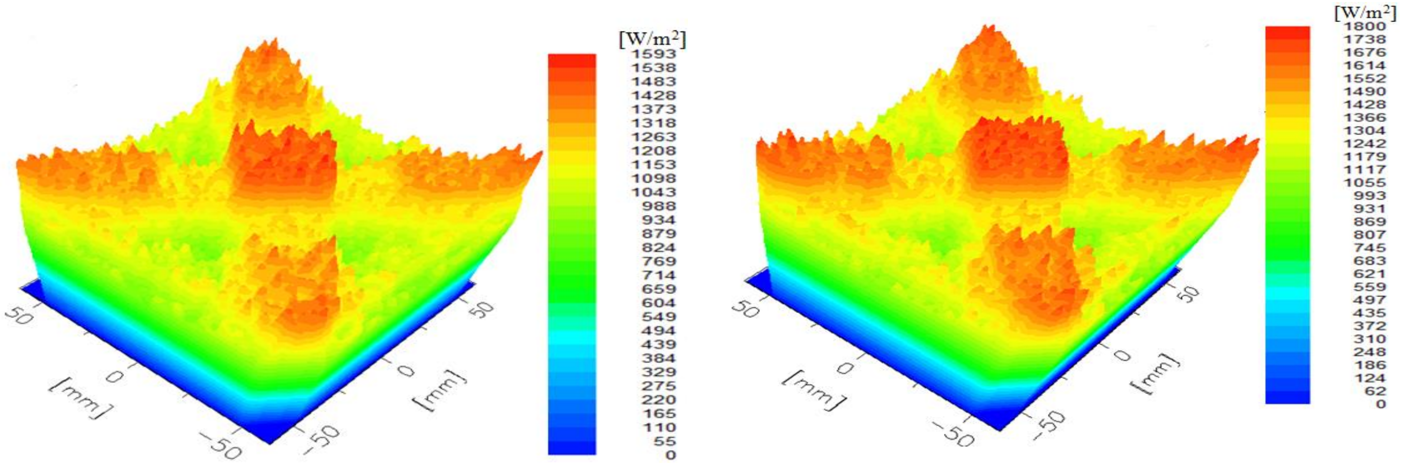

60% Reflectivity

70% Reflectivity

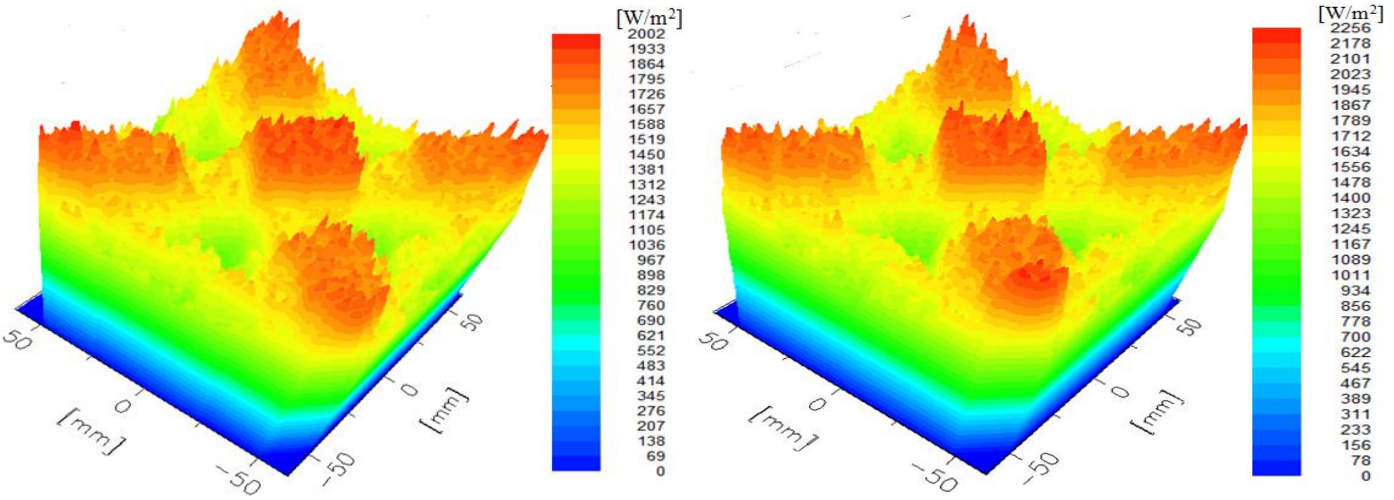

80% Reflectivity

90% Reflectivity

[A]

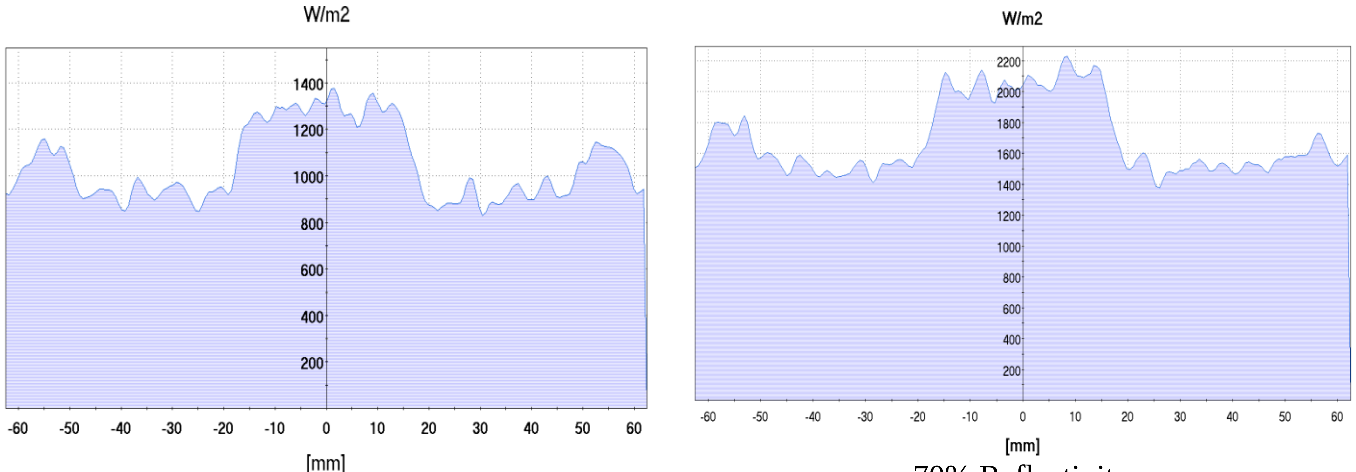

60% Reflectivity

70% Reflectivity

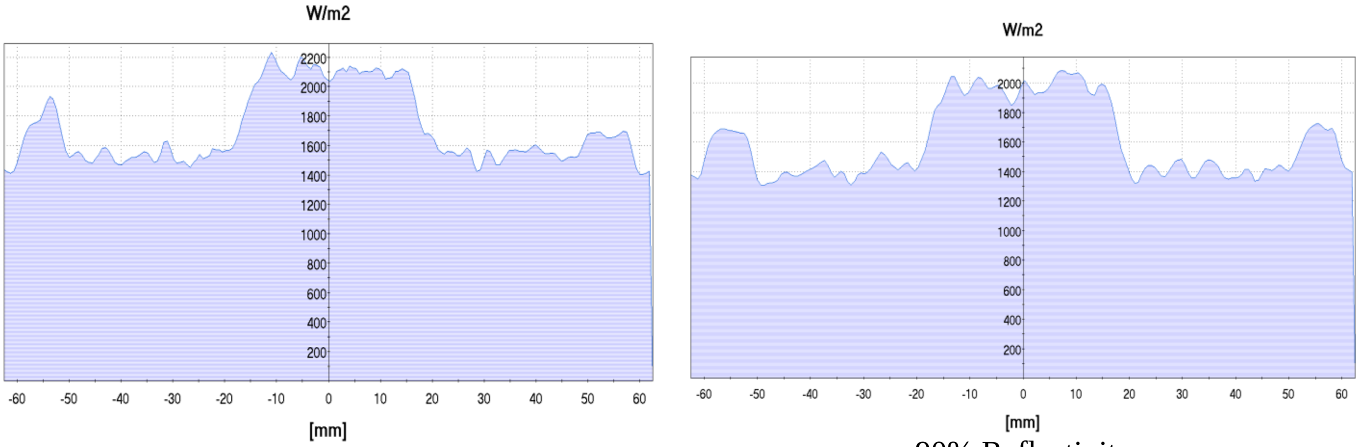

80% Reflectivity

90% Reflectivity

[B]

Figure 4.24 Optical irradiance distribution of the dusty 3D-PSCPV with different reflectivity values at (GCR= 6): (a) 3D contour mapping, (b) 2D distribution on the horizontal line

Detailed comparisons between the overall performance of the concentrators for clean and dusty conditions are provided in Figure **4.25** and Figure **4.26** in terms of optical efficiency and the average of the received irradiance with different surface reflectivity level and G_{cr}. These comparisons show that the maximum optical efficiency values of the clean condition are 95%, 87% and 66% for 2X, 4X and 6X, respectively. Whereas, the maximum optical efficiency values of the dusty condition are: 85%, 77% and 58.3% for 2X, 4X and 6X, respectively. The average received irradiance of both clean and dusty concentrators is shown in Figure **4.26**. This figure shows that the maximum average values of received irradiance are

950, 1740 and 1980 W/m^2 for clean concentrator with 2X, 4X and 6X, respectively, while maximum average received irradiance values for the dusty concentrator with 2X, 4X and 6X concentrators were 850, 1540 and 1750 W/m^2, respectively.

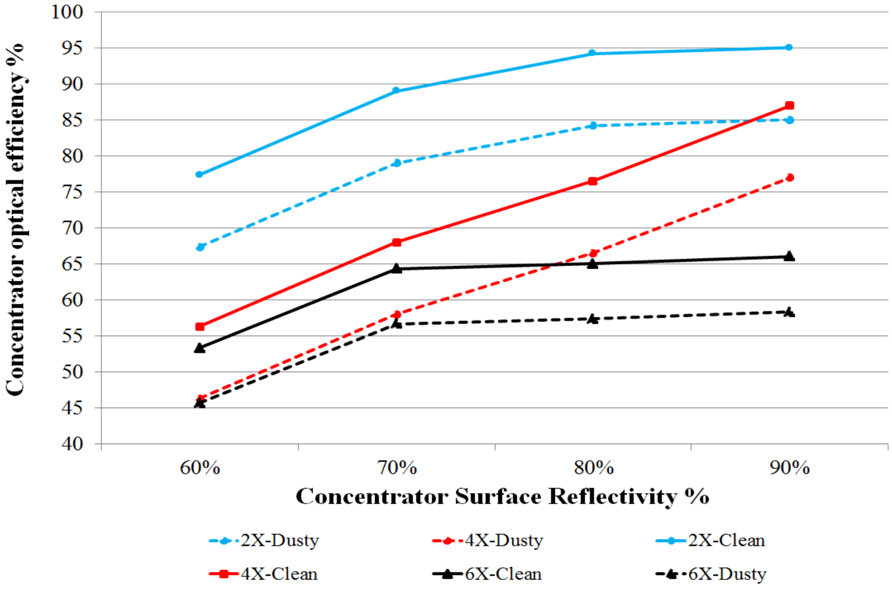

Figure 4.25 Optical efficiency of clean and dusty 3D-PSPCV conditions at different surface reflectivity

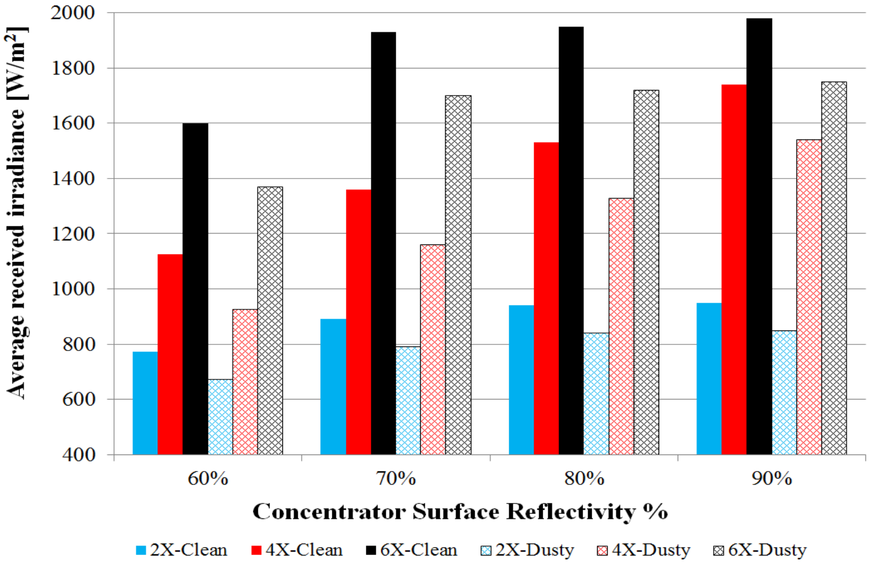

Figure 4.26 Average received irradiance of clean and dusty 3D-PSPCV at different surface reflectivity

The predicted actual optical concentration ratio has been determined using equation 2.16 for the 3D-PSPCV with different surface reflectivity values and G_{cr} under clean condition (solid lines) and dusty condition (dotted lines) as shown in Figure **4.27**.

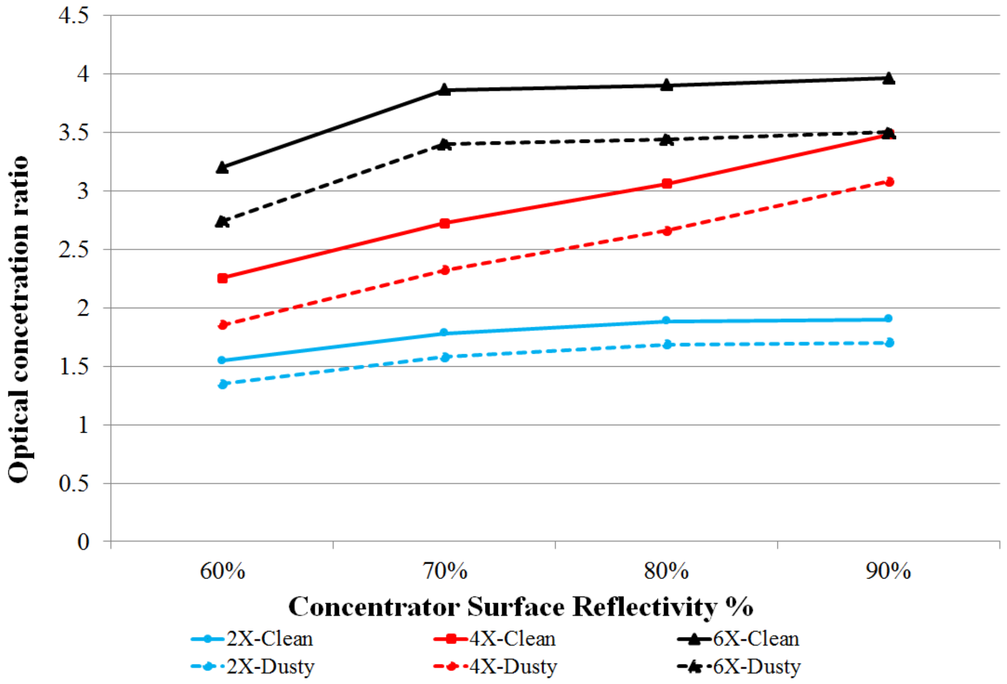

Figure 4.27 Actual optical concentration ratio for different 3D-PSPCV at different surface reflectivity

The actual optical concentration ratio of the 3D-PSPCV decreases as the geometric optical concentration ratio increase in clean and dusty conditions as shown in in Figure **4.27**, due to the optical losses caused by the reflecting and refracting elements and dust accumulation further decreasing the concentrated irradiance. The 6X profiles in Figure **4.27** shows no improvement in actual optical concentration ratio with the increase of the surface reflectivity and this is due to geometrical and optical characteristics of the optimised 3D-PSCPV.

It can be seen that Figure **4.28** to shows the impact of dust on the concentrator uniformity factor (CUF) values obtained using equation (4.5). The uniformity factor of the 3D-PSPCV decreases as the geometric optical concentration ratio increases and this is due to dust effect on the optical irradiance distribution. The dusty concentrator uniformity factors are 73%, 63%

and 54% for 2X, 4X and 6X, respectively. Whereas, the difference with respect to the clean condition (CUF) are: 8.7%, 10% and 11.4% for 2X, 4X and 6X, respectively.

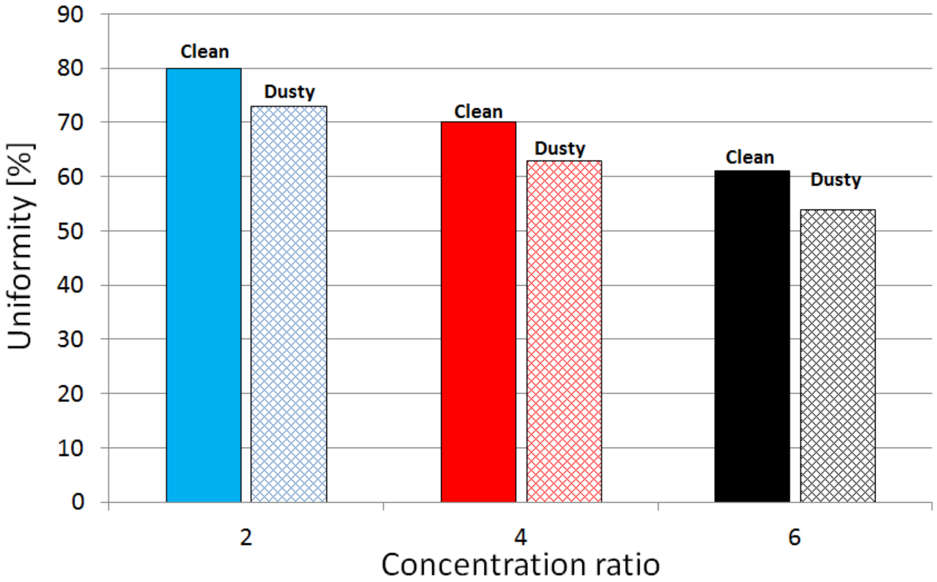

Figure 4.28 The dust accumulation effects on 3D-PSCPV uniformity factor

From these results it is shown that 2X have greater optical efficiency, but lower average received irradiance, than 4X and 6X at all conditions. Hence, the 2X geometrical profiles accept less radiation than 4X and 6X geometrical profiles but have fewer losses due to the fewer internal light-ray reflections. The dust accumulation also affects the 3D-PSCPV uniformity and shows no improvement in uniformity factor with the increase of the surface reflectivity and this is due to the geometrical and optical characteristics of the optimised 3D-PSCPV.

4.5 3D-PSCPV development and assembly

The main design development for any system relies on the materials selected for various parts and the specific part design and assembly. The parts of the 3D-PSCPV are: top aperture cover, reflectors, PV receiver and a reinforce casing. The specific part design and fabrication details are presented in this section.

4.5.1 3D-PSCPV entrance cover

Pilkington Optiwhite^{TM} low iron clear floating glass is used for the entrance aperture cover with 4mm thickness. It has a transmittance of 0.92, reflectance of 0.08 and negligible absorptance due to its low Fe_2O_3 content [2]. Figure **4.29** shows the cover dimensions and Table **4.3** gives its optical properties.

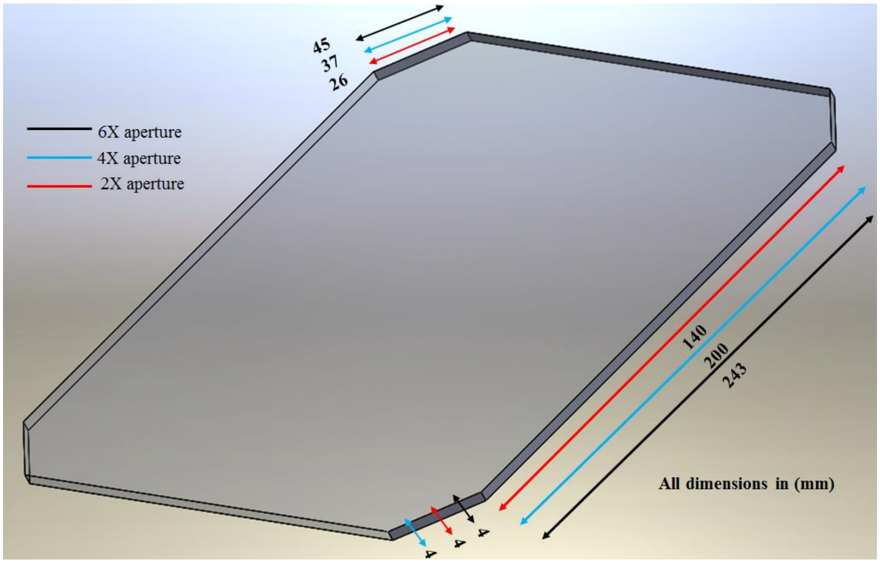

Figure 4.29 3D-PSCPV system aperture cover dimensions

Table 4.3 Glass performance data (Pilkington$^{@}$) [147]

Glass Thickness	Radiation (light)		Radiant (Heat)		
	Transmittance	Reflectance	Direct Transmittance	Reflectance	Absorbance
4 mm	0.92	0.08	0.91	0.08	0.01

The glass cover is used to reduce the deterioration in concentrator and PV cells performance due to direct exposure to sun light as follows:

- The reflecting material can be damaged and deformed due to the ultraviolet components of the direct sun beam as the glass is opaque to ultraviolet radiation.
- The EVA film's complete exposure to the sun beam can cause the change of colour from transparent clear to yellow [149]. This does not shift the PV cells spectral

response only, but reduces the falling solar radiation on the surface of the PV cells. This will reduce the PV system electrical power output and therefore the efficiency of the PV cells.

- The moistness and build-up salt impact the reflectance and PV materials by scattering the falling solar radiation [150].

The glass cover is positioned inside a wooden supported structure as shown in Figure **4.30**. The openings between the glass cover and the concentrator's entrance aperture were closed with clear silicon sealant to avoid water leak and moisture.

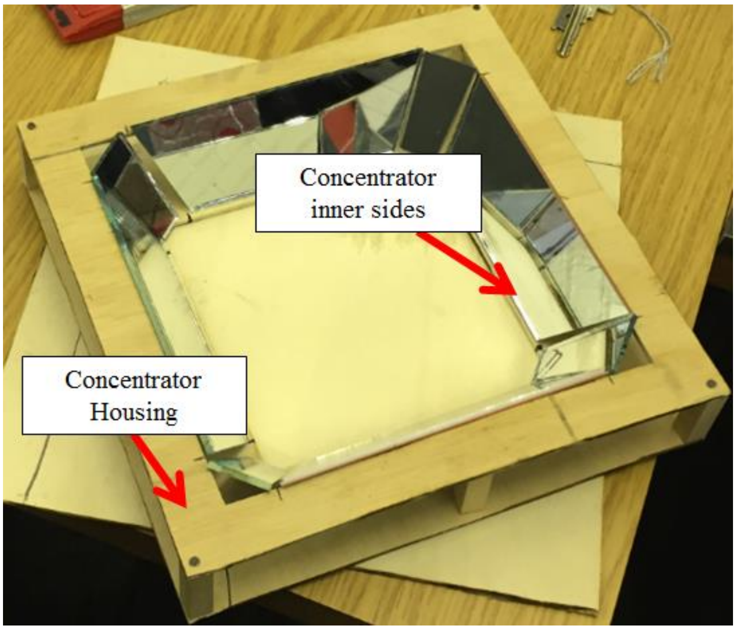

Figure 4.30 3D-PSPCV housing

4.5.2 Engineering graphics development of planes methods

Experimental prototypes of three 3D-PSCPVs were built employing the Engineering Graphics Development of Planes (EGDP) technique. The use of (EGDP) is very suitable as the shapes assembled can have a very complex profile and different reflectors thickness. In EGDP there are different techniques for developing the manufacturing drawing of parts includes:

- The parallel-line technique: It is applied for developing particular rounded planes like tubes, where all the sides / cohort of side planes are parallel to one another.
- The radial-line technique: It is applied for pyramids and single rounded planes and similar cones wherein the high point is considered as a midpoint and the inclined side as radius of its form.
- The approximate technique: It is applied for double arched planes similar to spheres, where they are theoretically unachievable to form. The plane of the sphere is formed by the approximate technique. When the plane is sliced through a sequence of slitting planes; the sliced plane is termed as a zone.

The radial-line technique is applied to draw the pseudo-square from a truncated pyramid. The process for the truncated pyramid development is similar to that of the standard pyramid except for the true measurement of all segments from the apex to the truncated line must be determined and shifted to the 3D pseudo-square form. Figure **4**.**31** shows the dimensions sketched into AutoCAD using (EGDP).

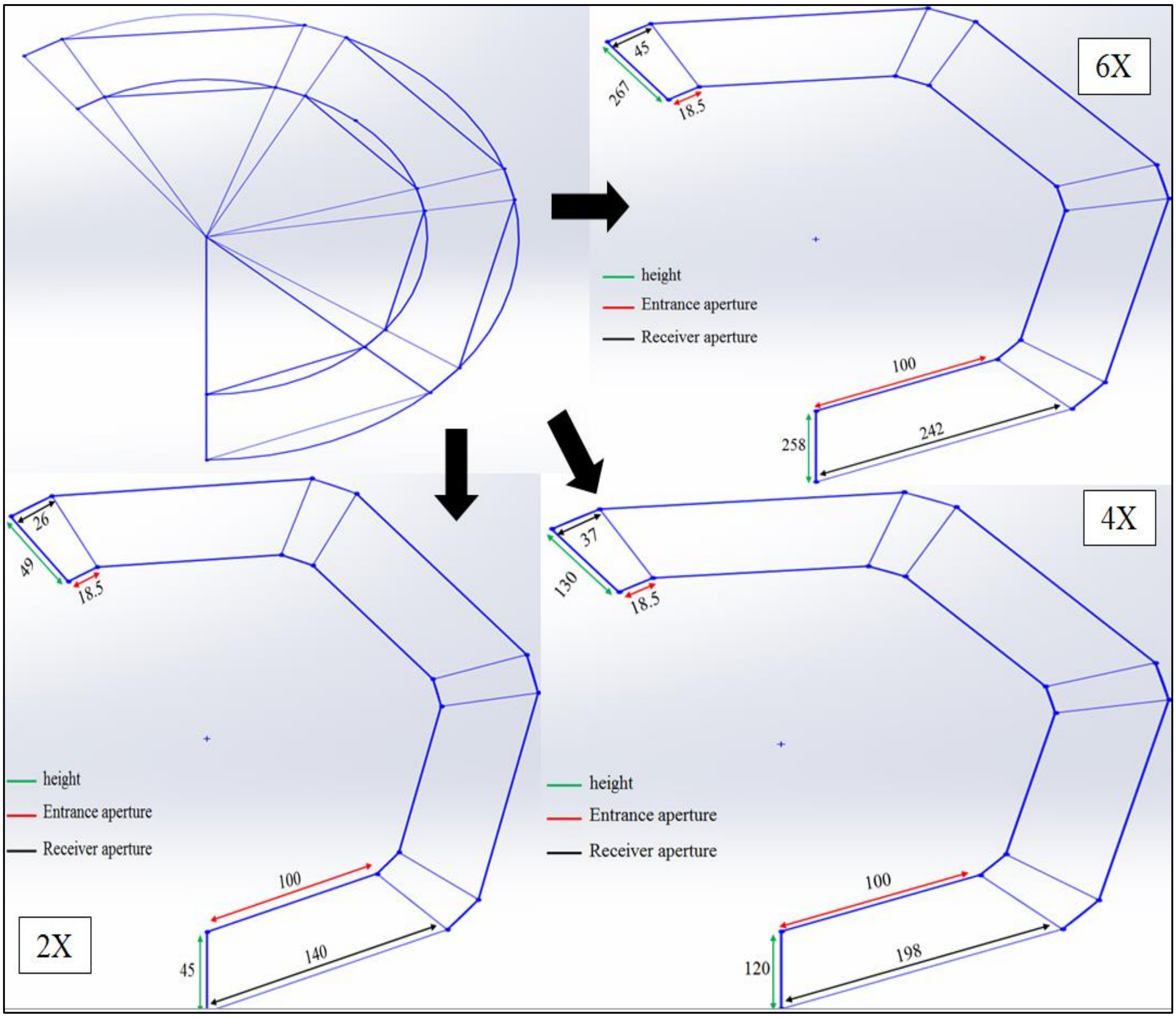

Figure 4.31 EGDP processes of the 2X, 4X and 6X concentration ratio profiles

The internal walls of the 3D-PSCPV are fitted with different reflective materials with reflectivity of 60, 70, 80 and 90% equivalent to the reflectivity value ranges inputted into the simulation parameters. Figure **4.32** shows the three experimental 3D-PSCPV concentrators having a receiver area of 0.015538 m^2 and a height of 45mm, 145mm and 250mm.

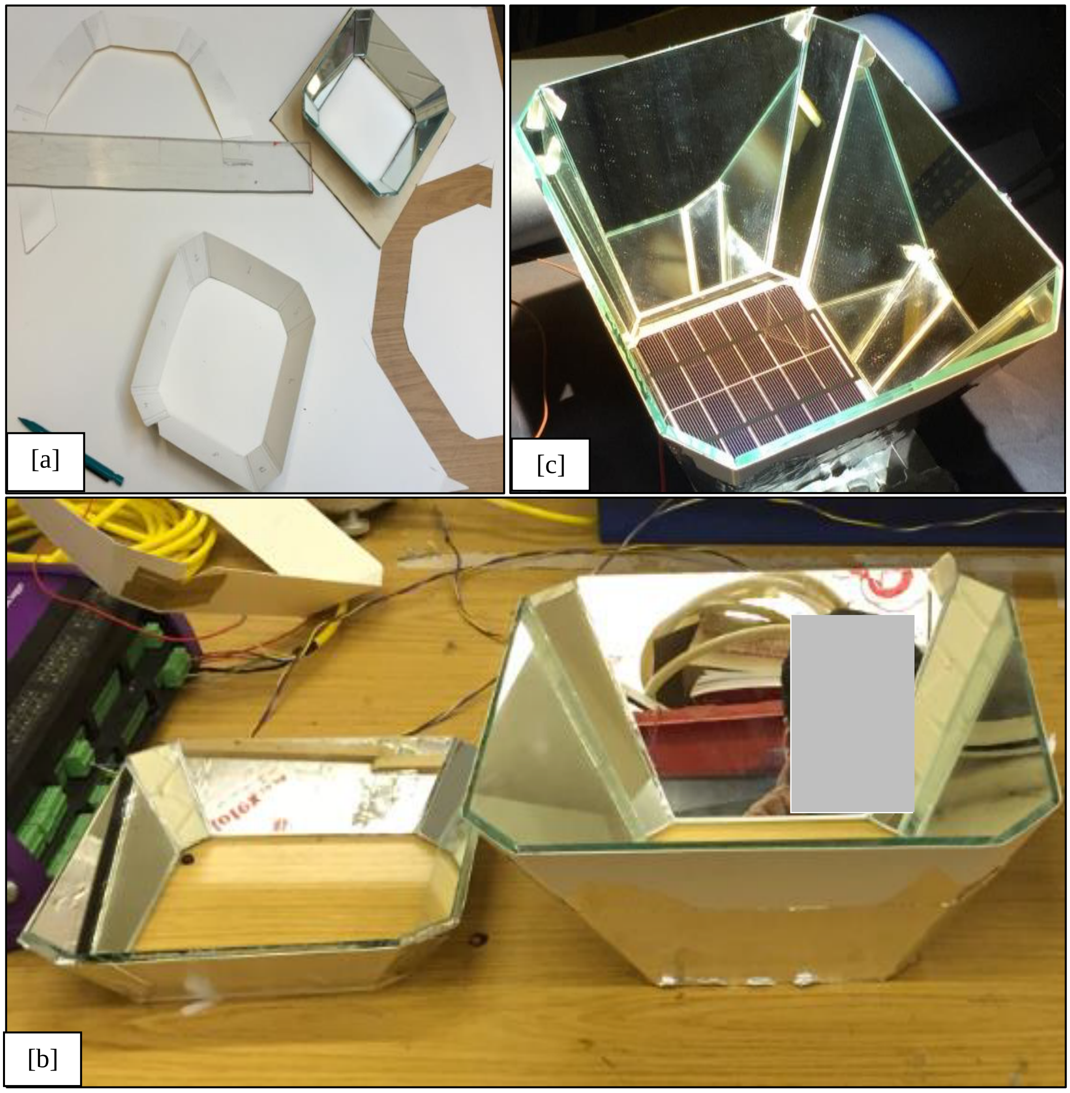

Figure 4.32 (a) EGDP methods employed to build the 3D-PSPCV frame and support (b) Experimental model of 3D-PSCPV built with mirrors; (c) PV module jointed with 3D-PSCPV receiver

4.5.3 3D-PSCPV reflector materials

The reflector materials used in this research include; a polished stainless steel sheet with reflectivity of 60%, polished aluminium with reflectivity of 90% and glass mirrors with reflectivities of 70 and 80% as described in Table **4.4**. The stainless steel and aluminium sheets were cut utilising a Programmable Electric Guillotine (PEG) device at the department of mechanical engineering, University of Birmingham. As for the glass mirror, it was slitted utilising a diamond point glass cutter. The glass mirrors' surface reflectivity was measured at KISR using the Cary-100 UV-Vis spectrometer. The polished stainless steel sheet reflectivity was measured at the University of Exeter, UK using a PerkinElmer UV–Vis spectrometer. While, the aluminium sheet reflectivity data was provided by the manufacturer as shown in Figure **4.33**.

Table 4.4 Characteristics of the 3D-PSCPV.

Concentration ratio	2	4	6
Area of entrance aperture	0.03092 m^2	0.06215 m^2	0.09276m^2
Area of receiver aperture	0.01553m^2	0.01553m^2	0.01553m^2
Depth of the concentrator	45mm	145mm	250mm
Reflectivity	60,70,80,90	60,70,80,90	60,70,80,90

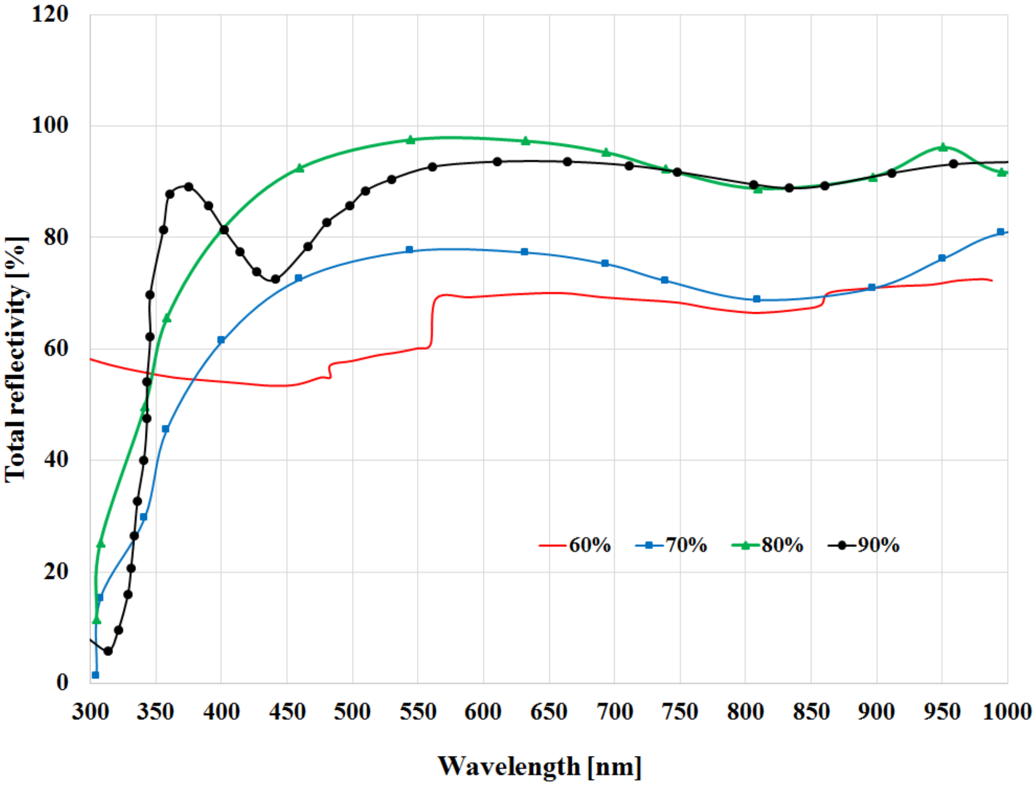

Figure 4.33 Reflectivity measurements for the 3D-PSCPV side reflectors.

4.6 Summary

A ray tracing model was developed and investigated at different geometric configurations of the 3D-PSCPV employing (OptisWorks^{TM}). The simulation has been applied to optimise the geometry of the 3D-PSCPV including the area of the entrance aperture, the concentrator's height, the surface reflectivity in terms of the geometric concentration ratio and optical efficiency. It has been observed that the concentrators with 2 and 4 concentration ratios have uniform optical irradiance distribution and high optical efficiency and the concentrator with a 6 concentration ratio has less uniform irradiance distribution and low optical efficiency. The actual optical concentration ratio is higher for the concentration ratio of the 6 concentrator with (3.9X) compared to the concentration ratios of the 2 and 4 concentrator with (1.9X and 3.4X), respectively. The dusty 3D-PSCPV geometric concentration ratios of 2, 4 and 6 obtained highest actual optical concentration ratios of 1.7X, 3.08X and 3.5X, respectively.

The geometrical characteristics impact of the 3D-PSCPV on the optical irradiance distribution uniformity was analysed in clean and dusty conditions to reveal that the higher the reflectivity the more uniform the optical irradiance distribution. Also, the 3D-PSCPV simulation results reveal that the higher the G_{CR} the lower is the optical efficiency.

CHAPTER 5

Electrical and Thermal Modelling

5.1 Introduction

In this chapter a details investigation of the 3D-PSCPV system electrical and thermal performance using single-diode circuit model and COMSOL Multiphysics modelling software, respectively. A mathematical model was developed to generate an I/V and P/V curves for the 3D-PSCPV receiver (PV module) in order to predict the electrical performance with various surface reflectivity and concentration ratios. For the thermal model, the 3D-PSCPV system integrated with aluminium water cooling channels was simulated with various cooling water velocity sets and PV operating temperatures. The design of the cooling channels were investigated based on the average module operating temperature and temperature distribution as well as inlet water velocity and temperature to determine the effect of active water cooling on 3D-PSCV performance.

5.2 3D-PSCPV electrical modelling

Electrical modelling of the designed 3D-PSCPV system was carried out to calculate the power, current and voltage outputs of the receiver at different irradiance and module temperature. The electrical outputs of concentrated PV module are simulated utilising the single-diode circuit model introduced in chapter 2 and the equations 2.1-2.12 were solved using Engineering Equation Solver Software (EES). The developed program code is shown in Appendix B. Equations 2.1-2.12 were used to model the current and voltage (I/V) and power and voltage (P/V) characteristics under clean and dusty conditions. The simulation has been performed for polycrystalline PV module with maximum power output of 1.4W, total of 18 PV cells and 2 parallel strings of 9 PV cells connected in series. The PV module technical data are listed in Table **5.1**.

Table 5.1 the 3D-PSCPV receiver (PV module) data information

Specifications	**values**
Power output	1.4W
Maximum voltage	8.415V
Maximum current	0.168A
Open-circuit voltage	10.065 V
Short-circuit current	0.180 A
Efficiency	18%
Temperature coefficients of I_{sc}	0.0001/°K
Temperature coefficients of V_{oc}	-0.0035/°K
Number of cells	18
Cell area	5.2 mm^2
Cell Thickness	0.3mm
Module area	15625mm^2
Module thickness	3mm

The electrical model simulation for the 3D-PSCPV assumes the following;

- The input solar radiation is assumed constant in the simulation
- The temperature of PV module was determined based on the average experimentally measured temperature.
- Model does not include bus-bars and grid lines [151-154].

5.2.1 PV module electrical modelling results:

Figure **5.1** and Figure **5.2** show the predicated I/V and P/V characteristics of the PV module under both clean and dusty condition at different irradiance levels and ambient temperature of 25 °C. Simulation results show that dust accumulation has a significant impact on short-circuit current output at all levels of irradiance. The drop in short-circuit current lead to decreasing the maximum power by up to 30%. The dusty module constantly produced a lower current output than clean module. This decrease in the current output increased as the irradiance increased from 26% at 400 W/m^2 to 28% at 1000 W/m^2. Similar reduction was reported in published studies [37, 106, 155] and in chapter 3.

It can be observed that dust accumulation does not have a considerable impact on the open-circuit voltage of the PV module at module temperature of 25 °C. The open circuit-voltage of the dusty module is marginally smaller than the clean module. The dusty module voltage was reduced by around 4% compared to the clean module at all irradiances levels. This is in agreements with results reported by [26, 47, 133, 156, 157].

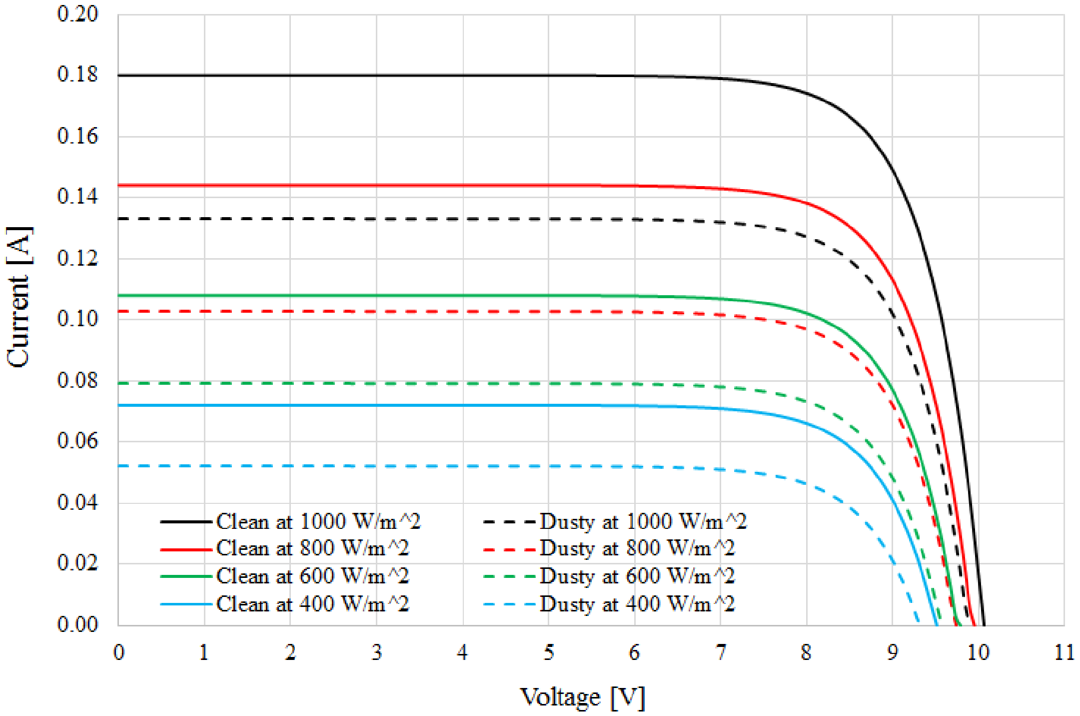

Figure 5.1 I/V curve of the clean and dusty PV modules at various irradiance and module temperature (non-concentrated condition)

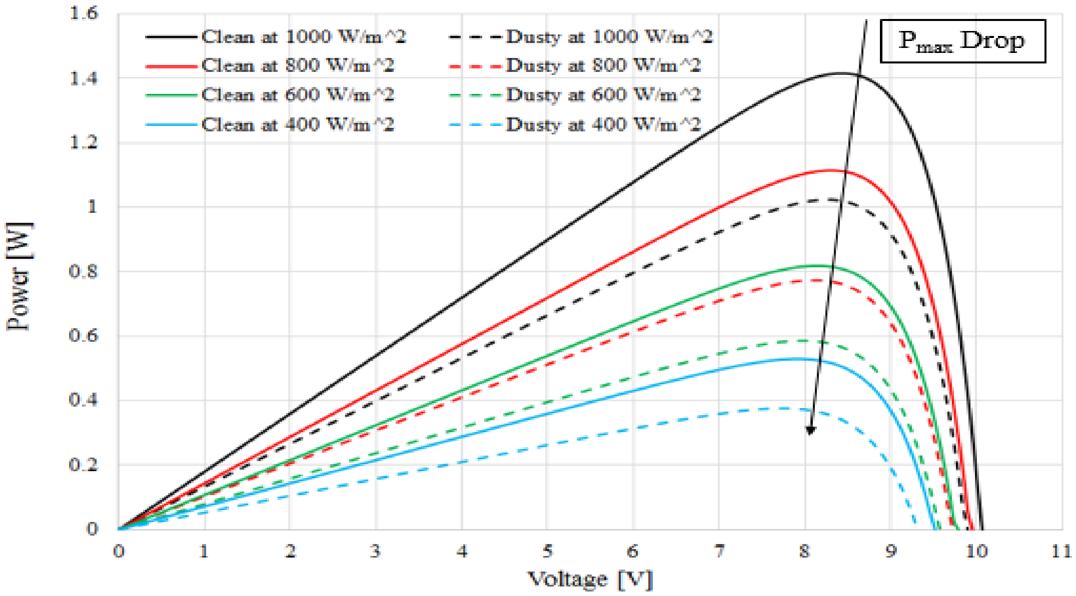

Figure 5.2 Power characteristics of the clean and dusty non-concentrated PV modules at 1000, 800, 600, 400 irradiance and 25C module temperature

5.3 Thermal modelling

The PV module temperature is important parameter that affects the output power generated by the PV module, therefore it is important to assess the temperature variation of the PV integrated with solar concentrators. Determining the temperature distribution provides an overview of the cooling rate needed for the 3D-PSCPV system. The thermal characteristics of 3D-PSPCV receiver in dusty condition are modelled using the COMSOL Multiphysics software. The simulation was carried out with the received irradiance by the 3D-PSCPVsystem in dusty condition, as predicted by the ray tracing model presented in chapter 4. The predicated concentrated irradiance on the PV module takes into account the received irradiance distribution by the dusty concentrator at different concertation ratios and surface reflectivities.

5.3.1 Cooling system geometry

Figure **5.3** shows 3D diagram of the 3D-PSCPV with cooling system. The PV module assembly placed between the concentrator and the water cooling channel. The cooling system consists of a set of parallel aluminium channels attached to the rear side of the PV module (solar concentrator receiver) in which water at a pre-set inlet temperature will pass and remove the heat from the PV module.

9 aluminium rectangular channels with 20mm width, 140mm length, 10mm height and 2mm wall thickenss were used to form the cooling channels to fully cover the bottom surface of the PV module. In addition, 2 aluminium rectangular channels were used for the coolant inlet and outlet flow with following sizes: 20mm width, 150mm length and 20mm height. Figure **5.4** shows the cooling channels configuration and dimensions, while Figure **5.5** shows the PV module and the cooling channel assembly. The computed hydraulic diameter of the cooling channels is 1.8×10^{-2}m.

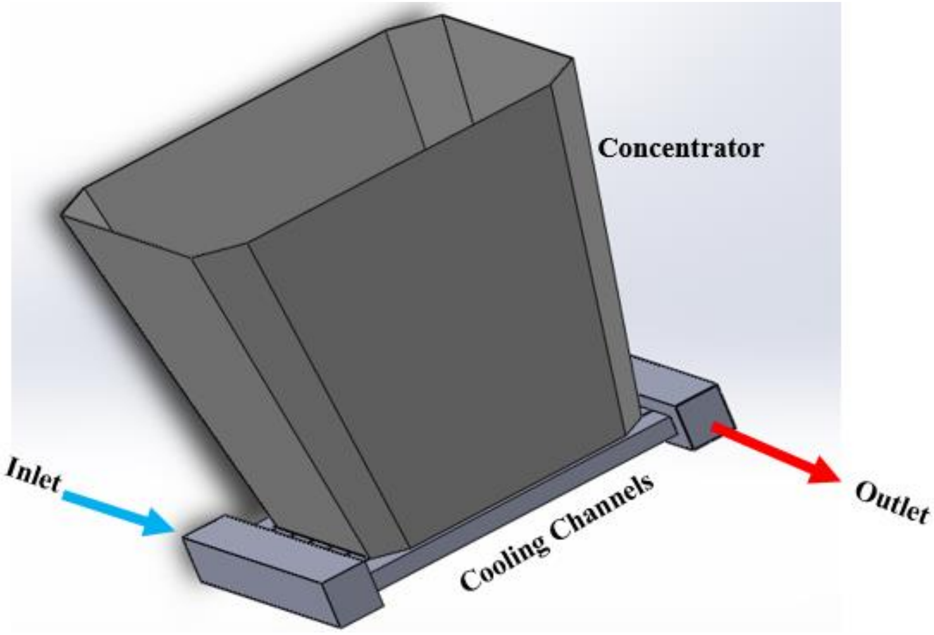

Figure 5.3 3D-CAD drawing of the 3D-PSCPV with cooling channels

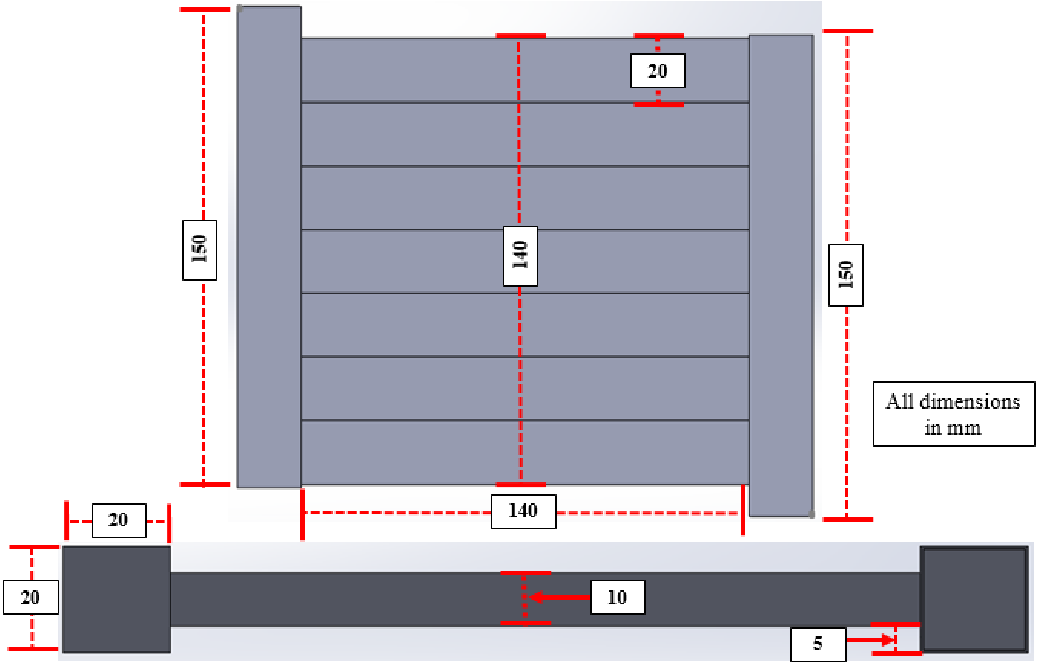

Figure 5.4 3D-PSCPV Cooling channels geometry obtained from Solidworks^{TM}

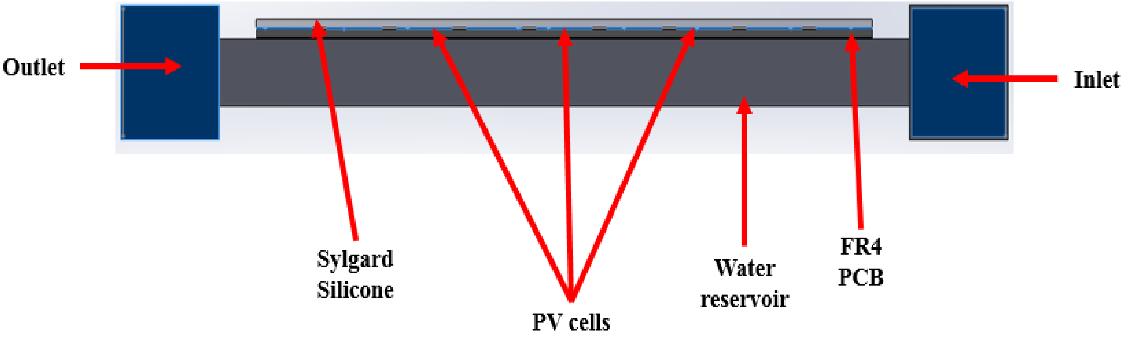

Figure 5.5 PV module assembly placed at the cooling channels

5.3.2 Thermal modelling governing equations

Some of the solar radiation energy falling on the 3D-PSCPV receiver is used to produce electricity by the PV module and the rest is transformed into thermal energy. Solar energy that is transformed into thermal energy ($Q_{thermal}$) can be expressed as [158]:

$$Q_{thermal} = CR_{solar} \cdot [1 - \eta_{electrical}] \tag{6.1}$$

where (CR_{solar}) is concentrated solar radiation received by the PV module planes. The PV module electrical efficiency, ($\eta_{electrcial}$), is expressed in equation 6.2 as a function of its efficiency (η_{Tref}) at reference temperature (T_{ref}), the PV module temperature (T_{module}), and the PV module thermal coefficient (β_{ref}) [158].

$$\eta_{electrical} = \eta_{T_{ref}}[1 - \beta_{ref}(T_{module} - T_{ref})] \tag{6.2}$$

Where (η_{Tref}) is the PV module efficiency at reference conditions (solar radiation =1000 W/m^2, $T_{ref} = 25°C$), and (β_{ref}) is the thermal coefficient of PV module with value of 0.048%.

In every iteration during this thermal modelling, the PV module electrical efficiency ($\eta_{electrical}$), is computed using equation 6.2 and inputted in equation 6.1 to determine the ($Q_{thermal}$) which in turn used to determine the module operating temperature.

There are different modes of heat transfer occurring in this 3D-PSCPV system; these modes are conduction, convection and radiation. Heat is transferred through the PV module and its assembly via conduction and then transferred from the PV module boundaries to the atmosphere and the cooling channels via free and forced convection, respectively. In addition, heat is transferred from the PV module top surface in the form of radiation (known as long-wave radiation) [159].

Steady state heat conduction between the PV module and the upper plane of the aluminium cooling channels system is expressed through equation 6.3 below.

$$\nabla \cdot (k\nabla T) = 0 \tag{6.3}$$

$$Q_{cond} = -k \cdot A \cdot \frac{dT}{dx}$$

(Q_{cond}) is the rate of heat transfer by conduction in (W), (A) is the heat transfer surface area in (m^2). k is The thermal conductivity of the medium in (W/m.K) and the term dT/dx is the temperature gradient that is the rate of change of temperature per unit length of path. The rate of heat transfer as a result of convection from both upper and lower planes of PV module construction is expressed in equation (6.4) [160-162]

$$Q_{conv} = A \cdot h \cdot \Delta T \tag{6.4}$$

Where, (Q_{conv}) is the rate of heat transfer by convection in (W), (h) is the heat transfer coefficient by convection in (W/m^2.K) and (ΔT) is the temperature difference between the PV surface and fluid expressed in (K).

The heat transfer to the atmosphere caused by radiation is expressed through equation (6.5) [160-162]

$$Q_{rad} = A \cdot \sigma \cdot \varepsilon \cdot [T_{surf}^4 - T_{amb}^4] \tag{6.5}$$

Where, (Q_{rad}) the rate of heat transfer by radiation in (W), A is surface area of the PV module (m^2), σ is Stefan–Boltzmann constant and ε is the PV module surface emissivity. The ambient temperature is termed as T_{amb} (K) and T_{surf} is the surface temperature (K).

For fluid flow in the cooling channel the Navier–Stokes equation of mass, momentum and energy conversation described in equations (6.6), (6.7) and (6.8), respectively [158] were used.

$$\nabla \cdot (\rho u) = 0 \tag{6.6}$$

$$\rho u \cdot \nabla u = -\nabla p + \nabla \cdot \nabla\left(\mu(\nabla u + (\nabla u)^T)\right) \tag{6.7}$$

$$E_{total} = \rho u E_{int} - k\nabla T + Q_{rad} - \sigma u \tag{6.8}$$

where (σu) is the convective stress-energy and (E_{int}) is the total internal-energy [163]. The energy balance equation transforms to the equation below (6.9):

$$\int_{\partial\Omega} E_{total} \cdot n dS = \int_{\Omega} Q_{ext} \, dV \tag{6.9}$$

The expression on the left side characterises the rate of the total net energy and the expression on the right side characterises the total heat source. The heat conduction and heat convection equations are similarly determined for the heat transfer in the coolant as expressed in equation (6.10) [159-162, 164].

$$\rho C_P u \cdot \nabla T = \nabla \cdot (k \nabla T) \tag{6.10}$$

For this simulation study, the flow in the channels can be characterised as laminar or turbulent by the Reynolds number determined by equation (6.11) [164]:

$$Re = \frac{U_{water} D_h}{\upsilon} \tag{6.11}$$

Where, (D_h) is the hydraulic diameter and (U_{water}) is the inlet water velocity and (υ) is kinematic viscosity of the water. In this cooling system the flow velocity values utilised generate laminar flow instead of turbulent flows. For every study case, the flow was calculated to be laminar through verifying that the Reynolds number, (Re), was under 2300. Hence, Conjugate heat transfer physics model with laminar flow setup was selected for this thermal modelling study. Although, turbulent flow is more efficient than laminar flow in heat transfer, laminar flow utilises less power as a result of the pressure drop within the cooling channels and that is less costly than turbulent flow systems [165].

5.3.3 Thermal model setup and assumption

The cooling channels were drown in 3D geometry employing SolidWorks and then imported to COMSOL for thermal modelling. Then, the radiation amount and distribution obtained using OptisWork^{TM} ray-tracing simulation was integrated in COMSOL as heat flux input on the PV module top surface. The following assumptions were used in the thermal modelling:

- The impact of dust accumulation was taken into account based on the received irradiance via the dusty concentrators as obtained from the optical simulation.
- The radiation applied on the PV module is partially used to produce electricity and the remaining is transformed into heat and determined using equations 6.1 and 6.2.
- The inlet water temperature of the cooling channels is presumed to be uniform at 24 ºC and the ambient temperatures is 25°C with wind speed of 1m/s

The materials utilised to model the thermal characteristics of the dusty 3D-PSCV receiver consist of encapsulation layer, silicon, FR4 printed circuit board, aluminium and water as cooling fluid. Moreover, thin layer of silicone thermal paste was placed between the PV module and the cooling channels. The PV cells are considered to be enclosed between epoxy resin material on the top surface and the back sheet is FR4-PCB. The thermo-physical characteristics of 3D-PSCPV with cooling system are given in Table **5.2**. The thermo-physical property of the water is specified to be temperature dependent and actively defined by the software in each step during the simulation.

Table 5.2 Thermophysical properties of the PV module and cooling channels layers

Materials	**Thickness (mm)**	**Density [kg/m^3]**	**Heat capacity [J/kgK]**	**Thermal conductivity [W/mK]**	**Emissivity**
Silicon	0.3	2330	700	130	0.7
Solder	0.1	9000	150	50	-
Encapsulation layer	1.3	1030	1100	0.16	0.8
FR4-PCB	1.6	1900	1369	0.3	-
Thermal paste	0.3	4000	800	10	-
Aluminium	2	2700	900	160	-

5.3.4 Meshing and solver

Three different mesh sensitivity investigations were executed to determine the impact of mesh type on the thermal simulation results and minimise the errors. The densities of the normal, fine and finer meshes are 1762431, 1944278 and 2085956, respectively. Figure **5.6** shows PV module and cooling channels meshed in COMSOL. The physical-controlled fine mesh type was selected for the PV module assembly components, and that includes Epoxy layer, PV cells, thermal paste and FR4-PCB in order to eliminate the errors and warning in the programme as larger size mesh was not running. The normal mesh of the physical-controlled option was selected for the remaining system components (cooling channels, fluid domain), to reduce computational time. Also, the “no slip” boundary conditions were selected to the inner walls of the channels. Figure **5.7** shows the thermal simulation results of the PV module temperature at different meshing type showing that both fine and finer mesh types produced similar results. Therefore fine mesh was used in the thermal simulation of the 3D-PSCPV.

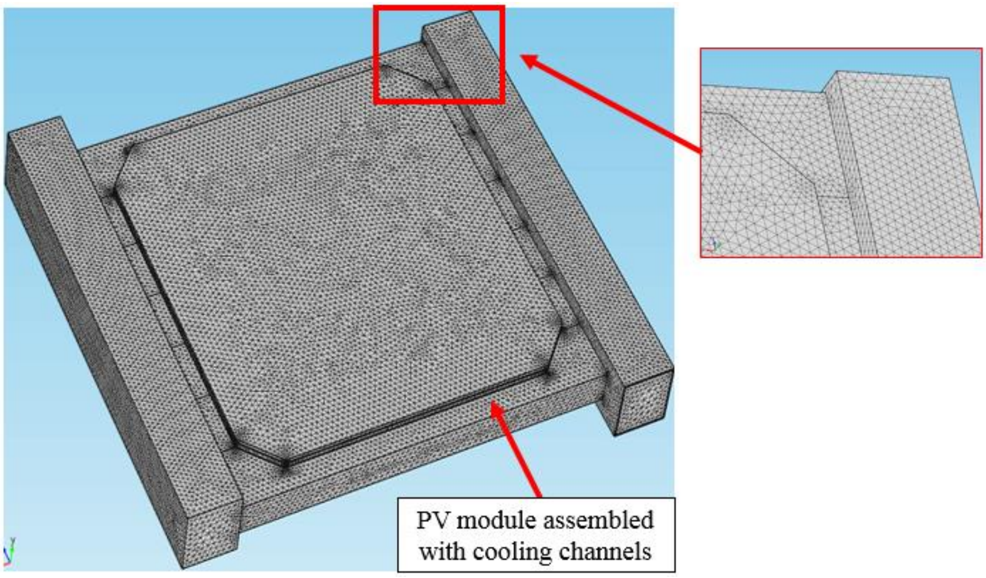

Figure 5.6 COMSOL mesh applied for the thermal simulation of a 3D-PSCPV cooling system

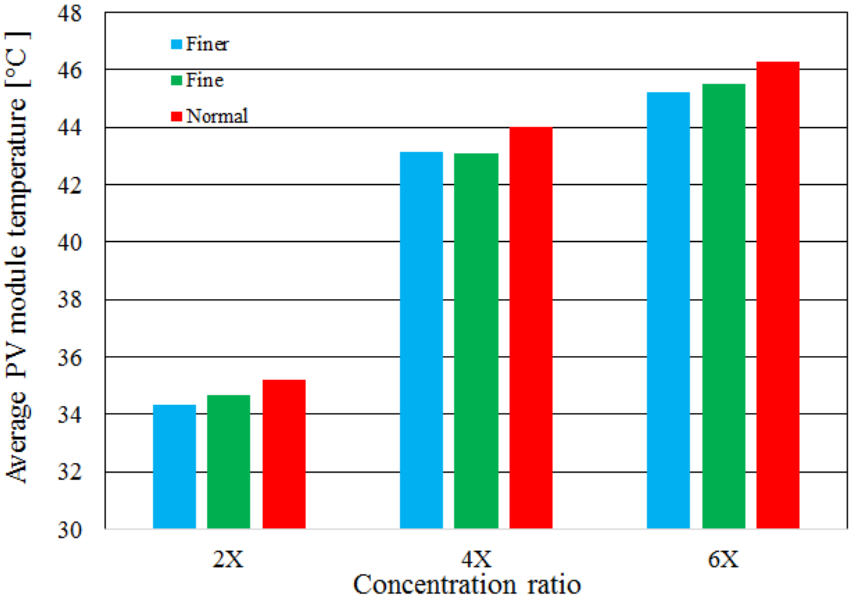

Figure 5.7 Average PV module temperature with different mesh type of the dusty 3D-PSCPV at different concentration ratios (2X, 4X and 6 X)

The model was executed by applying Generalized Minimum Residual (GMRES) solver that uses iterative approach to solve general linear systems. Therefore, with the iterative approach the local error can be estimated with the number of iterations [166]. In this study the relative tolerance was set at 0.0001 to produce more accurate solution, than that with the default value of 0.001. The solution time needed for mesh generation and thermal simulation at various water inlet flows is approximately 5 hours using personal computer with installed memory of 16GB, CPU at 3.40GHz and COREi7 Intel system.

5.4 Thermal and electrical modelling results

Figure **5.8** shows the temperature distribution on PV module surface obtained by COMSOL without cooling. This heat or temperature distribution shows similar pattern of the irradiance distribution which firstly achieved by ray-tracing simulation in chapter 4 (see Figure **4.22**Figure **4.23**Figure **4.24**). The conjugate heat transfer model was applied to solve the governing equations of heat conduction, convection and radiation.

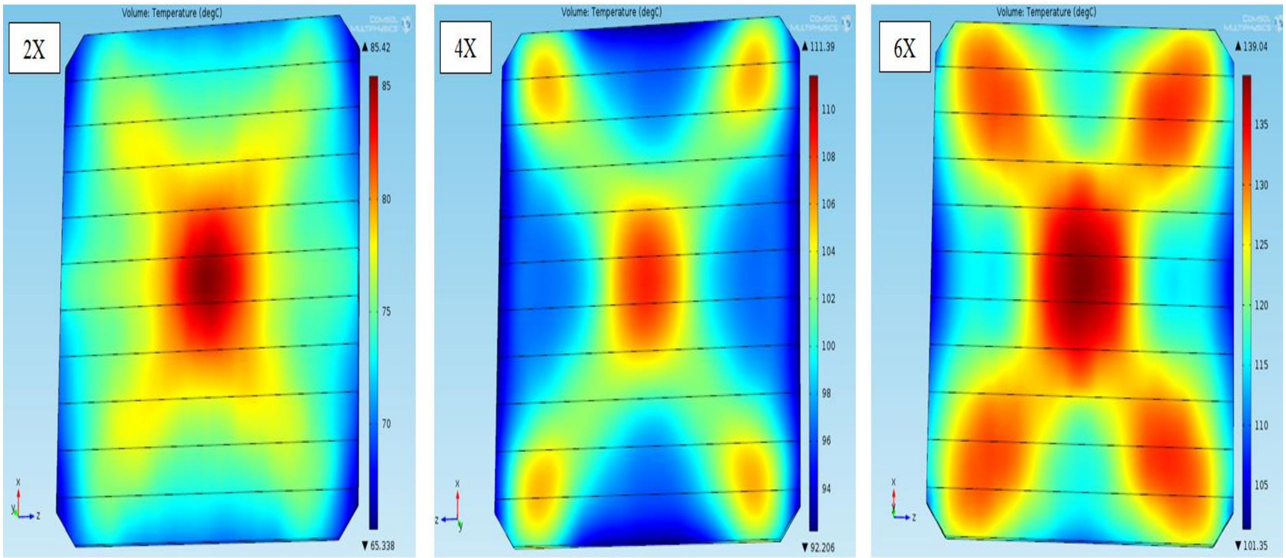

Figure 5.8 Temperature profile on PV module surface obtained by COMSOL at different concentration ratios in dusty condition.

The standard operating temperature of the crystalline PV module is 25°C [164], and that has to be sustained at various ambient temperatures and various solar concentrations. In the simulation, the water inlet temperature was assumed uniform at 24°C and the ambient temperature is 25°C while the inlet water velocity was varied from 0.0011 to 0.037 m/s.

Figure **5.9** shows the water velocity profile in the cooling channels at maximum inlet velocity, showing laminar flow profile. Figure **5.10** and Figure **5.11** show respectively the temperature distribution of the cooling water in the channels and the PV module temperature distribution at water inlet velocity of 0.018 m/s and concentration ratio of 6X. The coldest part is near the coolant inlet manifold area, while the warmest part is near the outlet manifold area. There is almost uniform temperature distribution and heat extraction process in all of the concentration ratios and this is caused by a uniform velocity profile taking place in the cooling channels.

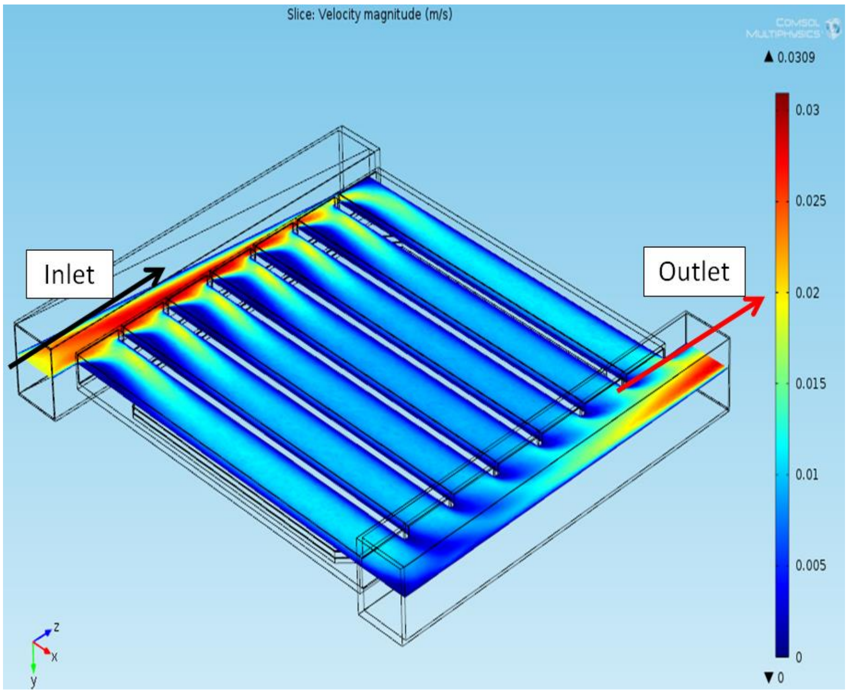

Figure 5.9 Water velocity profile of the cooling channels

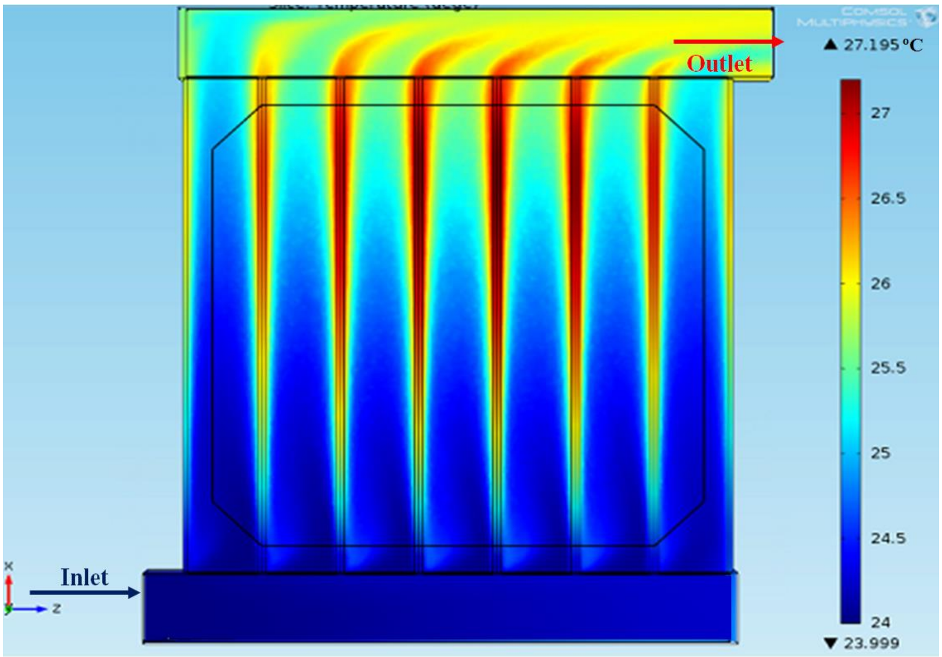

Figure 5.10 3D models of the cooling channels showing heat transfer mechanisms from the inlet to the outlet

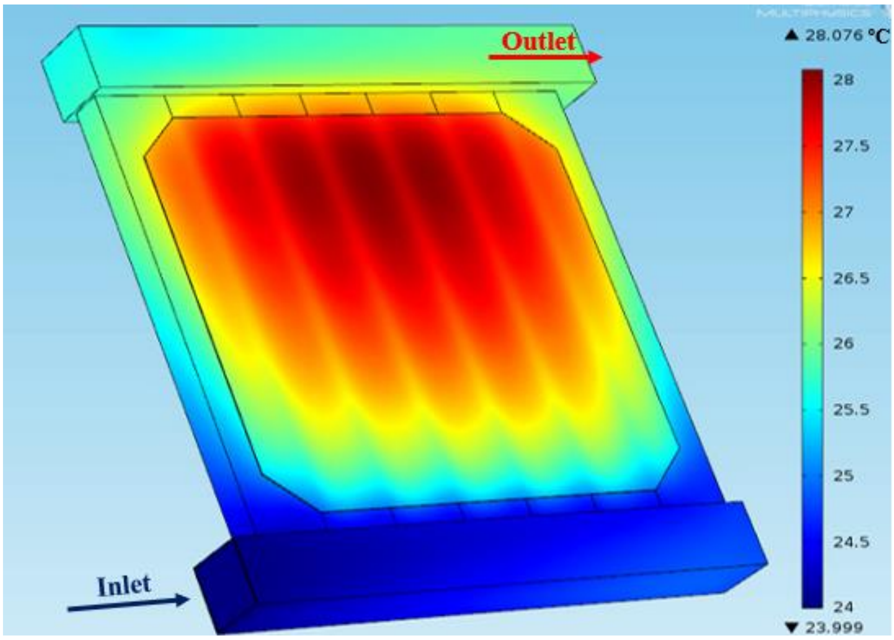

Figure 5.11 Temperature variation in the concentrated PV module with water cooling at velocity of 0.018m/s and concentration ratio of 6X

5.4.1 Effect of cooling on PV module and outlet temperature

The effect of varying the cooling water velocity magnitude at four different concentration ratios of 1X, 2X, 4X and 6X giving flux inputs of 750, 1620, 2920 and 3280 W/m^2, respectively, on the performance of cooling channels were investigated. The water velocity input was varied from 0.0011 to 0.037 m/s with the wind speed was equal to 1 m/s.

The PV module back surface and water outlet temperatures were predicted and the results were presented in Figure **5.12** and Figure **5.13**, respectively. From Figure **5.12**, it can be seen that the higher the inlet water velocity magnitude, the lower is PV module back surface temperature. This is due to the increase in heat transfer with the increase in the velocity magnitude. However the effect is more noticeable at higher velocity magnitude where the PV module back surface temperature decreased to 25.5, 26.5, 28.6 and 29 °C for concentration ratios 1X, 2X, 4X and 6X, respectively. Also the difference in average PV module back surface temperatures at velocity of 0.0011 m/s compared to velocity of 0.037 m/s increased with the increase of concentration ratio from 4°C at 1X to 15°C at 6X.

As the water inlet velocity was increased the outlet water temperature decreased as shown in Figure **5.13**. At an inlet velocity magnitude of 0.0011 m/s the outlet water temperature is approximately 29.27, 33, 41.5 and 44.6 °C for concentration ratios 1X, 2X, 4X and 6X, respectively. While at velocity magnitude of around 0.037 m/s the outlet water temperature decreased to approximately 24.2, 24.4, 24.8 and 24.84 °C for concentration ratios 1X, 2X, 4X and 6X, respectively.

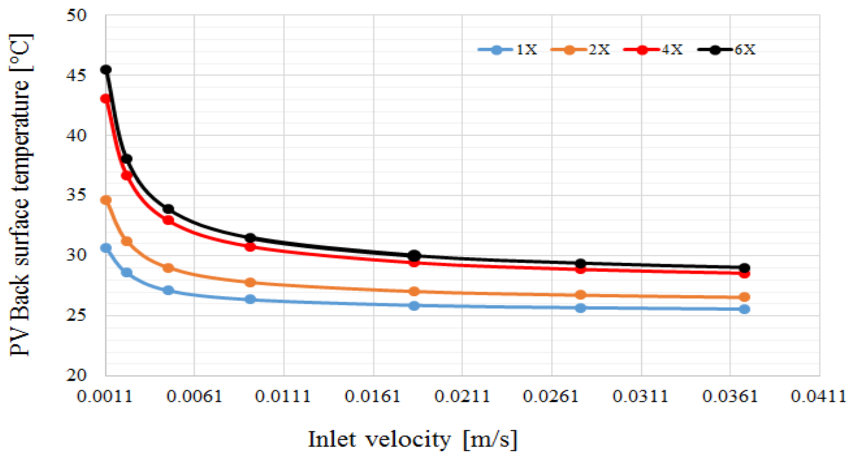

Figure 5.12 Variation of PV module assembly back surface temperatures with water velocity at different concentration ratios

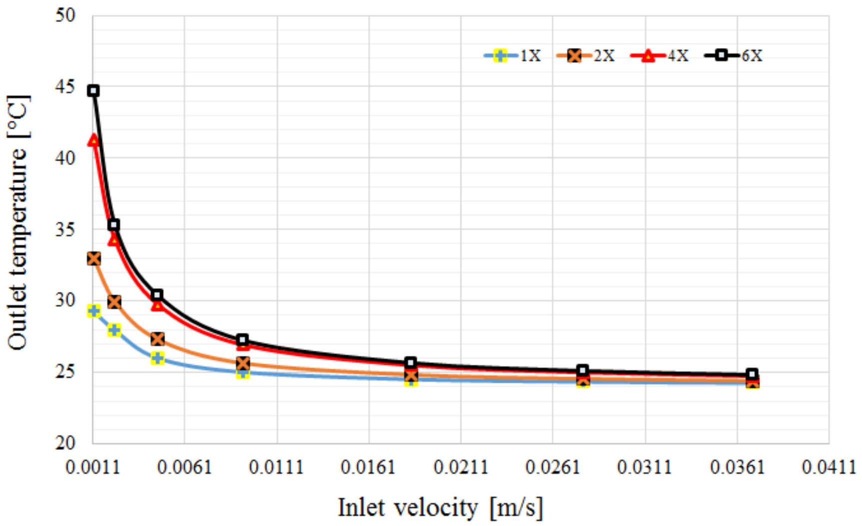

Figure 5.13 Influence of water velocity on the outlet temperature of 3D-PSCPV at different concentration ratios

5.4.2 Effect of cooling on the I_{sc} and V_{oc}

Figure **5.14** shows the open-circuit voltage at various cooling water inlet velocity for concentration ratios of 1X, 2X, 4X and 6X under dusty condition. It can be seen that open-circuit voltage of the actively cooled 3D-PSPCV improved significantly as the velocity magnitude increased under concentration and dusty conditions. It is found that at highest inlet velocity magnitude of 0.037 m/s, the open-circuit voltage increased by 12.3, 23.84, 42.2, 46.2% for concentration ratios of 1X, 2X, 4X and 6X, respectively, compared to the open-circuit voltage of the uncooled dusty 3D-PSCPV.

Figure **5.15** shows the short-circuit current at various cooling water inlet velocity for concentration ratios of 1X, 2X, 4X and 6X under dusty condition. It can be seen that the short-circuit current increases with the increase of concentration ratio but remains relatively constant with insignificant decrease noticed when higher inlet water velocity implemented.

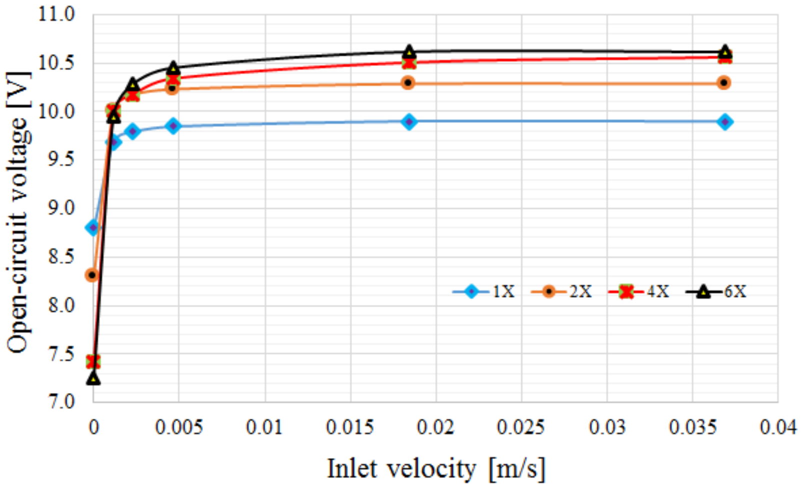

Figure 5.14 Variation of open-circuit voltage with water velocity at different concentration ratios

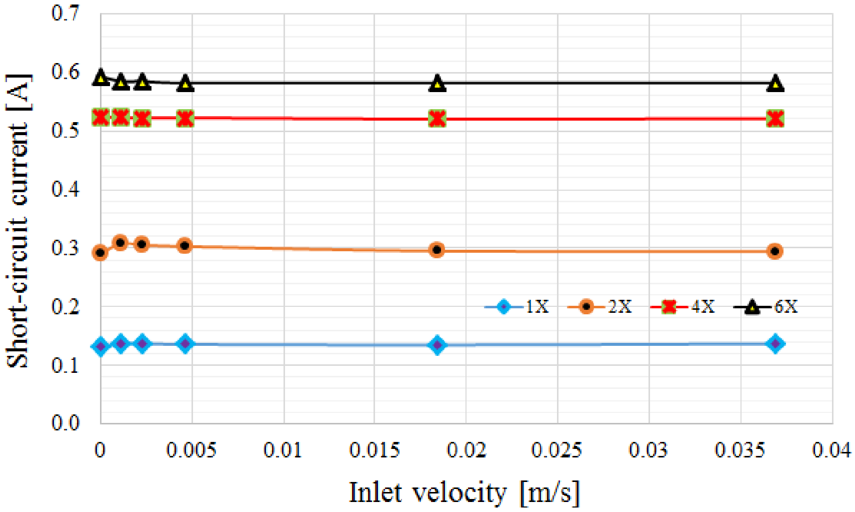

Figure 5.15 Variation of short-circuit current with water velocity at different concentration ratios

5.4.3 Effect of cooling on the maximum power

In order to find the optimum velocity magnitude, the maximum power output from the water cooled 3D-PSCPV receiver (PV module) was computed. Figure **5.16** shows variation of maximum power output and PV module temperature with water velocity magnitudes at different concentration ratios in dusty condition. Figure **5.16** shows that the maximum power output increases as the velocity magnitude of inlet water increases from 0.0011 to 0.037m/s, this increase is due to the decrease in the PV module operating temperature resulted from the increase in the rate of heat transfer to the cooling water [167]. It was observed that the largest increase in maximum power output is achieved at the velocity magnitude of 0.037m/s in all cases of concentration ratios. The 3D-PSCPV module generated up to 1.05, 2.4, 4.3 and 4.8W power output with concentration ratios of 1X, 2X, 4X and 6X, respectively in dusty condition. Thus, there is increase in the PV module performance with the decrease in the PV module temperature. It can be seen from Figure **5.16** that for velocity above 0.005m/s there is no significant effect of water velocity on the power output or PV temperature. Figure **5.17** shows the percentage increase in maximum PV module power output at different concentration ratios and water inlet velocity. The percentage increase of PV module maximum power output with cooling was computed using equation (5.12):

$$\text{percentage increase } (\%) = \frac{P_{with\ cooling} - P_{no\ cooling}}{P_{no\ cooling}} \tag{5.12}$$

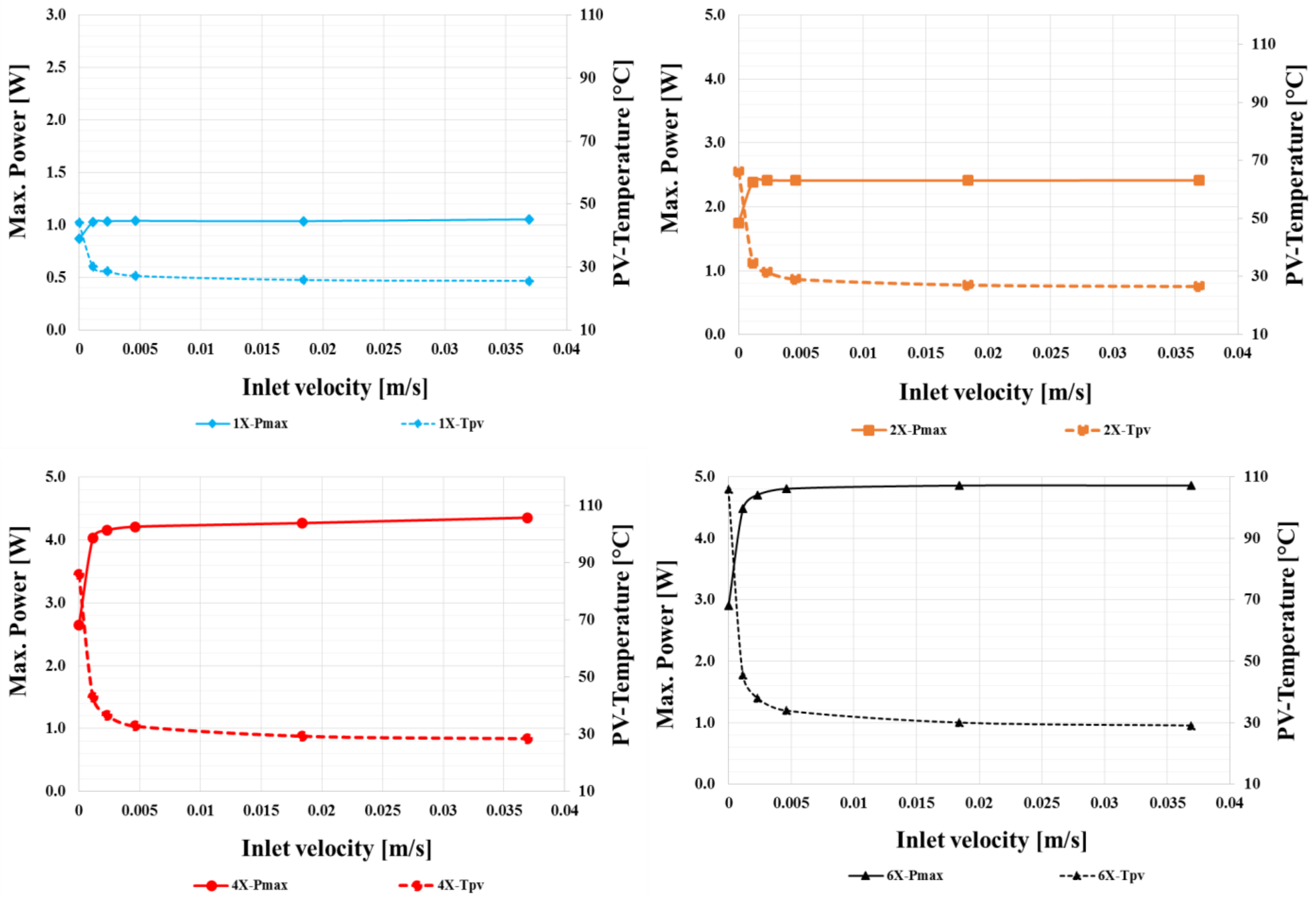

Figure 5.16 Variation of the maximum power output and PV module temperature with water velocity at different concentration ratios

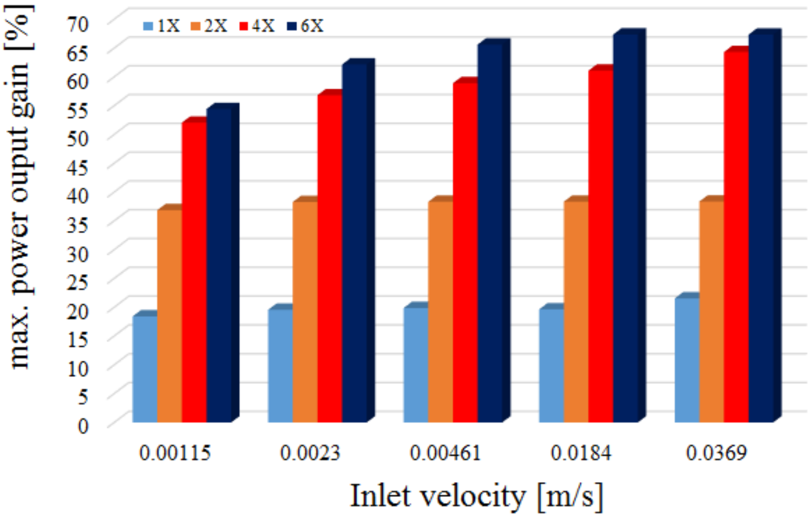

Figure 5.17 Variation of the maximum power output gain with the inlet velocity

5.4.4 Effect of cooling on the electrical efficiency

Figure **5.18** shows the variation of the electrical efficiency for cooling and no cooling cases under dusty and clean system conditions. The highest velocity of 0.037 m/s was used, in order to get the maximum electrical efficiency of the system. There was a significant increase in the maximum value of the electrical efficiency when water cooling was applied with the dusty 3D-PSCPV system.

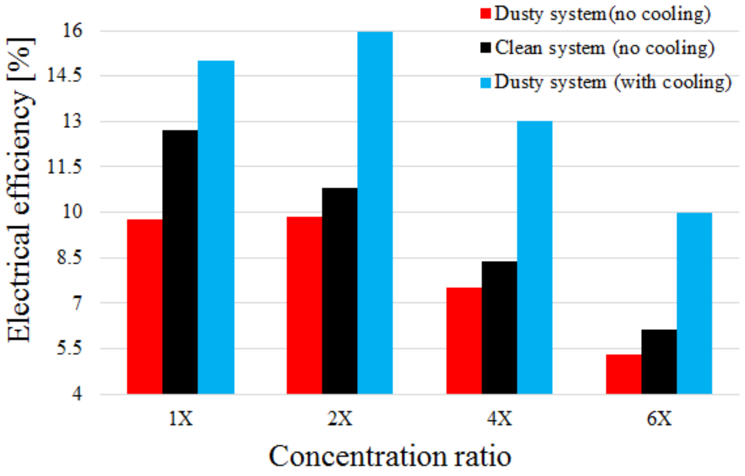

Figure 5.18 Electrical efficiency of the cooled and uncooled dusty 3D-PSCPV compared with clean 3D-PSCPV electrical efficiency at different concentration ratios

There is a maximum improvement of 80% in the electrical efficiency at a concentration ratio of 6X and a minimum improvement of 50% at a concentration ratio of 1X for cooling compared to no cooling conditions respectively. However, 3D-PSCPV with concentration ratio of 2X produced an efficiency close to the STC efficiency of 18% due to the high irradiance and irradiance uniformity. The temperature distribution was shown to have a positive impact on the PV module efficiency [168].

5.53D-PSCPV performance in Kuwait

Based on the studies investigated in previous sections, three different 3D-PSCPVs with the best height, surface reflectivity and optical efficiency were simulated under the weather of Kuwait during summer. Optical, electrical and thermal simulations of 3D-PSCPVs with different optical concentration ratios to predict the performances in term of PV module operating temperature and maximum power output produced with and without cooling. The concentrated irradiance applied on the 3D-PSPCV receiver (PV module) was obtained from the OptisWork^{TM} optical simulation using the concentrator with 90% surface reflectivity. July weather conditions of Kuwait such as solar irradiance, wind speed, ambient temperature, water inlet temperature was used because it has the highest direct irradiance and it is among the dustiest and hottest months of the year.

Direct irradiance of 1040W/m^2, wind speed of 5 m/s, ambient temperature of 45°C (the average temperature during noon in July) and water inlet temperature of 25°C were applied in the electrical and thermal modelling. Using the inlet velocity speed of 0.0037 m/s, the performance of the 3D-PSCPV was assessed based on the PV module power output, electrical efficiency and operating temperature.

5.5.1 3D-PSCPV system optical performance

The percentage losses of the dusty 3D-PSCPV irradiance compared to clean 3D-PSCPV irradiance are determined by equation (5.13).

$$\text{Losses Percentage (\%)} = \frac{\text{Clean}_{\text{Irr}} - \text{Dusty}_{\text{Irr}}}{\text{Clean}_{\text{Irr}}} \times 100 \tag{5.13}$$

Where $\text{Clean}_{\text{Irr}}$ is the amount of concentrated irradiance received by the clean 3D-PSCPV and $\text{Dusty}_{\text{Irr}}$ is the amount of concentrated irradiance received by the dusty 3D-PSCPV.

Figure **5.19** shows the concentrated irradiance losses with the 3D-PSCPV entrance aperture covered with dust at different optical concentration ratios. At direct solar radiation of 1040 W/m^2, 3D-PSCPV with different optical concentration ratios shows less optical losses compared to non-concentrated system. The non-concentrated system shows the highest losses of 27%. As for the 3D-PSCPV, the optical losses ranged from 12% at 2X to 14.2 at 4X to 14.6 at 6X. Thus the CPV system is better suited to the dusty environment of Kuwait than non-CPV systems.

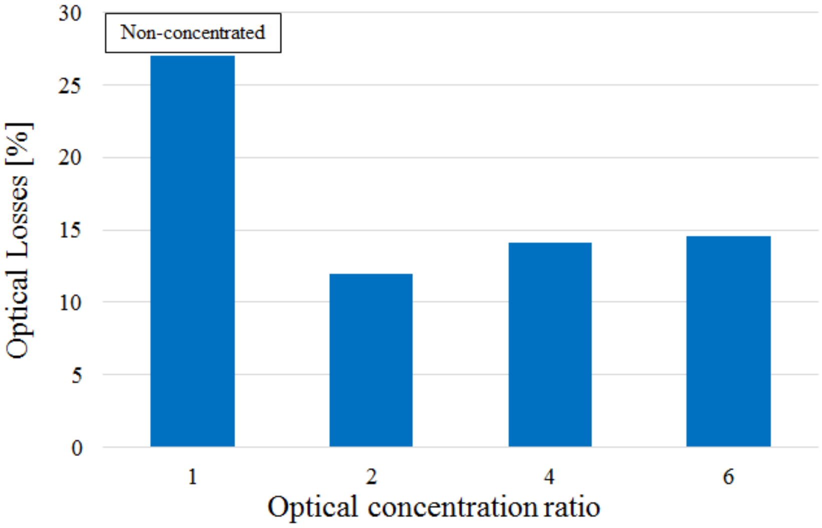

Figure 5.19 Predicted optical losses due to dust accumulation on 3D-PSCPV during July

5.5.2 PV module predicted temperature with different concentration ratios

Figure **5.20** shows the temperature contours of the PV module integrated with cooling channels for the 3D-PSCPV with optical concentration ratio of 6X in dusty condition at water inlet velocity of 0.0037 m/s. It can be seen from (right side picture) in the figure that the temperature variation from PV top surface to the cooling channel with the PV surface temperature increasing from 34°C close to water inlet to 38°C close to the water outlet. Figure **5.21** shows the PV module assembly average operating temperature with and without cooling of the 3D-PSCPV. Once the water cooling was applied, the PV module operating temperature of the clean 3D-PSCPV system dropped by 57.7, 87.05 and 98.8°C at optical concentration ratio of 2X, 4X and 6X ,respectively. While the PV module operating temperature of the dusty 3D- PSCPV system dropped by 53.7, 79.2 and 88°C for optical concentration ratio of 2X, 4X and 6X ,respectively.

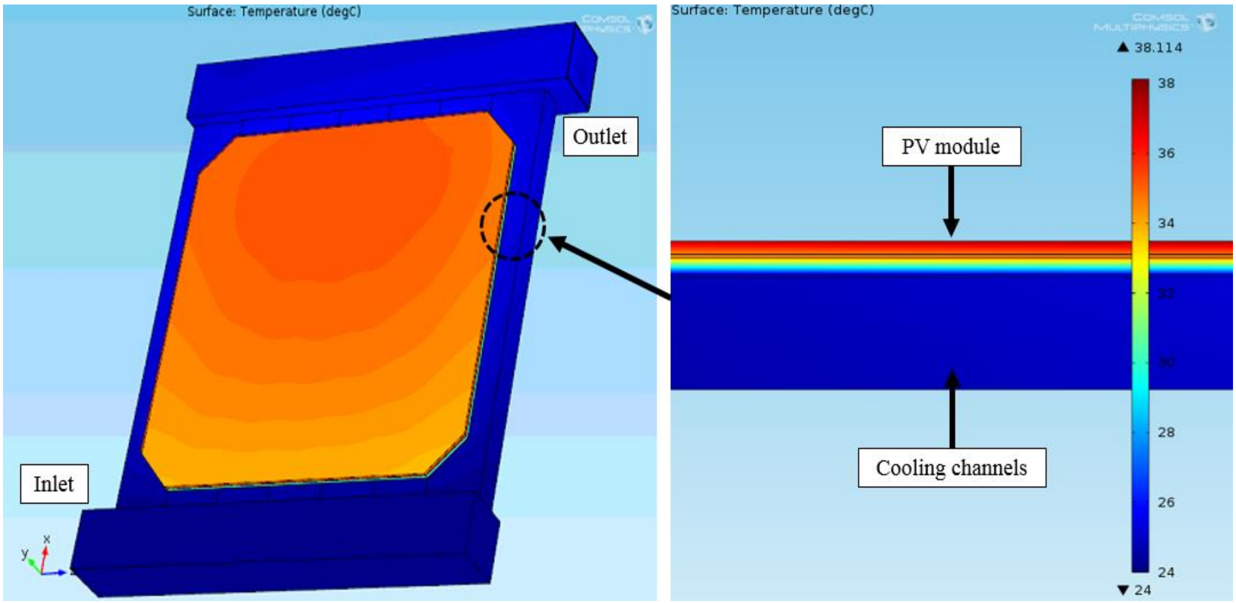

Figure 5.20 Temperature contours of the PV module assembly with cooling channels at concentration ratio of 6X and water velocity pf 0.037m/s

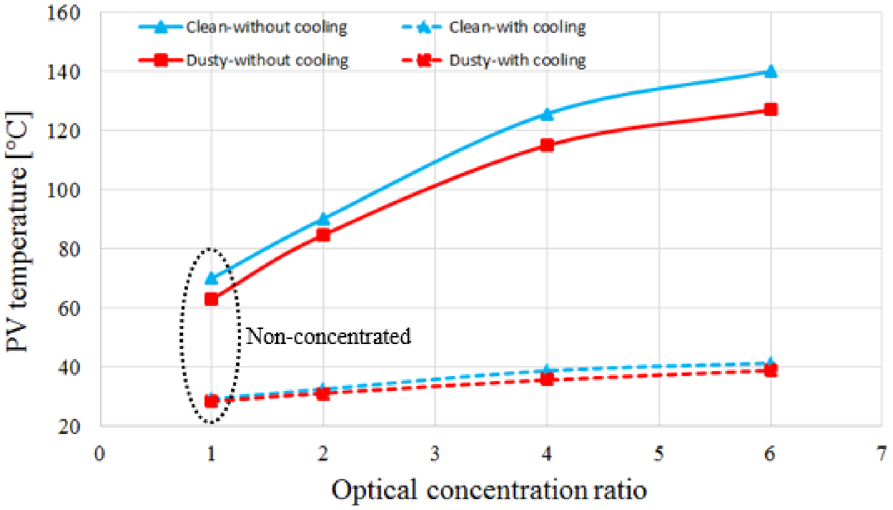

Figure 5.21 Predicted PV module operating temperature of 3D-PSCPV with and without cooling in both conditions clean and dusty during July

5.5.3 Predicted electrical power output at different concentration ratios

Figure **5.22** shows the predicted cooling effect on 3D-PSCPV maximum power output under the two conditions clean and dusty with four different concentration ratios. It can be seen that using water cooling the power output increases, starting around 1.106W with 1X to approximately 5.517W with the increase in the concentration ratio up to 6 under clean conditions. While the maximum power output increases for the dusty 3D-PSCV, starting approximately from 0.8W with 1X to about 4.71W at concentration ratio of 6. This considerable increase in maximum power output at concentration ratio of 2X, 4X and 6X, is due to the low PV operating temperature (Figure **5.21**) which increases the voltage output and therefore increases the power output.

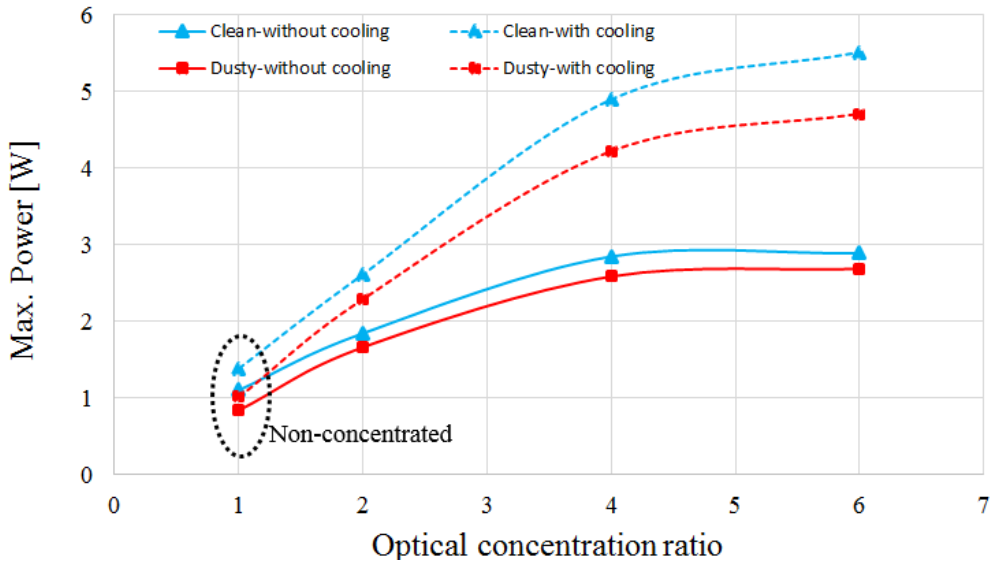

Figure 5.22 Predicted cooling effect on 3D-PSCPV maximum power with different optical concentration ratio

5.5.4 Predicated efficiency at different concentration ratio

Figure **5.23** shows the calculated electrical efficiency of the dusty non-concentrated and concentrated system with water cooling. It can be seen from the figure that the electrical efficiency of the 3D-PSCPV with effect of dust accumulation and cooling was able to reach high electrical efficiency close to the STC with only 4.2, 18.7 and 37.18% difference for optical concentration ratio of 2X, 4X and 6X, respectively. The 3D-PSCPV power losses due to dust accumulation were calculated using the following equation:

$$Power\ losses\ [\%] = \frac{Dusty\ maximum\ power - Clean\ maximum\ power}{Clean\ maximum\ power} \times 100 \tag{5.14}$$

while, The 3D-PSCPV power gain with cooling was calculated using equation (5.12).Figure **5.24** shows the percentage loss and gain of the maximum power output as a result of dust accumulation and active cooling (cooling channels) at direct irradiance level of 1040W/m^2. It can be seen that maximum improvement up to 28, 54 and 68% in maximum power output were achieved by cooling the dusty 3D-PSCPV. While, the maximum power output of the dusty non-concentrated only improved up to 20% by cooling. It can be deduced from the figure that power output gain by cooling overcome the dust accumulation losses for all concentrators.

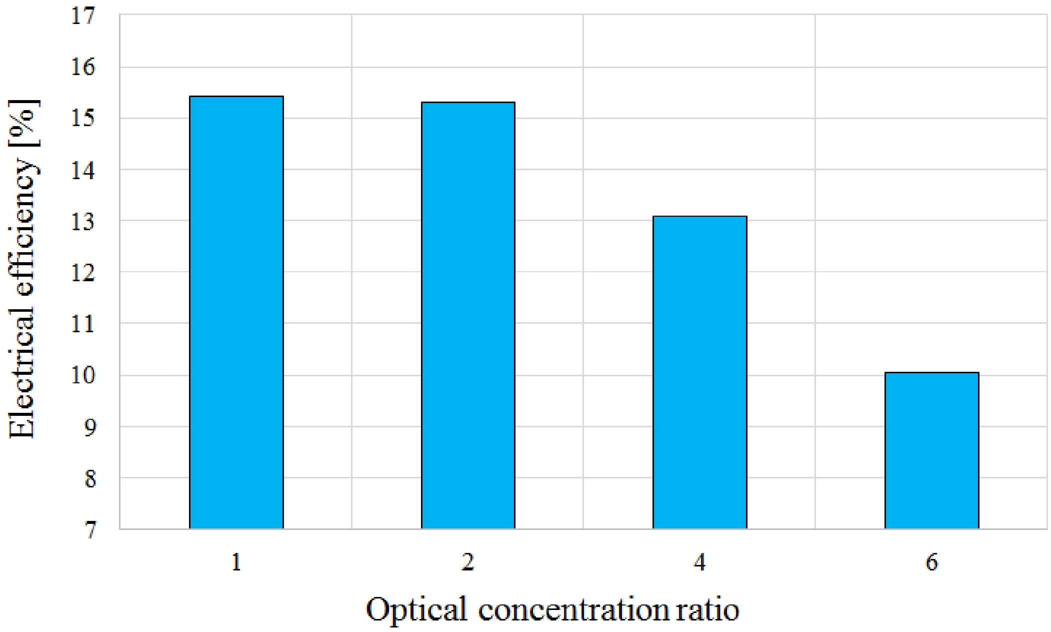

Figure 5.23 Predicted electrical efficiency of the dusty 3D-PSPCV with cooling effect

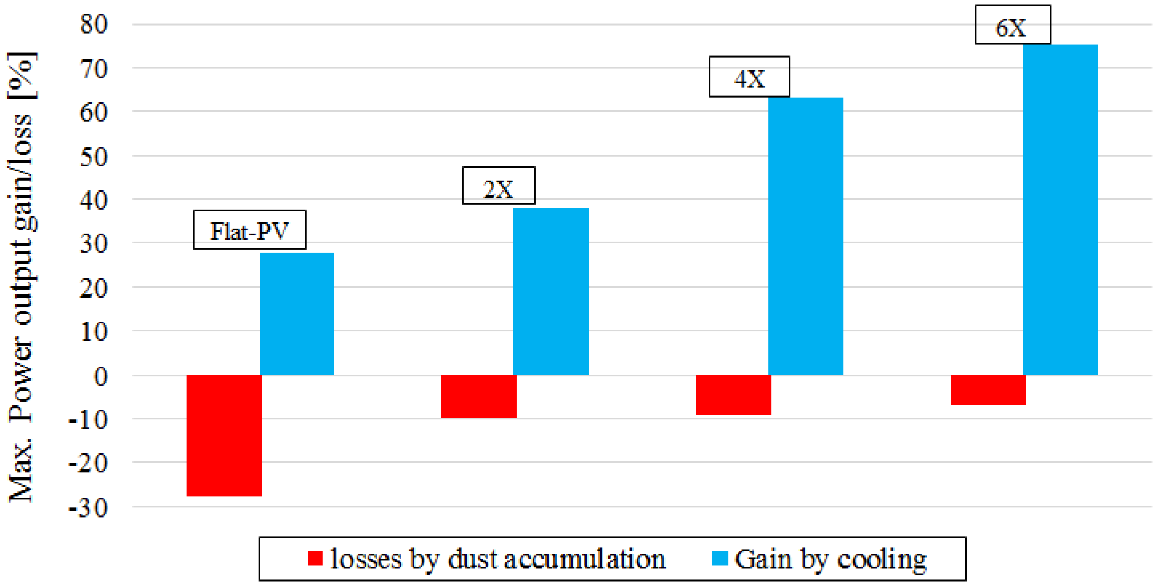

Figure 5.24 Predicted maximum power output losses due to dust accumulation and gain with cooling for the 3D-PSCPV

5.6 Summary

Extensive electrical and thermal simulation studies were carried out to investigate the effect of dust accumulation on the 3D-PSCPV electrical outputs. The electrical modelling shows that the open-circuit voltage was the most affected parameter, due to heat generated by the light concentration. Due to dust accumulation, the short-circuit current was most affected, the impact compared to non-concentrated PV is small. The short-circuit current decreased by 26.25% at 1X (non-concentrated) while, the reductions were 12.65%, 14.65% and 14.71% for concentration ratios of 2X, 4X and 6X, respectively.

Active cooling using water channels in 3D-PSCPV system were introduced for electrical and thermal performance enhancements. COMSOL Multiphysics modelling software was used to investigate the potentials of using cooling with dusty concentrator. Different inlet water velocity and optical concentration ratios are applied to the system. These include varying the concentration ratio of the 3D-PSCV to values of 2X, 4X and 6X, with varying cooling water velocity in the range of 0.0011 to 0.037m/s. Also the effect of cooling on PV module assembly and outlet temperature was investigated. It was concluded that increasing inlet water velocity has a significant effect on reducing PV module temperatures. PV module temperature was reduced to 26°C at all 3D-PSCPV concentration ratios with increasing velocity up to 0.037 m/s.

It had been observed that the electrical performance of the dusty 3D-PSCPV with cooling system is greatly improved compared to without cooling. The maximum power output is 4.85W at concentration ratio of 6X. The 3D-PSCPV system with 2X has reached highest electrical efficiency of about 16% among other systems (1X, 4X and 6X).

CHAPTER 6

CPV Experimental Setup

6.1 Introduction

The experimental setups for indoor and outdoor condition testing are presented in this chapter. The experimental setups were used to study the optical, electrical and thermal performance of the (3D-PSCPV) with concentration ratio values of 2X, 4X, and 6X under clean and dusty condition. The effect of dust accumulation on the concentrator optical efficiency and electrical output of 3D-PSCPV receiver (PV module) with water cooling was investigated by measuring the received irradiance, maximum power output and I/V curve. Detailed description of the experimental setups consist of solar simulator characterisation, dusty glass cover assembly, cooling channels assembly and calibration of measuring devices.

6.2 Solar simulator types

A solar simulator is an instrument that generates a level of spectrum close to that of the sun spectrum. Solar simulators can be classified as: Continuous (steady state) and Flashing (unsteady state). A continuous solar simulator offers a fixed irradiance on the test area for the required time period with intensity of radiation reaching up to 1000 W/m^2. The continuous solar simulator is preferable for slow spectral response solar cells and has the following advantages [169-172]:

- Utilising I/V tracer sweeps measurements to determine shunt resistance and series resistance in the circuit of module and solar cell.

- High and low temperature effects on the PV system can be examined.
- The output voltage and current measurement equipment is less complicated.
- The I/V curve characteristics can be measured over a wide range, and different level of temperature and radiation.

The main disadvantages of continuous solar simulators are:

- The light bulb life span is short.
- The needs for regular maintenance.
- Large power consumption as a result of the continuous light source.

Flashing solar simulators supply radiation intensity in a very short time, commonly in the range of one millisecond. Since the flash coming from the light source is for a short period, the electric power consumption of this form of solar simulator is smaller compared to a continuous solar simulator. The Flashing solar simulator main advantages are:

- Using xenon arc lamps across a 200mm × 200mm illuminated region and ±1% uniformity can be achieved.
- The thermal impact on the tested PV cell /module is minimal.
- A satisfactory spectral match to solar insolation can be achieved.

The main disadvantages of flashing solar simulators are:

- The solar cell has to have a fast reaction comparable to the flashing period.
- High and low temperature effects on PV cell performance cannot be examined.
- Data has to be recorded in a very short time, less than the flashing period [173].

Solar simulators are also categorised based on the standard tolerance for the four characteristics of their performances; light spectral match, temporal instability, non-uniformity and collimation angle [174]. The specifications are established by special international standardisation group in solar energy for instance Japanese Industrial Standards

(JIS), The International Electrotechnical Commission (IEC) and the American Society for Testing and Materials (ASTM).

6.3 Continuous solar simulator (light source)

The solar radiation level and other ambient conditions fluctuate frequently under outdoor conditions and are non-controllable. Therefore an indoor solar simulator has been developed at the University of Birmingham to investigate the performance of 3D-PSCPV under controlled condition. Intended for the 3D-PSPVC built for indoor experimental characterisation a maximum illuminated spot size of 350mm × 350mm is needed. The indoor solar simulator consists of a D'Artagnan spotlight with 2500W Metal Halide arc lamp [175] and table with adjustable height mechanism as shown in Figure **6.1** and Figure 6.2. The D'Artagnan spotlight is equipped with focal length and radiant region control switches that can be used to adjust the irradiance level and the size of the illuminated region.

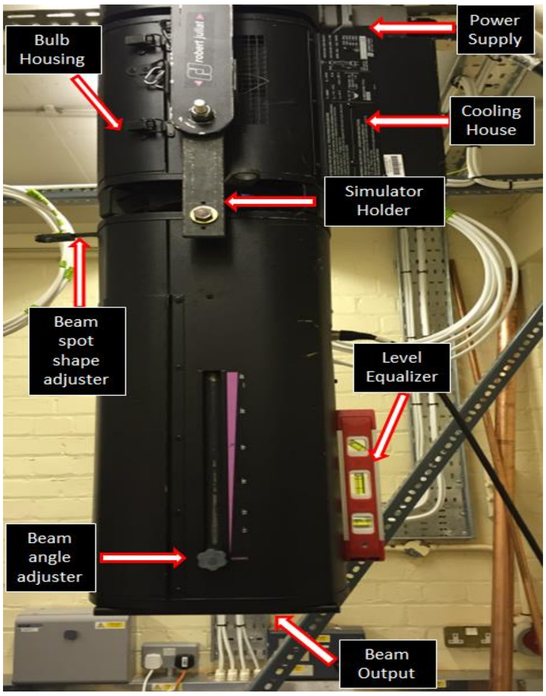

Figure 6.1 The installed continuous solar simulator for the indoor experimental of the 3D-PSCPV [175].

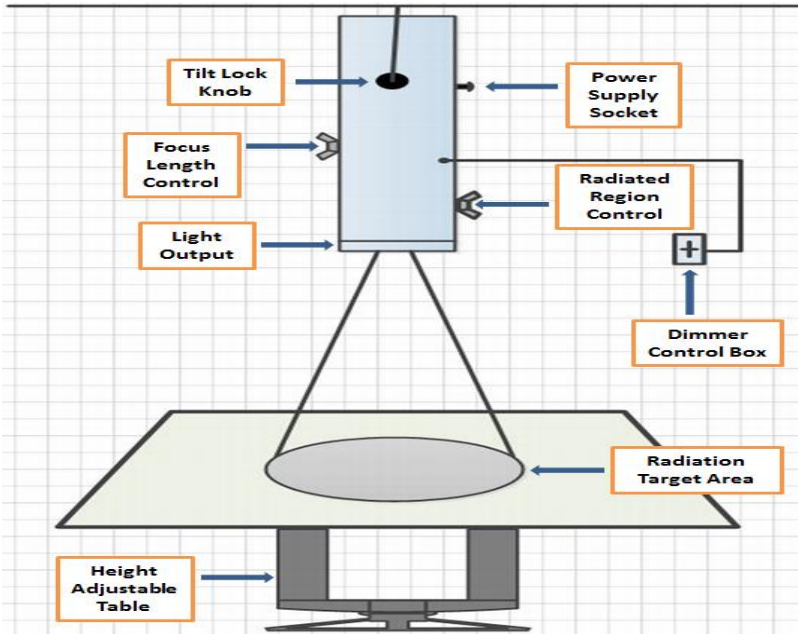

Figure 6.2 Schematic drawing of the solar simulator setup and controls.

6.3.1 Light spectral characteristic

Table **6.1** presents the lamp technical bulb specifications used in the solar simulator [176]. Figure **6.3** compares the spectral distribution for Philips MSR HMI 2500W metal halide lamps utilised in the solar simulator with 1.5 AM standard sun spectral. AM1.5G is selected as the typical spectrum of the sun radiation within the earth atmosphere. Using the rated wattage, the spectral distribution is very close to the sun spectrum.

Table 6.1 General specifications of Philips MSR HMI [176].

Parameter	**Value**
Watts	2500 [W]
Colour temperature	6000 [K]
Colour rendering index (cri)	95 [Ra]
Luminous flux	240000 [lm]
voltage	115 [kV]
Arc gap	127 [mm]
Rated average life	500 [h]

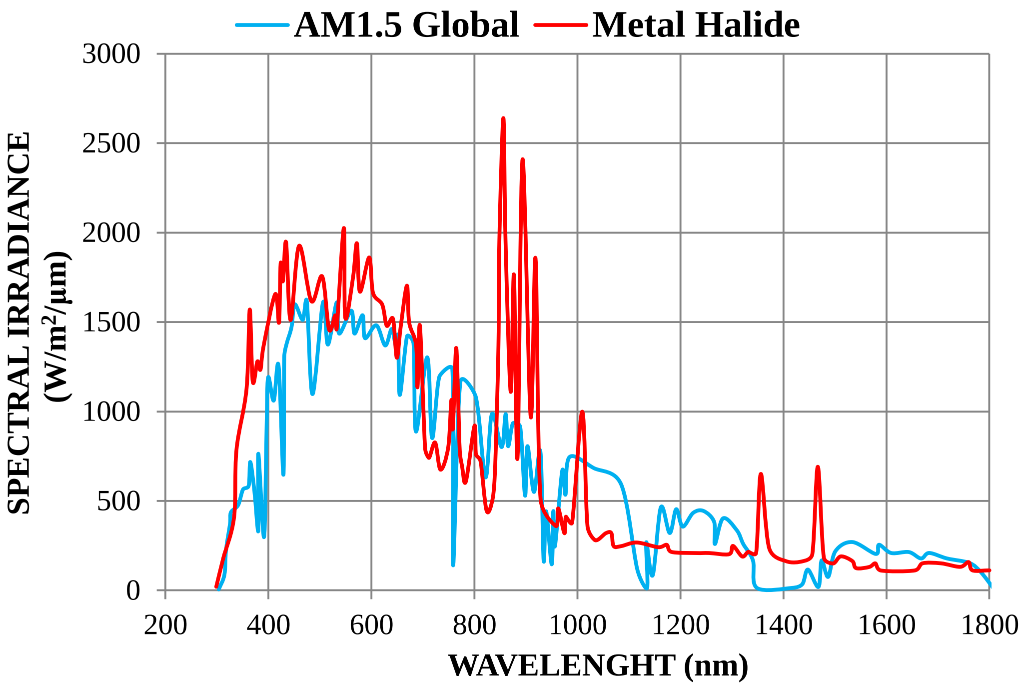

Figure 6.3 The Spectral distributions for MSR HMI 2500 W/GS lamp operated in continuous solar simulator Compared to the sun Spectral distributions [177]

6.3.2 Temporal instability characteristic

Temporal instability is a measure of the capability of the light source from a simulator to remain stable for a period ranging from 1 minute till 1 hour or more. The solar simulator instability can be computed by equation 6.1 [178]:

$$T_{\text{Instability}} = \left[\frac{R_{\max} - R_{\min}}{R_{\max} + R_{\min}}\right] \times 100\% \qquad (6.1)$$

Where R_{max} and R_{min} are the maximum and minimum irradiance recorded in W/m^2 on the selected location at particular time. Table **6.2** presents the standard allowance for the instability percentage as stated in the international standards.

Table 6.2 Temporal instability percentage allowance[179, 180].

Simulator Class	**JIS**	**IEC**	**ASTM**
A	1%	2%	2%
B	3%	5%	5%
C	10%	10%	10%

6.3.3 Irradiance non-uniformity

Irradiance uniform distribution insures that the simulated radiation is beaming uniformly on the surface of target area where the PV /module to be investigated is held. If light does not beam uniformly, it may impact on the current flow in PV cells/modules. The non-uniformity of solar simulator was evaluated using equation 6.2 [178]:

$$\text{Non} - \text{uniformity}\ (\%) = \frac{R_{max} - R_{min}}{R_{max} + R_{min}} \times 100\% \tag{6.2}$$

Rmax and Rmin are the maximum and minimum falling irradiances recorded on the measured surface. The international specifications define the solar simulator class depend on the non-uniformity distribution allowance as presented in Table **6.3**.

Table 6.3 Non-uniformity distribution allowance [179-181]

CLASS	**JIS**	**IEC**	**ASTM**
A	2%	2%	3%
B	3%	5%	5%
C	10%	10%	10%

When testing the non-uniformity, ASTM standard recommended a minimum of 36 mapping positions while IEC recommended 64 mapping positions.

6.3.4 Light rays collimation and integrated lens system

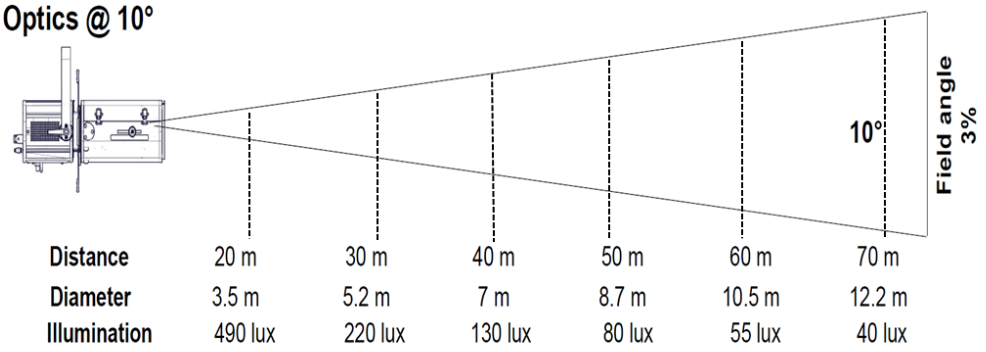

Figure 6.4 Solar simulator Photometric Beam range with MSR lamp[175]

The variation in beamed light with the distance from the middle of the irradiated region for different focal diameter is illustrated in Figure **6.4**. It is clear that the irradiance intensity increases when the irradiated region is reduced. The maximum diameter and irradiance are 12.2m and 2000 W/m^2 based on the given manufacturer data sheet [175].

6.4 Solar simulator characterisation experimental setup

The radiation output was recorded using high sensitivity CMP11 Pyranometer (see Figure **6.5**) manufactured by Kipp&Zenon^{TM} which sends out voltage signal. The pyranometer utilise a wire that is a low noise type specifically fitted to support the low voltage output of the pyranometer. Table **6.4** presents the manufacturer specification of the pyranometer devices used [182].

Table 6.4 The specifications of CMP11 pyranometer[182].

Spectral range	285 to 2800 nm
Sensitivity	7 to 14 µV/W/m^2
Response time	< 5 s
Detector diameter	3cm
Detector type	Thermopile
Directional response (up to 80° with 1000 W/m^2)	< 10 W/m^2
Temperature dependence of sensitivity (-10 °C to +40 °C)	< 1 %
Operational temperature range	-40 °C to +80 °C
Maximum solar irradiance	4000 W/m^2
Field of view	180 °

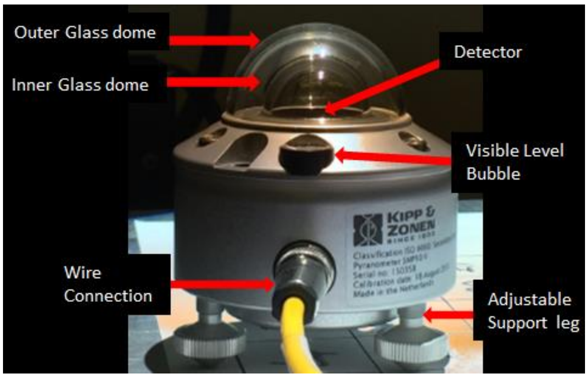

Figure 6.5 Pyranometer used in mapping the testing area.

The pyranometer's transmits signal to the data recorder (DT85) where its sensitivity and accuracy has been specified in the data recorder scaling to convert the output signal of the pyranometer to (W/m^2) using equation 6.3 [183]:

$$E = \frac{Vs}{S} \tag{6.3}$$

Where E is the direct irradiance in (w/m^2), Vs is the output voltage (μV) and S is sensitivity of the pyranometer. To determine the radiation at various distances from the continuous solar simulator and characterise the lamp, radiation mapping was performed as shown in Figure **6.6**.

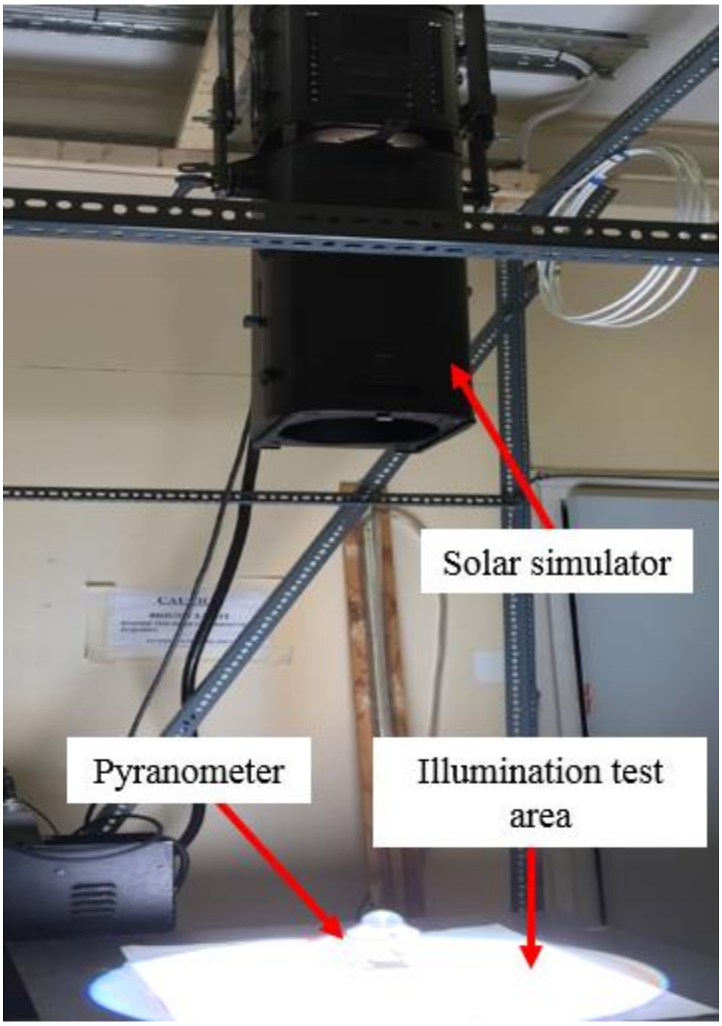

Figure 6.6 Photograph of the solar simulator characterisation test

An adjustable aluminium support was used to support and stabilise the radiation sensor on for the illuminated area. The illuminated area was covered with a sheet divided into equal positions as required by the ASTM standard. Moreover an adjustable scissor jack was used to vary the distances between the sensor surface plane and the solar simulator. Figure **6.7** shows a schematic drawing of the radiation measurement setup. The results of radiation mapping at 300mm distance from the light source output and different illuminated area dimension are evaluated in the following subsection.

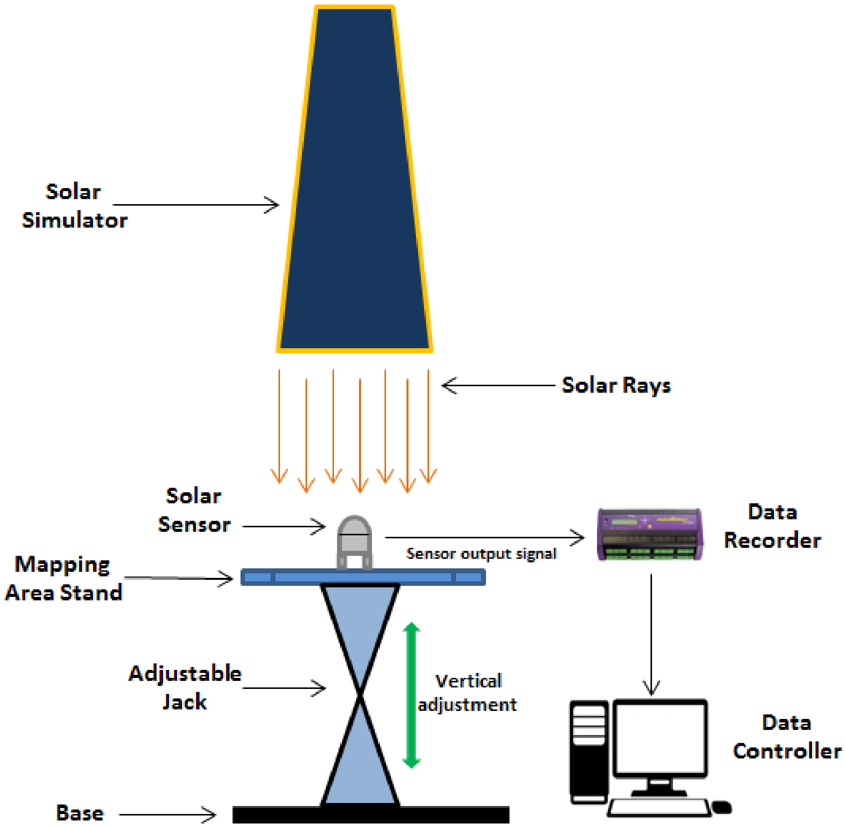

Figure 6.7 Schematic drawing of the irradiance mapping system

6.4.1 Solar simulator characterisation results

The ASTM criterion was applied to perform the temporal instability and non-uniformity test of the continuous solar simulator. Mapping method was developed for measuring the irradiance in the region under the continuous solar simulator light source output. 197 squares were outlined with average area of (24 x 24mm each) on paperboard and pyranometer sensor was positioned on the central of each square to record the irradiance on the mapped region. Figure **6.8** presents the mapping positions with yellow colour (1 to 197), orange colour (90) and red (30) representing 336 x 336 mm^2, 240 x240 mm^2 and 160 x160 mm^2 regions, respectively. The continuous solar simulator was turned on for 60 minutes to be stabilised before collecting any irradiance data. Three regions were studied to compute the non-uniformity and temporal instability percentages in such regions. Figure **6.9** shows the measured irradiance on 336 x 336 mm^2 region.

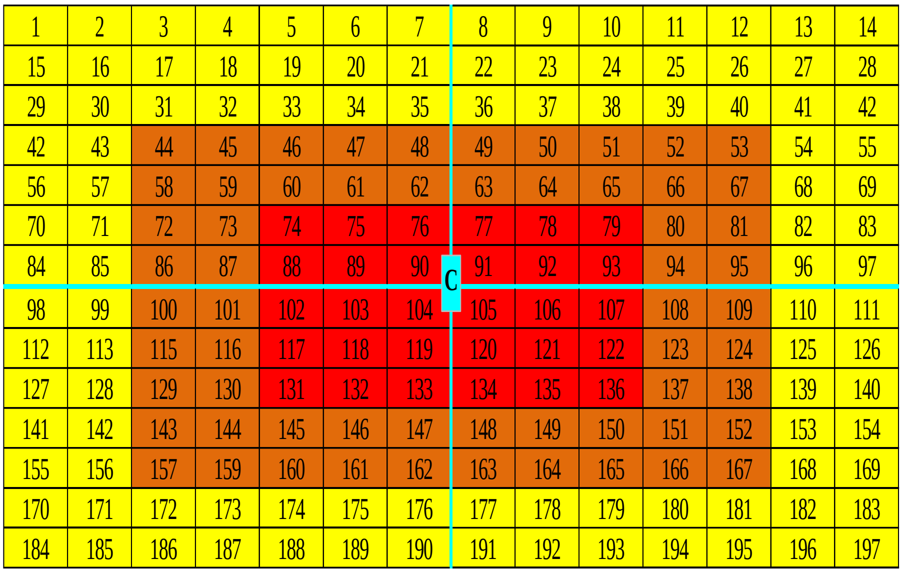

1	2	3	4	5	6	7	8	9	10	11	12	13	14
15	16	17	18	19	20	21	22	23	24	25	26	27	28
29	30	31	32	33	34	35	36	37	38	39	40	41	42
42	43	44	45	46	47	48	49	50	51	52	53	54	55
56	57	58	59	60	61	62	63	64	65	66	67	68	69
70	71	72	73	74	75	76	77	78	79	80	81	82	83
84	85	86	87	88	89	90	91	92	93	94	95	96	97
98	99	100	101	102	103	104	105	106	107	108	109	110	111
112	113	115	116	117	118	119	120	121	122	123	124	125	126
127	128	129	130	131	132	133	134	135	136	137	138	139	140
141	142	143	144	145	146	147	148	149	150	151	152	153	154
155	156	157	159	160	161	162	163	164	165	166	167	168	169
170	171	172	173	174	175	176	177	178	179	180	181	182	183
184	185	186	187	188	189	190	191	192	193	194	195	196	197

Figure 6.8 Irradiance mapping measurement regions

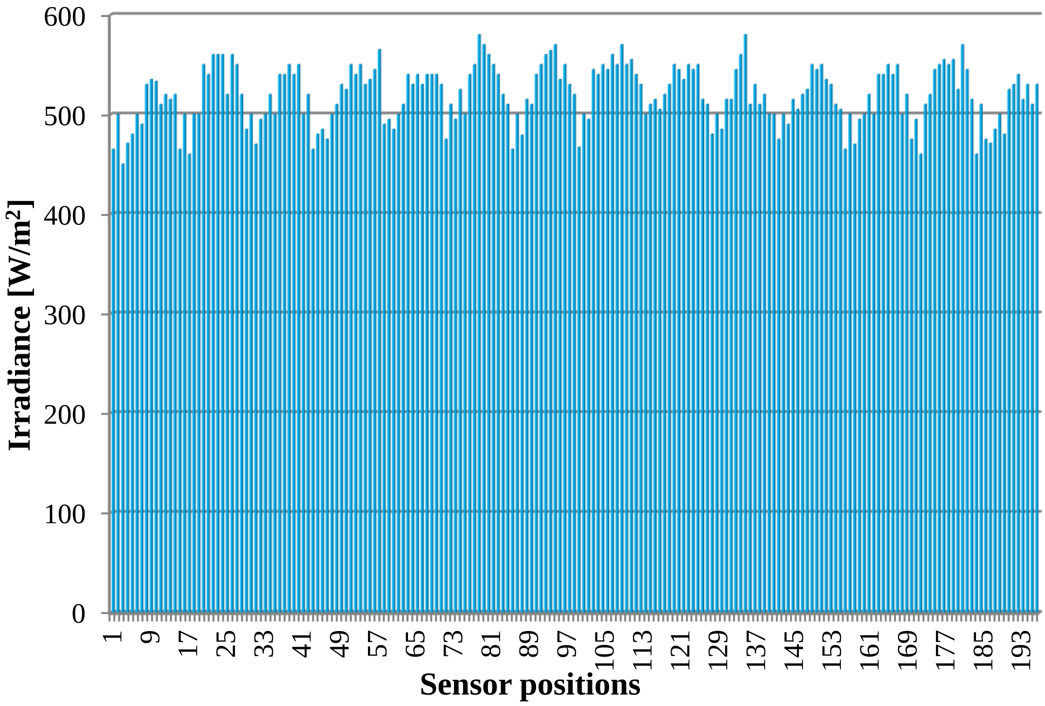

Figure 6.9 Irradiance distributions within a region of 336 x 336 mm^2

Figure **6.10** compares the non-uniformity percentage of the irradiance computed using equation 6.2 to the ASTM standard class C. It can be noticed that the non-uniformity decreases when the region area decreases. This continuous solar simulator nearly satisfies the acceptable tolerance of ASTM standard class C within 240 x 240 mm^2 region while the region 160 x 160 mm^2 satisfies the ASTM standard class C. This indicates that for best distribution of uniformity, the experimental setup of 3D-PSCPV should be positioned within 160 x 160 mm^2 or 240 x 240mm^2.

For measuring the temporal instability percentage, falling irradiance was measured on the 197 points over a period of two hour with one minute interval between each reading and equation 6.1 was applied to compute the temporal instability percentage. Figure **6.11** presents the temporal instability percentage for 336 x 336 mm^2, showing that the solar simulator is steady and attain class A specifications of ASTM standard for all the tested regions dimensions.

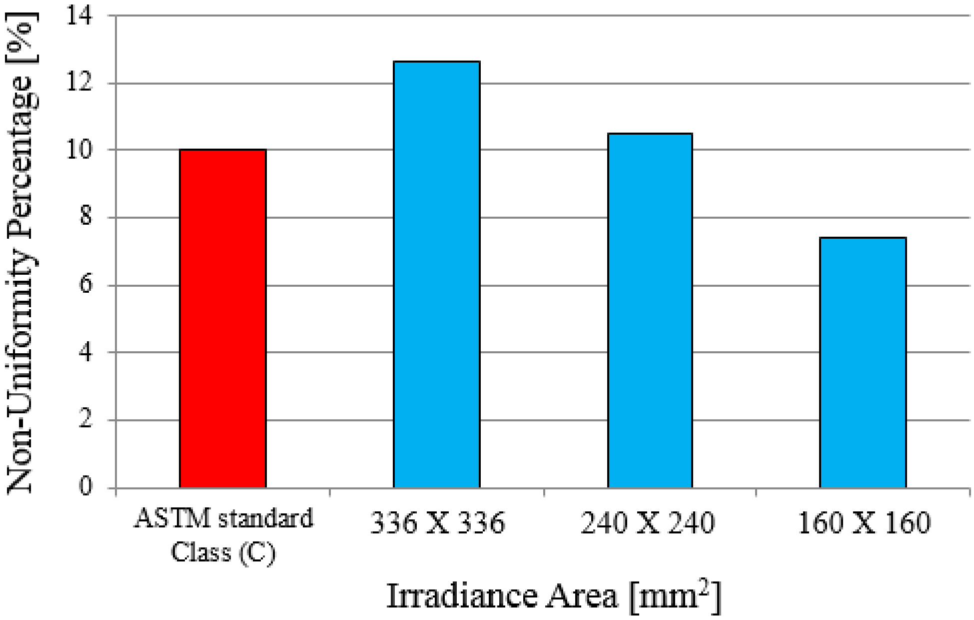

Figure 6.10 Non-uniformity percentage of the used solar simulator compared to ASTM standard class C

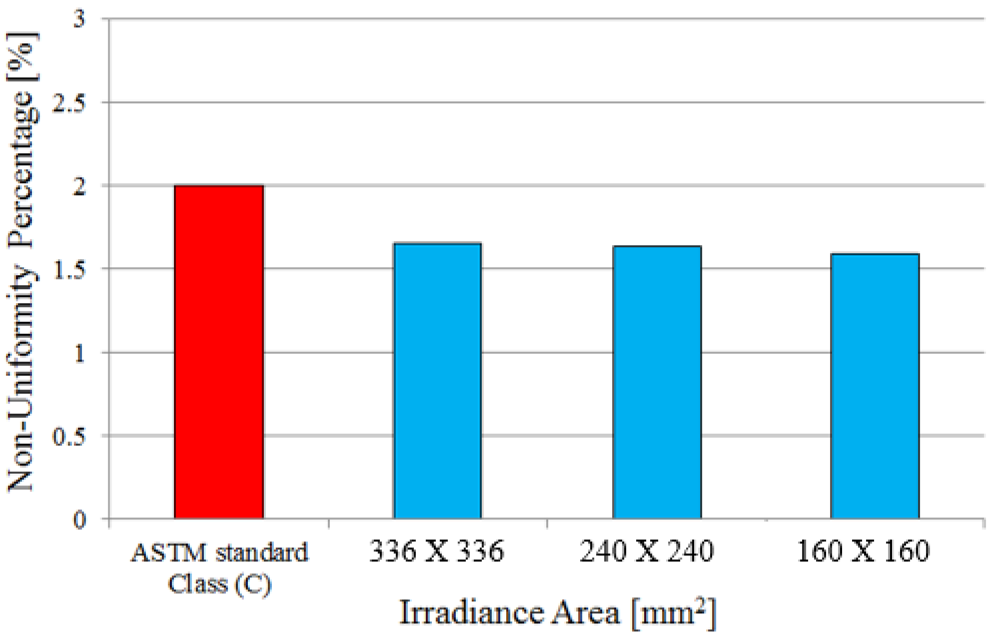

Figure 6.11 Temporal instability percentage of the used solar simulator compared to the ASTM standard class C

To measure the continuous solar simulator collimation angle a bendable stainless steel sheet with (L) frame was utilised as reported by [184]. Figure **6.12** illustrates the principle of measuring the collimation angle where the shadow length (SL) was measured and used to calculate the angle using equation 6.4:

$$\tan\theta = \frac{SL}{H} \qquad (6.4)$$

Figure **6.13** shows the measured collimation angles over the area of 336X336 mm^2 where the largest collimation angle is ±8°. In the area of 160X160 mm^2, a collimation angle of zero was obtained indicating of that the radiation is normal to the target area.

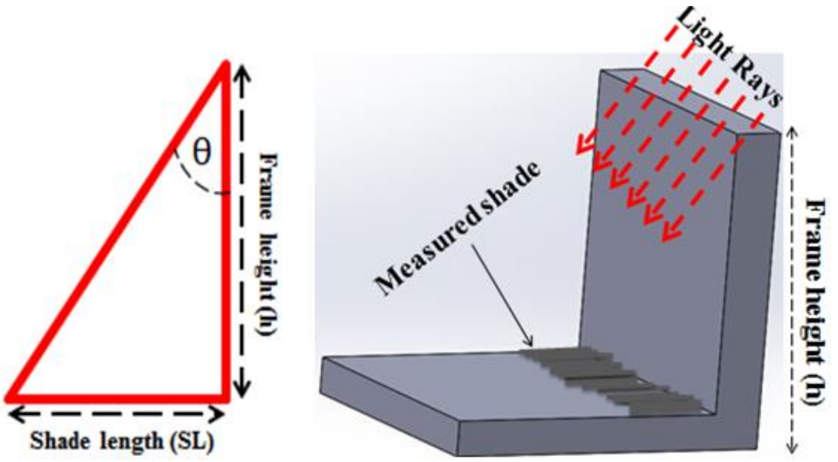

Figure 6.12 (L) frame stainless steel employed to calculate the collimation angle of the continuous solar simulator

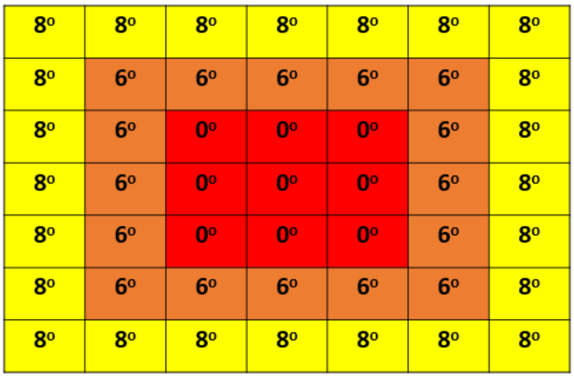

8°	8°	8°	8°	8°	8°	8°
8°	6°	6°	6°	6°	6°	8°
8°	6°	0°	0°	0°	6°	8°
8°	6°	0°	0°	0°	6°	8°
8°	6°	0°	0°	0°	6°	8°
8°	6°	6°	6°	6°	6°	8°
8°	8°	8°	8°	8°	8°	8°

Figure 6.13 The light collimation angles of the continuous solar simulator at illumination area of 336X336 mm^2

6.5 Indoor and outdoor experimental setups

Figure **6.14** and Figure **6.15** shows respectively a schematic drawing and picture of the indoor experimental test setup utilised in the characterisation of water cooled 3D-PSCPV with clean and dusty glass covers. It consists of the cooling system, PV module, dusty cover, radiant flux sensors, pyranometer, DT85 data logger and I/V measuring setup. Surface temperature sensors were attached on in the rear back of the PV module with insulating tape at several locations. The inlet and outlet of the water cooling channels were fitted with two temperature probes to measure the water temperatures. The inlet and outlet part is insulated with 28mm thick rubber insulator to avoid heat gain from the solar simulator. An electrical circuit (IV tracer system) was specifically built for measuring electrical parameter, I/V and P/V curves in indoor condition. The temperature and I/V readings were sent to two data recorder connected to a computer. The solar simulator used in investigating the 3D-PSCPV performance in indoor condition. The concentrator was placed perpendicular (90 degrees) on the PV module and cooling channels under the solar simulator.

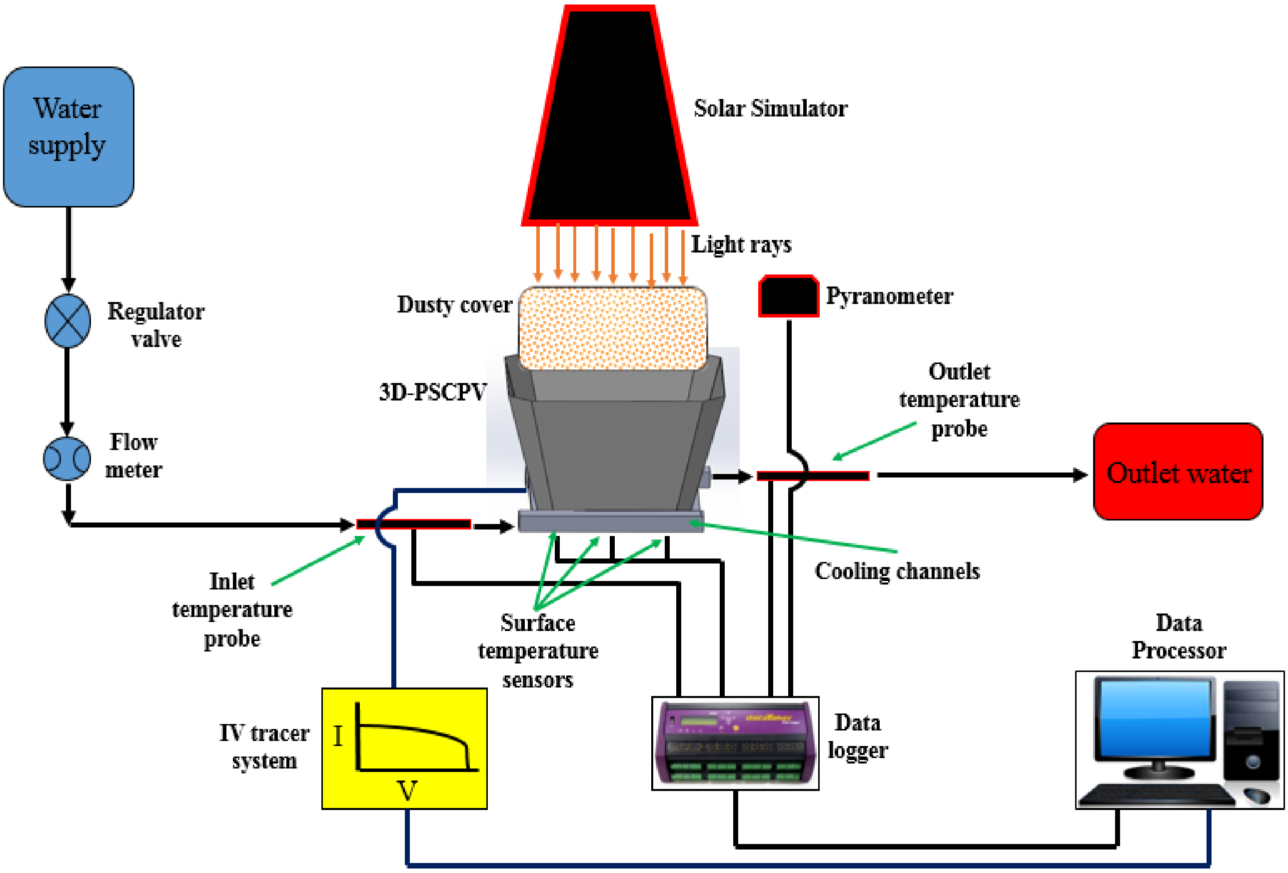

Figure 6.14 Schematic diagram of the indoor test setup of 3D-PSPCV system

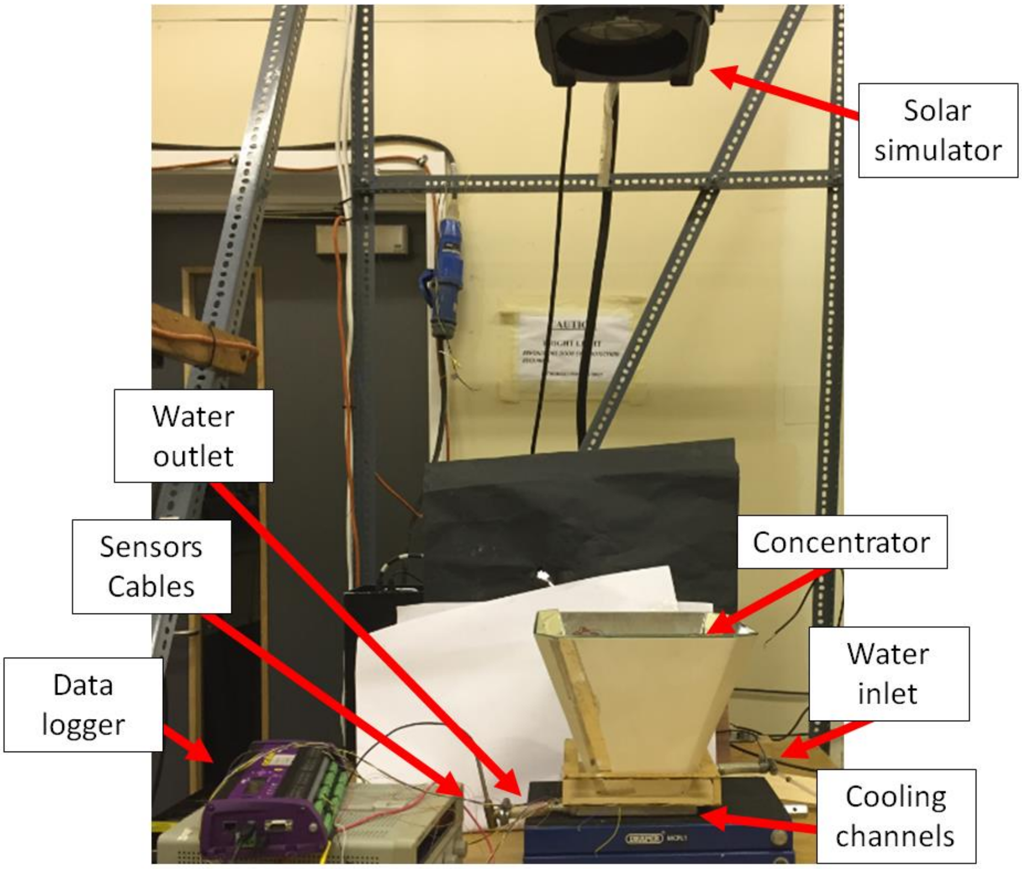

Figure 6.15 Photo of the indoor experimental setup of the 3D-PSCPV

Figure **6.16** and Figure **6.17** show a photo and schematic drawing of the experimental test set up utilised for optical, electrical and thermal outdoor testing. It consists of three 3D-PSCPV concentrators and PV module, the developed dusty glass cover (described in the following subsection), cooling channels, pyranometer, radiant flux sensors, anemometer and transportable tilting table to track the sun manually. The adjustable tilting angle stand is designed to be installed on a horizontal surface and allows to be mounted at zenith angles from 0° to 90°. The setup also consists of DT85 data logger and other instrumentations which are used in the indoor setup. For the outdoor experimental characterisation of the 3D-PSCPV in clean and dusty conditions, the current and voltage data acquisition system developed for indoor experimental setup (section 6.6.1) was replaced by Solmetric® wireless high speed data acquisition system (PVA-1000S) with (maximum speed of 500 I/V tracer point per 4 second). The I-V curve measurement provides I_{sc}, V_{oc}, I_{mp}, V_{mp} and P_{max}. The outdoor characterisation of the 3D-PSCPV was performed to investigate the actual performance in real sunlight. All of the measuring instruments and 3D-PSCPV with cooling channels were fixed on top of a setup which can be tilted and moved as required to measure the system performance in direct solar radiation. A detailed description of the various component of the indoor/outdoor test facility will be given in the following subsections.

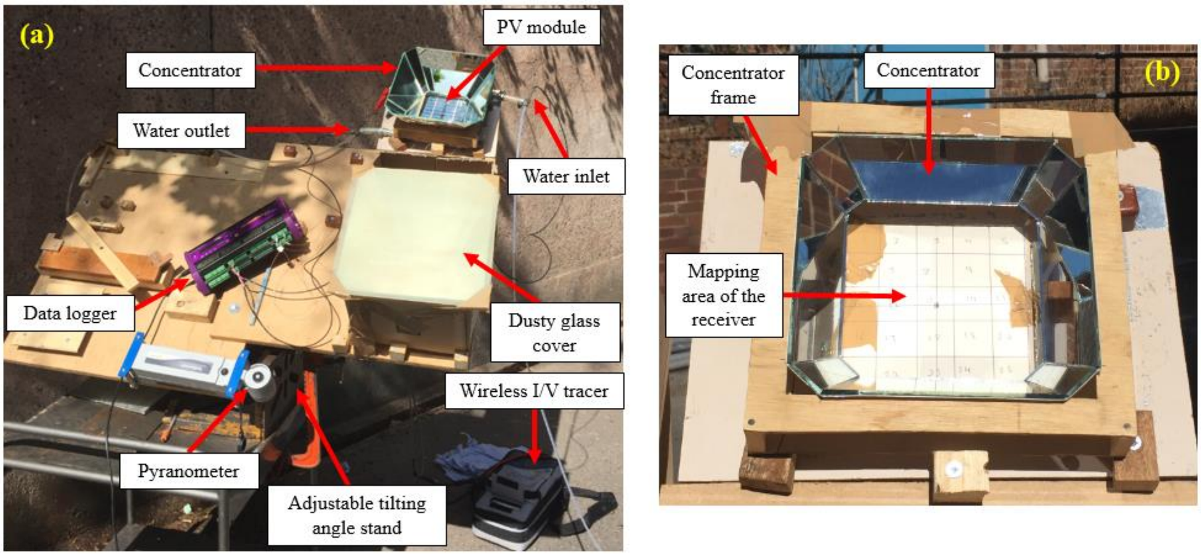

Figure 6.16 Picture of the outdoor experimental set up (a) electrical and thermal test set up (b) optical test set up

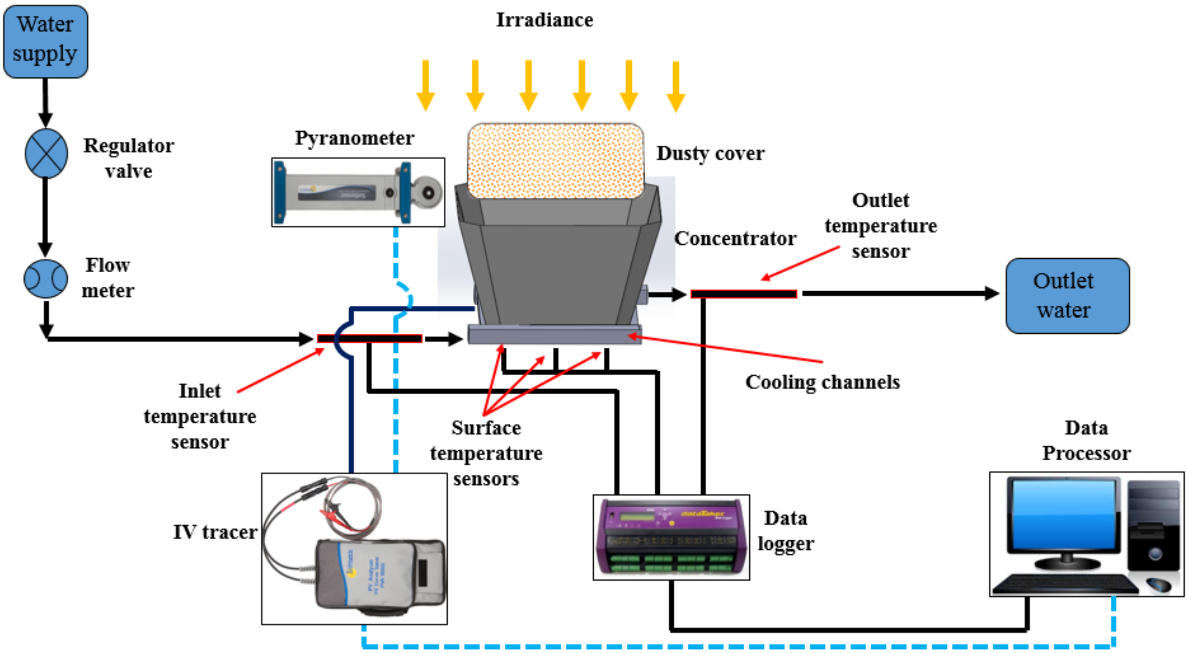

Figure 6.17 Schematic of the outdoor experimental setup

6.5.1 Dust distribution methods

Samples of real dust was removed and collected directly from the dusty module glass cover at (KISR) experimental site (see in chapter 3). A sieve was used to filter the samples and separate the sand and other accumulated solid elements before being used to cover the glass cover of the concentrators. The dust was also sieved to obtain dust sample with uniform size. This was prepared by vibratory sieve shaker (Endecotts Minor 200) and sieves with mesh size of 0.09mm as shown in Figure **6**.**18**.

Figure 6.18 dust sample sieving test setup

The dust particles were then spread uniformly on the transparent adhesive film [155] which was used to cover the glass of the concentrators. 3M^{TM} optically transparent film with properties shown in Table **6.5** was used. Figure **6**.**19** shows the total light transmission percentage of 3M™ transparent film provided by the manufacturer. The shaded section features the wavelength range of the tape used in dust optical test.

Table 6.5 The optical and physical specifications of 3M™ clear adhesive film [185]

Material	Acrylic
Light transmission	95%
Haze level	< 1% with incident light angle of 2.5°
Refractive index	1.47
Thickness	0.19 (mm)
Width	50 (mm)
Maximum Operating Temperature	+93 (°C)

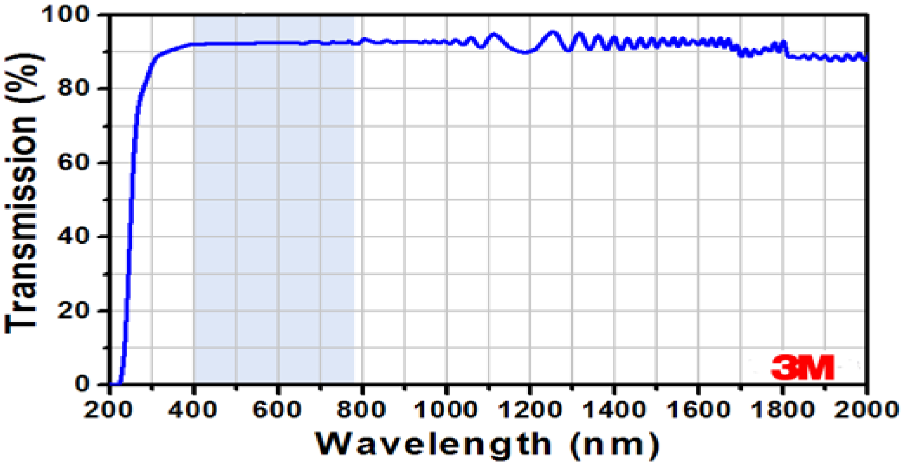

Figure 6.19 Total light transmission across 3M™ transparent film [185]

Tests were performed on a clean 3M™ film coated on glass to evaluate the effects of dust on the 3D-PSCPV optical performance. In each condition (clean and dusty cover), the experiment was carried out through measuring the irradiance produced by the solar simulator and natural sun light at various positions under the glass cover with and without dust. The optical transmittances of the glass samples with and without dust were measured utilising the pyranometer. Figure **6.20** and Figure **6.21** show schematic diagram and photos of the experimental technique applied for measuring the dusty glass transmittance respectively.

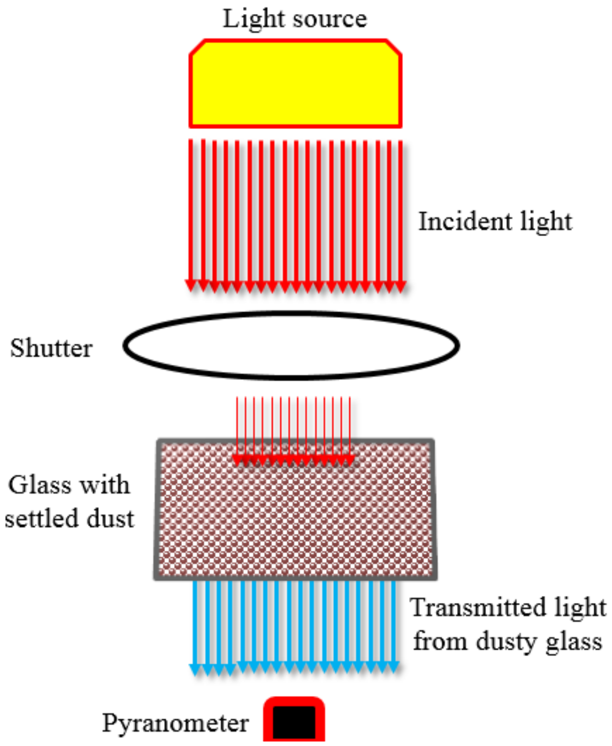

Figure 6.20 Schematic diagram of the measurements set up of dusty glass transmittance

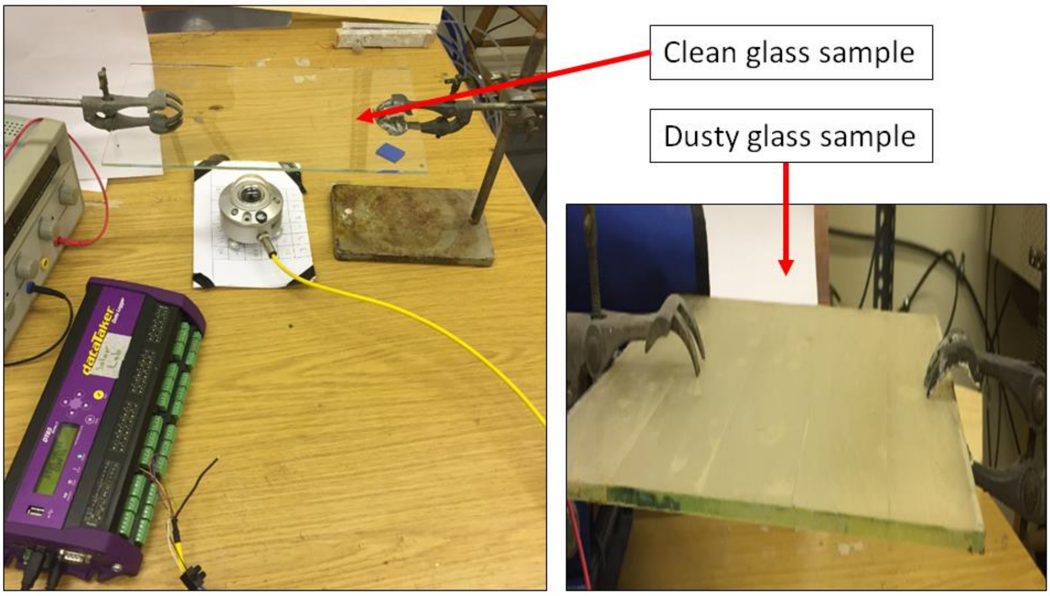

Figure 6.21 Photo of the measurement set up of the dusty glass transmittance

6.5.2 3D-PSPCV receiver (PV Module)

Futurlec^{TM} polycrystalline PV cell was utilised in this study to develop the 3D-PSCPV receiver; the selection of the PV cells was based on chapter 3 analysis showing that polycrystalline PV cells perform better in Kuwait climate than monocrystalline. The PV cells were specially ordered from the manufacturer to fit into the 3D-PSCPV receiver area and can operate at concentration ratio 1X-6X [186]. Figure **6.22** shows the image of the PV module used in this work. A 125mm^2 PV module array of cells is cut from polycrystalline PV panel. It consists of 18 PV cells wired in series and placed between PCB (printed circuit board) underneath the PV cell and PET (Acrylic-laminating formula with low-iron) encapsulation on the top surface of the PV module. Figure **6.23** presented the arrangement of the three layers encapsulation and the PV module dimensions. A PCB with 130mm width and 130mm length was designed to connect all the PV cells underneath the bus bars with the top bus bars to develop a full PV module. The rationale behind operating the PCB is that the extra usage of solder can cause short-circuits to the PV module and can increase the series resistance. The electrical connection process of the PV module is performed by the manufacture.

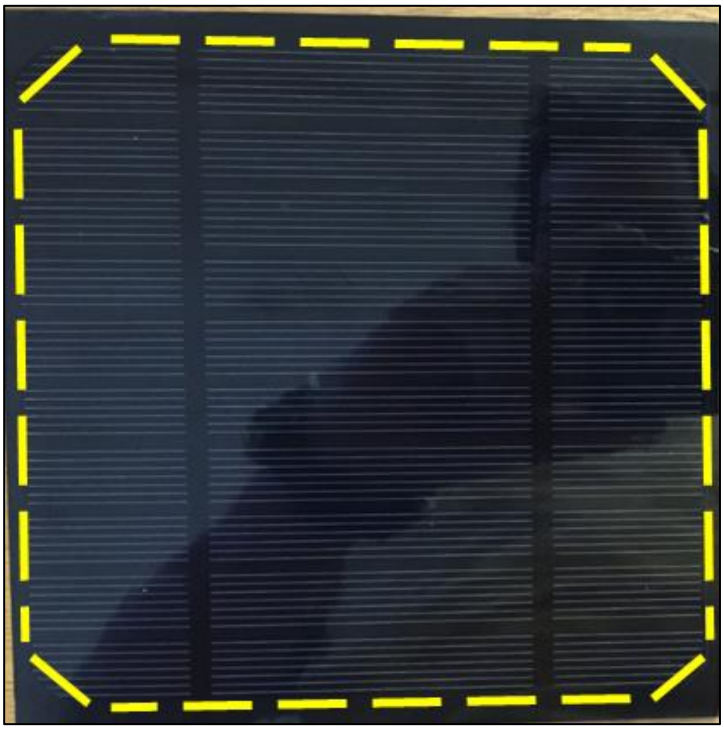

Figure 6.22 The original PV silicon cell modified to a 130 mm PV module to operate with 3D-PSCPV receiver

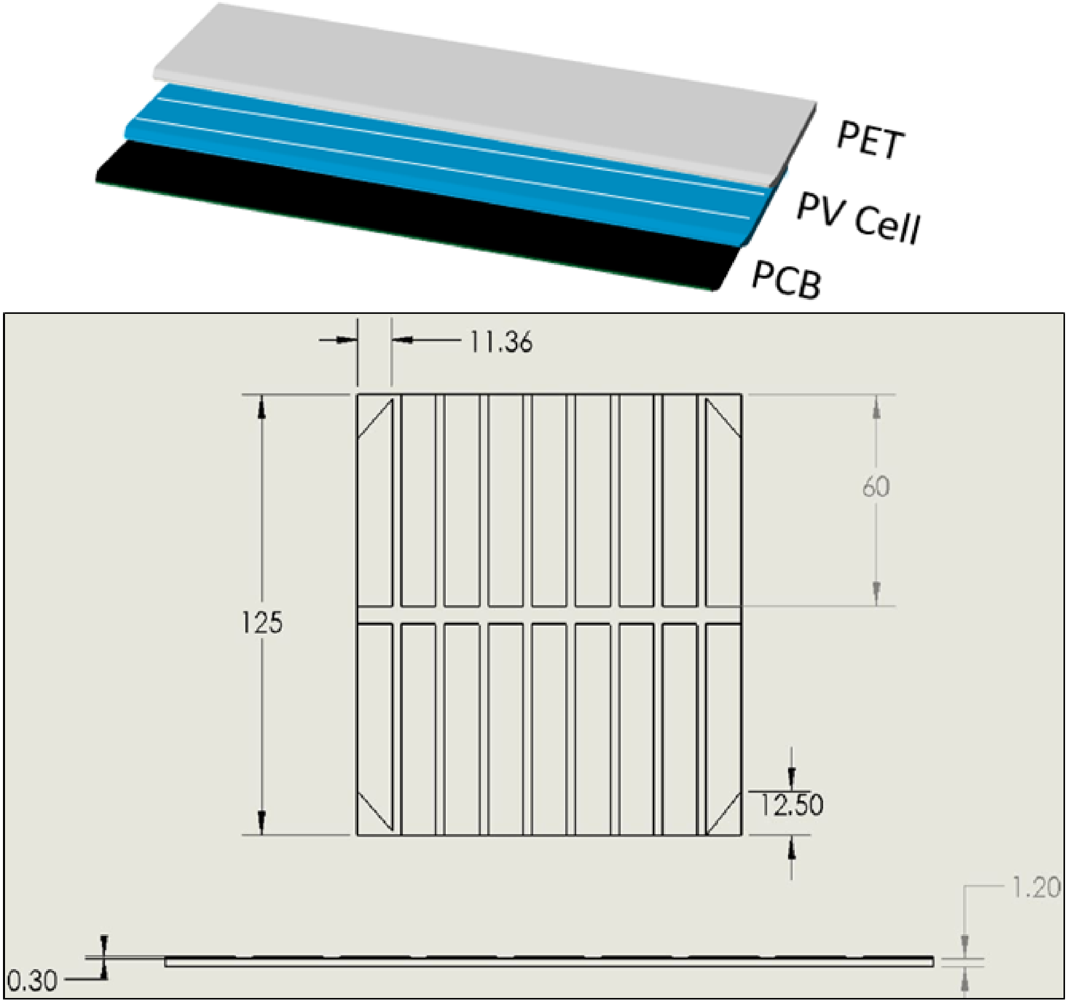

Figure 6.23 PV module encapsulation layers and 3D-PSCPV receiver (PV module) dimensions (mm)

6.5.3 Cooling channels of the 3D-PSCPV

A cooling setup was developed to study the performance of the dusty 3D-PSCPV fitted with cooling channels to validate the thermal modelling. Aluminium channels were cut based on the dimension presented in (Figure **5.4** in chapter 5) and aluminium oxide and contamination from cutting solvents on the surface of the aluminium channels were removed and polished. To avoid weld cracking the aluminium channels was preheated before the welding commence. Figure **6.24** shows the cooling channels welded together by (GTA) Gas Tungsten Arc welder.

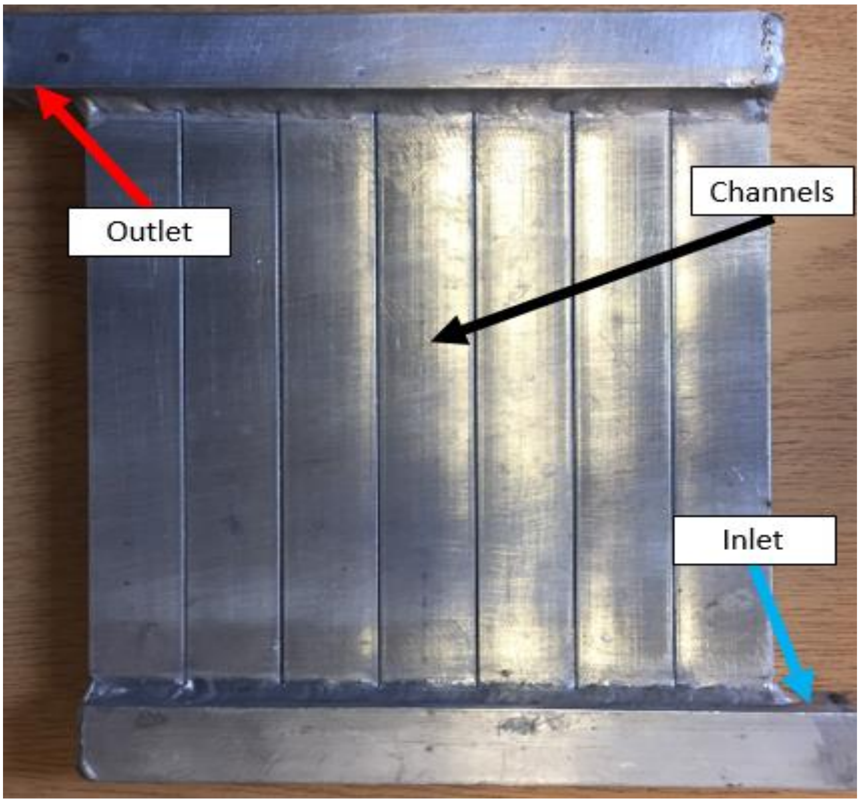

Figure 6.24 Photo of the Aluminium cooling channels

The PV module of the 3D-PSCPV receiver was attached on the cooling channels by a Silicone Heat Transfer Compound Plus (HTSP). In order to obtain a uniform bond surface between the cooling channels surface and the PV module, uniform pressure was applied on PV module. Finally the 3D-PSCPV together with frame were placed on the PV module and cooling channels.

6.6 Measuring devices

6.6.1 I/V curve measurements

An electrical circuit was built for measuring I/V and power outputs for indoor testing. The measuring circuit consists of the PV module assembly, adjustable resistance load, voltage sensor, current sensor and data recorder. Figure **6.25** shows a schematic diagram of the electrical circuit used for measuring the current and voltage across the PV module in both clean and dusty conditions using the four terminals procedure reported by [184, 187, 188]. When testing a small PV module, the measured voltage tends to be small and the changes to this voltage value due to the effect of radiation or dust may also be small, the accuracy of I/V measurement is important. Therefore, in operating the four-terminals procedure, the impacts of the cables internal resistance was reduced by minimising the cables length and separating the voltage/currents output terminals [184, 187, 188]. This involves using an ammeter connected in series to measure the current generated by the PV module and a voltmeter connected in parallel to measure the voltage obtained by the PV module once it is irradiated.

A heavy-duty adjustable resistance load with 0.005-999Ω range is connected in parallel through the voltmeter to gradually vary the inner circuit resistance allowing electrical current and voltage (maximum and minimum) to be continuously recorded. The voltmeter and ammeter are electronic digital multi-meter and data recorders (TENMA-72-7730) with voltage measuring range of 200mV-1kV with accuracy of ±0.1% and the current measuring range of 200μA-10A with accuracy ±0.25%. The current and voltage measurements were transmitted through USB link interface connected to a PC. The TENMA device comes with an interface programme for data recording and graphical display where the data saved in excel file format. Figure **6**.**26** shows the Photo of the 3D-PSCPV electrical measurement for the indoor setup.

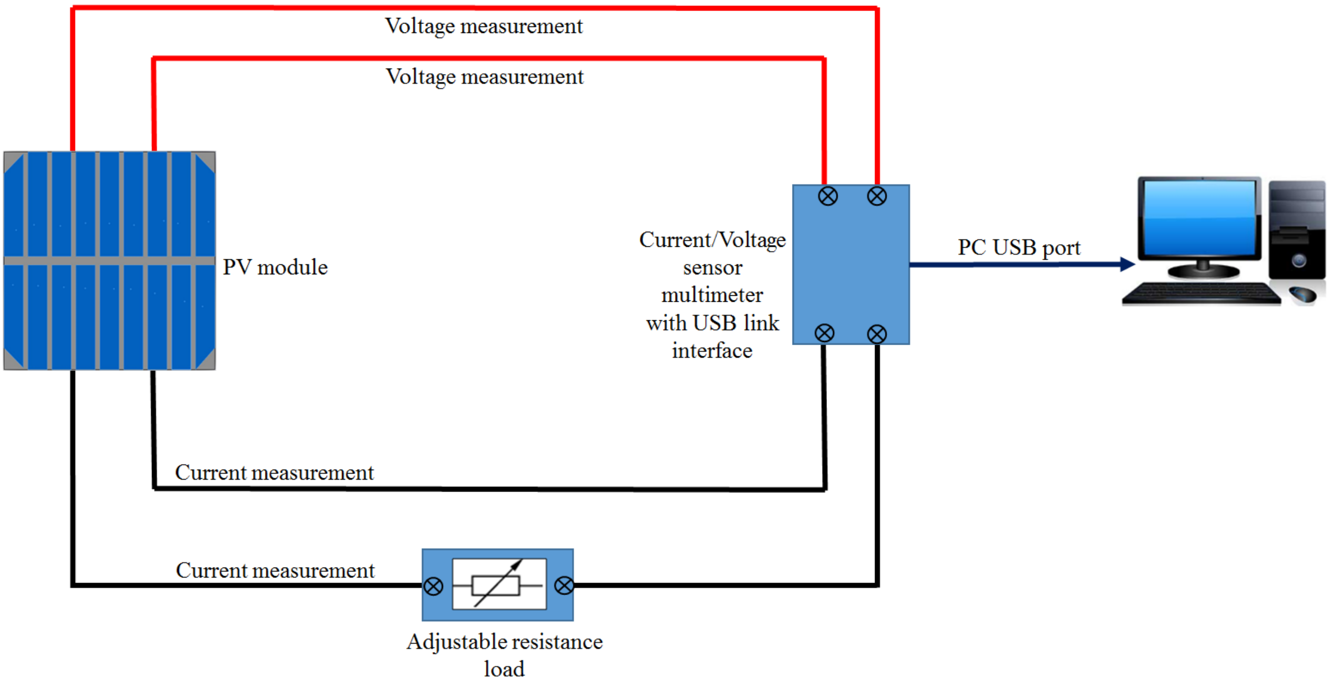

Figure 6.25 Electric circuit diagram for the I/V curve data acquisition system

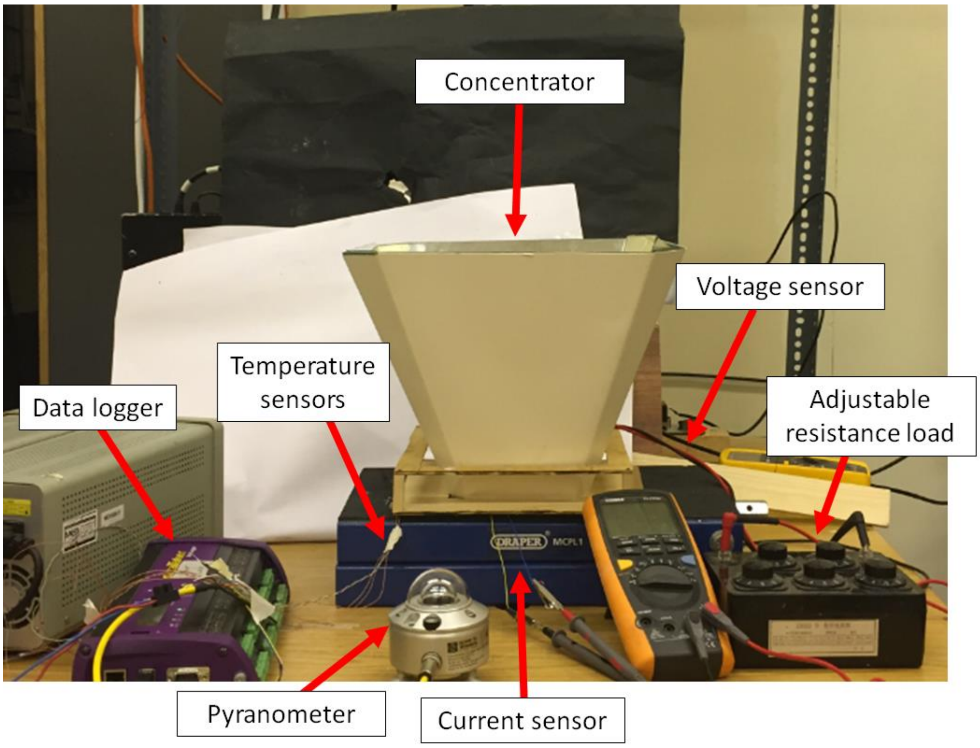

Figure 6.26 Photo of the indoor IV curve and electrical parameters measurements

In outdoor testing Solmetric PV analyser was utilised to characterise the electrical performance of the 3D-PSCPV with and without cooling. This PV analyser consists of two devices: wireless pyranometer and I/V tracer. The I/V tracer is capable of generating an P/V and I/V curves with same time for the PV module and measure the electrical outputs such as: open circuit voltage, short circuit current, maximum current, maximum voltage and maximum power output. Instantaneously, the wireless pyranometer measures the direct solar radiation at the 3D-PSCPV aperture in various angles to assess the system performance. Detailed specifications of Solmetric PV analyser are given in Appendix B.

6.6.2 Radiation flux sensor

Radiant flux sensors manufactured by CAPTEC^{TM} with 5 x 5mm sensing surface and operating temperature from 180°C to 200°C were used in mapping the concentrator receiver area. The sensors spectral response is within the range of 200-2000nm and the output voltage signals response time is 0.05 sec. Table **6.6** provides the sensitivity and calibrations of the sensors as given by CAPTEC^{TM}. To determine the irradiance concentrated and received through the 3D-PSPCV with different characteristics from the light source, an experimental radiation mapping was implemented using the mapping method in section 6.4.1. Figure **6.27** shows an image of radiant flux sensor, The data logger (DT85-datataker) receives signal as voltage input transmitted from the sensors where the sensor's sensitivities specified in the scaling of the data logger convert the voltage input to W/m^2.

Table 6.6 Sensitivity of the radiant flux sensors [167]

Flux sensor	**Sensitivity, (μV/ (W/m^2))**
1	0.112
2	0.117
3	0.0995
4	0.0833
5	0.111
6	0.0898

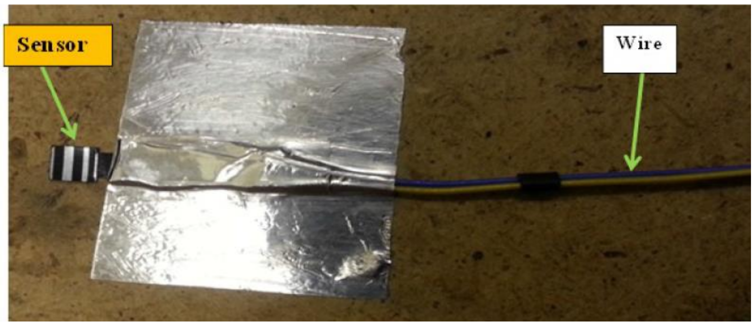

Figure 6.27 Image of the radiant flux sensor utilised in the 3D-PSCPV receiver mapping.

The radiant flux sensors were fitted in a plastic frame which was fabricated utilising 3D printer to keep the sensors steady in place. Figure **6.28** shows a photo of the radiant flux sensors frame, which was used to move the sensors over the illuminated area.

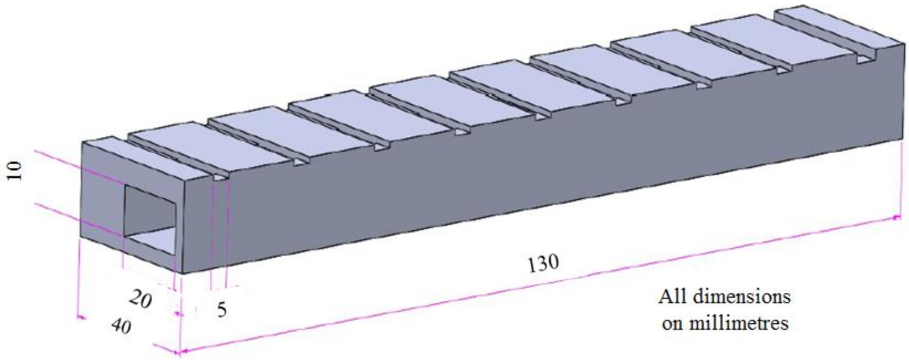

Figure 6.28 3D representation of the radiation mapping arrangement (nine sensors frame)

6.6.3 Surface and cooling water temperature measurements

In this experimental work two types of temperature measuring sensors were utilised: For the measurements of the inlet and outlet water temperatures, RTD (Resistance Thermometer Detector Platinum 100 model) manufactured by Omega® was utilised with ±0.025K accuracy [167]. While, Copper Constantine T-type insulated wire thermocouples with trimmed ends were utilised for surface temperature measurements. Omega STC-TT-TI-36-1M (see Table **6.7**) thermocouples were utilised for recording the PV module surface temperature and their calibration data are presented in appendix A. Thermocouples were placed on the PV module back side as shown in Figure **6.29**. All the temperature readings were recorded via the data taker DT85 and processed via PC.

Table 6.7 Thermocouple specifications for surface temperatures

Specification	**Code**	**Interpretation**
Insulation	TT	Neoflon
Type	T	thermocouple group T
Connectors	STC	copper strip connector
Wire gauge	36	0.13 mm Diameter
Length	1M	1 meter

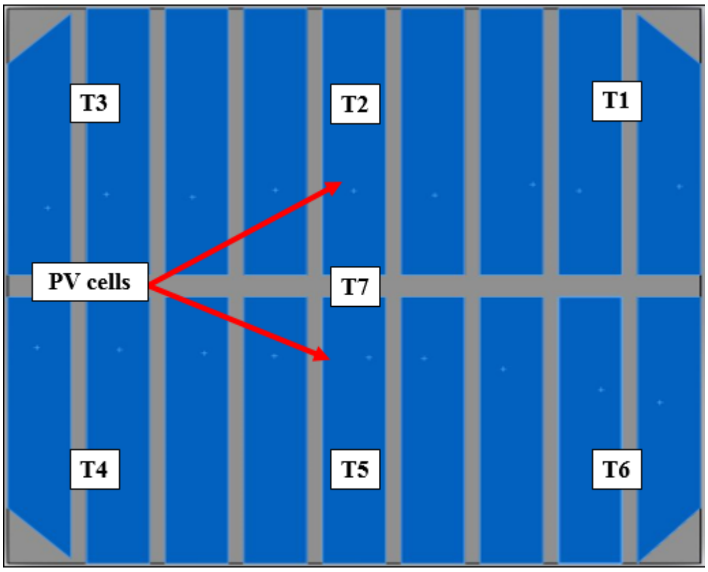

Figure 6.29 Diagram showing the position of thermocouples at the rear of the 3D-PSCPV receiver (PV module)

6.6.4 Flow meter

The water flow rate in the inlet is measured using a CT-Platon flow meter shown in Figure **6.30**. It measures flow rate ranging from 25 – 800 cm^3/min with accuracy of ±1.25% [189]. The water flow rate applied in this study is varying from 25-800 cm^3/min within the flow meter measurement range. A standard transparent 600ml graduated container and timer were used to calibrate the flow meter as discussed later in this chapter.

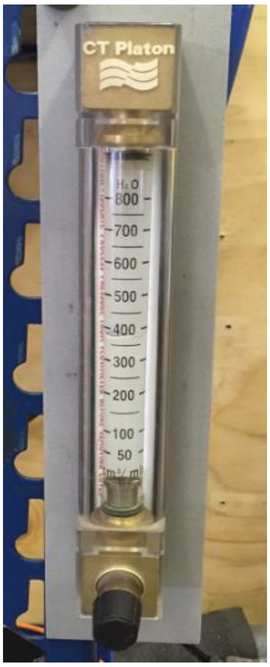

Figure 6.30 Image of the flow meter used in the experimental work (indoor and outdoor)

6.7 Calibration and uncertainty of the instruments

In this experimental work various instruments have been utilised for measuring cooling water flow rate and temperature, irradiance, PV current and voltage output. The recorded data were utilised for assessing the effects of parameters as surface temperature, flow rate, and water temperature, on the performance of the cooling channels and PV module. Errors are typically encountered in measuring devices are random or systematic. Random errors are unpredictable alterations in the experiment results due to measurement devices and environmental conditions. While systematic errors are inaccuracy of the experimental measurements. Random errors could be eliminated by uncertainty study whereas appropriate calibration can correct systematic errors. The calibration methods of the various measuring devices used are described in the following subsections while the calculations of the instruments uncertainty are discussed in Appendix A.

6.7.1 Calibration of the flow meter

The water flow meter (CT Platon) was calibrated using a standard 600ml measuring container and timer [167]. The timer was used to record the time taken to fill up the container with water. Several flow rate reading were recorded (50-600 mL/min) and flow rate was computed by applying equation 6.6. **Figure 6.31** shows the calibration curve of the flow meter (CT Platon) with an overall uncertainty of ±8.86 mL/min.

$$V_w = \frac{\text{recorded valume}(V_f)}{\text{recorded time (t)}} \tag{6.6}$$

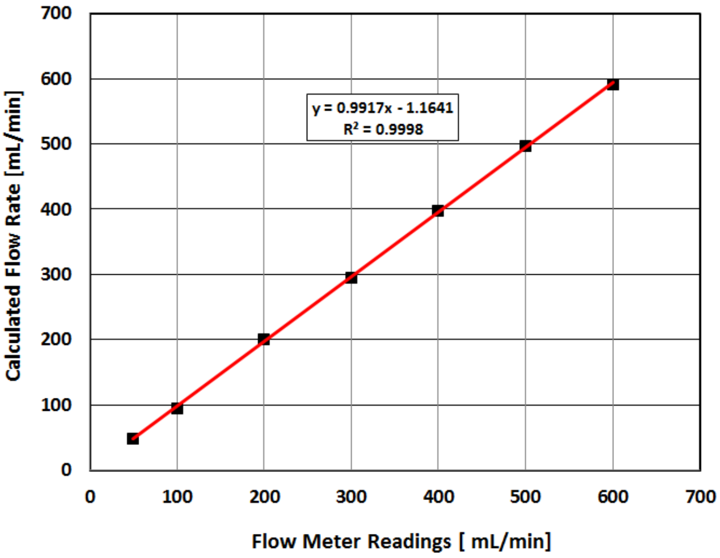

Figure 6.31 Calibration curve of the calculated flow rate and flow meter

6.7.2 Calibration of the surface thermocouples

Figure **6.32** shows the device used for calibrating the thermocouples used in this work. It consists of water vessel and an electrical heater equipped with thermostat to control the heat input. The standard RTD and T-type thermocouples were placed in the same level in vessel with water to measure the water temperature. The water temperature in the vessel was controlled by thermostat and varied between 20 to 100°C. The temperature values of the thermocouples were transmitted to a DT85-datataker and stored in a PC to be analysed. Figure **6.33** shows comparison of one T-type thermocouple reading versus RTD readings, this thermocouple was fitted at the centre of the PV module. The uncertainty for this thermocouple measuring the temperature of the centre of the PV is ±0.24°C which was predicted using standard deviation approach (see Appendix A).

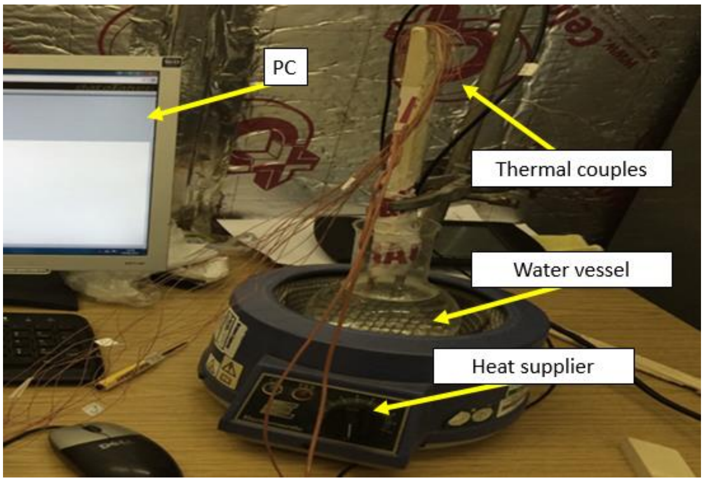

Figure 6.32 Calibration procedure of the surface thermocouples

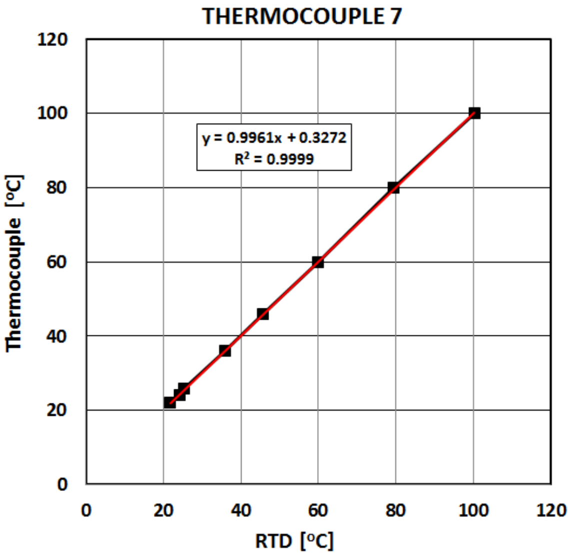

Figure 6.33 Calibration curve between surface thermocouple and RTD

6.7.3 Uncertainty in PV electrical output

Applying the uncertainty analysis of surface thermocouples and flow meter uncertainty, the PV electrical output uncertainty was calculated. The electrical measured data of the short-circuit current, open-circuit voltage and maximum power output was used to calculated the uncertainty values. The maximum power output was obtained from the measured I/V curve at 850 W/m^2 and PV temperature at 25.5^{o}C then calculated using equation (2.1). Table **6.8** shows the results of uncertainty estimation for the short-circuit current, open circuit voltage and maximum power output using excel sheet. The values in the table indicate that the uncertainty in power outputs computation is higher than the other parameters signifying that the PV module power output is more sensitive.

Table 6.8 Uncertainty results of PV module electrical parameters

Parameter	**Average reading**	**Uncertainty**	**uncertainty percentage error %**
Short-circuit current	0.1348 A	±0.0011 A	0.88%
Open-circuit voltage	9.9 V	±0.057 V	0.58%
Maximum power output	1.02 W	±0.013 W	1.21%

6.8 Experimental procedure for various performance characterisation

6.8.1 Optical performance characterisation

Figure **6.34** shows a schematic drawing of the experiential setup used to investigate the optical performance of the 3D-PSCPV with clean and dusty cover. The developed 3D-PSCPV and dusty glass cover were optically studied indoor and outdoor with different surface reflectivity and concentration ratio. The system includes clean glass cover, two pyranometers

(CMP11 for indoor setup and wireless for outdoor setup), radiant flux sensors, adjustable stand and data logger. The tested solar simulator in section 6.4 is used to investigating the 3D-PSCPV optical performance in indoor study, while natural sun light was used on the outdoor investigation. The irradiance was measured using the pyranometer by mapping the concentrator entrance plane while the concentrated irradiance was measured using radiant flux sensors by mapping the concentrator receiver area (the PV module surface). The 3D-PSCPV optical efficiency was calculated. Also, the light transmittance of the dusty glass cover was estimated.

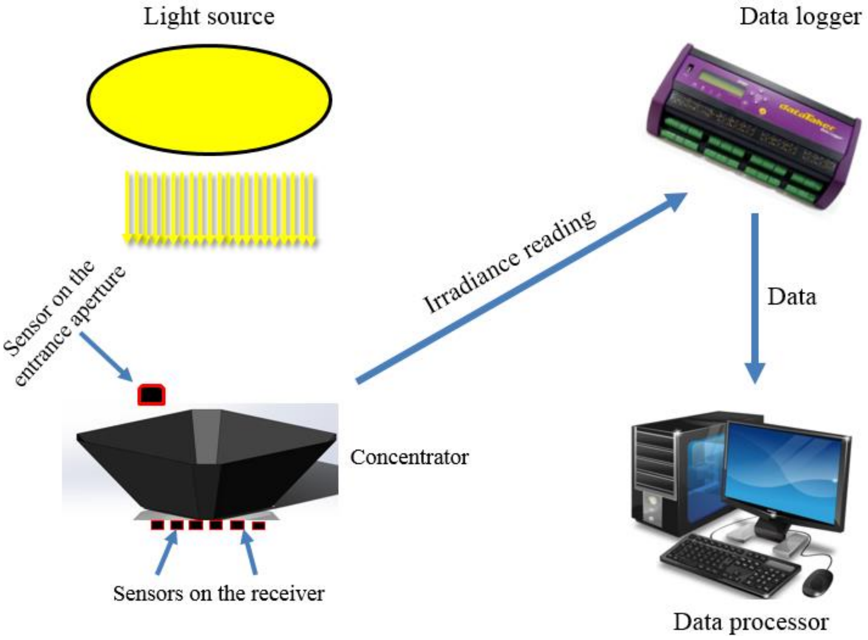

Figure 6.34 Schematic diagram of the experimental optical test

6.8.2 Electrical performance characterisation

For the indoor setup, the PV module electrical performance was measured using the electrical circuit described in section 6.6.1 by carrying out a current and voltage sweeps of the PV module. The open-circuit voltage was measured when the maximum voltage that the PV module produces without any load connected. The short-circuit current was measured when the voltage across the PV module is zero. The adjustable resistance load was used to vary the current and voltage outputs at different loads. Every single full set of current and voltage sweep took nearly 5 minutes. The maximum power output generated by the PV module can be calculated through the I/V sweeps. During the testing, a series of additional measurements is recorded such as incoming irradiances and module temperature in addition to the room temperature. The room temperature was kept 24ºC and all room entrances were sealed with insulation board to prevent undesirable air infiltration and temperature alterations.

The electrical performance of the 3D-PSCPV was also measured outdoor under different concentration ratios, clean and dusty covers and PV module temperatures using Solmetric PV analyser. The PV module electrical performance was evaluated in terms of I/V, P/V curves, maximum power outputs and electrical efficiency.

6.8.3 Thermal performance characterisation

The 3D-PSCPV with surface reflectivity of 70% and 90% were thermally studied outdoor and indoor, respectively, with dusty glass cover at various concentration ratio and cooling water velocity to study the effect of water cooling on the PV module temperature and the electrical parameters. To measure the PV module temperature with water cooling seven thermocouples were placed at the rear surface of the PV module at different positions and readings were recorded utilising the data taker. For the ambient temperature measurement, one thermocouple was connected to the data taker. The maximum power output and electrical efficiency were calculated with and without water cooling to evaluate the electrical performance of the 3D-PSCPV system. RTDs were used to measure the water temperature difference via the water cooling temperatures of the inlet and outlet.

6.9 Summary

In this chapter, indoor and outdoor experimental setups to investigate the performance of 3D-PSCV system were described. One of the investigations was carried out for classifying the continuous solar simulator according to standard specification of solar simulator ASTM

E927–10. The non-uniformity percentage varying from 7.5 to 13% was achieved based on the size of the illuminated region. Moreover it was observed that the temporal instability of the continuous solar simulator is 1.6% for irradiance region of 336 x 336 mm^2. This confirms that this continuous solar simulator achieved the temporal instability qualification of ASTM E927–10 standard of class A ($\leq$ 2%). In order to find a suitable collimation, the solar simulator light collimation angle was investigated. The largest collimation angle measured is 8^o and the smallest collimation angle is 0^o. Results revealed that the position of target region and size are important in determining the beams' collimation and the intensity level of irradiance. The selected continuous solar simulator, which met the solar simulator standard Class C, is sufficient for supporting the testing of the 3D-PSPCV experimentally. Furthermore the experimental setup includes developing the 3D-PSCPV system by assembling the dusty glass cover and cooling channels.

Different measurement devices were used for obtaining data from indoor experiments including monitoring setup to record surface temperature, coolant temperature, irradiance and water flow rate. Also, electrical circuit was developed for measuring the output current/voltage (I/V curve). The outdoor experimental setup included PVA-1000S PV tracer to record the incident irradiance, (I/V) curves, maximum power output for the 3D-PSCPV system. Flow meter and surface thermocouples were calibrated and their uncertainties evaluated. The surface thermocouples uncertainty did not exceed 0.6K, while the estimated uncertainty of flow meter was 8.8 mL/min utilising graduated cylinder procedure. The calibration and calculation of uncertainty is preformed to find the error in measured quantities and also to be used in finding the errors in the calculated parameters like maximum power output.

CHAPTER 7

Indoor and Outdoor Experimental Results and Validation of Simulation

7.1 Introduction

In this chapter a details description of results of the indoor and outdoor experimental testing carried out to study the dust accumulation effects on the optical, electrical and thermal performances of the 3D-PSCPV system. It includes the indoor and outdoor optical experimental results and validation of 3D-PSCV simulation, in term of optical efficiency under clean and dusty condition using three different concentration ratios of 2X, 4X, 6X with various surface reflectivity. Furthermore, electrical and thermal modelling validation of the dusty 3D-PSCVP system is offered by comparing the simulation and experimental studies of the 3D-PSCPV system with concentration ratio of 2X, 4X and 6X at different inlet water velocity. Lastly, the electrical characterises of the 3D-PSCPV using water cooling were described, such as I_{sc}, V_{oc}, maximum voltage, maximum current, maximum power output and electrical efficiency.

7.2 Optical results

7.2.1 Optical performance of the dusty glass cover

The experiment was repeated 3 times with different irradiance readings taken to ensure accurate transmittance prediction of the dusty cover and equation 3.7 was applied to determine the total transmission of the dusty samples. Figure **7.1** shows the pyranometer measurements at different combination of glass, film and dust at various levels of irradiance showing that with the increase of the irradiance the transmissivity of the dusty glass decreases compared to the clean glass cover. Furthermore, to ensure the uniformity of the dust particles distribution on the glass sample, irradiance measurements were taken at different position under the dusty glass sample, using the incoming irradiance 520 W/m^2 as can be seen in Figure **7.2**.

Figure **7.3** shows the results of dusty glass transmission for indoor and outdoor tests, the curves show that outdoor results are close to those obtained indoor with a small difference which due to the atmospheric conditions, where surrounding environment reflect more light such as the building and ground. The simulation and experimental results of glass transmittance measurements under dust accumulation were compared indicating good agreement with around ±3% difference as shown in Figure 7.4. The experiments have been performed utilising three different glass dimensions with 4mm thicknesses (see table 4.4) to represent the concentrators' entrance covers.

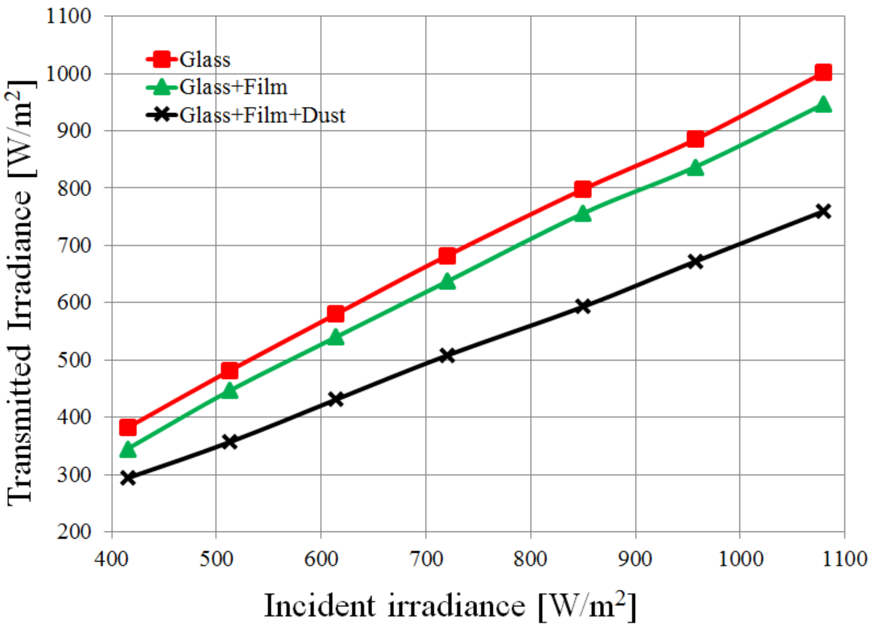

Figure 7.1 Measurements of different irradiance level at different combination of layers

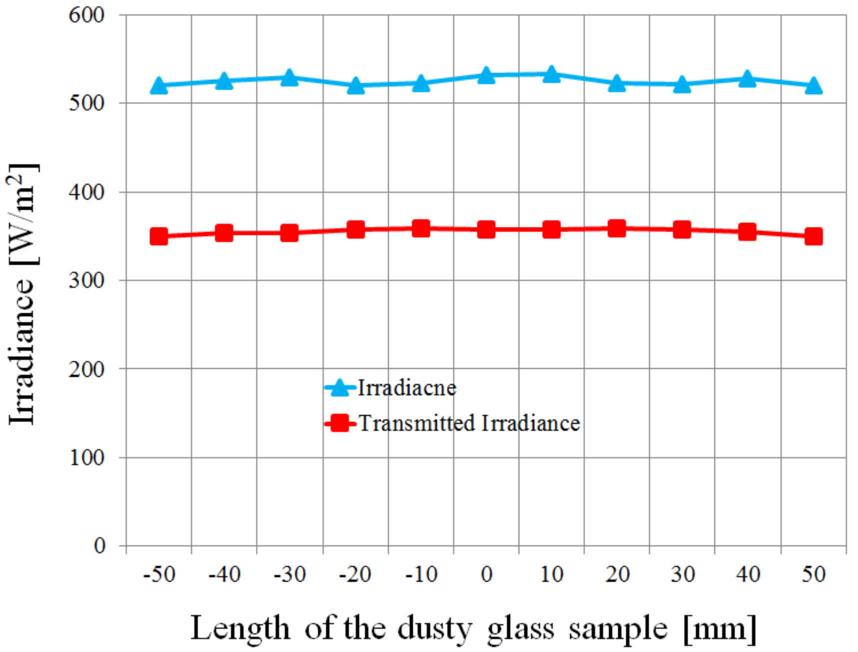

Figure 7.2 Measurements of irradiance under dusty sample at different positions

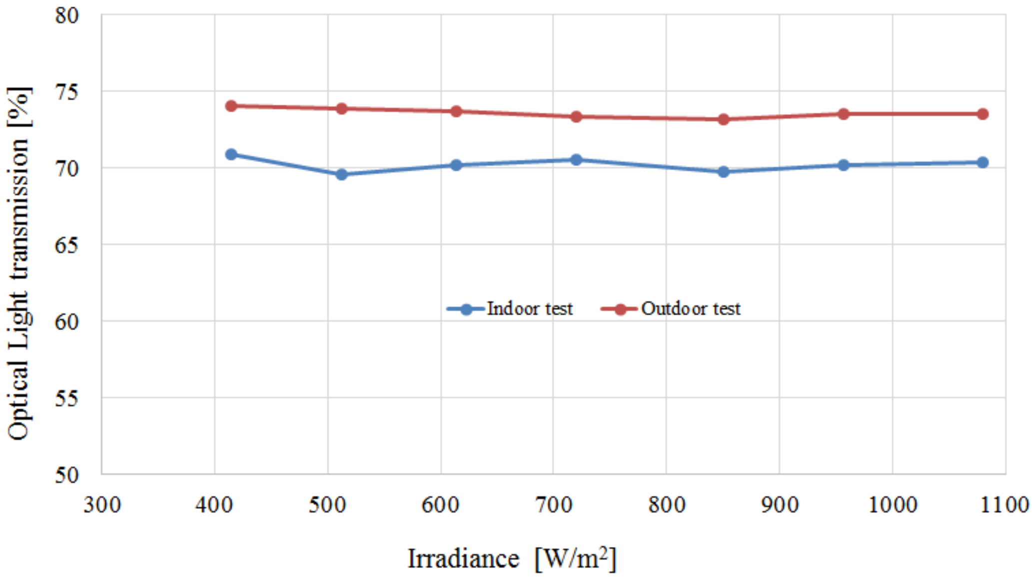

Figure 7.3 Variation of dusty glass transmission for indoor and outdoor tests

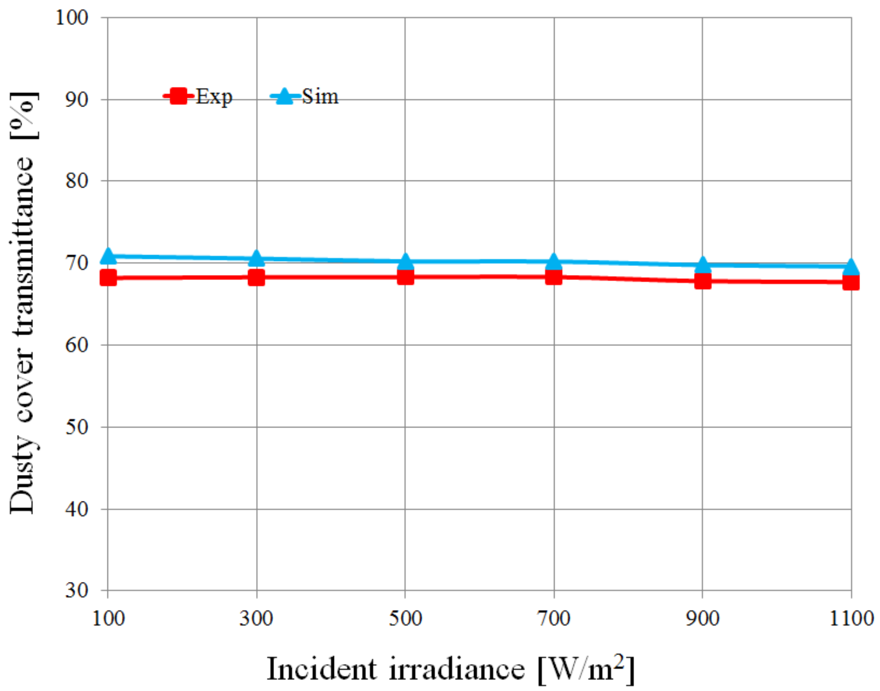

Figure 7.4 Light transmission comparison between experimental and ray-tracing simulation results of the dusty samples at different irradiance

7.2.2 Indoor optical experimental results of 3D-PSCPV

Concentrators were constructed and tested using different surface reflectivity of 60%, 70%, 80% and 90% and using different concentration ratios of 2X, 4X and 6X. The average incoming irradiance of 520W/m^2 was used with 0^o incident angle. Figure **7.5** compares the experimental results of the optical efficiency versus reflectivity for concentration ratio of 2X, 4X and 6X with the OptisWork^{TM} ray-tracing simulation results at 520W/m^2 and 0^o incident angle. A similarity was noticed between the simulation and experimental results, where a maximum difference of ±6% from the simulation was achieved. The results show that the concentrator optical efficiency decreases as the concentrator surface reflectivity decreases.

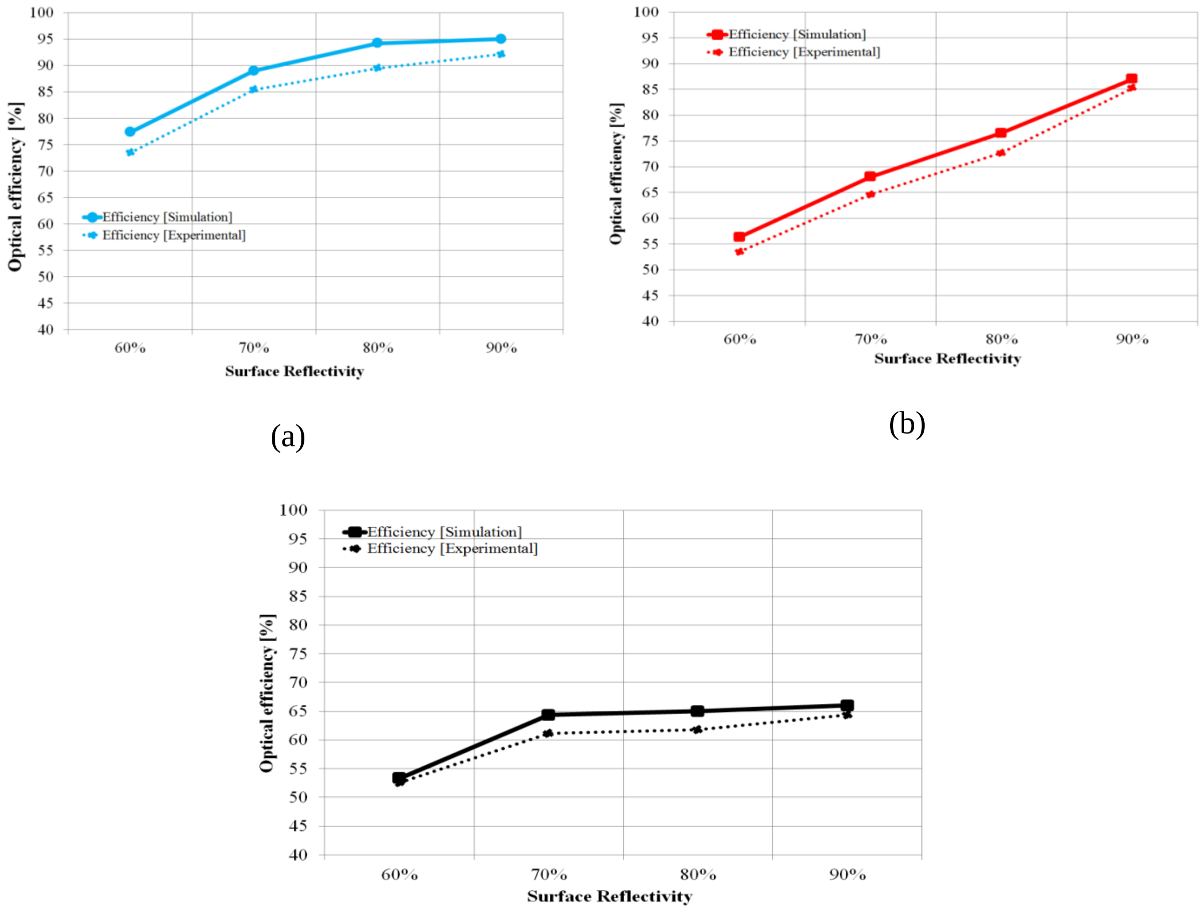

(a)

(b)

(c)

Figure 7.5 Comparison between ray-tracing simulation and experimental optical efficiency results for concentration ratio of: a) 2X, b) 4X and c) 6X

Figure **7.6** shows pictorial diagram of the received irradiance distribution pattern on the receiver plane acquired from the experimental and ray-tracing simulation showing similar pattern. This additionally verifies the validity of the developed 3D-PSCPV ray-tracing simulation.

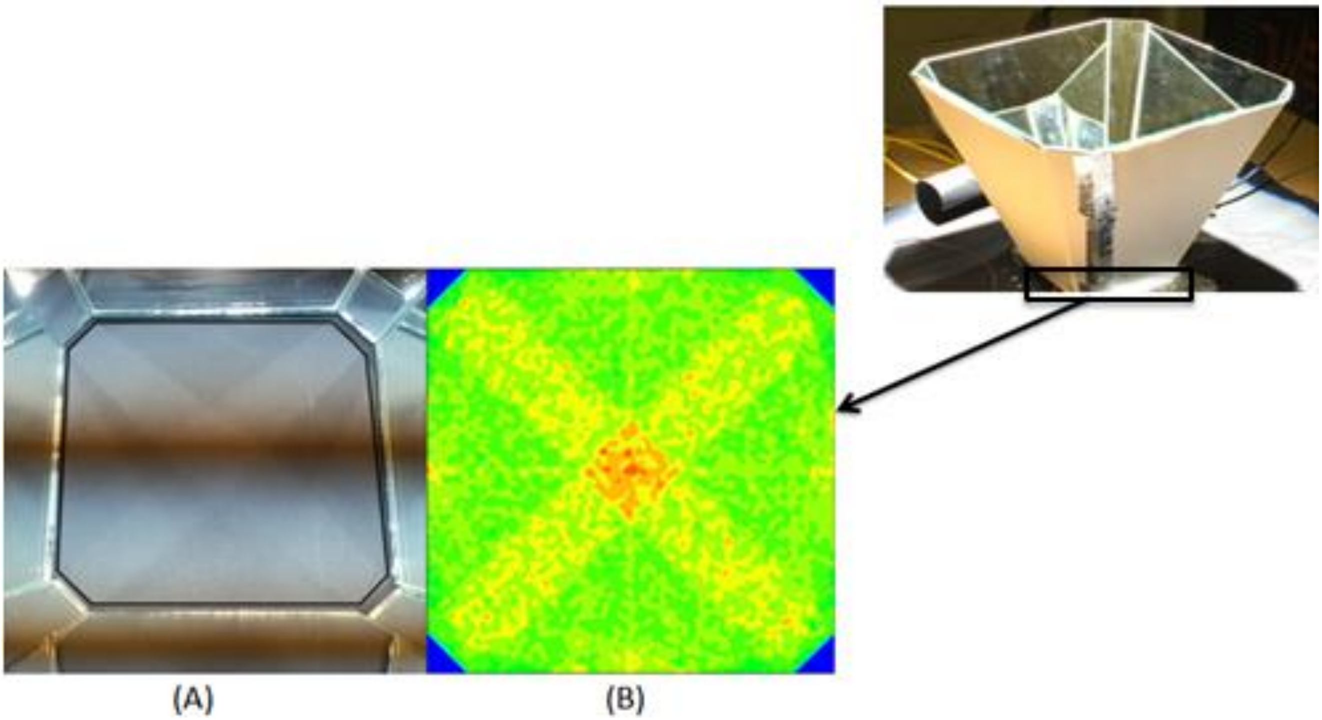

Figure 7.6 Photograph of the concentrated irradiance distribution on the receiver of the 3D-PSCPV, (A) obtained experimentally, (B) obtained by ray-tracing (OptisWork^{TM}) simulation

Figure **7.7** shows the optical efficiency of the dusty concentrators with 2X, 4X, 6X and dusty cover at various surface reflectivities 90%, 80%, 70%, 60% and irradiance at the entrance aperture of 520W/m^2. The graphs show that the experimental and simulation values of optical efficiency in dusty condition have a similar trend, and are in good agreement with around ±7% difference between the simulation and experimental results. This simulation results validation of the optical efficiency is important since they are an essential part in characterising the concentrated PV module (3D-PSCPV receiver).

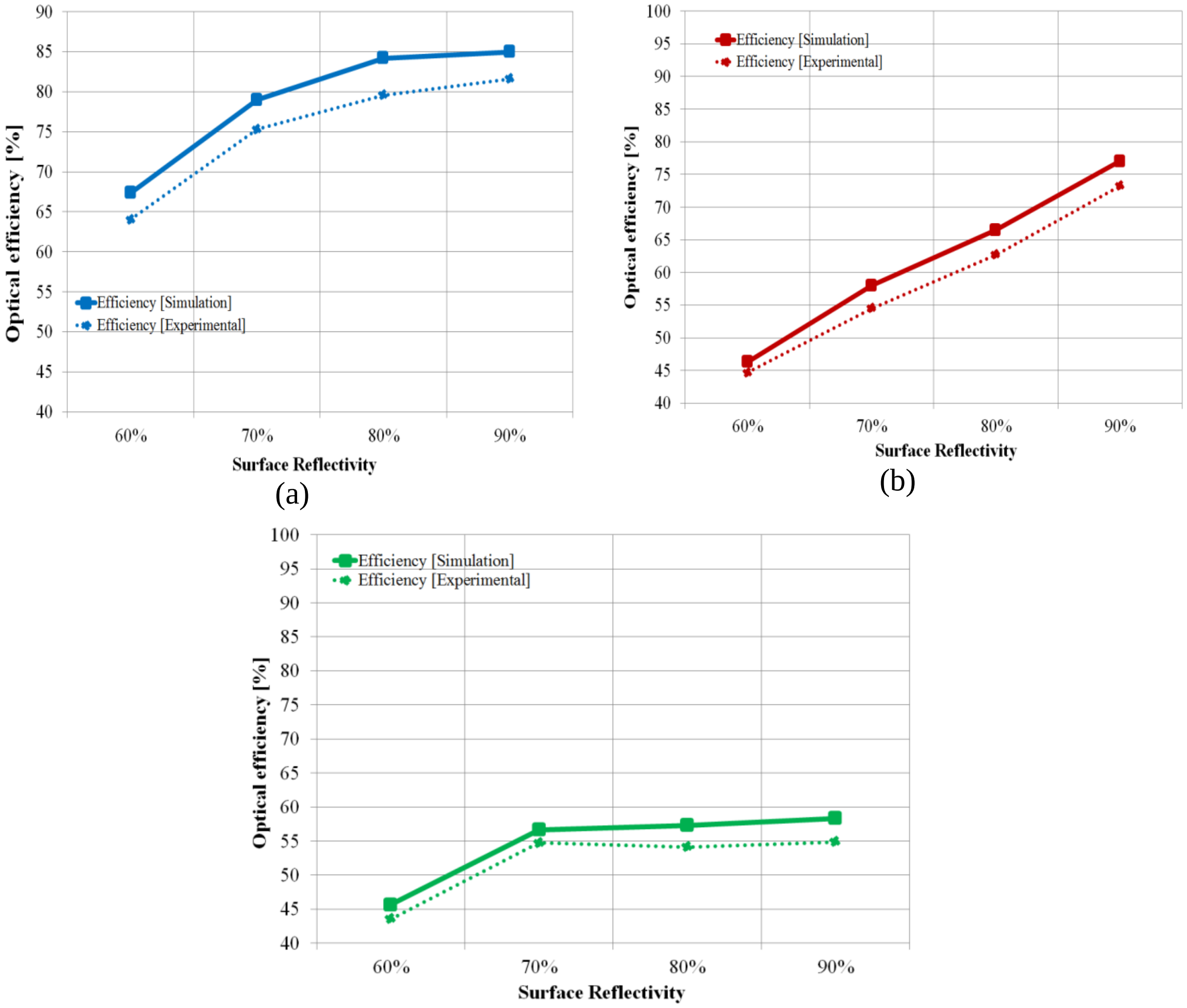

(a) (b)

(c)

Figure 7.7 Comparison of the ray-tracing simulation and experimental results of the dusty concentrator optical efficiency: (a) 2X, (b) 4X, (c) 6X

7.2.3 Outdoor optical experimental results of 3D-PSCPV

Concentrators were constructed and tested using 70% surface reflectivity with different concentration ratios of 2X, 4X and 6X. The average incoming irradiance of 870W/m^2 was used with 0^o incident angle. Figure **7.8** shows the outdoor experimental results of the 3D-PSCPV optical efficiency with concentration ratios of 2, 4 and 6 with three different conditions (uncovered, clean glass cover and dusty glass cover). It can be seen that the 3D-PSCPV with optical concentration ratio of 2X has higher optical efficiency compared to other concentration ratios of 4X and 6X at all conditions. It was observed that the 3D-PSCPV with optical concentration ratio of 2X produced higher optical efficiency of 77 and 87% for clean and dusty glass cover, respectively. But the 3D-PSCPV with optical concentration ratio of 4X and 6X produced higher concentrated irradiance with lower optical efficiency of 66 and 62% with clean glass cover, respectively. With dusty glass cover the 3D-PSCPV with optical concentration ratio of 4X and 6X produced lower optical efficiency of 56.8 and 53%, respectively. As a result of dust accumulation the optical efficiency decreased 11.2, 13.9 and 15% for the 3D-PSCPV at optical concentration ratios of 2X, 4X and 6X, respectively. It can be seen from such figure that the 2X is the least affected by dust accumulation compared to 4X and 6X.

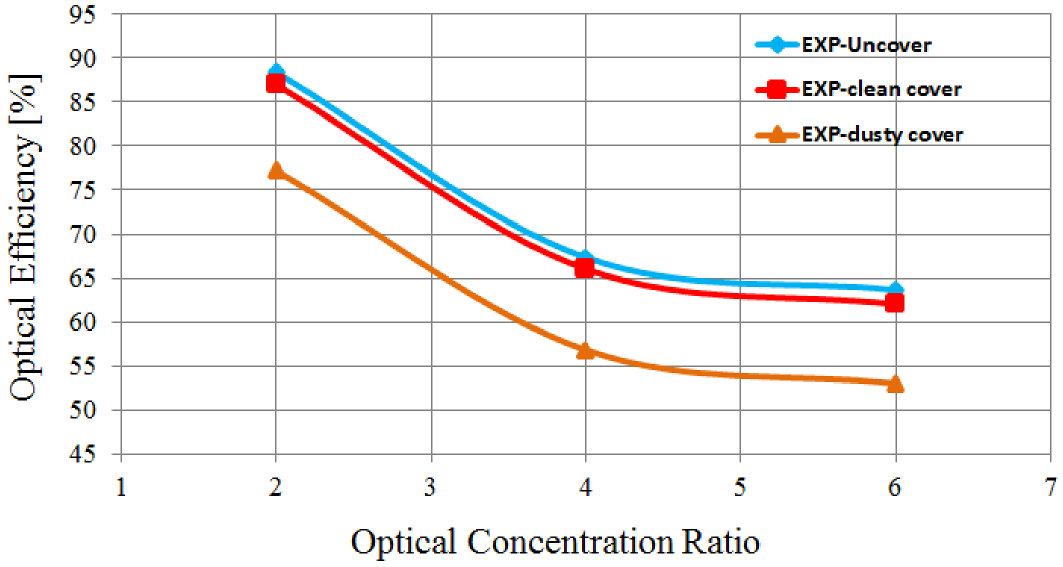

Figure 7.8 Variation of optical efficiency with the concentration ratio of the 3D-PSCPV in different conditions (uncovered, clean glass cover and dusty glass cover)

Ray-tracing analysis was performed by OptisWork^{TM} on a 3D-PSCPV with surface reflectivity of 70% and different concentration ratios. The simulation was run at different optical concentration ratios with uncover, clean glass cover and dusty glass cover, then the incoming and received concentrated irradiance were acquired and optical efficiency calculated. The simulation and experimental (outdoor) results were evaluated and they showed close agreement around ±3.8% difference as shown in Figure **7.9**.

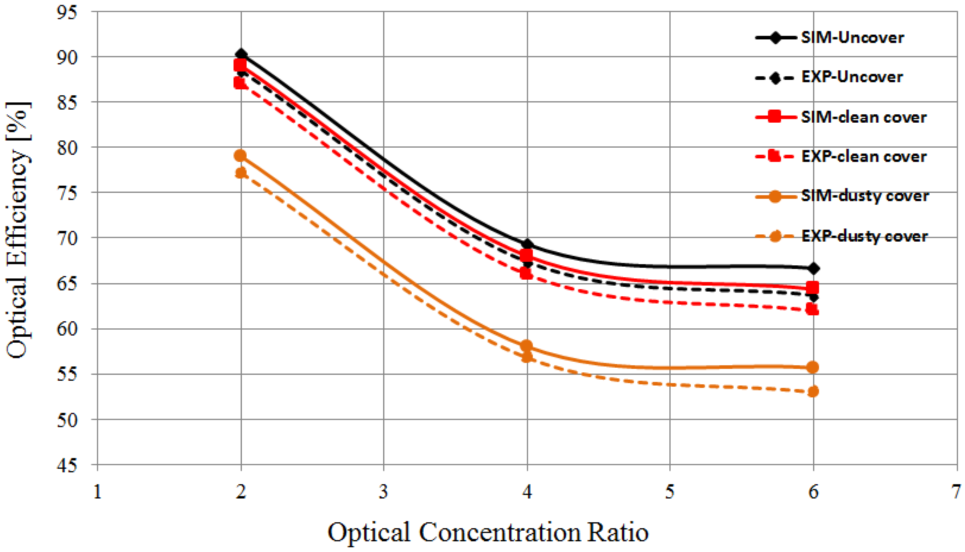

Figure 7.9 Comparison between experimental and simulation optical efficiency results of the 3D-PSCPV with different optical concentration ratios

A uniform irradiance distribution over the PV module surface is desired in CPV system for greater power output. However, it is challenging to develop a CPV system to achieve a concentrated light with uniform distribution on the receiver plane without the occurrence of high concentration areas [10, 139, 190]. Figure **7.10** shows that the irradiance concentrated on the receiver plane increases with the increase of the optical concentration ratio. The irradiance intensity distribution at receiver also varies with different optical concentration ratio of the concentrator in clean and dusty conditions. The variation of the amount distribution on 3D-PSCPV receiver with optical concentration ratio of 2X, 4X and 6X is shown in Figure **7.10** for concentrator with no cover (uncover), clean glass cover and dusty glass cover. It can be seen from such figure that the highest peak of irradiance is at the centre of the receiver, the uncover concentrator shows maximum irradiance of 1730, 2740 and 3900 W/m^2 for optical concentration ratios of 2X, 4X and 6X, respectively. Once the clean cover is used, the irradiance at the centre decreased to 1680, 2465 and 3620 W/m^2 for 3D-PSCPV optical concentration ratio of 2X, 4X and 6X, respectively. Finally, when the glass was covered with dust, the irradiance at the centre was further decreased to 1600, 2150 and 3200 W/m^2 for 3D-PSCPV optical concentration ratio of 2X, 4X and 6X, respectively.

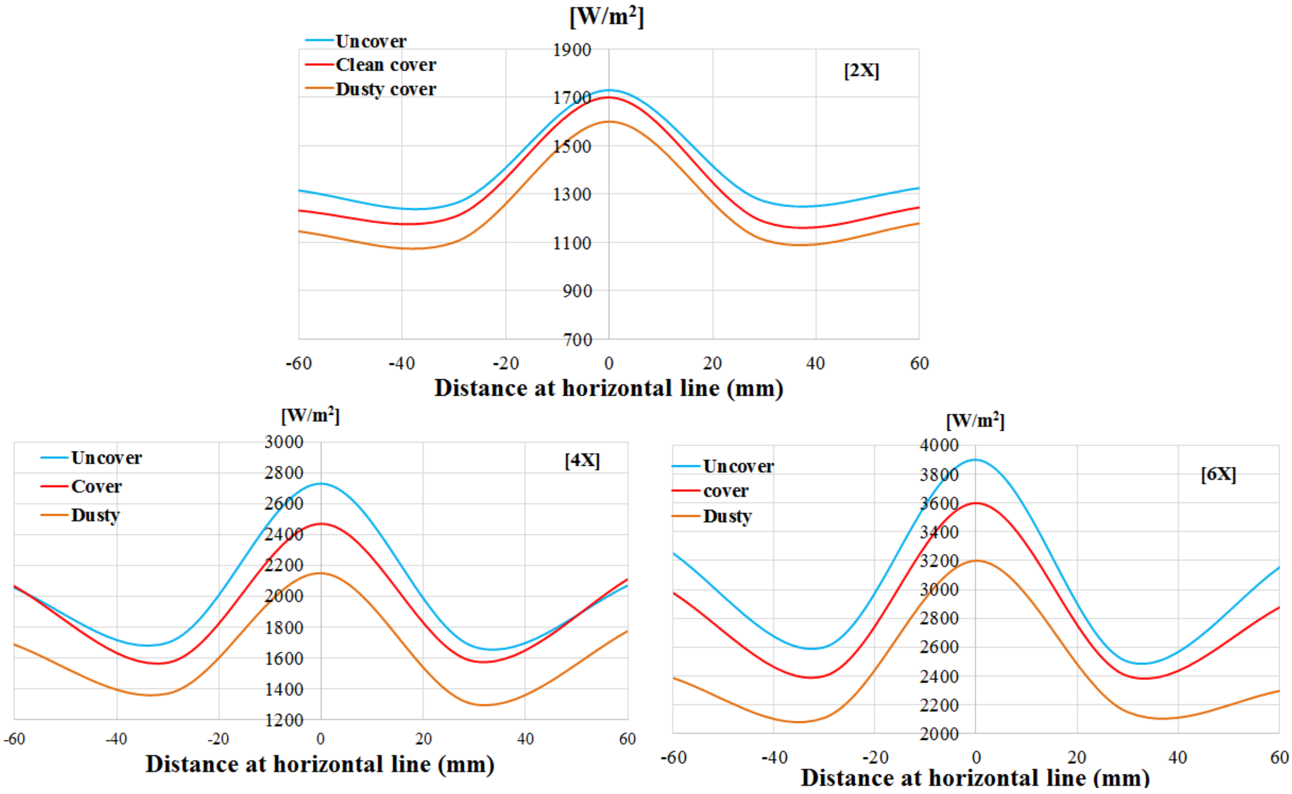

Figure 7.10 Irradiance distribution at the central line (62.5mm-horzintal) of the 3D-PSCPV receiver for light incident angle of 0° with different concentration ratio: 2X, 4X and 6X

7.3 Thermal experimental results

7.3.1 Temperature distribution under concentration in indoor condition

The temperature of the 3D-PSCV receiver at clean and dusty condition was investigated. The variation of temperature with different concentration ratio is shown in Figure **7.11** for radiation perpendicular to the 3D-PSCPV entrance aperture of 1000 W/m^2 at steady state condition achieved after 120 minutes. The temperature difference is changing between temperature sensor in locations T1 and T7 as the concentration ratio increases. The maximum PV module temperature of 66, 88.5, 126 and 135°C for 1X, 2X, 4X and 6X under clean condition, respectively was reached at the centre area of the PV module (T7). Under dusty condition, the maximum PV module temperature of 55, 81, 115 and 127°C for 1X, 2X, 4X and 6X, respectively, were reached in the central area of the concentrator receiver (T7) indicating lower PV operating temperature.

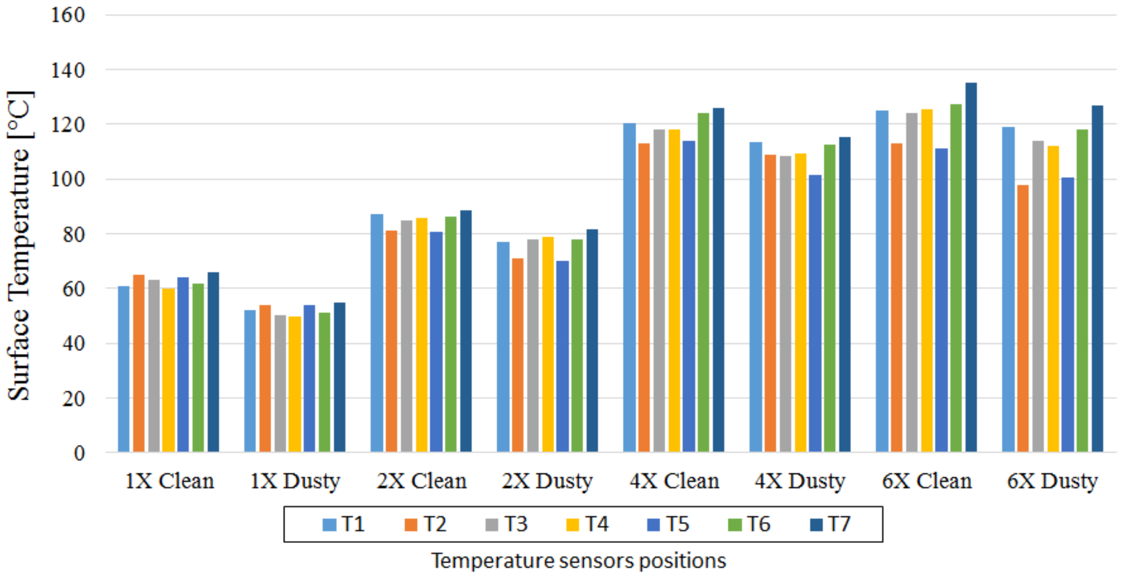

Figure 7.11 Measured temperatures for the 3D-PSCPV receiver at a constant incident radiation of 1000W/m^2 and 24ºC room temperature

7.3.2 Variation of PV module Temperature with cooling water inlet velocity in indoor condition

The experimental results of the PV module temperature is compared with the thermal simulation results at four concentration ratios and cooling water inlet velocity magnitude ranging from 0.0011 to 0.037 m/s as shown in Figure **7.12** in dusty condition. It can be seen that the PV module back surface temperatures for both experimental tests and CFD simulation have similar trend and are in good agreement with maximum difference of ±3%.

.

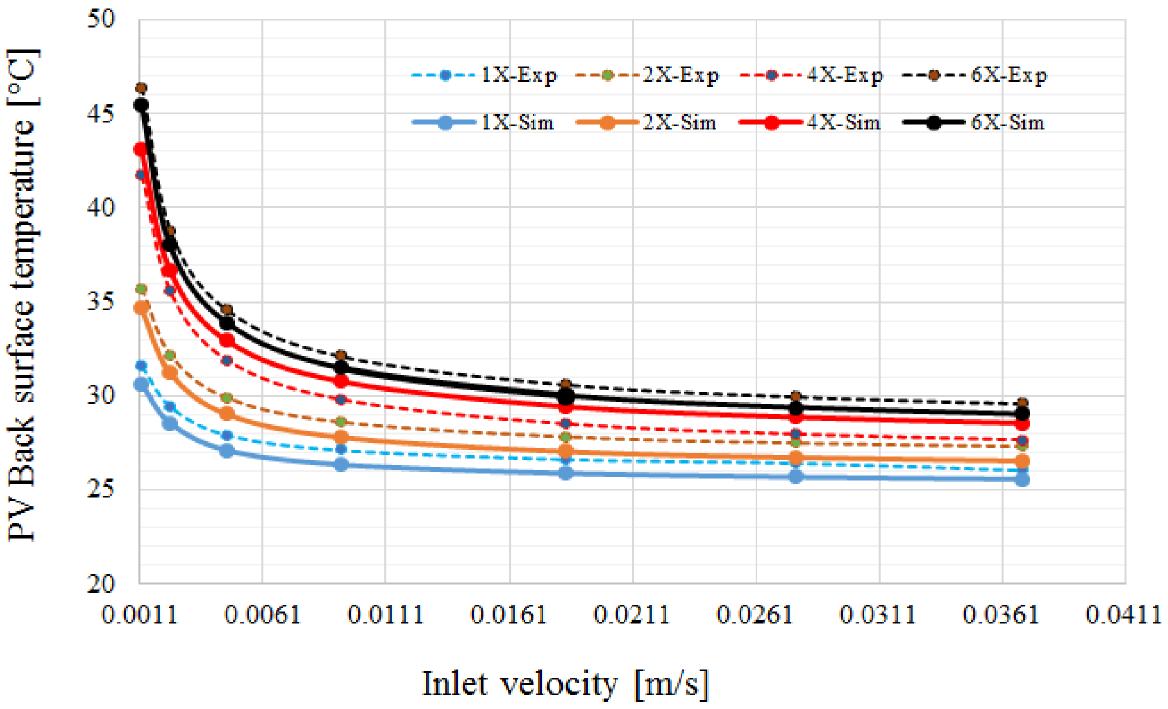

Figure 7.12 Comparison of the experiment PV module assembly back surface temperature with the predicted at different velocity and concentration ratios in dusty condition

Figure **7.13** compares the simulation and experimental water outlet temperatures at different concentration ratios when the velocity is 0.00461 m/s. It can be seen that the highest water outlet temperatures was obtained at the 4X and 6X concentration ratios. Also the experimental water outlet temperatures at different concentration ratios showed close agreement with the simulation with difference ranging from 1.7% at concentration ratio of 1X and 2X to 5.1% at concentration ratio of 4X and 6X.

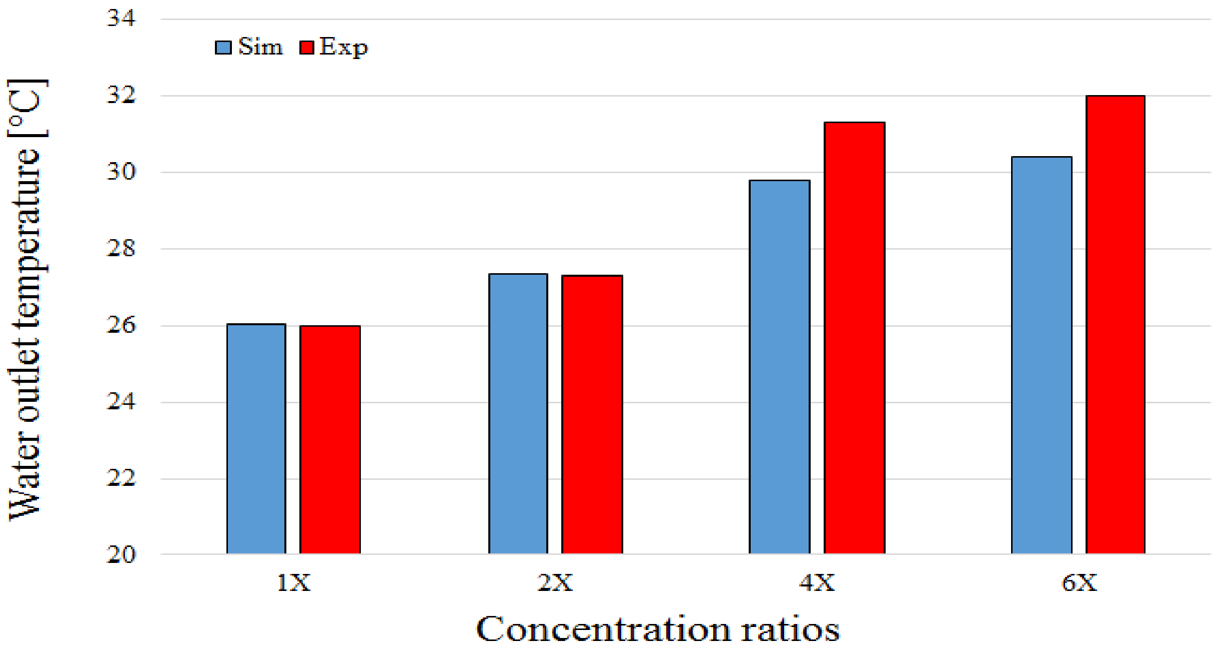

Figure 7.13 Comparison of the experimental water outlet temperature with predicted at different concentration ratios

7.3.3 Temperature distribution under concentration in outdoor condition

The measured temperature on the horizontal plane of the 3D-PSPCV receiver (PV module) for three different optical concentration ratios when the concentrator is with clean and dusty glass covers without cooling is shown in Figure **7.14** (a, b and c) at irradiance of 870W/m^2. It can be seen that the temperature distributions of the 3D-PSCPV on the receiver in the three figures present similar trend. It can also be deduced from the figures that there is hot spot occurring in the centre of the receiver which increased as the optical concentration ratio increased. The maximum hot spots temperature of the PV module are 76, 97 and 125°C for clean 3D-PSCPV with optical concentration ratio of 2X, 4X and 6X, respectively. Once the concentrator are covered with dusty glass these temperature values decreased to 73, 89 and 112°C for optical concentration ratios of 2X, 4X and 6X, respectively.

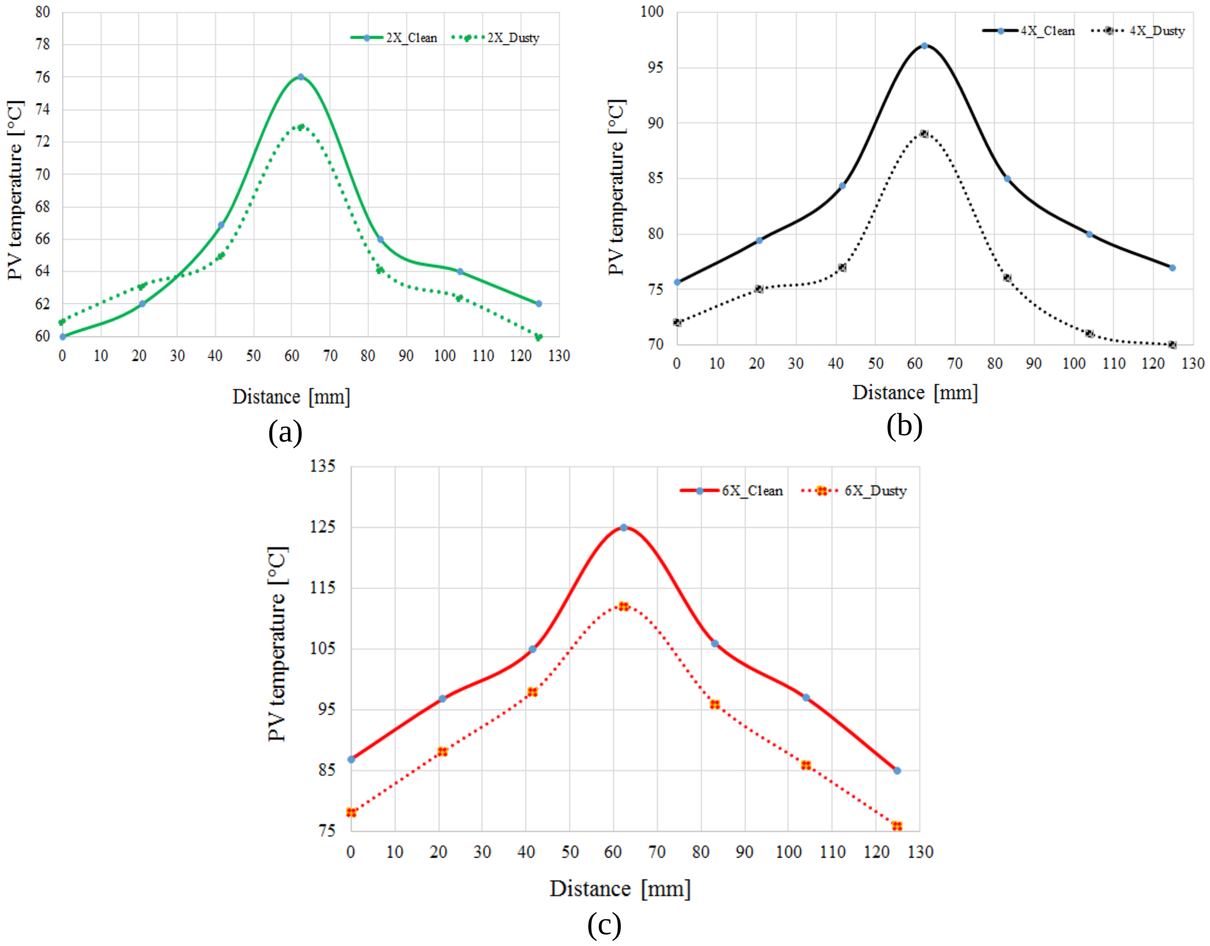

(a)

(b)

(c)

Figure 7.14 Temperature distribution at the horizontal line of the 3D-PSCPV receiver for light incident angle of 0º with different concentration ratio: (a) 2X, (b) 4X and (c) 6X

7.3.4 Variation of PV module Temperature with cooling water inlet velocity in outdoor condition

The thermal performance of the cooling channels integrated with concentrator was investigated outdoor at various water inlet water velocity. Figure **7.15** shows that the surface temperature of PV module decreases with the increase in the water inlet velocity.

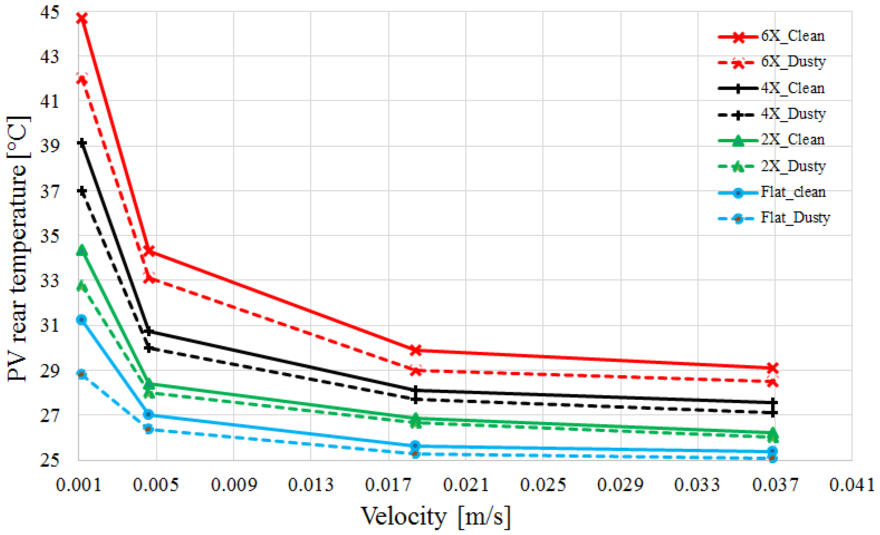

Figure 7.15 Change of the PV module average temperature with the inlet water velocity magnitudes at ambient temperature and wind speed of 26°C and 3 m/s, respectively

For the purpose of validation, six irradiance inputs from 3D-PSCPV receiver with different optical concentration ratio in clean and dusty conditions from section 7.2.3 were inputted to the PV module assembly surface considering the water inlet velocity to the cooling channels is uniform. Figure **7.16** shows the predicated and experimental water temperature difference between outlet and inlet for 3D-PSCV with different concentration ratios and non-concentrated PV showing close agreement around ±4%.

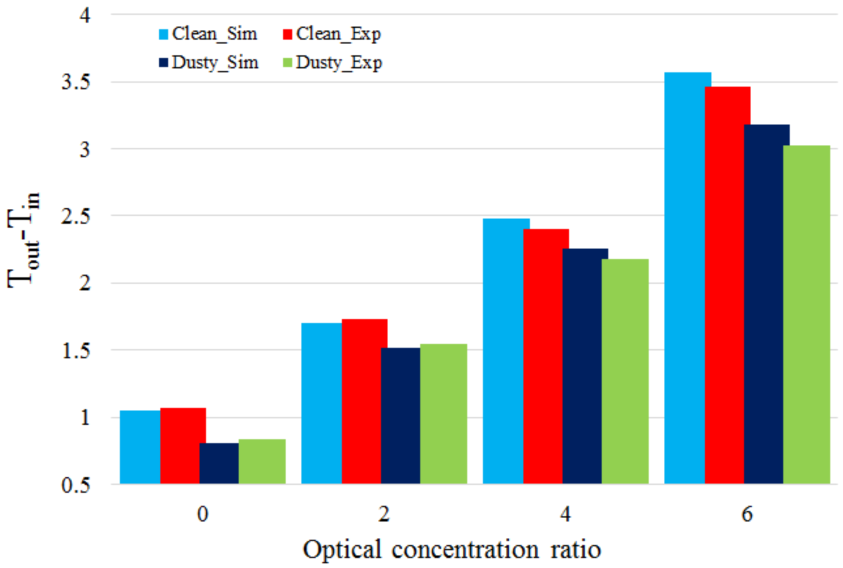

Figure 7.16 Comparison between experimental and simulation results

7.3.5 Variation of Thermal power with cooling water inlet velocity in outdoor condition

Figure 7.17 shows thermal power of 3D-PSCPV at clean and dusty condition with different concentration ratios of 2X, 4X and 6X and inlet water velocity. The thermal output power for both clean and dusty 3D-PSCPV increased with increasing the water velocity inlet and concertation ratio. However, the 3D-PSCV with dusty condition is constantly produced lower thermal output power than clean condition due to dust accumulation lowers the input radiation on PV surface. The maximum thermal output power are 23.7W, 42.27W, 46.68W, 6.15% for clean concentrator with concentration ratio of 2X, 4X and 6X, respectively, at water inlet velocity of 0.037m/s. Yet, the 3D-PSCPV maximum thermal power output decreased as dust accumulated on the entrance aperture, the decrease was around 12.02, 14.1 and 16.3% at concentration ratio of 2X, 4X and 6X, respectively. For the 3D-PSCPV with concentration ratio of 2X, 4X and 6X in clean condition the thermal power increased around 35, 28 and 23% with increasing water inlet velocity, respectively. At dusty condition the thermal power increased around 32, 25 and 20% of concentration ratio of 2X, 4X and 6X with increasing water inlet velocity, respectively

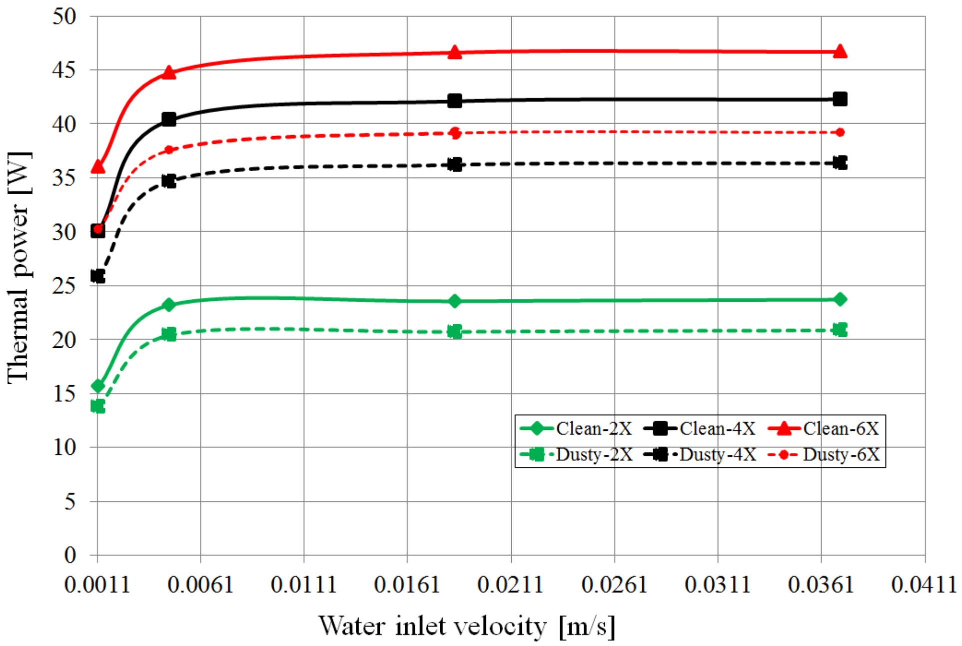

Figure 7.17 Thermal output power of 3D-PSCPV system at various water inlet velocity and concentration ratios

7.4 Electrical experimental results and validation

The electrical experimental work was performed for different cases as described below:

Indoor case 1: Non-concentrated module at 1X (1000 W/m^2) with clean and dusty glass cover.

Indoor case 2: A concentrating 3D-PSCPV with 90% surface reflectivity and concentration ratios of 2, 4 and 6 with clean glass cover and dusty glass cover.

Outdoor case 3: Non-concentrated module with clean and dusty glass covers at irradiance of 870W/m^2.

Outdoor case 4: A concentrating 3D-PSCPV with 70% surface reflectivity and concentration ratios of 2, 4 and 6 with clean glass cover and dusty glass cover.

7.4.1 Indoor experimental results

7.4.1.1 Indoor I/V curves characteristics

Figure **7.18** compares the simulation and experimental results of I/V curve at various concentration ratios in dusty and clean conditions. It can be seen that good agreement between the simulation and experimental results is achieved. Also, it is clear that the short-circuit current increases with increasing the concentration ratio while open circuit voltage decreases for both clean and dusty conditions. The clean 3D-PSCPV short circuit current increased by up to 1.82, 3.4 and 3.8 times the non-concentrated PV shorts circuit current at concentration ratios of 2X, 4X and 6X, respectively. Due to dust accumulation, the short-circuit current dropped by 12.65%, 14.65% and 14.71% for the dusty 3D-PSPCV with concentration ratios of 2X, 4X and 6X, respectively, compared to its corresponding clean 3D-PSCPV. The 3D-PSCPV with concentration 6X is the most affect by dust accumulation compared to other concentrators. Moreover, the drop in PV module short-circuit current under solar concentration is less compared with non-concentrated PV module, where the short-circuit current at 1X (1000 W/m^2) decreased by 26.25%. As expected the higher the concentration ratio, the higher the differences are between the clean and dusty short-circuit current.

As for the open-circuit voltage, it decreased with the increase of concentration ratios, but the dusty 3D-PSCPV always produced higher open-circuit voltage compared to the clean 3D-PSCPV. The insignificant increase of approximately 2.55% and 3.8 % of the dusty PV modules open-circuit voltage is related to the reduction in junction temperature caused by dust particles attenuating light and reducing the heat at the concentrator receiver. The absence of steps and notches in the I/V curves were a result of the good measurement circuit connections and to the lack of mismatches within the PV cells.

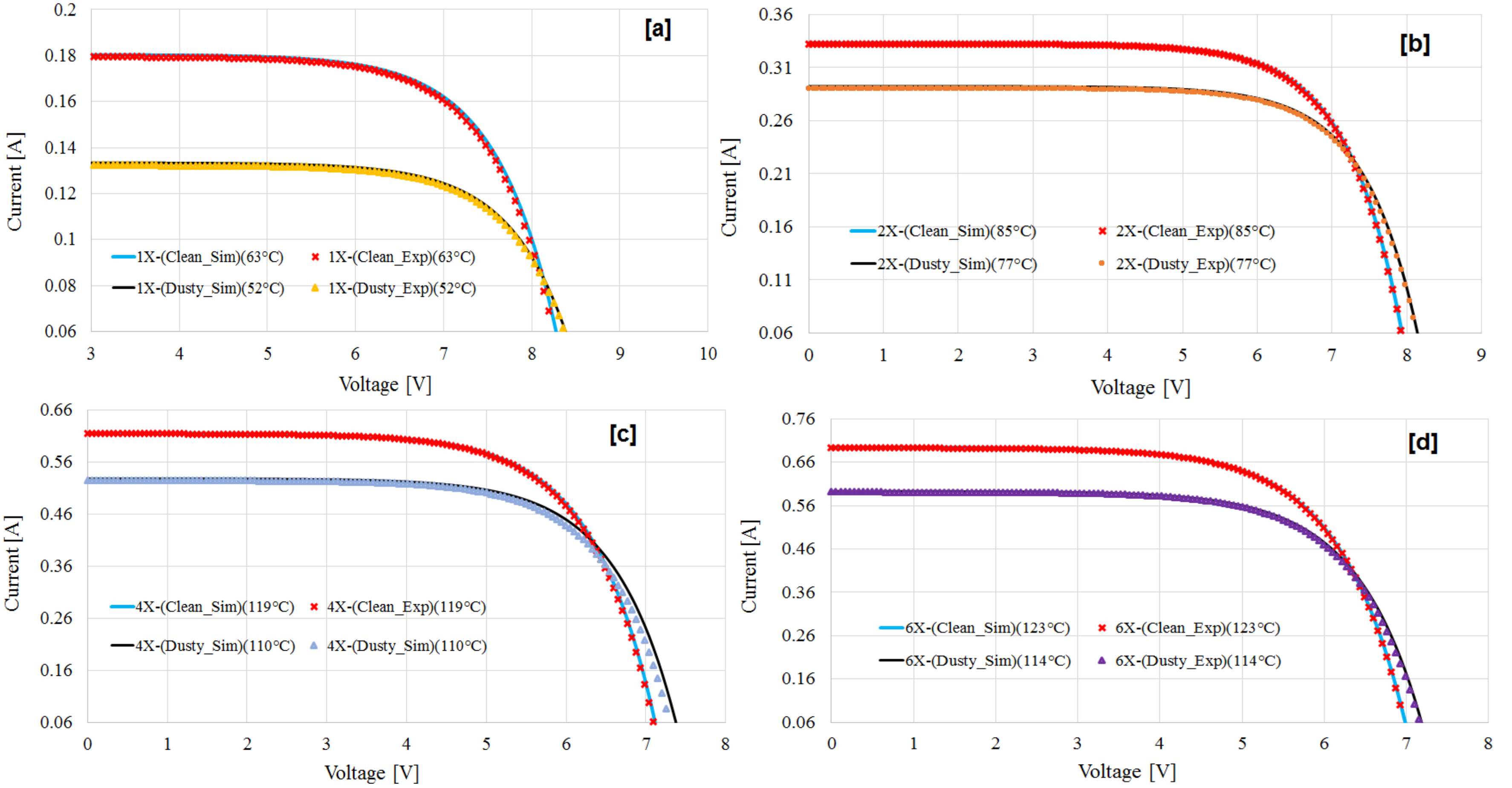

Figure 7.18 Indoor experiment of I/V characterisations of clean and dust 3D-PSCPV system at solar radiation intensity of 1000 W/m^2 and 24ºC ambient room ambient temperature,(a)1X, (b)2X, (c) 4X and (d) 6X

The simulation results of electrical outputs were compared with the experimental electrical outputs in similar test conditions (irradiance = 1000W/m^2, room ambient temperature = 24^{o}C) as shown in Table **7.1**. It can be seen that the fill factor values varied between 74% and 68%, which is within the range of the silicon PV cells [191, 192]. The obtained value of fill factor indicates a low series resistance of the PV module assembly. The simulation and experimental results were compared showing close agreement within ±1.5%, ±2%, ±1% difference for I_{sc}, V_{oc} and FF, respectively, at both clean and dusty condition of the 3D-PSCPV.

Table 7.1 Comparison between simulation and indoor experimental of 3D-PSCPV electrical outputs at different concentration ratios and conditions (clean and dusty)

	Concentration ratio	**Simulation (PV parameters)**			**Experimental (PV parameters)**		
		V_{oc}	I_{sc}	FF	V_{oc}	I_{sc}	FF
Clean Condition	1X	8.58	0.18	73.14	8.522	0.178	73.43
	2X	8.085	0.333	71.32	8.075	0.332	71.2
	4X	7.205	0.615	67.32	7.15	0.614	67.7
	6X	7.095	0.695	66.36	7.04	0.689	67
Dusty Condition	**Concentration ratio**	**Simulation (PV parameters)**			**Experimental (PV parameters)**		
		V_{oc}	I_{sc}	FF	V_{oc}	I_{sc}	FF
	1X	8.8	0.133	74.53	8.83	0.132	74.47
	2X	8.36	0.292	71.8	8.305	0.289	72.41
	4X	7.48	0.528	68.5	7.425	0.524	68.27
	6X	7.26	0.593	66	7.22	0.591	67.6

7.4.1.2 Effect of dust accumulation on the power output at different concentration ratios

The power output of the 3D-PSCPV at three different concentration ratios (2X, 4X and 6X) was experimentally investigated then simulated with solar radiation inputs of 1000 W/m^2.

Figure **7.19** compares the predicted maximum power output with those of the experiments for different concentration ratios and room temperature of 24°C for clean and dusty conditions, at irradiance of 1000 W/m^2 showing good agreement with deviation of ±1.2% and ±2%. There is significant increase in the maximum power output as the concentration ratio of the 3D-PSCPV increases in both dusty and clean conditions. This is due to the increase in the received irradiance as the concentration ratio increases. The maximum power output increased by 30.5, 115 and 135% at concentration ratio of 2X, 4X and 6X, respectively compared to the maximum power output with no concentration (1X). However, the 3D-PSCPV maximum power output decreased as dust accumulated on the entrance aperture, the decrease was around 10, 12 and 12.6% at concentration ratio of 2X, 4X and 6X, respectively. Figure **7.19** shows that the non-concentrated PV maximum power output significantly dropped by around 33% due to the accumulation of dust. Hence, the effect of dust accumulation is higher in the case of non-concentrated PV system than CPV system.

Figure **7.20** shows the PV module temperature and maximum power output at various concentration ratios for clean and dusty conditions at 1000W/m^2 input irradiance. It can be seen that increasing the concentration ratio of the 3D-PSCPV increases the maximum power output and increase the PV module temperature. However the presence of dust resulted in reducing the PV power output and PV module temperature compared to the clean PV due to the effect of dust in reducing the amount of radiation received by the PV module. Although the presence of dust resulted in reducing the PV temperature, cooling is still required to reduce the concentrated PV temperature to acceptable operating condition and increasing the power output.

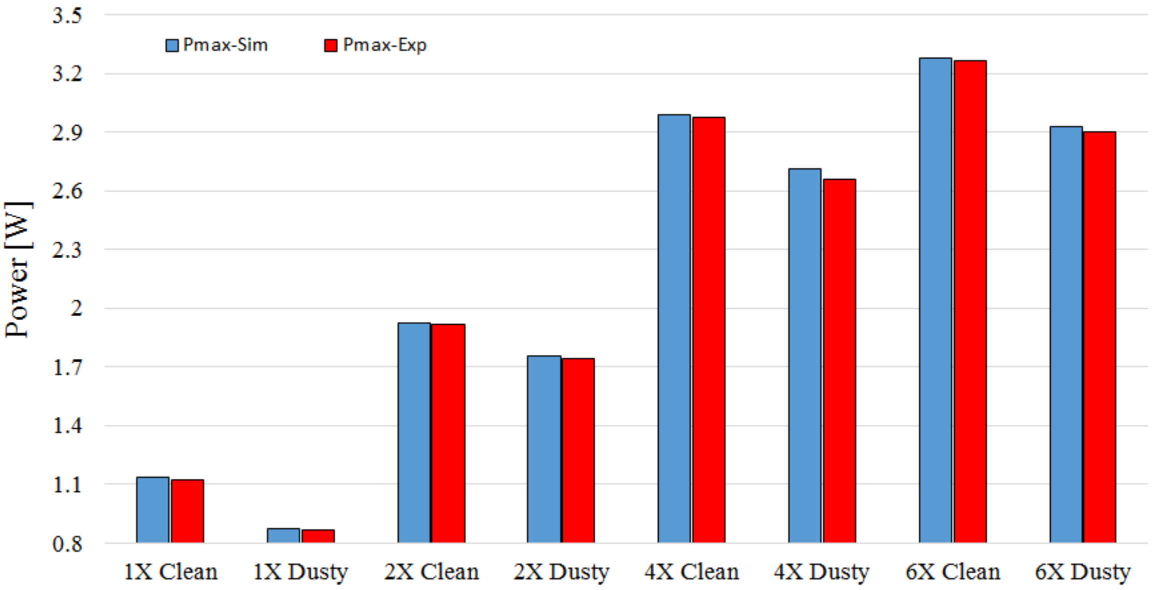

Figure 7.19 Comparison of the experimental maximum power output with predicted at various concentration ratio in clean and dusty conditions

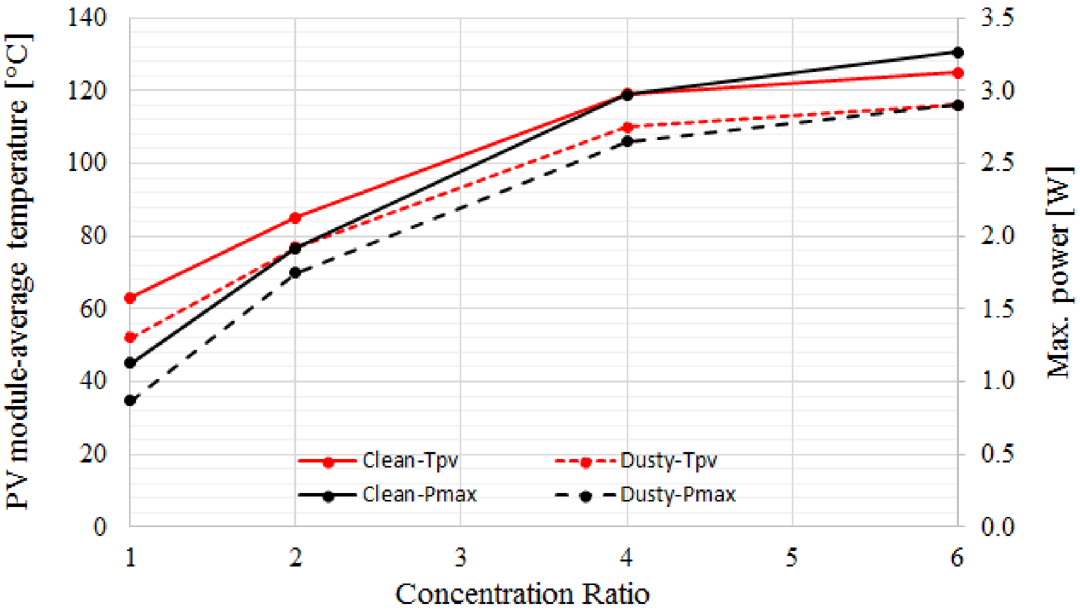

Figure 7.20 Variation of the average 3D-PSCPV receiver (PV module) temperature and maximum power with concentration ratio (in clean and dusty states)

7.4.1.3 Effect of dust accumulation on the voltage and current characteristics at different concentration ratios

Figure **7.21** shows the variation of open-circuit voltage and PV module temperature at various concentration ratio for the dusty and clean 3D-PSCPV at 1000 W/m^2. It can be seen that the open-circuit voltage decreases with the increase of concentration ratio. However, the open-circuit voltage for the dusty case is higher than that of the clean case. This could be attributed to the higher PV module temperature obtained with the clean 3D-PSCPV compared to that of the dusty one. Figure **7.22** shows the change of the PV module temperature and short circuit current with concentration ratio for dusty and clean 3D-PSCPV at 1000W/m^2. It can be seen that the short circuit current increases with the increase in concentration ratio due to the increase in received radiation. Also, the short-circuit current for the clean 3D-PSCPV is higher than that of the dusty one.

Figure **7.23** shows the variation of short-circuit current and open-circuit voltage at various concentration ratios for clean and dusty 3D-PSCPV at 1000W/m^2. Up to 3.2 % increase in open-circuit voltage outputs can be noticed in the 3D-PSCPV, due to the presence of dust. The open-circuit voltage of the clean system is found to vary from 8.52V to 7.04V with the concentration ratio vary from 1X to 6X. While, the open-circuit voltage of the dusty system is vary from 8.8V to 7.26V with the concentration ratios vary from 1X to 6X. The increase in dusty system open circuit voltage is due to lower PV module temperature compared to clean system as shown in Figure **7.21**. and Figure **7.23** shows up to 14 % decrease in the short-circuit current outputs of the 3D-PSCPV system due to the presence of dust with the concentration, while for the case of no concentration reduction of 23% is achieved. The short-circuit current of the clean system is vary from 0.179, 0.614 and 0.693A with the concentration ratios of 2X, 4X and 6X, respectively. While, the short-circuit current outputs of the dusty system is found to vary from 0.29, 0.524 and 0.59 amp with the concentration ratios of 2X, 4X and 6X, respectively. The reduction in dusty system current output is due to reduction in received radiation lowered by dust accumulation as shown in Figure **7.2**.

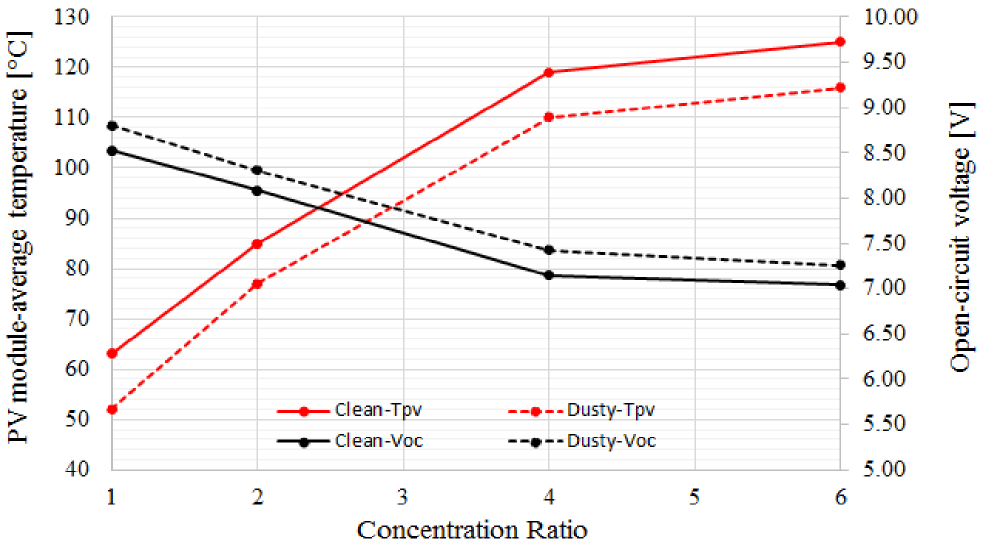

Figure 7.21 Variation of the open-circuit voltage and average PV module temperature with change in concentration ratio under clean and dusty states

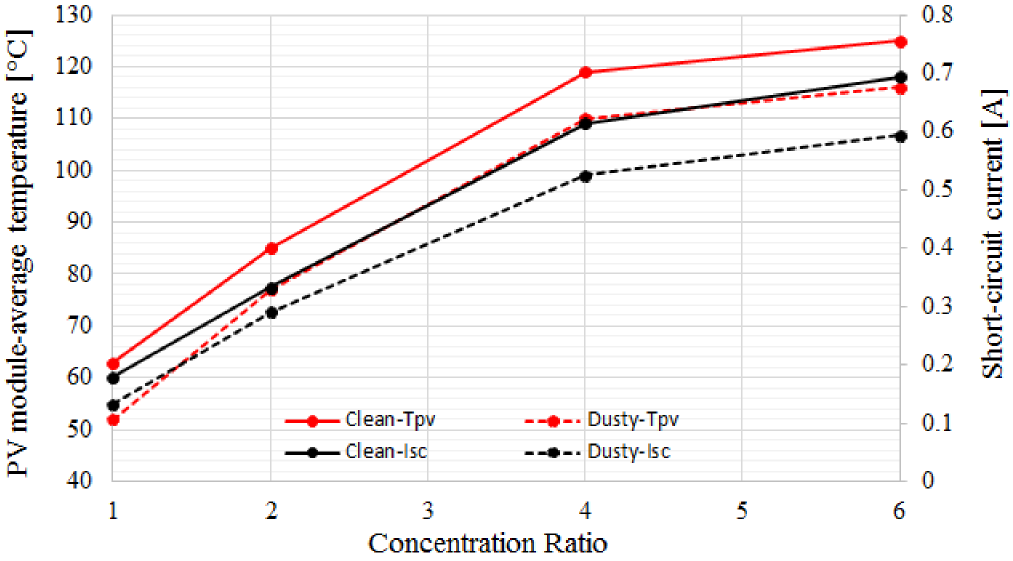

Figure 7.22 Variation of short-circuit current and average PV module temperature with change in concentration ratio under clean and dusty states

The results shown in Figure **7.23** clarifies some of the missing knowledge in literature on the effects of dust accumulation on CPV highlighting that the effect of dust is more significant on short-circuit current but insignificant on open-circuit voltage especially as the concentration ratio increases.

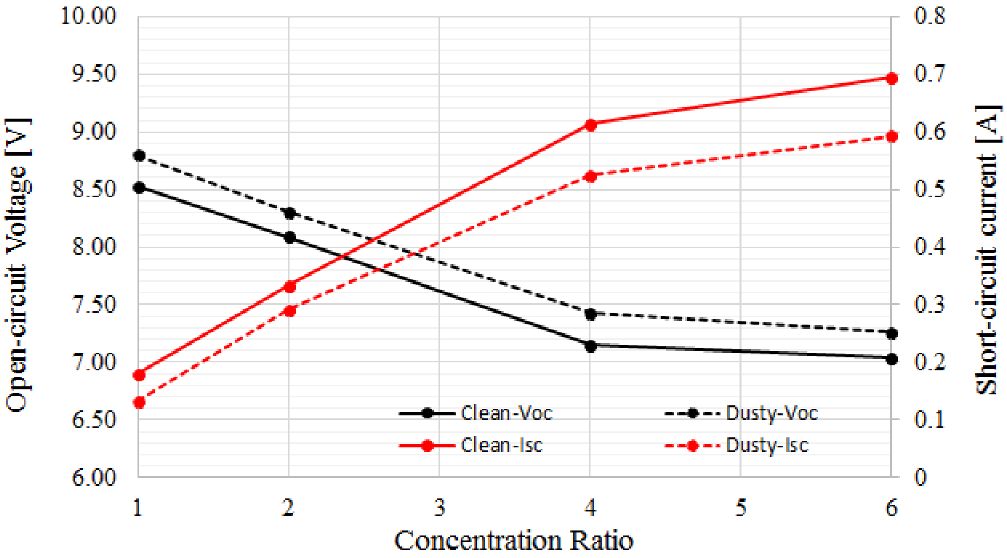

Figure 7.23 Variation of the short-circuit current and open-circuit voltage with change in concentration ratio under clean and dusty states

7.4.1.4 The Effect of dust accumulation on 3D-PSCPV system Efficiency

The system electrical efficiency η_{system} of concentrated PV system is determined by [117, 193]:

$$\eta_{system} = \eta_{electrical} \cdot \eta_{optical} \tag{7.1}$$

Where $\eta_{electrical}$ and $\eta_{optical}$ are the electrical conversion efficiency and the concentrator optical efficiency, respectively.

The system electrical conversion efficiency of the 3D-PSCPV with and without the dust accumulation and the maximum power output are shown in Figure **7.24** at various concentration ratios. It can be seen that the 3D-PSCPV without the dust accumulation (clean) had a higher efficiency than that with the dust accumulation with similar incoming irradiance (1000W/m^2) at the different concentration ratios used.

The system electrical conversion efficiency for both clean and dusty 3D-PSCPV decreased with increasing the concentration ratio, this is due to the increased cell temperature. The electrical conversion efficiencies are 12.7, 10.8, 8.4, 6.15% for clean concentrator with concentration ratio of 1X, 2X, 4X and 6X, respectively. Moreover, as a result of the dusty glass cover (dust accumulation phenomena) the system electrical efficiency decreased further down to 9.8, 9.7, 7.5, 5.4% with concentration ratios of 1X, 2X, 4X and 6X, respectively. The efficiency reduction is caused by the combination of high temperature and dust particles attenuating light. Also, the non-concentrated system and 3D-PSCPV with 2X, showed higher efficiency than other concentration ratios (4X and 6X), as the non-concentrated 1X and 3D-PSCPV with 2X concentration ratio has good light distribution and less hot spots than both; 4X and 6X as shown by the optical modelling presented in chapter 4 and the optical and thermal results presented in section 5.5. In regards to dust accumulation effects, non-concentrated system efficiency has the highest efficiency reduction with 23.4% compared to 2X, 4X and 6X which showed 10.09, 11.76 and 12.8% reduction, respectively, compared to the 3D-PSCPV system in clean condition.

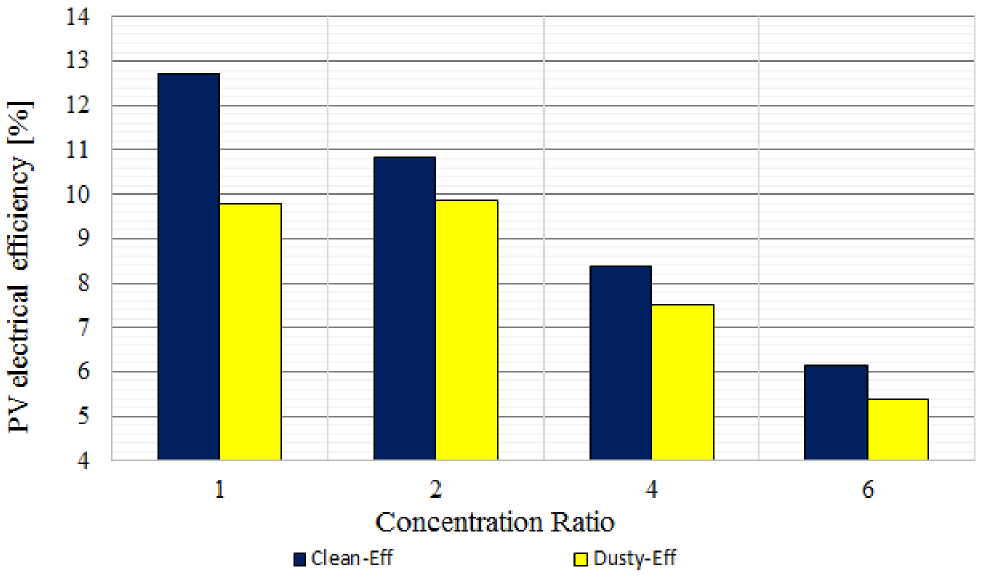

Figure 7.24 Variation of the electrical system conversion efficiency and maximum power out with concentration ratio under clean and dusty states

It can be concluded that the smaller concentration ratio of 3D-PSCPV, the better its electrical performance in both clean and dusty conditions in term of electrical efficiency. For instance, the 3D-PSCPV with 2X has better optical efficiency and uniform irradiance distribution on most of the receiver area and that results in higher system electrical efficiency. However, the increase of PV module temperature is still an issue that need to be overcome. Therefore, cooling the PV module will be investigated later in this chapter.

7.4.1.5 Variation of Fill Factor with concentration ratio and PV Temperature

The fill factors of 3D-PSCPV with clean and the dusty cover at different concentration ratios are shown in Figure **7.25**. It can be seen that the 3D-PSCPV with dusty cover had a higher fill factor than that with clean cover. The fill factor for both clean and dusty 3D-PSCPV decreased as the concentration ratio increased from 1X to 6X, but it tends to decrease more with clean cover as a result of the PV module temperature exceeding the operating temperature limit [165], as shown in Figure **7.26**. Higher optical losses and radiation non-uniformity at concentration ratio of 4X and 6X can be another cause for the decrease in fill factor causing hotspots on the PV module [194]. The measured fill factor of the clean and dusty cover with concentration ratio of 1X and 2X are considered acceptable for polycrystalline PV cells with values of 70-80% [190, 195]. A small difference between the clean and dusty fill factor of 1.2% was determined at all of the 3D-PSCPV concentration ratios. The largest reduction fill factor is 3.6% and 4.2% at concentration ratio of 4X for the 3D-PSCPV with clean cover and dusty cover, respectively.

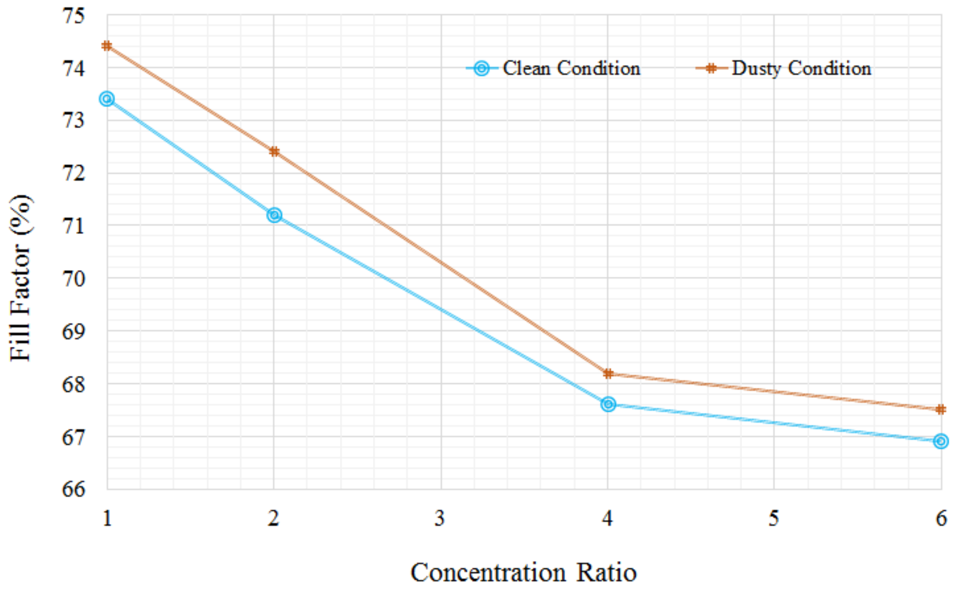

Figure 7.25 Difference of fill factor for 3D-PSCPV with and without dust at different concentration ratio

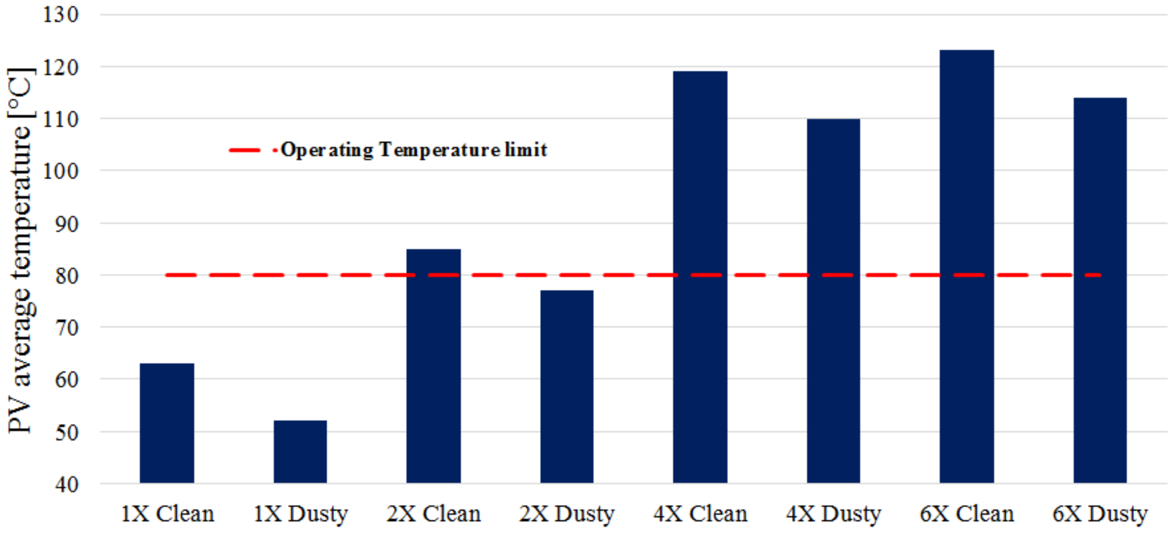

Figure 7.26 Comparison of PV module average temperatures between clean and dusty covers at different concentration ratio

7.4.1.6 Effects of water cooling on the electrical performance of the dusty 3D-PSCPV

The effects of the cooling channels on the electrical performance was experimentally investigated and compared with the simulation results at different concentration ratios. Figure **7.27** and Figure **7.28** compare the experimental and simulation I/V and P/V curves at different concentration ratios and inlet water velocity of 0.00461 m/s, the experimentally measured PV module temperature is utilised in the electrical stimulation to produce the I/V and P/V curves. It can be seen from both figures that good agreement between the experimental and the simulation results produced at various concentration ratios with incoming radiation of 1000 w/m^2. Despite, the increase in the short-circuit current with increase of concentration ratio is more pronounced compared to the increase of the open-circuit voltage, the two figures show that both electrical parameters are increasing with the increase of the concentration ratio.

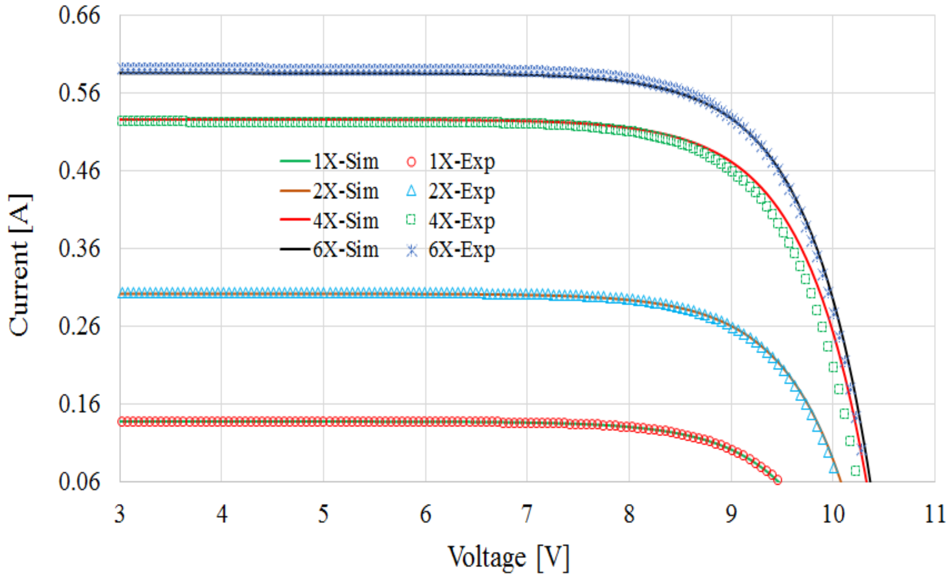

Figure 7.27 Comparison of the experimental I/V curves with predicted at different concentration ratios

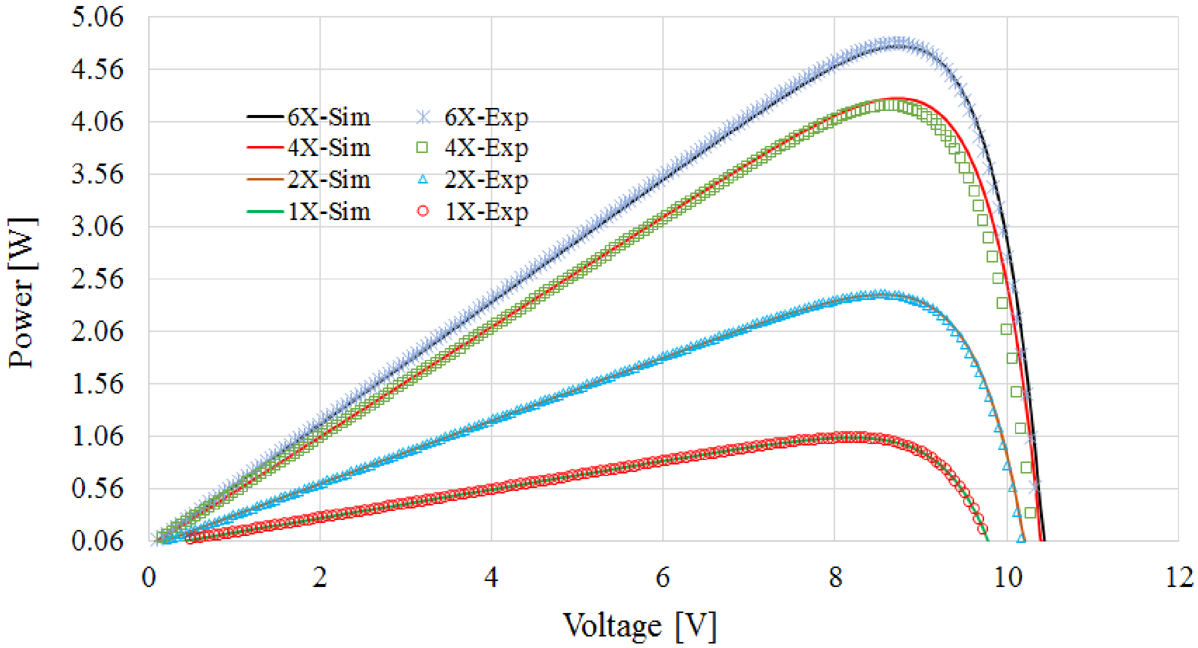

Figure 7.28 Comparison of the experimental P/V curves with predicted at different concentration ratios

Figure 7.29 shows the maximum power output of the dusty 3D-PSCPV at various inlet water velocity and concentration ratios (experimental and simulation). It can be seen that there is a reasonable agreement between the predicted and experimental maximum power output with difference of 5.3%. The variation can be caused by the losses in the wires internal resistance as the cooled PV module voltage and current outputs increases especially at the high concentration ratios which were not considered in the simulation.

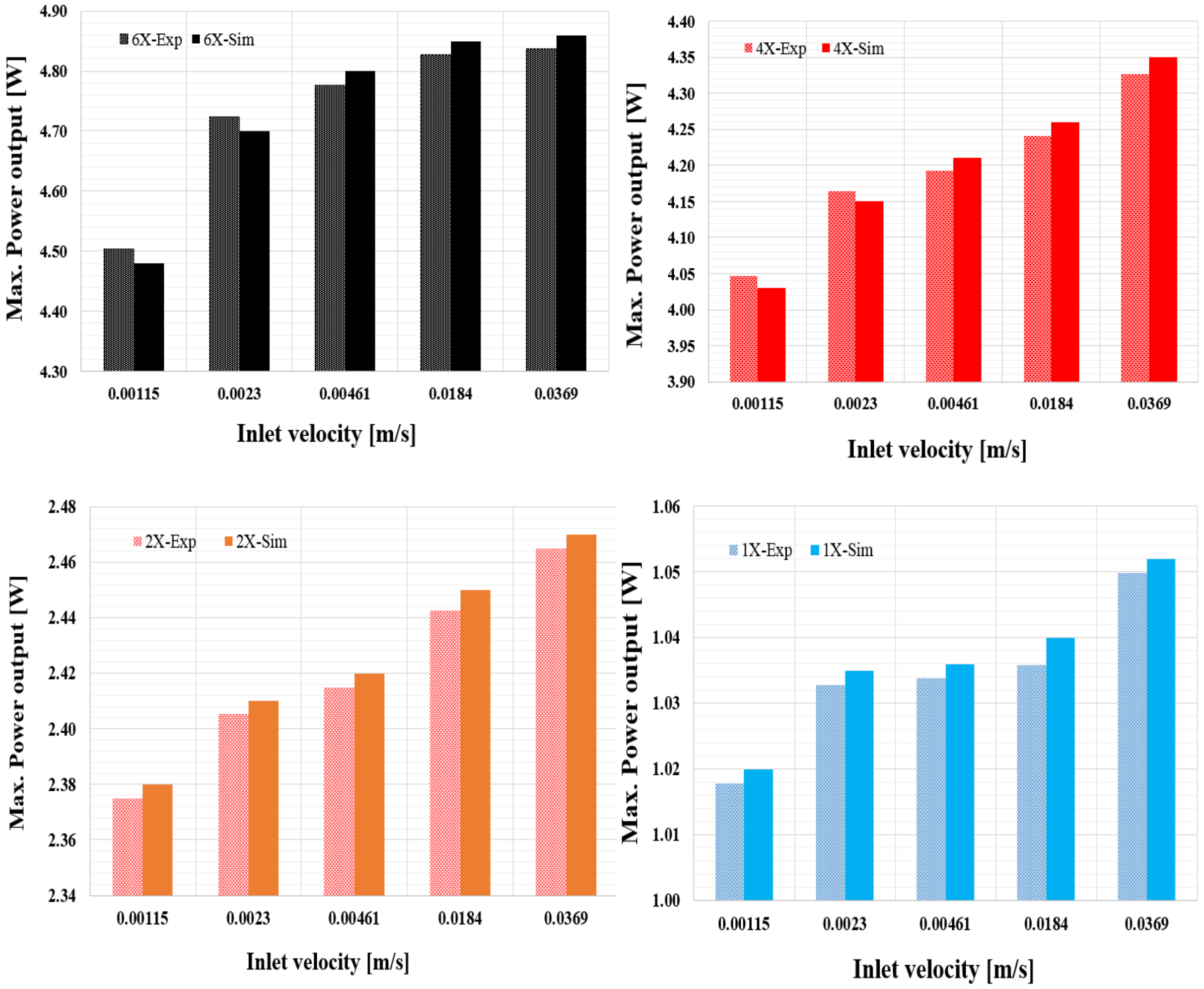

Figure 7.29 Variation of the maximum power out of the dusty 3D-PSCPV at different inlet water velocity and concentration ratios. (Experimental and simulation)

Upon validating the thermal and electrical models, the effects of the water cooling on the system electrical efficiency of the dusty 3D-PSCPVwas investigated. There was a sizable increase in the value of the system electrical efficiency once the water cooling channels was integrated with the dusty 3D-PSCPV system as shown in Figure **7.30**. The highest cooling water velocity of 0.037 m/s was used, in order to reach maximum electrical efficiency of the 3D-PSCPV.

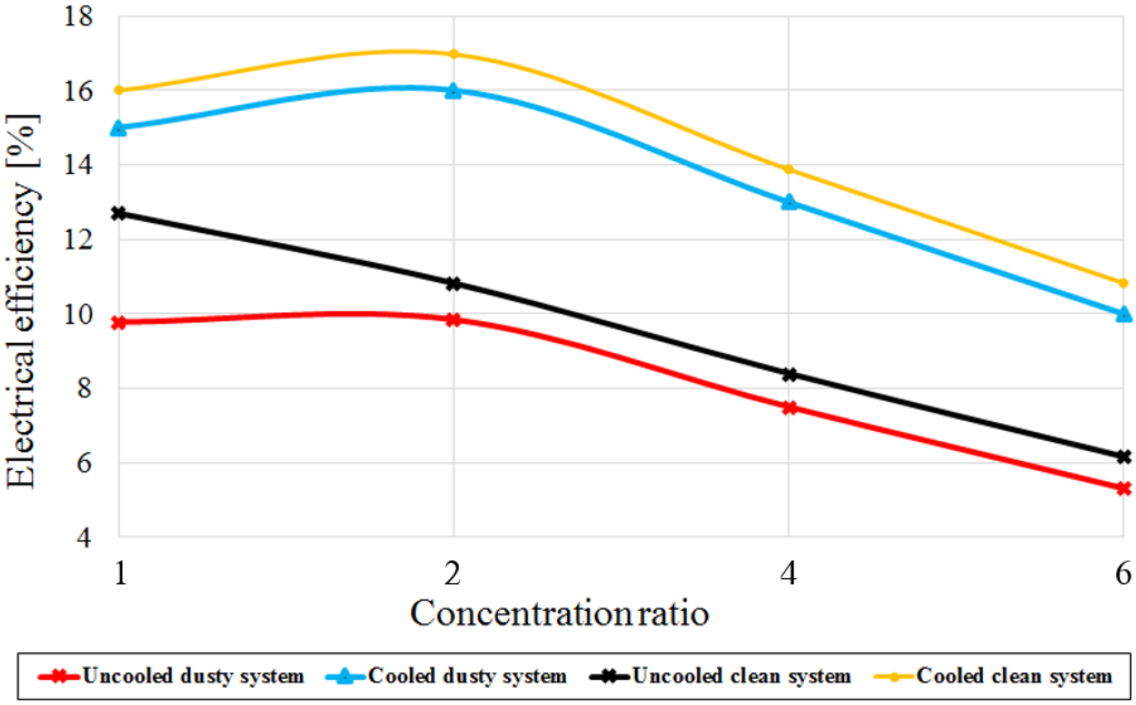

Figure 7.30 Electrical efficiency of the cooled and uncooled dusty 3D-PSCPV compared with clean 3D-PSCPV electrical efficiency at different concentration ratios

Figure **7.30** also shows a study on the variation of the electrical efficiency for cooling and no cooling cases under dusty conditions along with the uncooled clean system conditions. There is a maximum improvement of 80 % in the electrical efficiency of dusty 3D-PSCPV system at a concentration ratio of 6X and a minimum improvement of 50% at a concentration ratio of 1X with cooling compared to no cooling conditions respectively. However, only 3D-PSCPV with concentration ratio of 2X reached the STC efficiency of 16% due to the high optical efficiency and uniform received irradiance. The lower operating temperature achieved by cooling was shown to have a positive impact on the PV module efficiency [168].

7.4.2 Outdoor experimental results

The outdoor experimental results of the 3D-PSCPV performance (optical, thermal and electrical) for concentration ratio of 2X, 4X and 6X are presented in this section. Testing of 3D-PSCPV was carried out on a sunny day (19/ 08/2016) with irradiance of 870W/m^2.

The potential of recovering the power losses of dusty 3D-PSCPV was investigated using cooling channels. To further support this work, an investigation was carried out using the outdoor setup. This study is aimed at comparing the clean and dusty concentrator's power gain with cooling channels in an outdoor setup.

7.4.2.1 Water cooling effect on the I/V curve characteristics for clean and dusty module

The I/V curves of non-concentrated and concentrated PV module (3D-PSCPV receiver) was measured at different water inlet velocity of 0, 0.00115, 0.00461, 0.0184 and 0.0369 m/s. Figure **7.31** (a, b, c and d) compares the I/V characteristics of clean and dusty PV module with and without cooling of both non-concentrated and concentrated system. The significant increase in open-circuit voltage seen in the figures occurred due to a reduction in PV module operating temperature resulting from the use of water cooling. While the cooling system shows no effects on the short-circuit current on both clean and dusty 3D-PSCPV. This increase in open-circuit voltage is more dominant for lower PV module operating temperature (at 25°C for non-concentrated PV and for 3D-PSCPV at 26, 27 and 29°C for optical concentration ratio of 2X, 4X and 6X, respectively). Also, the figures clearly indicates that the open-circuit voltage is more temperature dependent than the short-circuit current.

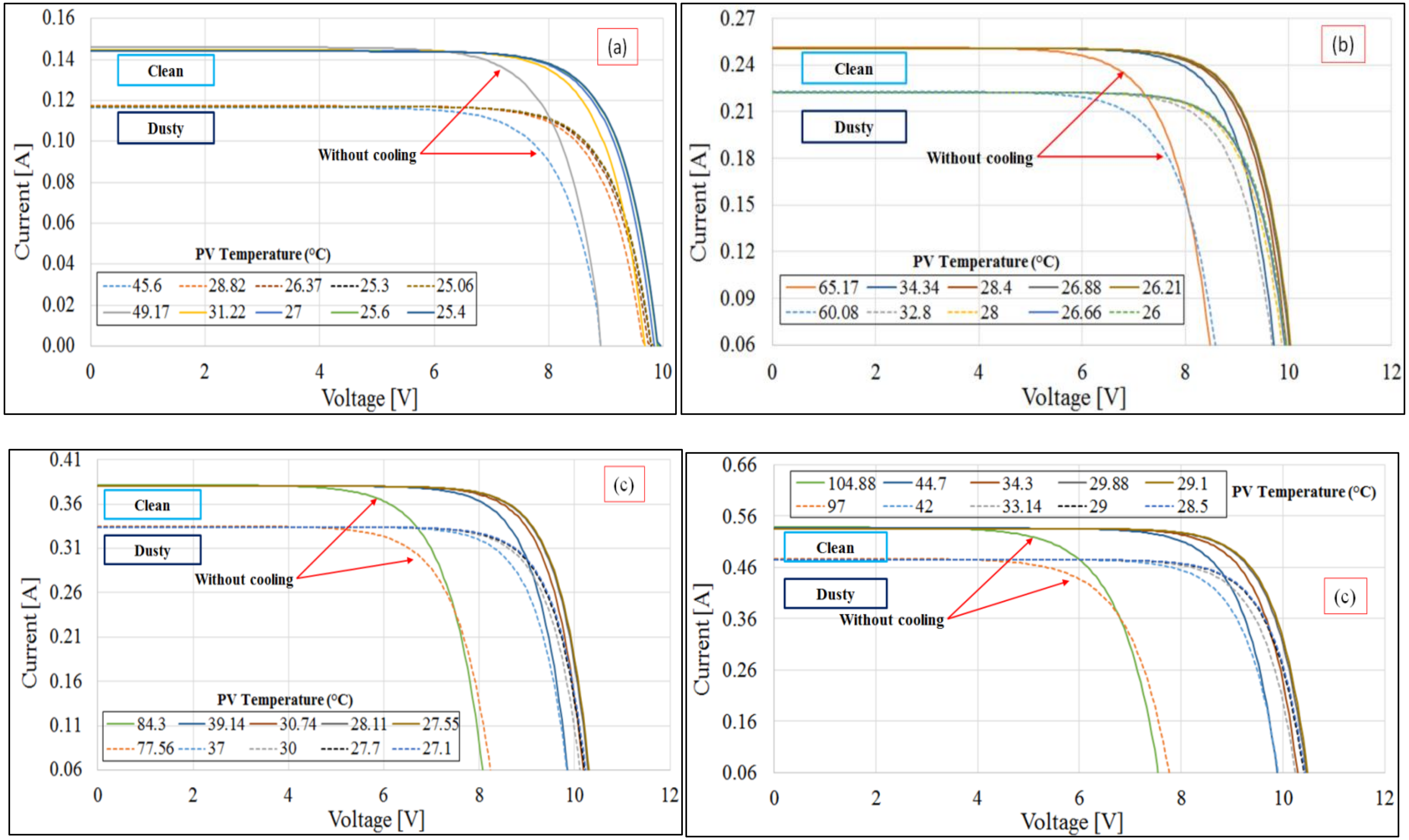

Figure 7.31 Variation of the I/V curve characteristics with water cooling at ambient temperature and wind speed of 26°C and 3 m/s, respectively, in clean and dusty condition. (a) Non-concentrated, (b) 2X, (c) 4X, (d) 6X

7.4.2.2 Cooling effect on the maximum power characteristics

Figure **7.32** shows the effect of cooling water velocity on the maximum power output of flat PV (1X) and 3D-PSCPV with different concentration ratios and water inlet velocity for both clean and dusty systems. An overall maximum power output improvement of 25, 38.6 and 56.06% for clean system, while for dusty system is 21.5, 33.5 and 49% all for 3D-PSCPVs with optical concentration ratio of 2X, 4X and 6X, respectively, was achieved with cooling at 0.0369 m/s inlet velocity as compared to a systems with 2X, 4X and 6X without cooling. The results of the system maximum output power without and with cooling channels at inlet velocity of 0.0369 m/s. are summarised in table 7.2.

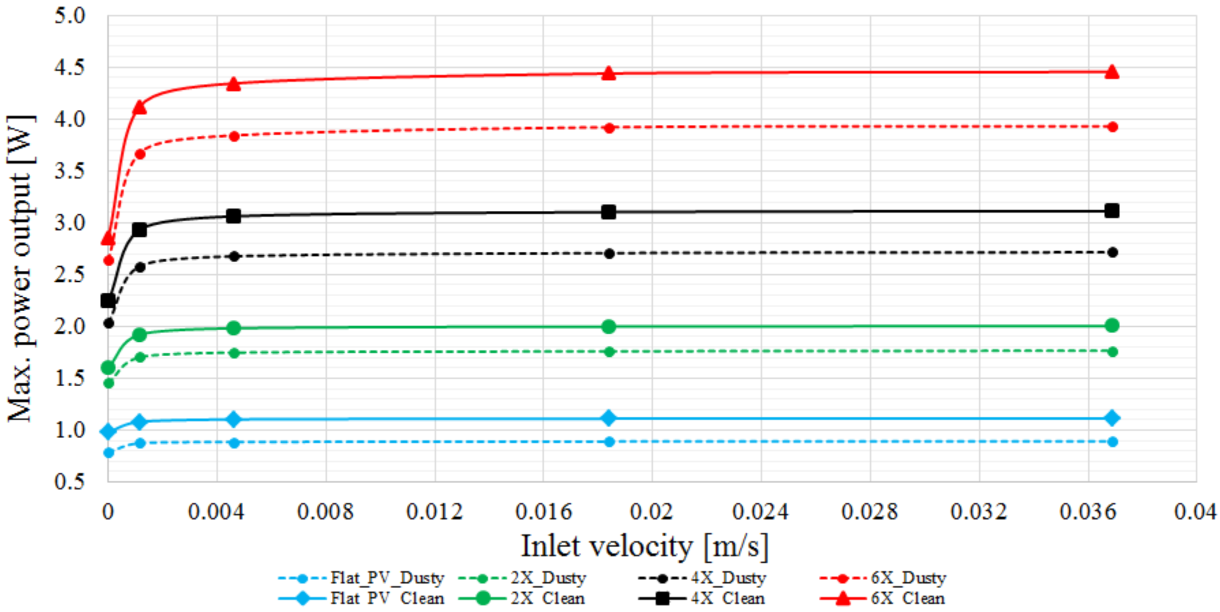

Figure 7.32 Variation of the PV module maximum power with inlet water velocity magnitudes at ambient temperature and wind speed of 26ºC and 3 m/s, respectively

Table 7.2 PV temperature and output power at non-concentrated and concentrated system with cooling and without cooling at clean and dusty states

Optical concentration ratio	**Without cooling**				**With cooling**			
	Clean		**dusty**		**Clean**		**dusty**	
	PV temp (°C)	**Output power (W)**	**PV temp (°C)**	**Output power (W)**	**PV temp (°C)**	**Output power (W)**	**PV temp (°C)**	**Output power (W)**
Flat-PV	49.17	0.982	45.6	0.785	25.4	1.112	25.06	0.981
2	65.07	1.604	60.08	1.453	26.21	2.005	26	1.766
4	84.3	2.244	77.56	2.033	27.55	3.111	27.1	2.716
6	104.88	2.854	97	2.638	29	4.454	28.5	3.931

7.4.2.3 Cooling effect on the 3D-PSCPV efficiencies

The system electrical efficiency of the PV module assembled with the 3D-PSCPV concentrator was calculated by applying equation 7.1 and using the maximum power output shown in Figure **7.32**, at different concentration ratios and different inlet velocity as shown in Figure **7.33**. It can be seen that the non-concentrated system outperformed the 3D-PSCPV with clean and dusty glass cover, due to uniformity of the falling irradiance on PV module surface and low PV module operating temperature. The maximum electrical efficiency of the non-concentrated PV module varies from 15.2% to 15.7%, with an average of 15.6% and 15.4% for clean and dusty condition, respectively, at different water inlet velocity as shown in Figure **7.33**. It can be seen that the 3D-PSCPV can perform well with optical concentration ratio of 2X where it gives maximum efficiency of 14.1 and 12.4%, for clean and dusty conditions, respectively, which is higher than 4X and 6X.

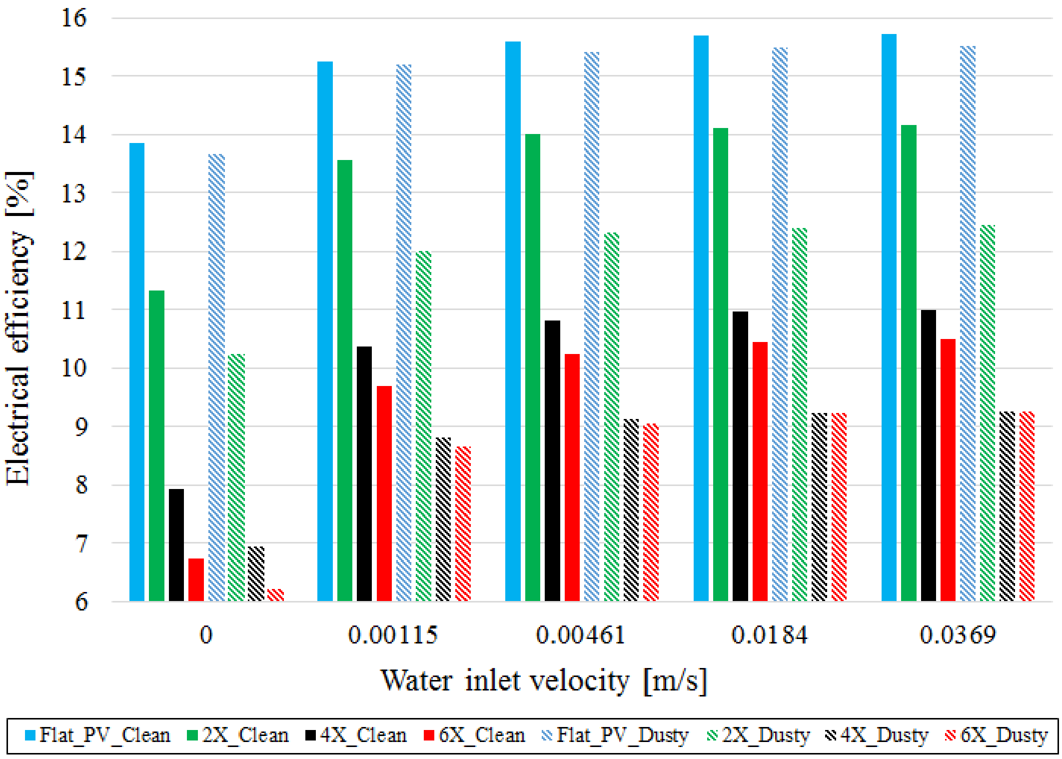

Figure 7.33 System electrical efficiency of the CPV and non-concentrating systems with variation of concentration ratio and inlet velocity in clean and dusty conditions

Figure **7.34** show the outdoor experimental results of the 3D-PSCPV system total efficiency with concentration ratios of 2X, 4X and 6X, at clean and dusty conditions with various cooling water velocity. It is can be seen that the 3D-PSPCV with lowest total system efficiency values are at the slowest water inlet velocity for both clean and dusty conditions, where the total system efficiency of the 3D-PSCPV in clean condition is around 68%, 66% and 70% for concentration ratios of 2X, 4X and 6X, respectively, and for 3D-PSCPV in dusty condition are 56%, 55% and 59% for concentration ratio of 2X, 4X and 6X, respectively. However with the increase of water inlet velocity the total system efficiency increased to reach it maximum at water inlet velocity of 0.037 m/s, the maximum total system efficiency of the 3D-PSCPV in clean condition are 96 %, 90 % and 88 % at concentration ratios of 2X, 4X and 6X, respectively. Moreover, as a result of the dusty glass cover the maximum total system efficiency of the clean 3D-PSCPV decreased down to 85%, 78%, 77.88% with concentration ratios of 2X, 4X and 6X, respectively.

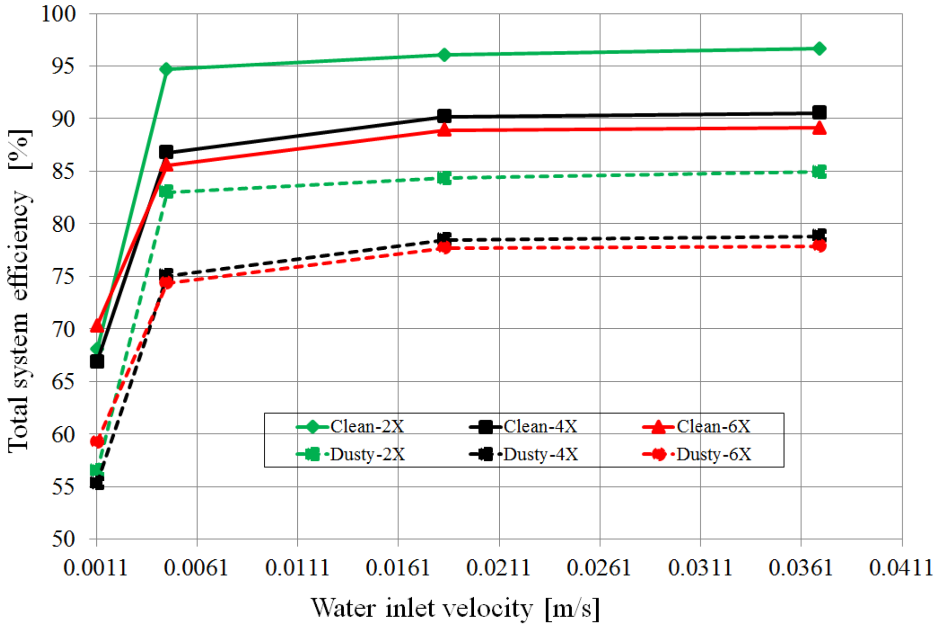

Figure 7.34 3D-PSCPV total efficiency at clean and dusty condition

7.5 Summary

Indoor and outdoor experimental studies were carried out in this work to investigate the effect of dust accumulation on the 3D-PSCPV optical, electrical and thermal performance. The optical performance validation of 3D-PSPCV presented close agreement between experimental results and simulation results obtained by OptisWorks^{TM} for the optical performance of dusty glass cover and optical efficiency with various surface reflectivities in clean and dusty condition.

The 3D-PSCPV with 90% surface reflectivity and concentration ratios of 2X, 4X and 6X, showed minimum difference in optical efficiency around ±3% and ±5% for clean and dusty condition tests, respectively. The difference between simulation and experimental results of the dusty glass procedure is within ±3% for indoor and ±2% for outdoor tests, in term of transmitted irradiance.

The 3D-PSCV at outdoor testing with optical concentration ratio of 2X showed the highest optical efficiency of 77 and 87% for dusty and clean glass cover, respectively. However, it produces lower irradiance than others. Also, the received irradiance distribution over the PV module area was tested, it was observed that the 3D-PSCPV with optical concertation ratio of 6X shows the highest peaks of irradiance concentrated at the centre of the receiver on both clean and dusty conditions.

The 3D-PSCPV electrical parameters such as open-circuit voltage, short-circuit current, fill factor and maximum power output were investigated in clean and dusty conditions. The results show that the open-circuit voltage was the most affected parameter, due to heat generated by the solar concentrators at different concentration ratio. Due to dust accumulation on the 3D-PSCPV entrance aperture, the received radiation decreased leading to the short-circuit current being reduced. The short-circuit current dropped 27% in 1X (1000 W/m^2 incoming irradiance on non-concentrated PV module) while, the reductions were 12.65%, 14.65% and 14.71% for concentration ratios of 2X, 4X and 6X, respectively.

Indoor thermal experimental and simulation results for the dusty 3D-PSCPV receiver (PV module) temperature with different concentration ratio and 90% surface reflectivity at different inlet water show maximum deviation of 3%, while outdoor thermal experimental and simulation results for the dusty and clean 3D-PSCPV outlet temperature with different concentration ratio and 70% surface reflectivity at inlet water 0.00461 m/s show maximum deviation of 4.5%. The electrical experimental and simulation results of the dusty 3D-PSCPV in indoor testing showed a strong agreement of maximum power output at different water inlet velocity with a difference of 5.3%.

The outdoor and indoor electrical experimental results of the 3D-PSCPV in clean and dusty condition showed an enhancement in maximum power output through the increase of inlet velocity and concentration ratio, and consequently the electrical efficiency improved. The 3D-PSCPV system at outdoor setup with optical concentration ratio 2X and 70% surface reflectivity shows maximum efficiency of 14.1 and 12.4%, for clean and dusty condition, respectively, which is higher than 4X and 6X. These results show the advantages of utilising cooling system in concentrated photovoltaic technology in dusty environment such as that of Kuwait.

CHAPTER 8

CONCLUSIONS AND RECOMMENDATIONS

8.1 Introduction

Interest in utilising of renewable energy technology is growing as a result of the energy crises around the globe and the issues affiliated with the usage of fossil fuel. State of Kuwait is challenged with major issues in power supply such as systematic outage during summer, inadequate power supply system and shortage of natural gas which is straining the power supply. Kuwait has great potentials of solar energy, where the solar irradiance reaches 2100 kWh/m²·yr, yet limited consideration is dedicated to its development.

Worldwide, photovoltaic is one of the fastest growing renewable energy technology, however in Kuwait, the growth in using photovoltaic is still limited. Furthermore, the use of concentrated photovoltaic was only introduced to Kuwait in 2013. The main challenges to utilizing photovoltaic in Kuwait are the high ambient temperature and the dusty environment. This project investigated means of enhancing photovoltaic using concentration of radiation and incorporating water cooling to recover the thermal energy taking into account the effect of dust. Detailed modelling and optimisation to improve the optical, electrical and thermal performance of the concentrated photovoltaic systems was carried out in developing effective water cooled concentrated photovoltaic system in dusty environment such as Kuwait.

8.2 Conclusions

This work developed a methodology for the design and optimisation of a novel 3D low concentration solar concentrator for concentrated photovoltaic system. The 3D solar concentrator is shaped as the Pseudo-Square and designed to be integrated into concentrated photovoltaic system (3D-PSCPV). The approach of this work is to enhance the performance of the 3D-PSCPV system by integrating an effective cooling system with the concentrated photovoltaic system to obtain higher efficiency in the elevated ambient temperature and dusty environment of Kuwait. Detailed experimental and modelling work has been carried out to assess the performance of the developed 3D PSCPV concentrators in terms of optical and electrical efficiencies for clean and dusty conditions and with and without cooling. Conclusions from this work are summarised in the following subsections.

8.2.1 Optical performance

The optical performance of clean and dusty 3D-PSCPV systems with low concentrating ratios of 2X, 4X, and 6X was investigated through advanced ray tracing techniques using OptisWorks^{TM} software. The optical model was developed using the optical characteristics of the concentrator material and geometry, the optical properties of the concentrator cover and the measured optical properties of the Kuwaiti raw dust including size, reflectivity and transmissivity. Also, experimental work was carried out to validate the modelling. The optical performance includes optical efficiency and irradiance distribution on the receiver PV area. Using raw dust from Kuwait with measured optical properties of average light reflectivity of 30%, Results showed that:

- Good agreement between optical simulation and experimental results of the 3D-PSCPV utilising material with 60%, 70%, 80% and 90% reflectivity values with maximum difference of 7% for three concentration ratios of 2X, 4X and 6X.
- The concentrators optical efficiency increased with the increase of surface reflectivity to reach 91% for the 3D-PSCPV with reflectivity of 90%.
- Comparison between ray tracing simulation and experimental results of the 3D-PSCPV optical efficiency under dust accumulation were performed employing solar simulator (indoor) and natural light source (outdoor), indicating good agreement with maximum difference 3.8% and 7% for indoor and outdoor setups, respectively.
- Received irradiance distribution produced by the three investigated concentrator geometries was estimated employing the concentrator uniformity factor (CUF), as highest value indicates better irradiance uniformity. (CUF) computation results indicated that the greatest uniformity among the three studied concentrator of 2X, 4X and 6X is 2X with (CUF) 82% and 73% for uncovered and covered with dust, respectively. The 3D-PSCPV with concentration ratio of 6X produces the worst irradiance distribution, which is a result of maximum concentrated irradiance located at the corners and centre therefore small irradiance is distributed on the remaining of PV area.
- The highest actual optical concentration ratio obtained at dusty condition are 1.7, 3.08 and 3.5 for 3D-PSCPV with concentration ratios of 2X, 4X and 6X, respectively, with surface reflectivity of 90%.

8.2.2 Electrical performance

Two experimental studies were conducted to compare the electrical performance of PV technology in clean and dusty condition. The results showed that: (i) the output open-circuit voltage of the clean modules are insignificantly lower than that of the dusty modules at all solar radiation levels. (ii) The dust accumulation ratio of short-circuit current of the dusty modules to the clean modules short-circuit current reaches 0.6-0.7 for monocrystalline and polycrystalline, respectively. (iii) The power losses related to dust accumulation is 25-45% with dusty modules. (iiii) Measurements revealed that the monocrystalline module efficiency is more affected by the dust with a drop of 29% while the polycrystalline module is less affected by the dust with a drop of 16.8%.

Extensive experimental (indoor and outdoor) studies were carried out to investigate the effect of dust accumulation on the 3D-PSCPV electrical parameters such as open-circuit voltage, short-circuit current, fill factor, maximum power output and efficiency in clean and dusty conditions at various concentration ratios and operating temperature. Also, electrical modelling for a PV module with single-diode circuit model has been employed to investigate the PV module electrical performance at various concentration ratios, surface reflectivities and operating temperatures in clean and dusty conditions. Results from the experimental testing and electrical modelling showed:

- The predicted maximum power output was compared to measured maximum power output for four different concentration ratios, revealing good agreement with deviation of 1.2% and 2% for clean and dusty conditions, respectively.
- Without cooling, the overall system efficiency decreases with the increase in concentration ratio for both dusty and clean conditions. For example the electrical efficiency of the 3D-PSCPV decreased from 12.7 % to 6.15% as the concentration ratio increased from 2X to 6X at clean conditions and from 9.8% to 5.3% at dusty conditions.

- Using water cooling, the dusty 3D-PSCPV system with 2X reached electrical efficiency of 16% at 1000W/m^2 irradiance and reflectivity of 90%.
- As the concentration ratio of the dusty 3D-PSCV increased up to 6X the maximum power increased to 4.85W in comparison with the maximum output power of the 1X (flat PV module) of 1.1W.

8.2.3 Thermal performance

- A 3D thermal model utilising COMSOL Advanced Multiphysics software was developed to investigate the performance of the 3D-PSCV system at different concentration ratios and water cooling in dusty and high ambient temperature climate where the ambient temperature can reach up to 45oC during summer season. By cooling, the PV module temperature was reduced to around 26°C at all 3D-PSCPV concentration ratios with increasing inlet velocity up to 0.037 m/s, leading to the increase in maximum output power of the dusty 3D-PSCPV.
- Experimental testing of the 3D-PSCPV system was carried out at various inlet water velocity ranging from 0.0011 to 0.037 m/s through 140X140mm aluminium rectangular channels fitted underneath the PV with different concentration ratios of 2X, 4X and 6X to validate the simulation models showing good agreement with difference of 5.2%. The highest electrical efficiency of the 3D-PSCPV with cooling reached 16% only 5.8% less than efficiency at STC.

8.3 Future work

For further development of this work, the following recommendations are presented below:

- The 3D-PSCPV system overall performance investigations was carried out at 0^o light incident angle, for further detailed behaviour of the system can be obtained by using different light incident angle to investigate the system performance at various sunlight hours.

- To develop a prototype model to study the performance of the 3D-PSCPV system in Kuwait at different sites and longer periods of time to allow for natural dust accumulation and to evaluate the 3D-PSCPV system durability.
- To develop a complete large scale 3D-PSCPV system with array and testing under natural sun in Kuwait for electrical power supply.
- Investigating the effect of corrosion on CPV system due to dust.

REFERENCES

1. Ren21, R., *Global status report.* Renewable Energy Policy Network for the 21st Century, Mexico, Mexico city, 2017.
2. Duffie, J.A. and W.A. Beckman, *Solar engineering of thermal processes*. Vol. 3. 2013: Wiley New York.
3. Hajiah, A., Khatib, T. and Sebzali, M., *Performance of grid-connected photovoltaic system in two sites in Kuwait.* International Journal of Photoenergy, 2012.
4. Khamooshi, M.,Salati, H. and Egelioglu, F., *A review of solar photovoltaic concentrators.* International Journal of Photoenergy, 2014.
5. Al-Dousari, A.M. and J. Al-Awadhi, *Dust fallout in northern Kuwait, major sources and characteristics.* Kuwait J Sci Eng, 2012. **39**(2A): p. 171-187.
6. Riebeek, H., *NASA Earth Observatory.* 2008.
7. Alnaser, W. and N. Alnaser, *The status of renewable energy in the GCC countries.* Renewable and Sustainable Energy Reviews, 2011. **15**(6): p. 3074-3098.
8. Research, K.I.f.S., *Solar radiation, KISR station Tech Report*. 2014, KISR: Kuwait.
9. Chapin, D.M., C. Fuller, and G. Pearson, *A new silicon p ‑ n junction photocell for converting solar radiation into electrical power.* Journal of Applied Physics, 1954. **25**(5): p. 676-677.
10. Sarmah, N., *Design and performance evaluation of a low concentrating line-axis dielectric photovoltaic system*. 2012, Heriot-Watt University.
11. Green, M.A. and Emery K, *Solar cell efficiency tables (version 47).* Progress in Photovoltaics: Research and Applications, 2016. **24**(NREL/JA-5J00-65643).
12. Martin, J., *Monocrystalline vs Polycrystalline Solar Panels: Busting Myths.* Solar choice, 2012(Solar Panels/Modules,Solar System Products).
13. Empa, *Empa takes thin film solar cells to a new level.* Swiss Federal Laboratories for Materials Testing and Research, 2015. A new world record for solar cell efficiency.
14. Strevel, N., L. Trippel, and M. Gloeckler, *Performance characterization and superior energy yield of First Solar PV power plants in high-temperature conditions.* Photovoltaics international, 2015. **17**(3): p. 148-154.
15. Miles, R., K. Hynes, and I. Forbes, *Photovoltaic solar cells: An overview of state-of-the-art cell development and environmental issues.* Progress in Crystal Growth and Characterization of Materials, 2005. **51**(1): p. 1-42.
16. De Vos, A., *Detailed balance limit of the efficiency of tandem solar cells.* Journal of Physics D: Applied Physics, 1980. **13**(5): p. 839.
17. Dimroth, F., Roesener, T and Essig, S, *Comparison of direct growth and wafer bonding for the fabrication of GaInP/GaAs dual-junction solar cells on silicon.* IEEE Journal of Photovoltaics, 2014. **4**(2): p. 620-625.
18. Green, M.A., Emery, K. and Hishikawa, Y., *Solar cell efficiency tables (Version 45).* Progress in photovoltaics: research and applications, 2015. **23**(1): p. 1-9.
19. Marion, B., Adelstein, J and Boyle, K., *Performance parameters for grid-connected PV systems*. in *Conference Record of the Thirty-first IEEE Photovoltaic Specialists Conference, 2005*. IEEE.
20. Rodrigues, E., Melicio, R. and Mendes, V, *Simulation of a solar cell considering single-diode equivalent circuit model*. in *International conference on renewable energies and power quality, Spain*. 2011.

21. Algora, C. and I. Rey-Stolle, *Handbook on concentrator photovoltaic technology.* 2016.
22. Antonio, L. and H. Steven, *Handbook of photovoltaic science and engineering.* Swanson, RM, Photovoltaic Concentrators. John Wiley & Sons Ltd, West Sussex, England, 2003: p. 373-374.
23. Vergura, S., *A complete and simplified datasheet-based model of PV cells in variable environmental conditions for circuit simulation.* Energies, 2016. **9**(5): p. 326.
24. Al-Hasan, A.Y., *A new correlation for direct beam solar radiation received by photovoltaic panel with sand dust accumulated on its surface.* Solar Energy, 1998. **63**(5): p. 323-333.
25. Qasem, H., Betts, T. and Mullejans, H., *Dust ‐ induced shading on photovoltaic modules.* Progress in Photovoltaics: Research and Applications, 2014. **22**(2): p. 218-226.
26. Mani, M. and R. Pillai, *Impact of dust on solar photovoltaic (PV) performance: Research status, challenges and recommendations.* Renewable and Sustainable Energy Reviews, 2010. **14**(9): p. 3124-3131.
27. Goossens, D. and E. Van Kerschaever, *Aeolian dust deposition on photovoltaic solar cells: the effects of wind velocity and airborne dust concentration on cell performance.* Solar Energy, 1999. **66**(4): p. 277-289.
28. Zaihidee, F.M. and S. Mekhilef, *Dust as an unalterable deteriorative factor affecting PV panel's efficiency: Why and how.* Renewable and Sustainable Energy Reviews, 2016. **65**: p. 1267-1278.
29. Salim, A., F. Huraib, and N. Eugenio. *PV power-study of system options and optimization*. in *EC photovoltaic solar conference. 8*. 1988.
30. Wakim, F., *Introduction of PV power generation to Kuwait.* Kuwait Institute for Scientific Researchers, Kuwait City, 1981.
31. Sayigh, A., S. Al-Jandal, and H. Ahmed. *Dust effect on solar flat surfaces devices in Kuwait*. in *Proceedings of the workshop on the physics of non-conventional energy sources and materials science for energy*. 1985.
32. Nahar, N. and J.P. Gupta, *Effect of dust on transmittance of glazing materials for solar collectors under arid zone conditions of India.* Solar & wind technology, 1990. **7**(2): p. 237-243.
33. Elminir, H.K., A, Ghitas and F. El-Hussainy *Effect of dust on the transparent cover of solar collectors.* Energy Conversion and Management, 2006. **47**(18): p. 3192-3203.
34. Hasan, A. and A. Sayigh, *The effect of sand dust accumulation on the light transmittance, reflectance, and absorbance of the PV glazing.* Renewable Energy. Technology and the Environment, Pergamon Press, Oxford, 1992: p. 461-466.
35. Pettit, R., J. Freese, and D. Arvizu, *Specular reflectance loss of solar mirrors due to dust accumulation*. 1978, Sandia Labs., Albuquerque, NM (USA).
36. Al-Hasan, A.Y. and A.A. Ghoneim, *A new correlation between photovoltaic panel's efficiency and amount of sand dust accumulated on their surface.* International Journal of Sustainable Energy, 2005. **24**(4): p. 187-197.
37. El-Shobokshy, M.S. and F.M. Hussein, *Effect of dust with different physical properties on the performance of photovoltaic cells.* Solar energy, 1993. **51**(6): p. 505-511.
38. Adinoyi, M.J. and S.A. Said, *Effect of dust accumulation on the power outputs of solar photovoltaic modules.* Renewable Energy, 2013. **60**: p. 633-636.
39. Nimmo, B. and S.A. Said. *Effects of dust on the performance of thermal and photovoltaic flat plate collectors in Saudi Arabia-Preliminary results*. in *Alternative energy sources II, Volume 1*. 1981.

40. El-Shobokshy, M.S. and F.M. Hussein, *Degradation of photovoltaic cell performance due to dust deposition on to its surface.* Renewable Energy, 1993. **3**(6-7): p. 585-590.
41. Touati, F., A. Massoud and J. Hamad, *Effects of environmental and climatic conditions on PV efficiency in Qatar*. in *International Conference on Renewable Energies and Power Quality (ICREPQ'13)*. 2013.
42. Alnaser, W.E., N.W. Alnaser, and I. Batarseh, *Dust Accumulation Study on Bahrain's BAPCO 5MWp PV Grid–Connected Solar Project.*
43. Al Hanai, T., R. Hashim, L. EL chaar and A. Lamont, *Environmental effects on a grid connected 900 W photovoltaic thin-film amorphous silicon system.* Renewable energy, 2011. **36**(10): p. 2615-2622.
44. Ibrahim, A., *Effect of shadow and dust on the performance of silicon solar cell.* Journal of Basic and applied scientific research, 2011. **1**(3): p. 222-230.
45. Hassan, A., A. Rahoma and K. Elminir, *Effect of airborne dust concentration on the performance of PV modules.* J. Astron. Soc. Egypt, 2005. **13**(1): p. 24-38.
46. Al-Alawy, I.T., *Wind and other factor requirements to solar energy applications in Iraq.* Solar & Wind Technology, 1990. **7**(5): p. 597-600.
47. Kaldellis, J. and M. Kapsali, *Simulating the dust effect on the energy performance of photovoltaic generators based on experimental measurements.* Energy, 2011. **36**(8): p. 5154-5161.
48. Sanusi, Y., *The performance of amorphous silicon PV system under Harmattan dust conditions in a tropical area.* Pacific Journal of Science and Technology, 2012. **13**(1): p. 168-175.
49. Iqbal, M., *An introduction to solar radiation Academic Press Toronto 390.* 1983.
50. Martín, N. and J. Ruiz, *Annual angular reflection losses in PV modules.* Progress in Photovoltaics: Research and Applications, 2005. **13**(1): p. 75-84.
51. Winston, R., J. Miñano, and P. Benítez, *with contributions by N. Shatz and J. Bortz, Nonimaging Optics*. 2005, Elsevier.
52. Davies, P., *Edge-ray principle of nonimaging optics.* JOSA A, 1994. **11**(4): p. 1256-1259.
53. Winston, R. and W. Welford, *Design of nonimaging concentrators as second stages in tandem with image-forming first-stage concentrators.* Applied optics, 1980. **19**(3): p. 347-351.
54. Ochieng, R.M. and F.N. Onyango, *Some Techniques in Configurational Geometry as Applied to Solar Collectors and Concentrators*. 2010, Citeseer.
55. Luque, A. and S. Hegedus, *Handbook of photovoltaic science and engineering*. 2011: John Wiley & Sons.
56. Mallick, T.K., *Optics and heat transfer for asymmetric compound parabolic photovoltaic concentrators for building integrated photovoltaics*. 2003, University of Ulster.
57. Kreider, J.F., F. Keith, and J. McGowan, *Solar heating and cooling: active and passive design.* American Journal of Physics, 1984. **52**(8): p. 766-766.
58. Enteria, N. and A. Akbarzadeh, *Solar Energy Sciences and Engineering Applications*. 2013: CRC Press.
59. Miller, D.C. and S.R. Kurtz, *Durability of Fresnel lenses: a review specific to the concentrating photovoltaic application.* Solar Energy Materials and Solar Cells, 2011. **95**(8): p. 2037-2068.
60. Weber, K., V. Everett and P. Deenapanray, *Modeling of static concentrator modules incorporating lambertian or v-groove rear reflectors.* Solar energy materials and solar cells, 2006. **90**(12): p. 1741-1749.

61. Nilsson, J., *Optical design and characterization of solar concentrators for photovoltaics*. 2005.
62. Kritchman, E., A. Friesem, and G. Yekutieli, *Highly concentrating Fresnel lenses.* Applied Optics, 1979. **18**(15): p. 2688-2695.
63. Zaibel, R., *An astigmatic corrected target-aligned heliostat for high concentration.* Solar Energy Materials and Solar Cells, 1995. **37**(2): p. 191-202.
64. Kalogirou, S., *Use of parabolic trough solar energy collectors for sea-water desalination.* Applied Energy, 1998. **60**(2): p. 65-88.
65. Schramek, P. and D.R. Mills, *Heliostats for maximum ground coverage.* Energy, 2004. **29**(5): p. 701-713.
66. Mallick, T., C. Eamaes and J. Hyde, *Experimental characterisation of an asymmetric compound parabolic photovoltaic concentrator designed for building integration in the UK.* International journal of ambient energy, 2004. **25**(2): p. 85-96.
67. Bett, A., B. Burger, F. Dimroth and G. Siefer, *High-concentration PV using III-V solar cells*. in *2006 IEEE 4th World Conference on Photovoltaic Energy Conference*. 2006. IEEE.
68. Sangani, C. and C. Solanki, *Experimental evaluation of V-trough (2 suns) PV concentrator system using commercial PV modules.* Solar energy materials and solar cells, 2007. **91**(6): p. 453-459.
69. Reddy, K. and N.S. Kumar, *Combined laminar natural convection and surface radiation heat transfer in a modified cavity receiver of solar parabolic dish.* International Journal of Thermal Sciences, 2008. **47**(12): p. 1647-1657.
70. Royne, A., C.J. Dey, and D.R. Mills, *Cooling of photovoltaic cells under concentrated illumination: a critical review.* Solar energy materials and solar cells, 2005. **86**(4): p. 451-483.
71. Philipps, S., A Bett, K. Horowitz and S. Kurtz, *Current status of concentrator photovoltaic (CPV) technology.* National Renewable Energy Laboratory (NREL), Golden, CO, 2015.
72. Shaltout, M.M., A. Ghettas, and M. Sabry, *V-trough concentrator on a photovoltaic full tracking system in a hot desert climate.* Renewable energy, 1995. **6**(5): p. 527-532.
73. Tripanagnostopoulos, Y., H. Nousia and M. Souliotis, *Hybrid photovoltaic/thermal solar systems.* Solar energy, 2002. **72**(3): p. 217-234.
74. Brogren, M., P. Nostell, and B. Karlsson, *Optical efficiency of a PV–thermal hybrid CPC module for high latitudes.* Solar Energy, 2001. **69**: p. 173-185.
75. Mallick, T., P. Eames, and B. Norton. *Asymmetric compound parabolic photovoltaic concentrators for building integration in the UK: An optical analysis*. in *World Renewable Energy Congress-VII. 29th June–5th July*. 2002.
76. Wu, Y., M. Smyth, P. Eames and T. Mallick, *Optical and thermal analysis of different asymmetric compound parabolic photovoltaic concentrators (ACPPVC) systems for building integration*. in *Proceedings of ISES World Congress 2007 (Vol. I–Vol. V)*. 2008. Springer.
77. Nakata, Y., N. Shibuya, T. Kobe and K. Okamoto, *Performance of circular Fresnel lens photovoltaic concentrator.* Japanese Journal of Applied Physics, 1980. **19**(S2): p. 75.
78. O'neill, M.J., *Solar concentrator and energy collection system*. 1978, Google Patents.
79. Sala, G., C. Arboiro, A. Luque, I. Anton and M. Gasson,*480 kWpeak EUCLIDESTM Concentrator Power Plant Using Parabolic Troughs*. in *Proceedings of the 2nd World Conference on Photovoltaic Energy Conversion, Vienna, Austria*. 1998.
80. Coventry, J.S., *Performance of a concentrating photovoltaic/thermal solar collector.* Solar Energy, 2005. **78**(2): p. 211-222.

81. Bhatnagar, M. and J. Joshi, *Field performance of concentrated photovoltaic modules.* Solar cells, 1990. **28**(4): p. 343-350.
82. Araki, K., H. Uozumi, T. Egami, *A 550× concentrator system with dome-shaped fresnel lenses–reliability and cost*. in *20th European photovoltaic solar energy conference*. 2005.
83. Garboushian, V., K. Stone, and A. Slade, *12 The Amonix High-Concentration Photovoltaic System.* Concentrator Photovoltaics, 2007. **130**: p. 253.
84. Hein, M., F. Dimroth, G. Siefer and A. Bett, *Characterisation of a 300× photovoltaic concentrator system with one-axis tracking.* Solar energy materials and solar cells, 2003. **75**(1): p. 277-283.
85. Luque, A.L. and A. Viacheslav, *Concentrator photovoltaics*. 2007: Springer.
86. Zhangbo, Y., L. Qifen and Z. Qunzhi, *The cooling technology of solar cells under concentrated system*. in *Power Electronics and Motion Control Conference, 2009. IPEMC'09. IEEE 6th International*. 2009. IEEE.
87. van Kessel, T., A. Abduljabar and H. Khonkar, *Concentrator photovoltaic reliability testing at extreme concentrations up to 2000 suns*. in *Photovoltaic Specialists Conference (PVSC), 2009 34th IEEE*. 2009. IEEE.
88. Florschuetz, L., *Extension of the Hottel-Whillier model to the analysis of combined photovoltaic/thermal flat plate collectors.* Solar energy, 1979. **22**(4): p. 361-366.
89. Russell, G.F., *Uniform surface temperature heat pipe and method of using the same*. 1982, Google Patents.
90. Coventry, J. *Performance of the CHAPS collectors*. in *Conference record, Destination Renewables–ANZSES*. 2003.
91. Zhu, L., F Boehm, Y. Wang, C. Halford and Y. Sun, *Water immersion cooling of PV cells in a high concentration system.* Solar Energy Materials and Solar Cells, 2011. **95**(2): p. 538-545.
92. Chenlo, F. and M. Cid, *A linear concentrator photovoltaic module: analysis of non-uniform illumination and temperature effects on efficiency.* Solar Cells, 1987. **20**(1): p. 27-39.
93. Verlinden, P., *Will we have a 20%-efficient (PTC) photovoltaic system*. in *Proceedings of the 17th european photovoltaic solar energy conference*. 2001.
94. Lasich, J.B., *Cooling circuit for receiver of solar radiation*. 2006, Google Patents.
95. Anderson, W.G., M. Dussinger and B. Sarraf, *Heat pipe cooling of concentrating photovoltaic cells*. in *Photovoltaic Specialists Conference, 2008. PVSC'08. 33rd IEEE*. 2008. IEEE.
96. Araki, K., H. Uozumi, and M. Yamaguchi. *A simple passive cooling structure and its heat analysis for 500 X concentrator PV module*. in *Conference Record IEEE photovoltaic specialists conference*. 2002. IEEE.
97. Mo, S., Z. Chen, and P. Hu. *Performance of a passively cooled fresnel lens concentrating photovoltaic module*. in *Power and Energy Engineering Conference (APPEEC), 2011 Asia-Pacific*. 2011. IEEE.
98. Othman, M.Y.H., B. Yatim, K. Sopian and M. Bakar, *Performance analysis of a double-pass photovoltaic/thermal (PV/T) solar collector with CPC and fins.* Renewable energy, 2005. **30**(13).
99. Luque, A., G. Sala, C. Arboiro and T. Bruton, *Some results of the EUCLIDES photovoltaic concentrator prototype.* Progress in Photovoltaics: Research and Applications, 1997. **5**(3): p. 195-212.
100. Feldman Jr, K., D. Kenney, and M. Edenburn. *A passive heat pipe cooled photovoltaic receiver*. in *15th Photovoltaic Specialists Conference*. 1981.

101. Akbarzadeh, A. and T. Wadowski, *Heat pipe-based cooling systems for photovoltaic cells under concentrated solar radiation.* Applied Thermal Engineering, 1996. **16**(1): p. 81-87.
102. Hammond, G.P., A Haraijli, C. Jones and B. Winnett, *Whole systems appraisal of a UK Building Integrated Photovoltaic (BIPV) system: energy, environmental, and economic evaluations.* Energy Policy, 2012. **40**: p. 219-230.
103. Hottel, H. and B. Woertz, *Performance of flat-plate solar-heat collectors.* Trans. ASME (Am. Soc. Mech. Eng.);(United States), 1942. **64**.
104. Deffenbaugh, D.M., S.T. Green, and S.J. Svedeman, *The effect of dust accumulation on line-focus parabolic trough solar collector performance.* Solar Energy, 1986. **36**(2): p. 139-146.
105. Gombert, A., T. Gemstmaier, M. Rottger and J. Schulz, *Performance of Concentrix CPV systems in different climates.* power, 2009. **20**(40): p. 60.
106. El-Shobokshy, M., A. Mujahid, and A. Zakzouk, *Effects of dust on the performance of concentrator photovoltaic cells.* IEE Proceedings I-Solid-State and Electron Devices, 1985. **132**(1): p. 5-8.
107. Stone, K.W., H. Hayden and V. Garboushian, *Four years of operation of the AMONIX high concentration photovoltaic system at arizona public service utility*. in *ASME 2004 International Solar Energy Conference*. 2004. American Society of Mechanical Engineers.
108. Vivar, M., R. Herrero, I Anton and F. Martines, *Effect of soiling in CPV systems.* Solar Energy, 2010. **84**(7): p. 1327-1335.
109. Glassner, A.S., *An introduction to ray tracing*. 1989: Elsevier.
110. Colina-Marquez, J.A., A.F. Lopez-Vasquez, and F. Machuca-Martinez, *Modeling of direct solar radiation in a compound parabolic collector (cpc) with the ray tracing technique.* Dyna, 2010. **77**(163): p. 132-140.
111. Groulx, D. and B. Sponagle, *Ray-tracing analysis of a two-stage solar concentrator.* Transactions of the Canadian Society for Mechanical Engineering, 2010. **34**(2): p. 263.
112. Pei, G.L., Guiqiang Su, Yuehong Ji, Jie Riffat, Saffa Zheng, Hongfei, *Preliminary ray tracing and experimental study on the effect of mirror coating on the optical efficiency of a solid dielectric compound parabolic concentrator.* Energies, 2012. **5**(9): p. 3627-3639.
113. Muhammad-Sukki, F., S. Abu-Baker, *Mirror symmetrical dielectric totally internally reflecting concentrator for building integrated photovoltaic systems.* Applied energy, 2014. **113**: p. 32-40.
114. Selimoğlu, Ö., *Design And Realization Of A New Concentrating Photovoltaic Solar Energy Module Based On Lossless Horizontally Staggered Light Guide*. 2013, Middle East Technical University.
115. Al-Shohani, W.A., R. Al-Dadah, S. Mahmoud and A. Algareu, *Optimum design of V-trough concentrator for photovoltaic applications.* Solar Energy, 2016. **140**: p. 241-254.
116. Wardhana, A.S., H. Suryoatmojo, and M. Ashari. *Design of parabolic solar concentrator to improve the optical efficiency for thermal engine generator using dual reflector Gregorian method*. in *Intelligent Technology and Its Applications (ISITIA), 2016 International Seminar on*. 2016. IEEE.
117. Schuetz, M.A., K. Shell and A. Brown, *Design and construction of a ∼ 7× low-concentration photovoltaic system based on compound parabolic concentrators.* IEEE Journal of Photovoltaics, 2012. **2**(3): p. 382-386.
118. Maiti, S., N. Sarmah, P. Bapat and T. Mallick, *Optical analysis of a photovoltaic V-trough system installed in western India.* Applied optics, 2012. **51**(36): p. 8606-8614.

119. Nilsson, J., H. Håkansson, and B. Karlsson, *Electrical and thermal characterization of a PV-CPC hybrid.* Solar Energy, 2007. **81**(7): p. 917-928.
120. Rabl, A., *Comparison of solar concentrators.* Solar Energy, 1976. **18**(2): p. 93-111.
121. Tiwari, G.N., *Solar energy: fundamentals, design, modelling and applications*. 4th ed. 2011: Alpha Science Int'l Ltd.
122. Environment Public Authority of Kuwait, *Record of solar radiation*, in *Environment Public Authority of Kuwait report*. 2013: Kuwait.
123. Kuwait, E.P.A.o., *Kuwait Environmental Report 2014*. 2014, Environment Public Authority of Kuwait: Kuwait.
124. Duffie, J.A. and W.A. Beckman, *Solar engineering of thermal processes*. Vol. 3. 1980: Wiley New York etc.
125. Al-Dowaysan, K., *Ambient Temperature Report 2013*. 2014, Directorate General of Civil Aviation, Meteorological department Kuwait.
126. Al-Dousari, A.M. and J. Al-Awadhi, *Dust fallout in northern Kuwait, major sources and characteristics.* Kuwait Journal of Science, 2012. **39**(2A): p. 171-187.
127. Kuwait, E.P.A.o., *Record of atmospheric dust*. 2013, Environment Public Authority of Kuwait: Kuwait.
128. Al-Dousari, A.M., J. Al-Awadhi, and M. Ahmed, *Dust fallout characteristics within global dust storm major trajectories.* Arabian Journal of Geosciences, 2013. **6**(10): p. 3877-3884.
129. Goossens, D., Z.Y. Offer, and A. Zangvil, *Wind tunnel experiments and field investigations of eolian dust deposition on photovoltaic solar collectors.* Solar energy, 1993. **50**(1): p. 75-84.
130. Mekhilef, S., R. Saidur, and M. Kamalisarvestani, *Effect of dust, humidity and air velocity on efficiency of photovoltaic cells.* Renewable and Sustainable Energy Reviews, 2012. **16**(5): p. 2920-2925.
131. Slingo, A., P. Ackerman and R. Allan, *Observations of the impact of a major Saharan dust storm on the atmospheric radiation balance.* Geophysical Research Letters, 2006. **33**(24).
132. Otto, S., E. Biewirth, B. Weinzierl and K. Kandler, *Solar radiative effects of a Saharan dust plume observed during SAMUM assuming spheroidal model particles.* Tellus B, 2009. **61**(1): p. 270-296.
133. Said, S.A. and H.M. Walwil, *Fundamental studies on dust fouling effects on PV module performance.* Solar Energy, 2014. 107: p. 328-337.
134. Bohren, C.F. and D.R. Huffman, *Absorption and scattering of light by small particles*. 2008: John Wiley & Sons.
135. Welford, W.T., *High collection nonimaging optics*. 2012: Elsevier.
136. Abdullahi, B., R. Al-dadah, and S. Mouhmud, *Optical performance of double receiver compound parabolic concentrator.* Energy Procedia, 2014. 61: p. 2625-2628.
137. Carvalho, M., M. Collares, J. Gordon and A. Rabl, *Truncation of CPC solar collectors and its effect on energy collection.* Solar Energy, 1985. 35(5): p. 393-399.
138. Meng, X.-l.S., Nazmi Knox, Andrew R Montecucco, Andrea Siviter, Jonathan Mullen, Paul Ashraf, Ali Samarelli, Antonio Llin, Lourdes F Paul, Douglas J, *A novel absorptive/reflective solar concentrator for heat and electricity generation: An optical and thermal analysis.* Energy Conversion and Management, 2016. **114**: p. 142-153.
139. Sellami, N. and T.K. Mallick, *Optical characterisation and optimisation of a static Window Integrated Concentrating Photovoltaic system.* Solar Energy, 2013. **91**: p. 273-282.

140. Ma, S.-H.T., Chun-Ming Lee, Yun-Parn, *Generation of a uniform-square focal spot by a compound lens for solar concentration applications.* Applied optics, 2013. **52**(13): p. 3058-3065.
141. Daabo, A.M.M., Saad Al-Dadah, Raya K, *The effect of receiver geometry on the optical performance of a small-scale solar cavity receiver for parabolic dish applications.* Energy, 2016. **114**: p. 513-525.
142. Reis, F., *Development of photovoltaic systems with concentration.* 2013.
143. Moreno, I., *Illumination uniformity assessment based on human vision.* Optics letters, 2010. **35**(23): p. 4030-4032.
144. Ensor, D. and M. Pilat, *The effect of particle size distribution on light transmittance measurement.* The American Industrial Hygiene Association Journal, 1971. **32**(5): p. 287-292.
145. Barber, P.W. and S.C. Hill, *Light scattering by particles: computational methods*. Vol. 2. 1990: World scientific.
146. Al-Attar, I.S., *The effect of pleating density and dust type on performance of absolute fibrous filters*. 2011, © Iyad Shareef Al-Attar.
147. Pilkington, *Glass Range for Architects and Specifiers.* Technical Information Datasheet, 2010. **1**.
148. Ahmed, Z., H.A. Kazem, and K. Sopian, *Effect of dust on photovoltaic performance: review and research status.* Latest trends in renewable energy and enviromental informatics, 2013: p. 193-199.
149. Richard, J. and J. Komp, *Practical Photovoltaics electricity from solar cells*. 2001, Aatec Publications, Ann Arbor, Michigan.
150. Rauchenbach, H., *Solar Cell Arrays*. 1980, Van Nostrand-Reinhold, New York.
151. Nema, R., S. Nema, and G. Agnihotri, *Computer simulation based study of photovoltaic cells/modules and their experimental verification.* International Journal of Recent Trends in Engineering, 2009. **1**(3): p. 151-156.
152. Nguyen, D.D. and B. Lehman. *Modeling and simulation of solar PV arrays under changing illumination conditions*. in *2006 IEEE Workshops on Computers in Power Electronics*. 2006. IEEE.
153. Gow, J. and C. Manning, *Development of a photovoltaic array model for use in power-electronics simulation studies.* IEE Proceedings-Electric Power Applications, 1999. **146**(2): p. 193-200.
154. Hishikawa, Y., Y. Imura, and T. Oshiro. *Irradiance-dependence and translation of the IV characteristics of crystalline silicon solar cells*. in *Photovoltaic Specialists Conference, 2000. Conference Record of the Twenty-Eighth IEEE*. 2000. IEEE.
155. Kazem, H.A., T. Chaichan, S. Saif and A. Dawood, *Experimental Investigation of Dust Type Effect on Photovoltaic Systems in North Region, Oman.* International Journal of Scientific & Engineering Research, 2015. **6**(7): p. 293-298.
156. Qasem, H., H. Albusairi and R. Betts, *Effect of dust shading on photovoltaic modules.* 2011.
157. Boykiw, E., *The effect of settling dust in the Arava valley on the performance of solar photovoltaic panels.* Senior thesis, Allegheny College, Meadville, PA, 2011.
158. Kerzmann, T. and L. Schaefer, *System simulation of a linear concentrating photovoltaic system with an active cooling system.* Renewable Energy, 2012. **41**: p. 254-261.
159. Theristis, M., N. Sarmarh and T. Mallick, *Design and numerical analysis of enhanced cooling techniques for a high concentration photovoltaic (HCPV) system.* School of Engineering & Physical sciences, Herriot-Watt University Edinburgh, United Kingdom, 2012.

160. Eveloy, V., P. Rodgers, and S. Bojanampati. *Enhancement of photovoltaic solar module performance for power generation in the Middle East*. in *Semiconductor Thermal Measurement and Management Symposium (SEMI-THERM), 2012 28th Annual IEEE*. 2012. IEEE.
161. Edenburn, M., *Active and passive cooling for concentrating photovoltaic arrays*. 1980, Sandia Labs., Albuquerque, NM (USA).
162. Beard, D.A., S.-d. Liang, and H. Qian, *Energy balance for analysis of complex metabolic networks.* Biophysical journal, 2002. **83**(1): p. 79-86.
163. F.bocchi. *How to calculate mass conservation and energy balance*. COMSOL 2015 [cited 2016 11.6.2016]; Available from: http://www.comsol.com/blogs/author/fabio-bocchi/.
164. Teo, H., P. Lee, and M.N.A. Hawlader, *An active cooling system for photovoltaic modules.* Applied Energy, 2012. **90**(1): p. 309-315.
165. Aldossary, A., S. Mahmoud, and R. AL-Dadah, *Technical feasibility study of passive and active cooling for concentrator PV in harsh environment.* Applied Thermal Engineering, 2016. **100**: p. 490-500.
166. Frei, W., *Solutions to Linear Systems of Equations: Direct and Iterative Solvers.* COMSOL Blog, 2013.
167. Abdullahi, B., *Development and optimization of heat pipe based compound parabolic collector*. 2015, University of Birmingham.
168. Chemisana, D., J Lopez and A. Coronas, *Building integration of concentrating systems for solar cooling applications.* Applied Thermal Engineering, 2013. **50**(2): p. 1472-1479.
169. Aberle, A., S. Wenham, and M. Green. *A new method for accurate measurements of the lumped series resistance of solar cells*. in *Photovoltaic Specialists Conference, 1993., Conference Record of the Twenty Third IEEE*. 1993. IEEE.
170. Thomas, H., B. Kroposki, C. Witt, W. Bower and R. Bonn, *Testing to Support Improvements to PV Components and Systems*. in *16th European Photovoltaic Solar Energy Conference and Exhibition", Glasgow, Scotland, UK*. 2000.
171. Witt, C., T. Surek, L. Mitchell and M. Symko, *Terrestrial Photovoltaics Technologies œ Recent Progress in Manufacturing R&D.* 2000.
172. Chawla, M.K. and P.E. Tech, *A step by step guide to selecting the "right" solar simulator for your solar cell testing application.".* Photo Emission Tech., Inc, 2013.
173. Ho, A. and S. Wenham. *Intelligent strategies for minimizing mismatch losses in photovoltaic modules and systems*. in *17th European Photovoltaic Solar Energy Conference and Exhibition, Munich-Germany*. 2001.
174. E927-10, A., *Standard Specification for Solar Simulation for Photovoltaic Testing.* ASTM Int'l, 2012.
175. Company, R.J. *DSEN083_933SNX Data sheet*. D'Artagnan [Product Specifications] 2015 [cited Product Specifications; Available from: http://www.robertjuliat.com/Product_Specifications/Fiches_EN/Standard/DSEN083_933SNX.pdf.
176. Håkansson, H. and B. Fredlund. *A new solar simulation facility for calorimetric measurements on windows and shading devices*. in *Proceedings of the Fifth Symposium on Building Physics in the Nordic Countries, Gothenburg*. 1999.
177. Müller-Schöll, C., S. Brunold, and U. Frei. *Significance of Spectral Correction of Collector Measurements Performed in Solar Simulators*. in *Proceedings of the Eurosun 2002 Conference, Bologna (I)*. 2002.
178. Domínguez, C., I. Antón, and G. Sala, *Solar simulator for concentrator photovoltaic systems.* Optics express, 2008. **16**(19): p. 14894-14901.

179. IEC60904-9, *Photovoltaic devices: Solar Simulator Performance Requirements.* 2007.
180. ASTME927-10, *Standard Specification for Solar simulation for Terrestrial Photovoltaic Testing.* ASTM Internationa, 2010.
181. Grandi, G., A. Ienina, and M. Bardhi, *Effective low-cost hybrid LED-halogen solar simulator.* IEEE Transactions on Industry Applications, 2014. **50**(5): p. 3055-3064.
182. Kipp&Zonen, *CMP11 Pyranometer.* Data sheet, 2016.
183. Sάnchez, G., A. Serano and M. Cancillo, *Comparison of shadow‐ring correction models for diffuse solar irradiance.* Journal of Geophysical Research: Atmospheres, 2012. **117**(D9).
184. Wu, Y., *Thermal management of concentrator photovoltaics*. 2009, University of Warwick.
185. Tapes, M.I.A.a., *Resources Data sheet*. 2015: USA.
186. Cole, A., I. Baistow, L. Brown and S. Devenport, *Silicon based photovoltaic cells for concentration–research and development progress in laser grooved buried contact cell technology*. in *7TH INTERNATIONAL CONFERENCE ON CONCENTRATING PHOTOVOLTAIC SYSTEMS: CPV-7*. 2011. AIP Publishing.
187. Antonini, A., *Flat facetted PV concentrator systems and dichroic evolution*. 2006, Phd thesis, Ferrara, Italy.
188. Hochberg, J. and P. Foster, *Four Point Probe IV Electrical Measurements using the Zyvex Test System Employing a Kethley 4200.* Zyvex Corp, 2005.
189. Platon, C., *Glass Variable Area Flowmeters.* .http://www.ctplaton.com/uploads/pdf/En/deb_ng_lg.pdf 2017.
190. Sarmah, N. and T.K. Mallick, *Design, fabrication and outdoor performance analysis of a low concentrating photovoltaic system.* Solar Energy, 2015. **112**: p. 361-372.
191. Lei, P., Y. Li, and J.E. Seem, *Sequential ESC-based global MPPT control for photovoltaic array with variable shading.* IEEE Transactions on Sustainable Energy, 2011. **2**(3): p. 348-358.
192. Sellami, N. and T.K. Mallick, *Optical efficiency study of PV crossed compound parabolic concentrator.* Applied Energy, 2013. **102**: p. 868-876.
193. Brogren, M., *Optical efficiency of low-concentrating solar energy systems with parabolic reflectors.* 2004.
194. Sellami, N., *Design and characterisation of a novel translucent solar concentrator.* 2013, Heriot-Watt University.
195. Abu-Bakar, S.H., F. Muhammed and D. Freier, *Performance analysis of a novel rotationally asymmetrical compound parabolic concentrator.* Applied Energy, 2015. **154**: p. 221-231.

Appendix A

Accuracy and Uncertainty Analysis

For all measurements in thermocouples temperature and flow rate, the overall uncertainty was predicted using standard deviation approach based on fixed and random errors with a confidence level of 95%.

$$\mathrm{U_{Overall}} = \pm\sqrt{\mathrm{U_{Sys}^2} + \mathrm{U_{random}^2}} \qquad \text{(A.1)}$$

$$\mathrm{U_{random}} = \mathrm{t_{N-1,95\%}}\sigma_{\bar{\mathrm{S}}} \qquad \text{(A.2)}$$

Where: N is samples number, t is student distribution coefficient and $\sigma_{\bar{S}}$ is the mean deviation which can be estimated as:

$$\sigma_{\bar{\mathrm{S}}} = \frac{1}{\sqrt{\mathrm{N}}}\sqrt{\frac{\sum_{\mathrm{i}=1}^{\mathrm{N}}(\mathrm{X_i}-\bar{\mathrm{X}})^2}{\mathrm{N}-1}} \qquad \text{(A.3)}$$

The systematic error can be predicted as:

$$\mathrm{U_{Sys}} = \sqrt{\sum_{\mathrm{i}=1}^{\mathrm{M}} \mathrm{U_{i,Sys}^2}} \qquad \text{(A.4)}$$

Table A.1 and A.2 summarises the calibrations and uncertainty of the thermocouples and flow meter

Table A-1 Calibration and uncertainty of thermocouples

Thermocouple	Position	Curve fit formula	Uncertainty (˚C)
1	Corner at outlet	0.9961T + 0.3272	±0.2447
2	Side near outlet	0.9976T + 0.3512	±0.2099
3	Corner neat outlet	0.9975T + 0.3972	±0.2368
4	Corner near inlet	0.9961T + 0.2254	±0.1904
5	Side near inlet	0.9938T + 0.3191	±0.1612
6	Corner at inlet	0.9955T + 0.1837	±0.2344
7	Centre	0.9957T + 0.3398	±0.1822

Table A-2 Calibration and uncertainty of water flow meter

Flowmeter	Curve fit formula	Uncertainty (mL/min)
CT Platon	0.9961Q + 1.1641	±8.857

Appendix B

Engineering Equation Solver (EES) programing code of electrical modelling for PV module

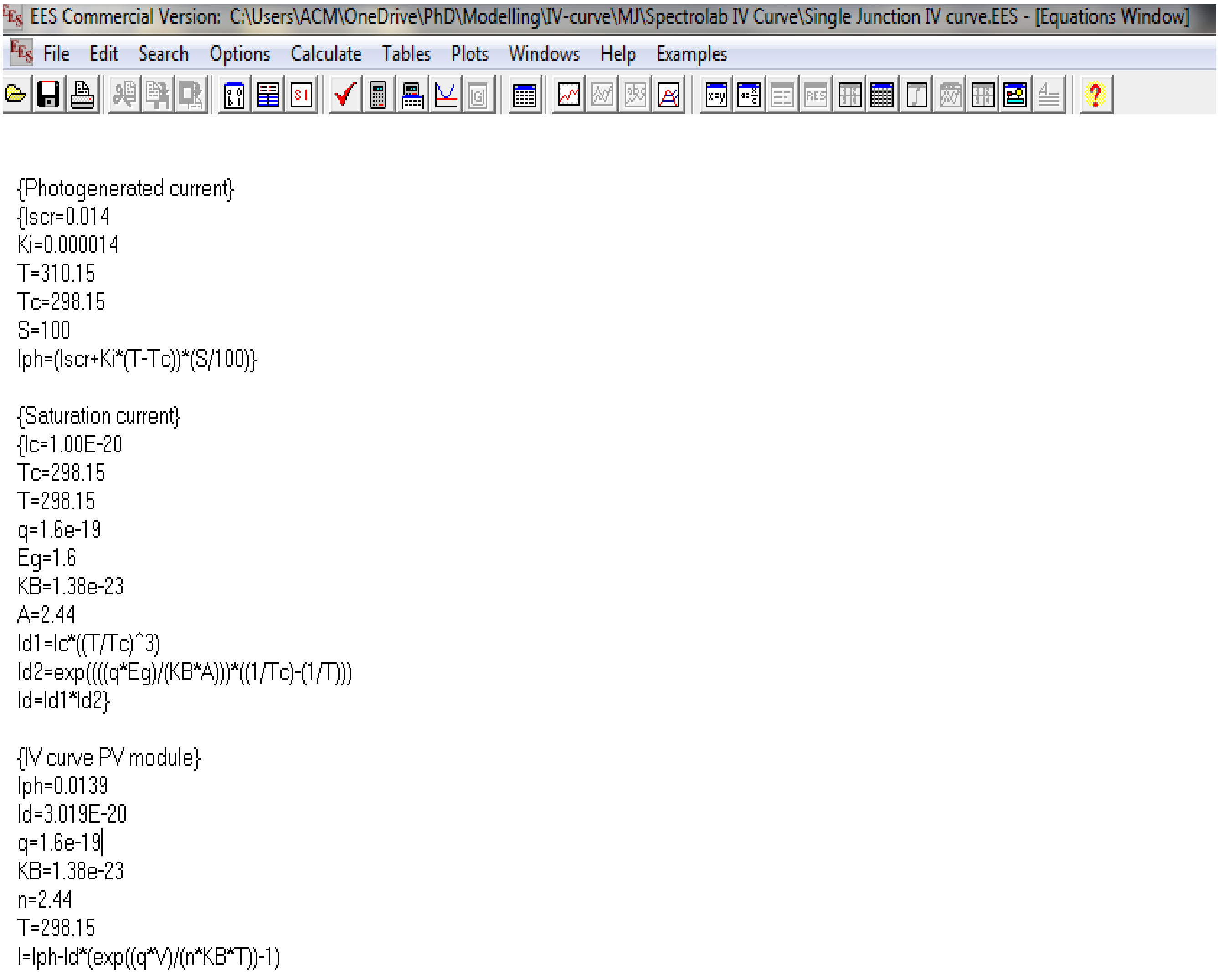

```
{Photogenerated current}
{Iscr=0.014
Ki=0.000014
T=310.15
Tc=298.15
S=100
Iph=(Iscr+Ki*(T-Tc))*(S/100)}

{Saturation current}
{Ic=1.00E-20
Tc=298.15
T=298.15
q=1.6e-19
Eg=1.6
KB=1.38e-23
A=2.44
Id1=Ic*((T/Tc)^3)
Id2=exp((((q*Eg)/(KB*A)))*((1/Tc)-(1/T)))
Id=Id1*Id2}

{IV curve PV module}
Iph=0.0139
Id=3.019E-20
q=1.6e-19
KB=1.38e-23
n=2.44
T=298.15
I=Iph-Id*(exp((q*V)/(n*KB*T))-1)
```

Accuracy and specification of the wireless I/V curve tracer (PVA-1000S) and SolSensor

Table B-1 PVA-1000S I-V Curve Tracer Specifications

Parameter	Value
PV voltage range	0–1000 V
Current range	0-20 A
Voltage accuracy 0 to 55°C	±0.5% ± 0.25 V
Current accuracy 0 to 55°C	±0.5% ± 0.04 A
Voltage resolution	25 mV
Current resolution	2 mA
Measurement duration	4s
I-V sweep duration	0.05 - 2s
I-V trace points	100 or 500
Operating temp range	-10 to +65°C
Battery life	12 hr continuous operation
Wireless range	100m

Table B-2 SolSensor (pyranometer) Specification

Parameter	Value
Irradiance accuracy	±2% typical, 0 to 1,500 W/m2
Cell temp. accuracy	±2°C
Tilt accuracy	±1 degree typical, 0-45 degree
Wireless range	100m with open line of sight
Operating temp	-10 to +65°C
Measurement interval	Irradiance: 0.1s Temperature: 1s